Karlsruhe Institute of Technology

Photochemical Synthons as Advanced Tools in Macromolecular Science

Zur Erlangung des akademischen Grades eines

DOKTORS DER NATURWISSENSCHAFTEN

(Dr. rer. nat.)

von der KIT-Fakultät für Chemie und Biowissenschaften

des Karlsruher Instituts für Technologie (KIT)

genehmigte

DISSERTATION

von

M. Sc. Janin Tanja Offenloch

aus

Mannheim-Neckarau, Deutschland

1. Referent: Prof. Dr. Christopher Barner-Kowollik

2. Referent: Prof. Dr. Hans-Achim Wagenknecht

Tag der mündlichen Prüfung: 09.05.2019

Die vorliegende Arbeit wurde von Oktober 2015 bis März 2019
unter Anleitung von Prof. Dr. Christopher Barner-Kowollik
am Karlsruher Institut für Technologie (KIT) - Universitätsbereich angefertigt.

Per aspera ad astra

"[...] Jemand hat gelernt, wie man sein Leben vergeuden kann.

Jemand hat gelernt, wie schön der Tau auf den Blütenblättern einer Blume ist. [...]"

Andreas Brandhorst, Der Zeitkrieg (Kantaki-Triologie, Band 3), Heyne Verlag, 2005.

ABSTRACT

The fusion of polymer chemistry and photo-induced ligation reactions creates a powerful platform technology to generate innovative materials, which embrace future challenges. On the one side, material properties are influenced by chemical composition and architecture of macromolecules, and on the other side, photochemistry allows spatiotemporal control over the reaction site, efficiency and sustainability of chemical reactions. Therefore, the current thesis explores novel approaches for photoreactive moieties in order to extend the horizon of photochemistry in the field of polymer chemistry and soft matter material science.

First, the current thesis covers pyrene-substituted 2*H*-azirines as a light-triggered ligation tool in polymer chemistry. Specifically, synthetic routes to a functional pyrene-substituted 2*H*-azirine were investigated, resulting in a successful strategy for a 2*H*-azirine derivative equipped with a methyl ester followed by the analysis of the photoreactivity *via* nuclear magnetic resonance (NMR) spectroscopy. Furthermore, a pyrene-substituted 2*H*-azirine was utilized to interrupt the copper(I)-catalyzed azide-alkyne cycloaddition (CuAAC) ligation of two distinct polymer blocks, allowing for synthetic access to a fluorescently labeled block copolymer. Simultaneously, a vinyl functionality as a tethering point for diverse thiol species (*i.e.*, a small molecule thiol derivative and two macromolecular thiols) in following radical thiol-ene additions was introduced at the junction point of the block copolymer species. The resulting modified block copolymer and mikto-arm star polymers were in-depth characterized *via* size exclusion chromatography (SEC), differential scanning calometry (DSC), attenuated total reflection-

infrared spectroscopy (ATR-IR) as well as NMR, UV/Vis and fluorescence spectroscopy. Further dynamic light scattering (DLS) studies of the herein obtained polymer species revealed stability against temperature and concentration changes of the micelles in water, resembling unimolecular micelles.

New aspects for the light-induced cycloaddition of *ortho*-methylbenzaldehydes are described in the subsequent chapter of the current thesis. Specifically, the photoreactive unit was coupled to a short block of polyethylene (PE). UV light-induced ligation at high temperatures with distinct maleimide moieties as dienophiles afforded an end group modified PE species and block copolymers, which were analyzed by high temperature (HT) NMR and SEC studies. Further stability tests at elevated temperatures confirmed the presented results.

The final project of the current thesis explores the photochemistry of pyrene-substituted chloro oximes and oxime esters in the realm of polymer chemistry. Photochemical properties were introduced to chloro oximes by attaching pyrene as a light harvesting unit in a two-step synthesis. The photoreactivity towards different dienophiles in combination with the orthogonality of the cycloaddition was proven, and the characteristics of the light-induced reaction were carefully monitored *via* NMR spectroscopy. Subsequently, the highly efficient end group modification of two functional polyethylene glycol (PEG) species was evidenced *via* electrospray ionization-mass spectrometry (ESI-MS) measurements. Last but not least, a photolabile oxime ester unit tethered to pyrene as chromophore was designed, and subsequently introduced into a polystyrene backbone *via* copolymerization of a corresponding monomer and styrene. The properties of the polymer species possessing varying amounts of the pyrene-substituted oxime ester unit before and after LED light exposure were investigated by employing SEC, UV/Vis and fluorescence spectroscopy as well as diffusion-ordered NMR spectroscopy (DOSY NMR).

ZUSAMMENFASSUNG

Die Kombination aus Polymerchemie und lichtinduzierten Verknüpfungsreaktionen zeigt sich als mächtiger Zusammenschluss, um innovative Materialien für eine Vielzahl von Herausforderungen zu erschließen. Auf der einen Seite können die Materialeigenschaften durch die chemische Zusammensetzung und Topologie von Makromolekülen beeinflusst werden, auf der anderen Seite ermöglichen photochemische Reaktionen die zeitliche und örtliche Kontrolle über den Verlauf von Reaktionen, die überwiegend durch Effizienz und Nachhaltigkeit geprägt sind. Aus diesen Gründen beschreibt die vorliegende Arbeit mehrere neue Methoden auf der Basis von photoreaktiven Strukturen, um den Horizont der Photochemie im Kontext der makromolekularen Chemie und der Materialwissenschaften zu erweitern.

Zu Beginn wird die Nutzung von Pyren-substituierten 2*H*-Azirinen als ligationsvermittelnde photochemische Gruppe in der Polymerchemie beschrieben. Zunächst werden möglichen Synthesewege für die Herstellung ebenjenes Heterozyklus erläutert. Hierbei wurde erfolgreich ein Pyren-substituiertes 2*H*-Azirin mit einem Methylester funktionalisiert, und die Photoreaktivität wurde mittels Kernresonanzspektroskopie (engl. nuclear resonance spectroscopy, (NMR)) belegt. Des Weiteren wurde ein Pyren-substituiertes 2*H*-Azirin eingesetzt, um die von Kupfer(I) katalysierte Cycloaddition von Azid- und Alkin-terminalen Polymerblöcken (engl. copper(I)-catalyzed azide-alkyne cycloaddition (CuAAC)) abzufangen. In diesem Zusammenhang konnte eine fluoreszierende Blockcopolymerspezies erhalten werden, die an ihrem Verknüpfungspunkt eine Vinylfunktion aufweist. Diese Doppelbindung wurde als Angriffspunkt für Thiole in einer darauffolgenden radikalischen Addition verwendet. Die so hergestellten

modifizierten Blockcopolymere und Mikto-Arm Sternpolymere wurden eingehend mittels Größenausschlusschromatographie (engl. size exclusion chromatography (SEC)), dynamischer Differenzkalometrie (engl. differential scanning calometry (DSC)), ATR-Infrarotspektroskopie (engl. attenuated total reflection-infrared spectroscopy (ATR-IR)) sowie NMR, Absorptions- und Fluoreszenzspektroskopie charakterisiert. Darüber hinaus haben Untersuchungen mit Hilfe der Dynamischen Lichtstreuung (engl. dynamic light scattering (DLS)) gezeigt, dass die synthetisierten Polymerspezies temperatur- und konzentrationsstabile Mizellen in Wasser bilden analog zu Einzelmolekülmizellen (engl. unimolecular micelles).

Neue Aspekte über die lichtinduzierte Cycloaddition von *ortho*-Methylbenzaldehyden werden im darauffolgenden Abschnitt dargestellt. Zunächst wurde die photoreaktive Gruppe mit einer kurzkettigen Polyethylen (PE) Einheit verknüpft. Die so erhaltene photoreaktive PE-Spezies wurde bei erhöhten Temperaturen in Cycloadditionsreaktionen induziert durch UV Licht eingesetzt. Die Verwendung von verschiedenen Molekülen, die aufgrund einer endständigen Maleimideinheit als Dienophil dienten, ermöglichte die lichtinduzierte Synthese von einer Endgruppen-funktionalisierten Polymerspezies und verschiedenen Blockcopolymeren, die mittels Hochtemperatur-NMR und -SEC analysiert wurden. In diesem Zusammenhang wurde auch die Stabilität der Produkte bei erhöhten Temperaturen bestätigt.

Abschließend wird die Photochemie von Pyren-substituierten Chloroximen und Oximestern für den Bereich der Polymerchemie beleuchtet. Die Reaktivität von Chloroximen bei Bestrahlung wurde durch direkte Verknüpfung mit Pyren als Chromophor erreicht. Das entsprechende Zielmolekül konnte in einer Zwei-Stufen Synthese erhalten werden. Die lichtinduzierte Cycloaddition wurde mit einer Reihe von verschiedenen Dienophilen im Hinblick auf die Orthogonalität gegenüber unterschiedlichen funktionellen Gruppen untersucht. Außerdem konnten hierbei die Eigenschaften der Reaktion und der Cycloaddukte mit Hilfe von NMR Spektroskopie festgestellt werden. Weitere massenspektrometrische (engl. electrospray ionization-mass spectrometry (ESI-MS)) Messungen zeigten die quantitative Endgruppenmodifikation von unterschiedlich funktionalen Polyethylenglykol-Spezies (PEG) mittels lichtinduzierter Cycloaddition des Pyren-substituierten Chloroxims. Darüber hinaus wurden photosensitive Oximester Einheiten in ein Polystyrolrückgrat durch Copolymerisation der entsprechenden Monomere integriert. Daraufhin konnten die Eigenschaften der Polymere vor und nach der Bestrahlung mit LED Licht im Hinblick auf den Einfluss der Menge an Pyren-substituierten Oximestern mittels SEC, DOSY (engl. diffusion-ordered spectroscopy) NMR, UV/Vis und Fluoreszenzspektroskopie ausgewertet werden.

CONTENTS

ABBREVIATIONS

ACN	Acetonitrile
AIBN	Azobisisobutyronitrile
APTES	(3-Aminopropyl)triethoxysilane
ARGET ATRP	Activator regenerated by electron transfer ATRP
a.t.	Ambient temperature
ATR-IR	Attenuated total reflection-infrared spectroscopy
ATRP	Atom transfer radical polymerization
CCG	Catalyzed chain growth
CDB	Cumyl dithiobenzoate
CMC	Critical micelle concentration
COSY	Correlation spectroscopy
CTA	Chain transfer agent
CuAAC	Copper(I)-catalyzed azide-alkyne cycloaddition
$Đ$	Dispersity index
DA cycloaddition	Diels–Alder cycloaddition
DBU	1,8-Diazabicyclo(5.4.0)undec-7-ene
DCM	Dichloromethane
DIPEA	*N*,*N*-Diisopropylethylamine

DLS	Dynamic light scattering
DMAP	4-Dimethylaminopyridine
DMF	*N*,*N*-Dimethylformamide
DMSO	Dimethylsulfoxide
$\overline{DP}_n$	Degree of polymerization
Dode-SH	1-Dodecanethiol
DoPAT	2-(Dodecylthiocarbonothioylthio)propionic acid
DOSY	Diffusion-ordered spectrocopy
DSC	Differential scanning calometry
D*t*BPF	1,1'-Bis(di-tert-butylphosphino)ferrocene
DTT	Dithiothreitol
EDC·HCl	1-Ethyl-3-(3-dimethylaminopropyl)carbodiimide hydrogenchloride
EDG	Electron-donating group
ESA	Excited state absorption
ESI-MS	Electrospray ionization-mass spectrometry
ETU	Energy transfer upconversion
EWG	Electron-withdrawing group
FMO	Frontier molecular orbital
FRP	Free-radical polymerization
HMTETA	1,1,4,7,10,10-Hexamethyltriethylenetetramine
HOMO	Highest occupied molecular orbital
HT	High temperature
IC	Internal conversion
ISC	Intersystem crossing
LED	Light emitting diode
LCMT	Lower critical micellization temperature
LUMO	Lowest unoccupied molecular orbital
MCRs	Multicomponent reactions
M_n	Number-average molar mass

M_w	Weight-average molar mass
NCS	*N*-chlorosuccinimide
NICAL	Nitrile imine carboxylic acid ligation
NIR	Near infrared
NITEC	Nitrile imine-mediated tetrazole-ene cycloaddition
NMP	Nitroxide-mediated polymerization
NMR	Nuclear magnetic resonance spectroscopy
PA	Photon avalanche
PAT	Pyrene acyl tetrazole
PE	Polyethylene
PEG	Poly(ethylene glycol)
PMMA	Poly(methyl methacrylate)
ppm	Parts per million
PS	Polystyrene
PyOCl	*N*-hydroxypyrene-1-carbimidoyl chloride
PyOHSty	Pyrene-1-carbaldehyde *O*-(4-vinylbenzoyl) oxime
RAFT	Reversible addition-fragmentation chain transfer
RDRP	Reversible-deactivation radical polymerization
RI	Refractive index
ROMP	Ring-opening metathesis polymerization
ROP	Ring-opening polymerization
SCNP	Single-chain nanoparticle
SEC	Size exclusion chromatography
TBAF	Tributylammonium fluoride
TBTA	Tris(benzyltriazolylmethyl)amine
TCB	Trichlorobenzene
TCE	Tetrachloroethylene
TCEP	Tris-(2-carboxyethyl)-phosphin
TEMPO	2,2,6,6-Tetramethylpiperidinyloxyl

TFA	Trifluoroacetic acid
THF	Tetrahydrofuran
TIPS	Triisopropylsilyl group
TMS	Tetramethylsilyl group
ToF-SIMS	Time-of-flight seconday ion mass spectrometry
TPA	Two-photon absorption
UCNP	Upconversion nanoparticle
UV/vis	Ultraviolet-visible
VR	Vibrational relaxation
VLPC	Visible light photoredox catalysis

CHAPTER 1

INTRODUCTION AND MOTIVATION

Without any doubt, nature has proven to be the master of customizability in regard to the creation of living beings. May it be hydrophobic surfaces, semi-permeable membranes or specific mechanical properties, nature has reached a high level of functionality and adaptability in order to exist under the various conditions present on the planet. Nevertheless, with polymer chemistry and material science mankind has a strong tool at its disposal for creating complex and functional soft matter materials that can be controlled in their performance by their chemical composition and architecture. In other words, each chemically distinct unit gives rise to diverse features in the desired product. Furthermore, the properties of soft matter materials are adjustable by the sequence of the monomer units and the shape of the macromolecules featuring either simple or highly complex macromolecular architectures such as block copolymers, nanoparticles, star and ring structures. Thus, polymer based materials have found application in everyday objects as well as advanced technologies. In fact, our lives today would not be possible without sophisticated soft matter materials. Therefore, improving existing materials and designing novel products in order to address future challenges have been the key driving forces behind the success of polymer chemistry. Contemporary outstanding examples for polymer based materials with tailored properties are depicted in the following examples. Stimuli-responsive polymers enable targeted drug delivery upon changes of temperature or pH value.[1, 2] Furthermore, bio-degradability allows for the decomposition into non-toxic small compounds of the material, which is conventionally stable for several years. Consequently, bio-degradable polymer species are highly beneficial for the application in living

beings and valuable due to environmental concerns.[3–6] Further, self-healing soft matter materials are able to initiate healing upon physical damage, and consequently, allow for applications in coatings and composites for engineering.[7–9] In addition, polymers play an essential role in nanotechnology as matrix for composites,[10] in supramolecular chemistry,[11, 12] and electronic devices including batteries,[13, 14] and as conductors, *e.g.*, in solar cells.[15]

Indeed, the modification of polymeric materials *via* chemical reactions is crucial to insert structural motifs and provide diverse functionality in order to obtain advanced materials. Therefore, simple yet powerful reaction protocols play a key role in polymer functionalization, especially to avoid tedious purification steps. Examples of this type of transformations are found in the context of click chemistry.[16, 17] Specifically, light-induced ligation reactions are mild as elevated temperatures are avoided, and usually require no catalyst or other additional reagents. Moreover, photochemistry can directly address current environmental issues including global warming and decreasing stocks of fossil fuels due to the utilization of sunlight as an infinite source of energy.[18, 19] In fact, plants have utilized light to trigger chemical transformation during synthesis for billions of years, demonstrating the elegance of light for precision chemistry.[20] On top of that, photochemistry adds a new dimension of control to polymer science, *i.e.* the use of light allows chemical reactions to be controlled in a spatiotemporal fashion.[21, 22] Reactions rates can also be influenced by altering the light flux and the wavelength. Consequently, these straightforward reaction protocols – resulting either in bond formation, bond cleavage or isomerization – triggered by light are highly beneficial for polymer chemistry,[23] opening high-level research opportunities and applications in the field of photochemistry in polymer science. The applications include spatial-resolved patterning of surfaces with small molecule derivatives or polymer strands,[21, 24] or the light-induced synthesis of sophisticated macromolecular architectures and networks.[25] Likewise, photochemistry allows for an accurate control over polymerization processes,[26, 27] and an access to responsive polymer films,[28, 29] *e.g.*, soft matter materials with shape-memory effect triggered upon light irradiation.[30]

The fusion of polymer science and photochemistry has resulted in a vast range of complex materials.[31–37] Nevertheless, the processes in nature are still superior compared to the present methods available for photo and polymer scientists by far. Unfortunately, the efficiency and sustainability of naturally occurring processes cannot be reached with current methods. As a result, the aim of the current research at the interface of photochemistry and polymer science is the investigation and improvement of existing light-induced

chemical reactions. Specifically, reaction pathways which are accessible *via* the utilization of visible light or sunlight are explored. Compared to ultraviolet light, irradiation sources of longer wavelengths are less energetic and possess a higher penetration depth into soft matter, eventually mimicking the conditions of the natural environment.

Chapter 3 discusses the synthesis of a functionalized pyrene-substituted 2*H*-azirine species and its implementation into a chain transfer agent suitable for reversible deactivation radical polymerization. In this context, a novel ligation technique for polymer strands is described employing conventional conditions for copper(I)-catalyzed azide-alkyne cycloaddition in combination with a pyrene-substituted 2*H*-azirine. With the resulting multicomponent reaction, a fluorescently labeled midpoint-reactive block copolymer is obtained in a facile fashion. Furthermore, the vinyl group at the junction point of the block copolymer species allows the synthesis of mikto-arm star polymer species *via* radical thiol-ene addition. The frontiers of current photochemistry are further investigated in Chapter 4. By equipping a polyethylene block with a photoreactive *ortho*-methylbenzaldehyde unit, the applicability of this photochemistry and the stability of the reaction products at high temperatures are explored. In the subsequent chapter, the reactivity of chloro oximes and oxime ester derivatives upon irradiation with visible light (or sunlight) for the modification of macromolecules is discussed. In detail, a pyrene-tagged chloro oxime is used as an efficient agent to generate a highly reactive nitrile oxide upon exposure to visible light (or sunlight) in order to introduce the pyrene moiety as fluorescent marker. Polymer species bearing pyrene-substituted oxime esters in the lateral backbone release the chromophore *via* visible light-induced fragmentation. In-depth analysis suggests subsequent chain collapse *via* radical coupling forming single-chain nanoparticles.

Each project is schematically summarized in **Figure 1.1** as they expand current knowledge and frontiers of photochemistry for macromolecular design.

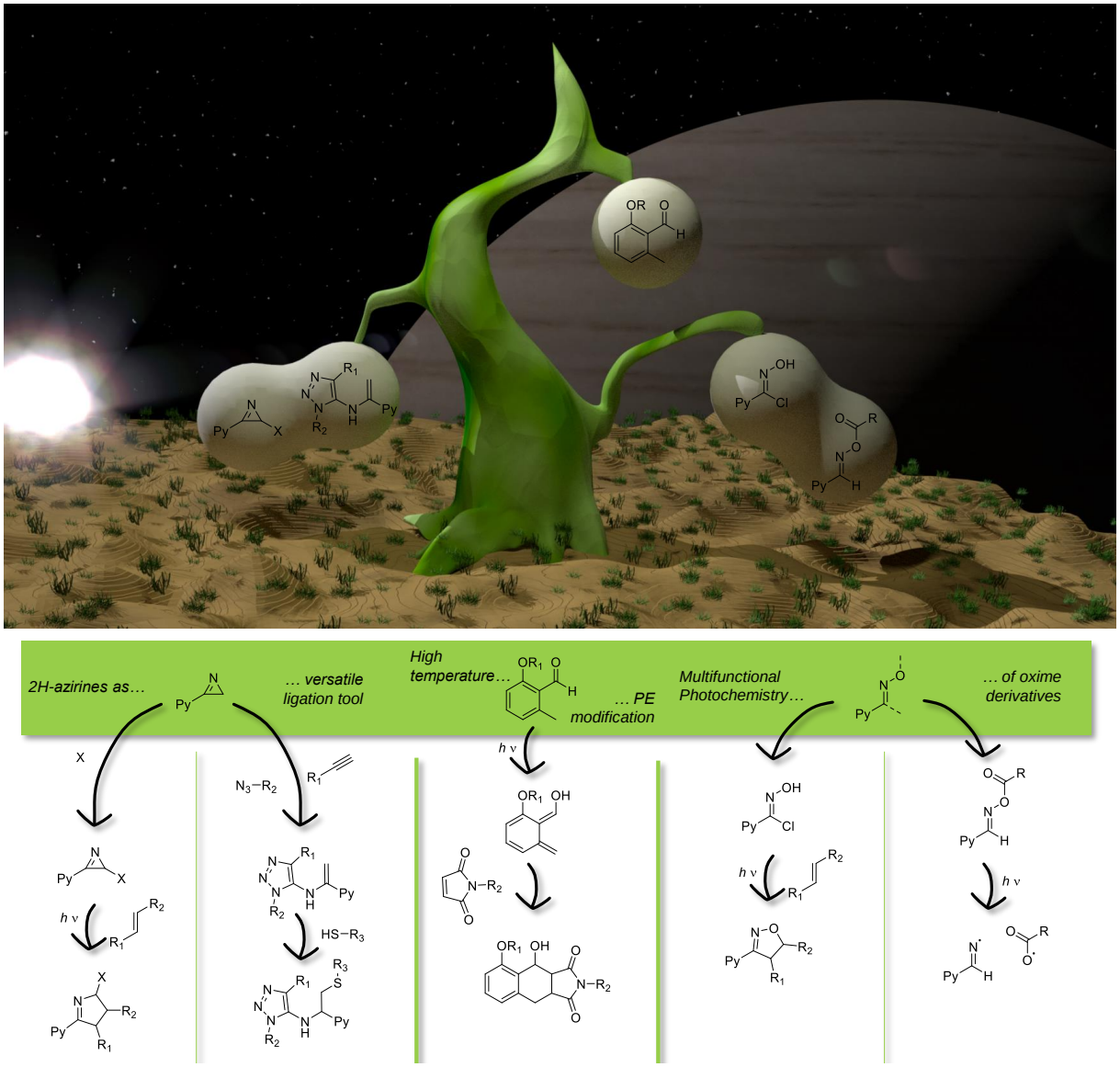

Figure 1.1. Graphical overview of the different studies included in the current thesis (Py = pyrene). Left column: Functionalization of the light-reactive pyrene-substituted 2*H*-azirine with X as connection for further relevant structures, and synthesis of block copolymer and mikto-arm star polymer species *via* copper(I)-catalyzed azide-alkyne cycloaddition (CuAAC) interrupted by 2*H*-azirines (with R_1,R_2 = polymer chain, R_3 = small molecule or polymer chain). Middle column: *Ortho*-methylbenzaldehydes-mediated ligation of polyethylene (PE) derivatives at high temperatures (with R_1 = PE, R_2 = small molecule or polymer chain). Right column: Light-induced ligation and fragmentation of pyrene substituted chloro oximes and oxime ester, respectively (with R_1,R_2 = *e.g.*, COOEt, Ph, H; R = polymer backbone).

CHAPTER 2

THEORETICAL BACKGROUND

The current chapter provides an overview of the theoretical background in combination with recent literature reports, which are related to the scientific studies included in the thesis. The chapter commences with polymer chemistry as main topic with the emphasis on free-radical and reversible-deactivation radical polymerization processes. In this context, polymer ligation techniques and macromolecular architectures will subsequently be discussed. Beer-Lambert's law, the Franck-Condon principle, the Jablonski diagram and molecular electronic transitions as physical fundamentals of photochemistry are covered in the second section, which is concluded with the description of photochemically induced transformations applied to polymer ligation. As the main topic of the current thesis, visible light-induced ligation techniques will be in-depth discussed in a separate subsection in the end. In this context, methods for a bathochromic shift of the excitation wavelength for chemical reactions are elucidated by means of, *e.g.*, the substitution of photoreactive moieties with pyrene, and further approaches such as photoredox catalysis, simultaneous two-photon absorption and upconversion nanoparticles.

2.1 Macromolecular Synthesis and Architecture

From simple products, *e.g.*, packaging and casing, to high end applications like self-healing material and drug delivery agents, polymers are smart objects omnipresent in our everyday lives. They are essential for our daily routine, for instance as eyeglasses, textiles or protective parts in vehicles. Moreover,

polymeric material possesses superior properties such as a low density and low manufacturing costs in combination with the ability to merge a vast range of distinct features, including hard- and softness, ductility, adhesiveness and responsive characteristics. On top of this, polymers are significant for the industrial sector due to their facile producibility and processability.

The triumph of polymers began with their discovery as large molecules in 1920 by Hermann Staudinger,[38] who later coined the term 'macromolecules'.[39] The experimental validation of his thesis eventually resulted in the Nobel Prize award in 1953.

Polymer chains are obtained *via* the connection of monomers during a polymerization process. However, various chain lengths are obtained due to the statistical behavior of polymerizations (refer to **Sections 2.1.1** to **2.1.2.2**). Consequently, the dispersity $Đ$, the number-average and the mass-average molar mass (M_n and M_w, respectively) represent significant key data for the characterization of polymers. They are defined in **Equation 2.1** to **2.3** (with M_i = molar mass of a chain with *i* units, and N_i = number of chains with *i* units).[40]

$$Đ = \frac{M_w}{M_n} \tag{2.1}$$

$$M_n = \frac{\sum N_i M_i}{\sum N_i} \tag{2.2}$$

$$M_w = \frac{\sum N_i M_i^2}{\sum N_i M_i} \tag{2.3}$$

If all chains of a sample possess the same chain length, a dispersity of 1.0 is obtained. In contrast, the $Đ$ value for reversible-deactivation radical polymerizations conventionally lies between 1.1 and 1.4, while the ideal value for free-radical polymerization is between 1.5 and 2.0 depending on the predominant termination mode. Therefore, the more uniform the polymer chains are, the lower the $Đ$ value.[40]

Various characterization methods for polymer samples exist. Methods that measure the colligative properties of a solution (*e.g.*, cryoscopy and vapor pressure osmometry) provide M_n. In comparison, M_w is obtained *via* light scattering.[40]

After Staudingers fundamental studies, in-depth investigations in the field of macromolecular chemistry have led to exceptional developments concerning polymerization methods, macromolecular architectures and soft matter properties, which are outlined in the subsequent subsections.

2.1.1 Free-Radical Polymerization

Due to its simplicity and excellent price/performance ratio next to the possibility to polymerize the broadest range of monomers, free-radical polymerization (FRP) has become the most dominant polymerization method in the industrial sector. The commercial plastic products, which are obtained *via* the FRP process, hold a dominant position in our everyday lives. Nevertheless, it is also a valuable tool for academia if low dispersity values are not necessary. The mechanism of the FRP process is depicted in **Scheme 2.1**.

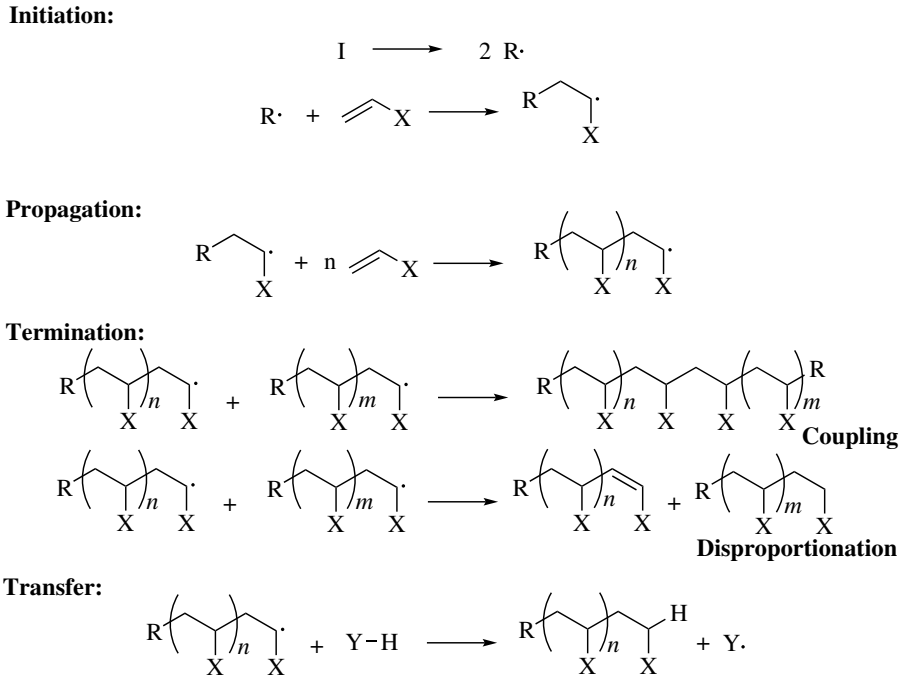

Scheme 2.1. The mechanism of free-radical polymerization consists of four main events. In the initiation step, radicals are generated upon homolytic cleavage, which initiate the chain growth. In the subsequent propagation steps, monomer units (with X as substituent) are added to the radical center forming a growing polymer chain. The chain growth is stopped *via* a bimolecular termination event. Depending on the structure of the monomer, either termination by disproportionation or coupling of two macromolecular radicals occurs. Furthermore, the radical center can be transferred to any molecule present in the polymerization including polymer chains, monomer, solvent or a deliberately added transfer agent.[41]

The generation of radicals is accomplished by thermally or photochemically induced homolytic cleavage of covalent bonds present in so-called initiators, or more rarely by redox processes.[42] Specifically, the quality of an initiator is defined as the fraction of initiator-derived radicals successfully starting the propagation. Several events during the polymerization process lower the initiator efficiency *f*, such as competitive branching and crosslinking as a result of H-abstraction induced by primary radicals. Moreover, primary radical termination *via* combination or disproportionation in the solvent cage - also termed "cage

effect"[43, 44] - lowers the efficiency.[41] The values for the initiator efficiency lie between 0.3 (less suitable initiator) and 0.8 (good initiator),[40] strongly depending on the viscosity of the polymerization mixture, the degree of conversion, the temperature, and the solvent.[41, 45, 46] Typical initiators entail labile azo and peroxide derivatives including 2,2'-azobisisobutyronitrile (AIBN), dimethyl 2,2'-azobisisobutyrate (MAIB),[47] and benzoyl peroxide (BPO). Some monomers are even able to undergo (co)polymerization without an additional initiator.[48, 49] For example, the thermally induced Diels–Alder cycloaddition between two styrene units yields a dimer, which generates a diradical after H-abstraction able to initiate chain growth.[50, 51] The formation of radicals by photochemical means is especially advantageous due to the (spatiotemporal) control over the radical formation and the rate of initiation.[52] Photoinitiators are categorized into two groups depending on their type of fragmentation. Type I initiators decompose *via* an unimolecular photofragmentation process such as α-fragmentation of carbonyl groups (*e.g.*, benzoin ethers and acyl phosphine oxides),[53, 54] or β-scission of α-substituted haloketones (*e.g.*, trichloromethyl-*S*-triazines).[55] In contrast, aryl-aryl ketones are conventional examples for type II initiators, which create radicals either *via* the abstraction of a H-atom from the solvent/ether/alcohol,[56] or by photoinduced electron and hydrogen transfer in combination with a coinitiator (*e.g.*, tertiary amines).[57] Additionally, azo and peroxide compounds are photolabile initiators as well.[41]

The decomposition of the initiator generates radicals, which each add to a monomer unit forming primary propagating radicals, which in turn add further monomers with high regioselectivity for head-to-tail linkages. Herein, the rate coefficient for propagation is independent of the chain length of the propagating chain radical, while the chain growth is strongly affected by steric and electronic factors introduced by the substituents of the double bond. Following thermodynamic aspects, the propagation step requires to be exothermic in order to increase the value for the ceiling temperature (T_c). For instance, low T_c values are experimentally determined for α-substituted styrene derivatives, and as a consequence, their polymerization needs to be conducted at low temperature, if possible at all.[41, 58, 59]

Nevertheless, propagation steps are not the only process for propagating radicals. The transfer of the radical center from the chain end to any substrate present in the polymerization mixture - also termed chain transfer reaction - decreases the molar mass. In case of inter- and intramolecular (backbiting) transfer to polymer, long and short chain branching is obtained, respectively.[60] In other cases, chain transfer agents are deliberately added to reduce the degree of polymerization and to increase the amount of polymer

molecules. Simultaneously, functional groups are introduced to the chain termini. Typical examples for chain transfer agents include mercaptanes and carbon tetrachloride.[41] In addition, for specific monomers the propagating species prefers to shift the radical center to a side chain in an isomerization reaction yielding branched polymer species.[61]

Eventually, the propagating radicals are consumed by bimolecular termination processes. Coupling reactions afford chains with twice the value of the molar mass. In contrast, saturated and unsaturated chain ends are obtained *via* disproportionation. Therefore, the termination event affects the outcome of the molecular structure. Ideally, the dispersity (refer to **Equation 2.1**) is 1.5 for recombination and 2.0 for disproportionation. The type of termination depends on steric effects of the propagating radical and the accessibility of easily abstractable β-hydrogens.[41] For instance, the polymerization of styrene mainly terminates by combination, whereas disproportionation is dominant for polymerizations of methyl methacrylate.[62] In general, the termination event is divided into three steps: In the beginning, two propagating chains approach each other *via* translational diffusion. In the following step, the arrangement of the propagating chain ends occurs, also referred to segmental diffusion. The final step includes the chemical reaction of the two chain radicals. As a result, the termination process is highly controlled by diffusion.[59, 63]

2.1.2 Reversible-Deactivation Radical Polymerization

As described in the preceding section, FRP polymerization is a highly important commercial process, since it provides a facile way to synthesize (co)polymers by employing a wide range of monomers. Nevertheless, chain-stopping reactions in FRP processes occur due to the type of the propagating species or because of the present reagents in the mixture. Low control over some significant properties including molar mass, dispersity and polymer architecture are the consequence. As a result, the aim is obvious: Suppressing termination events (coupling or disproportionation) and transfer reactions.[40, 64, 65] Under specific conditions, ionic polymerizations are able to fulfill these requirements. Anionic polymerizations even meet the criteria of being "living" by lacking any termination processes, and thus enable the synthesis of block copolymers.[66–69] The limited choice of polymerizable monomers and the stringent conditions necessary for a successful ionic polymerization are its main drawbacks. As a consequence, it is highly desirable to polymerize monomers by free-radical means in a controlled fashion. For polymerizations

following a radical mechanism, the lifetime of radicals needs to be extended from seconds to hours by suppressing bimolecular termination reactions. Two different principles are successful in the extension of the lifetime of the reactive species: The introduction of either dormant states or reversible chain transfer reactions for propagating radicals. Therefore, these approaches allow the synthesis of block copolymers by the sequential addition of monomers to the polymerization mixture, and deliver a narrow distribution of molar masses. Furthermore, the evolution of molar mass displays a linear growth over monomer consumption. Despite several discussions about the terminology of these polymerizations, they are now termed reversible-deactivation radical polymerization (RDRP).[65, 70] Over the last years, three different approaches have gained the most attention: The nitroxide-mediated polymerization (NMP), the atom transfer radical polymerization (ATRP) and the reversible addition-fragmentation chain transfer (RAFT) polymerization.[64, 65] The latter two methods in combination with the catalyzed chain growth (CCG) concept as a special case for the polymerization of ethylene will be discussed in the following subsections.

2.1.2.1 Atom Transfer Radical Polymerization

The atom transfer radical polymerization (ATRP) method allows for the synthesis of polymer strands in a controlled fashion introducing dormant states for the radical species. First reported in 1995 by the groups of Matyjaszewski and Higashimura,[71, 72] the ATRP process is nowadays a well-established polymerization protocol with a wide field of applications.[64]

The ATRP polymerization originates from atom transfer radical additions (ATRA), in which adducts of olefin derivatives and alkyl halides are formed.[73] As a result, the equilibrium reaction that reduces the concentration of propagating radicals during the polymerization, relies on a reversible redox reaction catalyzed by a transition metal complex (refer to **Scheme 2.2**). The dormant species P_n-X (with X as (pseudo)halogen atom) is activated by the abstraction of X, while the transition metal complex is simultaneously oxidized. The ligands of the metal complex solubilize the complex in the polymerization medium with Y as an additional counterion. *Vise versa*, the metal complex is reduced, and the propagating radical species terminates, generating the halogen adduct as the dormant species. The chain growth proceeds analogous to the free-radical polymerization by the sequential addition of monomers to the radical species. Nevertheless, termination still occurs, however, to a substantially lower degree.[64]

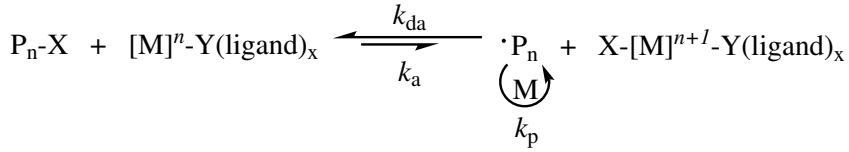

Scheme 2.2. Mechanism of the ATRP process. The radical concentration is reduced due to the formation of a dormant species P_n-X, which is reactivated by the transfer of the (pseudo)halogen atom X to the transition metal complex [M]. In the process, the transition metal is oxidized. The interplay between the propagation rate coefficient k_p and the equilibrium constant $K = k_a/k_{da}$ determines the polymerization rate.[64]

For a successful ATRP polymerization, numerous factors have to be taken into account: The monomer, the catalytic system with its counterions and ligands, the (pseudo)halogene-containing initiator, the solvent, the temperature, the concentration, the solubility and the order of addition of the individual components. Consequently, for a conventional ATRP procedure, metal halides with two neighboring oxidation states and affinity towards halogens, *e.g.*, CuBr, are employed. Common solubilizing ligands entail *e.g.*, 2,2'-bipyridine (bipy), 1,1,4,7,10,10-hexamethyltriethylenetetramine (HMTETA) or triphenyl phosphine. The initiator needs to possess a cleavable C-X bond as present in *e.g.*, benzyl halides and α-halo esters.[64] The polymerization can be conducted in bulk, solution, suspension,[74] emulsion,[75] or dispersion.[76] Yet, the presence of oxygen and nitrogen- or carboxylic acid-containing monomers draws attention, since the facile oxidation of Cu(I) to Cu(II) and the competitive complexation of Cu ions by monomer units, potentially result in deviations in the polymerization process.[64, 77, 78]

Beside the conventional ATRP process, other variations have been developed to establish the dormant species as depicted in **Scheme 2.2**. In a reverse ATRP protocol, thermal or photochemical initiators are utilized in order to generate the radical species. In this process, deliberately added Cu(II) halides and the propagating radical form the dormant species.[79, 80] Furthermore, reducing agents prevent the loss of Cu(I) species due to termination reactions during the polymerization process, and simultaneously, reduce the required amount of catalyst. Various approaches rely on the application of reductants, indeed, the way how the Cu(I) complex is generated *in situ* differs (*e.g.*, by electrochemical or radical means). Among these approaches, the activators regenerated by electron transfer (ARGET) ATRP polymerization is one of the most widely used concept. Non-radical reducing agents, such as ascorbic acid or tin 2-ethylhexanoate, allow the polymerization of various monomers with a concentration level of the copper complex in the ppm-range. The reductant generates Cu(I) at the beginning of a polymerization and maintains its concentration throughout the process. Therefore, high concentrations of copper complexes and the use

of oxygen-labile copper compounds is circumvented.[81–83] Moreover, an excess of nitrogen ligands, *e.g.*, HMTETA, fulfills the role as reducing agent as well, making the addition of further reagents to the polymerization mixture obsolete.[84]

ATRP and its variations are powerful tools for polymer chemists. Complex macromolecular architectures are readily realized including block copolymers,[85, 86] graft polymers[87, 88] and star-shaped structures.[89] Since a halogen atom is installed at every chain terminus, variable chemical transformations are feasible. In order to remove the bromine end group, hydride donors including tributyltin hydride replace the halogene functionality with a hydrogen atom.[90] Furthermore, the introduction of azide and cyclopentadiene end groups *via* substitution is possible, which are suitable for subsequent polymer ligation using cycloaddition reactions (refer to **Section 2.1.3.2**).[91, 92] A further hydrolysis of the azide unit allows synthesis of polymer strands with amino termini.[91] Pursuing the concept of the ATRA reaction, non-polymerizable monomers by the ATRP process such as maleic anhydride are introduced at the chain end as functionality by employing CuBr and bipy.[93]

2.1.2.2 Reversible Addition-Fragmentation Chain Transfer Polymerization

In contrast to the ATRP polymerization protocol, reversible addition-fragmentation chain transfer (RAFT) polymerization limits the formation of termination products through the establishment of reversible chain transfer reactions. The RAFT process was introduced in 1998 by Chiefari *et al.*, and it is the latest addition in the field of RDRP methods.[94–96]

The mechanism of the RAFT polymerization is depicted in **Scheme 2.3**. In the initiation step, the delivery of primary radical species can proceed *via* the fragmentation of heat-labile initiators (*e.g.*, azo- or peroxy type initiators) or photoactivable compounds (*e.g.*, benzoin and derivatives). In order to reduce the amount of termination products, the chain growth of the propagating radical species is stopped by a reversible chain transfer to the RAFT agent (also referred to as chain transfer agent, CTA), that features the R- and Z-group as vital structural parameters. Either dithioesters, trithiocarbonates, thiocarbamates or xanthates are added to a RAFT polymerization as CTA to introduce reversible chain transfer reactions. In the preequilibrium, the reversible addition of the growing chain generates a labile intermediate stabilized by the Z-group, which either releases the recently added chain radical or the R-group. For an efficient RAFT process, the fragmentation liberating the R-group as propagating radical has to be preferred. As

a consequence, the structural design of the R-group is highly important since it needs to effectively reinitiate the polymerization of a given monomer. The propagating chain initiated by the R-group is reversibly terminated by the addition to a macroRAFT agent, that carries a polymer chain instead of the R-group. Nevertheless, termination processes still exist, yet their occurrence is significantly reduced by the reversible chain transfer.[97, 98]

Initiation:

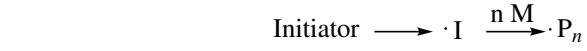

Preequlibrium:

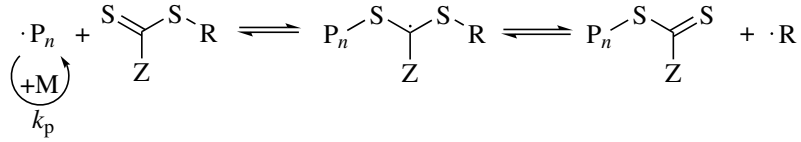

Reinitiation:

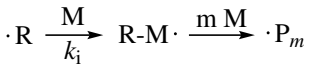

Main equilibrium:

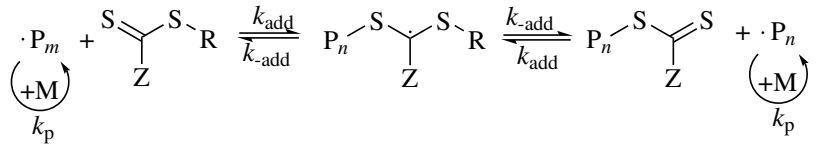

Termination:

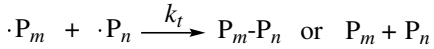

Scheme 2.3. Mechanism of the RAFT process. While the initiation step proceeds similar to conventional free-radical polymerizations, the establishment of the main equilibrium ensures that termination events are reduced. In the preequilibrium, the propagating chain reversibly adds to the RAFT agent in order to form a labile intermediate stabilized by the Z-group, which either liberates the R-group as propagating radical or the chain radical. In the following step, the R-group reinitiates chain growth with k_i as rate coefficient. The propagating chain derived from the reinitiation step is reversibly terminated in the main equilibrium. k_{add} represents the rate coefficient for the addition of the macromolecular radical in the main equilibrium, while k_{-add} governs the release of the chain radical. k_t and k_p are the rate coefficients for bimolecular termination and for propagation, respectively.[97, 98]

The main equilibrium of the RAFT process is responsible for the reduction of the termination events, while maintaining the concentration of propagating chains. With the same amount of initiator, FRP and RAFT polymerization are equally fast. In contrast, the ATRP process is slower due to reduction of the radical species.

The choice of the R- and Z-group of the CTA determines the control over the polymerization of a selected monomer, and therefore, influences the outcome - the molar mass and dispersity - of a polymerization

process. On the one hand, efficient and fast reinitiation of the polymerization process is a strict condition for the R-group. As a result, the structure of the released radical (either tertiary or secondary) and its stability (influenced by groups including phenyl or cyano) have to be adjusted to the characteristics of the propagating radical of the monomer. The radical derived from the R-group needs to be a good leaving group and to preferentially add to monomer. On the other hand, the Z-group needs to stabilize the intermediate in order to favor the addition of the propagating chain to the RAFT agent. Nevertheless, if the intermediate is too stable, the release of growing radical chains is hindered, which leads to inhibition of the polymerization. As a consequence, there is no universal RAFT agent for all types of monomers, and the RAFT agent has to carefully selected. For a successful RAFT polymerization with low dispersities, the RAFT agent to initiator concentration ratio should be between 5 to 1 and 10 to 1.[40, 97, 98]

Block copolymers are obtained in a facile way employing either the method of sequential addition of monomers during polymerization or by isolating the macroRAFT agent. Nonetheless, the monomer which generates the more stable radical has to be polymerized first.[99–101] In addition, various ways exists for the introduction of an end group functionality. If the requested chemical group is orthogonal to the polymerization conditions, it can be directly tethered to the RAFT agent. The functional groups are preferentially incorporated into the R-group, since the polymer chains, which terminate by radical coupling or disproportionation, do not feature the Z-group. Furthermore, the C-S double bond - also referred to as RAFT end group - is able to undergo variable transformations, which are readily detectable and quantifiable *via* UV/Vis measurements, because the RAFT group is colored (yellow, orange, pink or red).[102, 103] Nucleophiles, especially primary and secondary amines, convert the RAFT end group into thiols that are susceptible towards oxygen forming disulfide species without additional reducing agents.[104–106] Depending on the structure of the employed CTA, elevated temperatures between 120-200 °C induce fragmentation of the end group providing unsaturated termini.[103, 107] Moreover, a radical source causes addition to the C-S double bond followed by recombination with another radical fragment or a hydrogen atom of a deliberately added H-donor, yielding saturated chain ends.[108] In addition, the electron-deficient nature of the C-S double bond enables RAFT end groups to participate in hetero-Diels–Alder cycloadditions as dienophile. For example, trifluoroacetic acid (TFA) triggers the ligation of pyridinyl-dithioformate end groups with cyclopentadiene-modified cellulose at ambient temperature, while hexadiene moieties are coupled with diethoxyphosphoryl-dithioformate termini at 50 °C assisted by

$ZnCl_2$.[109, 110] In contrast, the reversible cycloaddition between cyanodithioesters and cyclopentadienes, as well as the irreversible reaction of dithiobenzoates and *ortho*-quinodimethanes at ambient temperature proceeds without any additional reagents.[111, 112] At last, oxidizing agents, *e.g.*, *tert*-butyl hydroperoxide, and UV irradiation (360 nm) transform dithioester into thioester and radicals, respectively.[113–115]

Compared to the NMP and ATRP polymerization, the RAFT process is applicable to a broader field of monomers.[96, 97] However, the color and the odor of polymers obtained *via* RAFT polymerization can cause issues in certain fields.[40] The broad range of chemical transformation of the end group towards various reagents and under certain conditions as discussed in the preceding paragraph potentially result in undesired instability of the polymer species. Nevertheless, it also holds the potential for various postpolymerization modification reactions.

2.1.2.3 Catalyzed Chain Growth Concept

Polymerization by coordination chemistry (*e.g.*, the Ziegler-Natta process) has provided access to various important polyolefins, such as high density and linear low density polyethylene and isotactic polypropylene, which are highly valuable for many applications due to their favorable mechanical properties.[116] Depending on the nature of the employed monomer, typical Ziegler-Natta catalysts consist of a combination of an organometallic compound possessing a metal from the main groups I, II or III (*e.g.*, triethylaluminium) and a transition metal complex (*e.g.*, $TiCl_4$).[117] During the initiation process, the combination of such metal compounds yields a transition metal species with a vacant coordination site and a metal-carbon bond. Subsequently, the polymerization is accomplished by the coordination of an olefin to the transition metal complex followed by insertion of the monomer into the metal carbon bond (refer to **Scheme 2.4A**).[116, 118, 119]

Certain catalytic systems indicate an exceptional behavior: Transfer reactions between the transition metal complex (*e.g.*, lanthanidocene complexes) and the main group compound (*e.g.*, dialkyl magnesium) occur, that are in specific cases fast and reversible, eventually resulting in pseudo living polymerization of olefin derivatives with low dispersities and a linear increase in molar mass. As a consequence, the main group organometallic species act as a reversible CTA - similar to the RAFT process - storing the polymer chains during growth, which is catalyzed by the transition metal complex (refer to **Scheme 2.4B**).[116, 120, 121] Thus, this phenomenon was termed catalyzed chain growth (CCG) by Gibson and

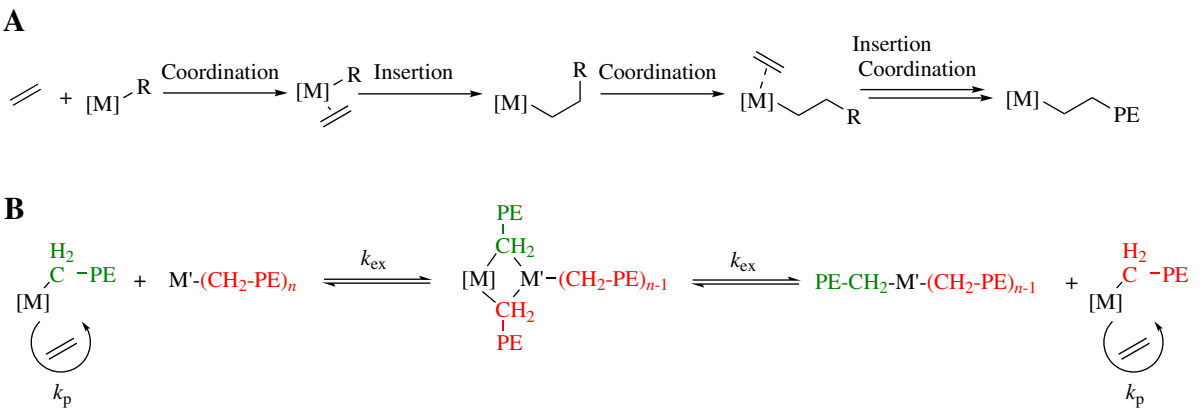

Scheme 2.4. Comparison between the Ziegler-Natta process (**A**) and the catalyzed chain growth (CCG) concept (**B**). The Ziegler-Natta process is a valuable tool for industry to produce thermoplastics such as high density polyethylene using a transition metal species [M] with a carbon metal bond and a vacant coordination site (refer to part **A**). In contrast, the CCG concept has found its way into academic laboratories due to the possibility to polymerize olefins, *e.g.*, ethylene, in a controlled fashion. Similar to the RAFT process, a main group organometallic species M' is employed as CTA during chain growth catalyzed by the transition metal [M] (refer to part **B**).[116, 120, 121]

co-workers.[122, 123] In comparison to RDRP processes, termination reactions *via* radical coupling are absent in the CCG concept, while β-H elimination presents a potential transfer reaction, which reduces the controlled character of the polymerization. Nevertheless, the careful adjustment of the electronic and the steric nature of the catalyst suppresses chain stopping events, allowing the block copolymer synthesis of various olefins.[116, 124] The facile introduction of a functional group at the chain termini presents a further benefit of the CCG concept, since every chain end is coupled to a metal, and consequently, they are highly nucleophilic.[116, 125, 126] Functional groups including iodo, azido, amino, thiol, hydroxy, vinyl, and phosphonic acid can be successfully tethered to the chain ends of polyethylene.[125, 127–130] Long considered a non-functional polymer, the gate opened for unpolar polyolefins such as polyethylene to be utilized in the synthesis of macromolecular architectures for example as monomer, building block or transfer agent.[126, 131–133] However, one drawback for the polymerization of olefins by the CCG concept exists. High molar masses are not accessible, since with increasing chain length during the polymerization, the polyolefins become substantial more insoluble in the reaction medium. Higher temperatures or the addition of a comonomer in order to decrease the crystallinity are two methods that enhance the solubility of the growing chains. Nevertheless, elevated temperatures support β-H elimination as termination event as well.[126]

2.1.3 Polymer Ligation Protocols

Chemical composition and macromolecular architecture have a high impact on the properties of synthetic polymers. Certainly, a straightforward approach to fuse two polymer-types with distinct features is accomplished by the random copolymerization of their respective monomers. However, specific monomer combinations are difficult to polymerize due to a large disparity in radical reactivity.

Nevertheless, selected applications including nanostructured thin film systems and micelles for drug delivery require separated yet connected domains of properties.[99] (Multi)block copolymers possessing distinct polymer blocks connected by covalent bonds to form a linear chain are able to address the latter issue. The development of RDRP techniques provides access to block copolymers by the sequential polymerization of monomers. However, some sequences of monomer block copolymerization cannot be realized or some restrictions exists. In this regard, in the RAFT process the monomer which forms the more stable radical has to be polymerized first. Meanwhile, block copolymer formation *via* ATRP polymerization is also limited in the sequence of monomer addition, despite that it is offering the opportunity for a halogen exchange in order to change the order of polymerization.[134, 135] Due to the limitations of RDRP processes, polymer ligation protocols are a powerful tool to manipulate macromolecular structures, and therefore the properties of soft matter. Nevertheless, high demands are placed on these chemical reactions since the purification of polymers is very challenging, and hence the reactivity of individual groups in the polymer backbone or at the chain termini can be lowered compared to reactions involving small molecules.

The properties of chemical reactions in the context of the *click* philosophy including the demands of polymer chemistry will be discussed in the subsequent subsection followed by examples of ligation chemistry, which have been successfully employed within in the current thesis. In contrast, photochemical transformations that depict *click* characteristics are covered in **Section 2.2.4**.

2.1.3.1 *Click* Chemistry

The number of organic chemical reactions is vast, still many of them are kinetically slow, require harsh conditions, or proceed with many side reactions and with limited selectivity. In order to establish a novel category of superior chemical reactions, H. C. Kolb, M. G. Finn and K. B. Sharpless introduced the *click* chemistry concept in 2001.[16] Taking processes in nature as a role model, they demonstrated their concept

by plain yet highly efficient carbon-heteroatom bond forming reactions, while describing the criteria for fulfilling the essence of *click*. The criteria are as follows:

- Modular reaction conditions. Modularity entails the concept of linking different molecules and the possibility to exchange reactants to obtain novel products easily.
- Quantitative yields of the desired product.
- The reactions need to proceed highly selectively and rapidly. The underlying cause for these properties are high thermodynamic driving forces, which are usually greater than 20 kcal mol^{-1}.
- Wide in scope, *i.e.*, the reaction must be applicable to a broad range of compounds and to small- or large-scale synthesis.
- Simple product isolation (either by recrystallization or distillation, no chromatographic methods).
- Non-toxic by-products (if any).
- Stereospecific.
- Non-demanding reaction conditions, *i.e.*, no compound is sensitive towards oxygen or moisture.
- Readily available starting materials and reagents.
- Reactions should proceed in bulk if possible, if not the solvent should be benign and easily to remove.

The evaluation of the above mentioned criteria displays that most of the chemical reactions are not able to address these points. Indeed, Sharpless and co-workers clearly illustrated some specific examples fulfilling their concept including additions to carbon-carbon multiple bonds (*e.g.*, epoxidation), nucleophilic substitutions (*e.g.*, ring-opening of aziridines and epoxides), "non-aldol" type carbonyl chemistry (*e.g.*, the formation of ureas, oxime ethers, hydrazones and amides) and cycloadditions including 1,3-dipolar cycloadditions and Diels–Alder reactions.[16]

As strict as these criteria for the *click* concept may seen, nonetheless, for application in polymer science the challenge for chemical reactions is even harsher. The cause lies with the difficult purification methods of polymers. The main options to purify a polymer are precipitation and dialysis. In small molecule organic synthesis, a vast range of methods are available including precipitation, distillation, column chromatography and recrystallization. As a result, a reaction within the realm of polymer science

must proceed quantitatively using equimolar ratios unless the starting material can be recovered. Excess molar ratios might be applied if the removal by selective precipitation is successful. However, for large-scale polymer-polymer conjugation it is practically impossible to separate a mixture of almost identical polymer blocks. This situation clearly underlines the significance of equimolarity, very high yields and high selectivity of reactions in the field of polymer chemistry. Small-scale reactions can be purified *via* preparative size-exclusion chromatography, regardless it is a tedious method violating the spirit of *click* chemistry.[17] Nevertheless, the concept of *click* chemistry had an enormous influence on polymer chemistry. A potentially larger impact on the modification of soft matter materials than on the synthesis of biorelevant molecules as Sharpless *et al.* intended to.[17, 136] A true paradigm shift in the design of macromolecular architectures took place, redefining the way we access complex macromolecular architectures.[137, 138]

2.1.3.2 [4+2] and 1,3-Dipolar Cycloadditions

Cycloadditions present by far the most important class of chemical reactions for polymer functionalization. Depending on the number of participating electrons and the structure of the starting material, diverse versions of the reaction are in-depth described, which proceed either thermally or photochemically. In the presented section, only cycloadditions under thermal control are depicted.

In a [4+2] cycloaddition, a diene reacts with a dienophile to form a cyclohexene derivative. The reaction proceeds pericyclic, *i.e.*, the four conjugated π-electrons of the *cis*-diene and the two π-electrons of the dienophile are rearranged in a single cyclic transition state without intermediates, driven by the formation of a σ-bond at the expense of a π-bond (refer to **Scheme 2.5A**).[139] O. Diels and K. Alder, who first reported the reaction in 1928, have gained much approval since this cycloaddition reaction is highly valuable due to the formation of a C-C bond, while being atom-efficient without the in-principle need of a catalyst.[140] As a consequence, their work was recognized with the Nobel Prize in 1950, and since then the [4+2] cycloaddition is often referred to as Diels–Alder (DA) cycloaddition.

Due to its efficiency, the DA cycloaddition is an in-depth studied reaction. According to the Woodman-Hoffmann rules,[141] which predict the process of pericyclic reactions and the geometry of the products, the π-electrons of the diene and dienophile of this thermally allowed process undergo suprafacial-suprafacial interactions prior to product formation (refer to **Scheme 2.6**). Which regioisomer is preferentially formed

strongly depends on the nature of the starting material. In this regard, substituents, either electron-donating or electron-withdrawing, and their position influence frontier orbital energies and coefficients. Generally, the regioisomer is preferred for which the diene and dienophile indicate similar frontier orbital energies and coefficients (refer to **Scheme 2.5B**).[142] In addition, the DA cycloaddition is stereoselective as well. By taking the exemplary reaction of cyclobutadiene and a substituted dienophile, two stereoisomeres can be realized. The endo-product is favored at low temperatures since either secondary orbital interactions or Coloumb interactions reduce the energy of the transition state. In contrast, elevated temperatures promote the formation of the exo-product due to the fact that the endo-product is usually sterically hindered, and it is therefore less thermodynamically stable (refer to **Scheme 2.5C**).[143–145]

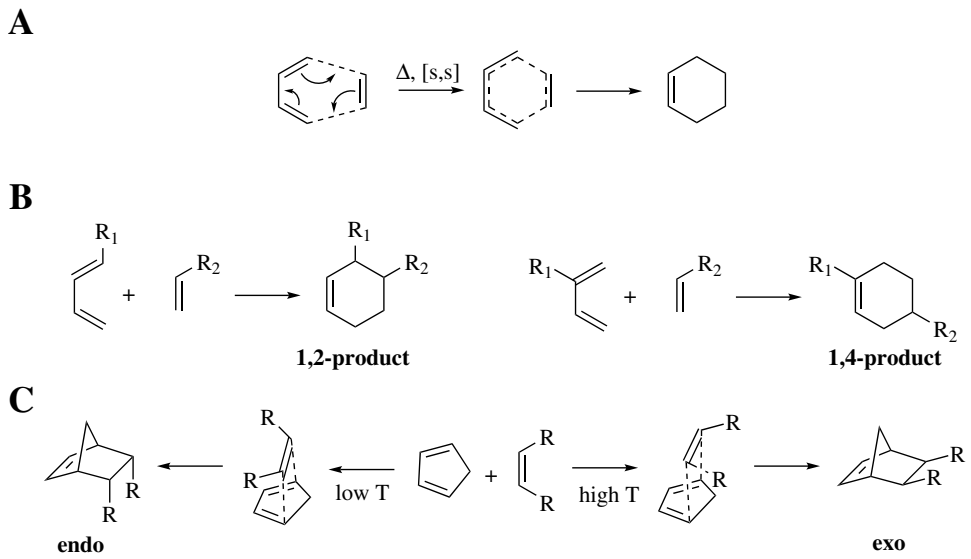

Scheme 2.5. The Diels–Alder cycloaddition proceeds pericyclic without intermediates. The cyclic transition state is depicted in part **A**. The regioselectivity is determined by frontier orbital energies and coefficients. Typically, 1-substituted dienes prefer to generate 1,2-substituted products, and 2-substituted dienes favor cyclohexenes with 1,4-substitution, if the diene and the dienophile carry opposing electron-donating and -withdrawing groups (part **B**). The stereoselectivity of the DA reaction depends on the temperature as shown in part **C**. High temperatures support the thermodynamically more stable exo-product, while the endo-product is preferred at low temperatures due to secondary orbital interactions or Coloumb interactions.[139, 142–145]

Finally, even the reaction rate and yield can be qualitatively predicted by employing frontier molecular orbital (FMO) theory in which the interaction or energy gap between the highest occupied molecular orbital (HOMO) of one reactant and the lowest unoccupied molecular orbital (LUMO) of the other reactant is evaluated.[146] If the energy levels are close, the reaction is faster (refer to **Scheme 2.6**). As a result, three different cases for the DA cycloaddition can be established. The neutral DA reaction as the first

variant indicates similar energy levels for the diene and the dienophile receiving large and equal energy spacing between the individual HOMOs and LUMOs. Consequently, the neutral DA reaction is slow, or/and low yields are obtained. However, the energy levels can be tuned by substitution of the reactants. While electron-donating substituents (EDG), *e.g.*, methoxy and alkyl groups, increase the relative FMO energy, the energy is reduced by additional electron-withdrawing groups (EWG), *e.g.*, carboxy or carbonyl functionalities. In comparison to the neutral DA reaction, Diels-Alder reactions with normal electron demand, classified as the second case, are exceptionally successful by utilizing electron-rich dienes and electron-poor dienophiles. As a consequence, the energy distance between the HOMO of the diene and the LUMO of the dienophile is reduced in favor of the cycloaddition. Compared to the DA with normal electron demand, the diene and dienophile feature substitution with opposite electronic influence in DA reactions with so-called inverse electron demand. Therefore, the LUMO of electron-poor dienes interacts with the HOMO of dienophiles with electron-donor substituents due to similar energies.[145, 147, 148]

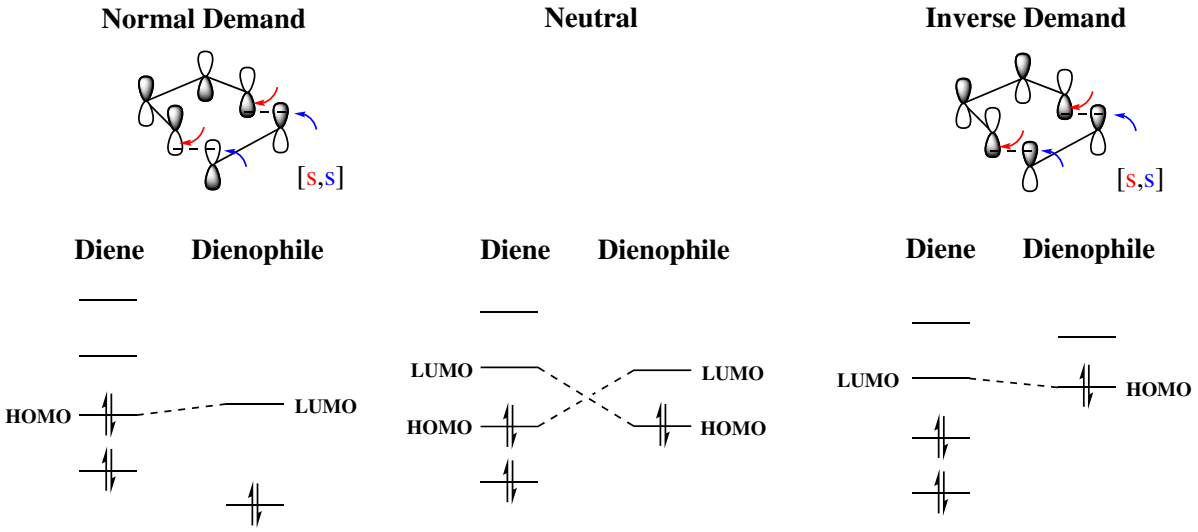

Scheme 2.6. Comparison between the three different cases in Diels-Alder reactions according to FMO. Electron-rich dienes and electron-poor dienophiles react in a Diels–Alder cycloadditions with normal electron demand (left part). As a result, the HOMO of the diene is raised due to electron-donating substitution, while electron-withdrawing groups lower the energy of the LUMO of the dienophile, providing a minimized energy cap. Neutral Diels–Alder reactions are classified by a large difference of the reacting orbitals; may it be the LUMO of the diene and the HOMO of the dienophile or *vise versa* (middle part). Compared to the version with the normal electron demand, the Diels–Alder reaction with inverse electron demand indicates an inverted substitution pattern. The diene is functionalized with electron-withdrawing groups lowering the LUMO, and the HOMO of the dienophile is raised by electron-donating substituents (right part), leading to a small energy difference between the HOMO of the dienophile and the LUMO of the diene.[141, 145–148]

Selected Diels–Alder cycloadditions directly address most of the *click* criteria including fast reaction rates, the absence of a catalyst, high yields and selectivity. Therefore, this cycloaddition is commonly utilized in polymer chemistry.[149] Among the combinations of suitable compounds, the cycloaddition of maleimides and furans is the most employed one. Still, maleimides are also able to react with cyclopentadienes and anthracenes.[150] For the incorporation into soft matter materials, maleimides require protection prior to polymerization or modification reaction,[151, 152] whereas cyclopentadiene can be readily introduced at the chain termini *via* substitution.[153] Additionally, electron-deficient dithioester end groups of RAFT polymers are able to act as dienophile in hetero-Diels–Alder reactions enabling the straightforward synthesis of block copolymers and star architectures (refer to **Section 2.1.2.2**).[111, 154, 155] Furthermore, triazolinediones (TADs) either react irreversibly with dienes in a hetero-DA cycloaddition or reversibly with indoles in an Alder–Ene reaction.[156] The TAD compound also allows for the synthesis of block copolymers and graft copolymers.[157, 158] A further appealing feature of the Diels–Alder cycloaddition is its reversible nature. The synthesis of self-healing soft matter materials is feasible using DA chemistry.[159] Hereby, the temperature for the retro-DA reaction depends on the chain length and the location of the linkage in block copolymers.[160, 161] In the present thesis, the light-triggered generation of *ortho*-quinodimethanes as highly reactive diene species for Diels-Alder cycloaddition is covered in **Section 2.2.4**.

In 1,3-dipolar cycloadditions, a dipolarophile and a 1,3-dipole generate a five-membered heterocycle in a concerted reaction. Herein, 1,3-dipoles are chemical compounds with at least one heteroatom, and its structure is described with a minimum of one mesomeric structure containing positive and negative charges. Typical examples for 1,3-dipoles are ozone, azides, nitrile imines, nitrile ylides, nitrile oxides and diazo compounds, whereas alkenes and alkynes are able to participate as dipolarophile. Similar to the Diels–Alder [4+2] cycloaddition, two π-electrons of the dipolarophile and four π-electrons of the 1,3-dipole move pericyclically, and the addition proceeds suprafacially resulting in a $[2_s+4_s]$-cycloaddition.[162–164] Reaction rates and yields as well as the regioselectivity of 1,3-dipolar cycloadditions can be derived from the inspection of frontier orbital energies and their respective coefficients (in combination with resonance integrals due to the involvement of heteroatoms).[145]

Apparently, the most prominent reaction within the class of 1,3-dipolar cycloadditions is the reaction between azides and terminal alkynes to afford 1,2,3-triazoles, which is also known as Huisgen cycloaddition

(refer to **Scheme 2.7A**). Azide derivatives present the most stable 1,3-dipole, *e.g.*, towards dimerization and hydrolysis, and they are readily introduced *via* nucleophilic substitution to any chemical structure. This cycloaddition was one of the first examples recognized as a *click* reaction.[16] While the Huisgen cycloaddition requires energy in the form of heat to reach high conversions in a reasonable time frame, the copper(I)-catalyzed azide-alkyne cycloaddition (CuAAC) attains rapidly high conversion at ambient temperature. However, the mechanism is not concerted anymore due to presence of the metal species.[165–167] Either Cu(I) compounds in combination with a ligand, *e.g.*, CuI and *N,N*-diisopropylethylamine (DIPEA), or Cu(II) species in the presence of a reductant, *e.g.*, $CuSO_4$ and sodium ascorbate, are accelerating the cycloaddition. Hereby, the metal has an influence on the regioselectivity. Whereas copper catalysis results in 1,4-substituted triazoles (refer to **Scheme 2.7B**), the reaction with ruthenium or iridium as catalyst delivers 1,5-substituted heterocycles (Ru/IrAAC, refer to **Scheme 2.7C**).[168] Furthermore, internal electron-rich double bonds are able to participate in the Ir-catalyzed version.[169, 170] Additionally, many variations of the CuAAC reaction exist because the protonation of the triazole can be avoided by the addition of electrophiles resulting in an interrupted CuAAC process.[171] Iodo-,[172] alkane-,[173–175] amino-,[176, 177] and thio-substituted heterocycles are accessible *via* electrophilic substitution of the heterocyclic ring during its formation.[177] Particularly intriguing is the possibility to functionalize the 1,2,3-triazole with an enamine substituent if a 2*H*-azirine is employed under conventional CuAAC conditions.[178]

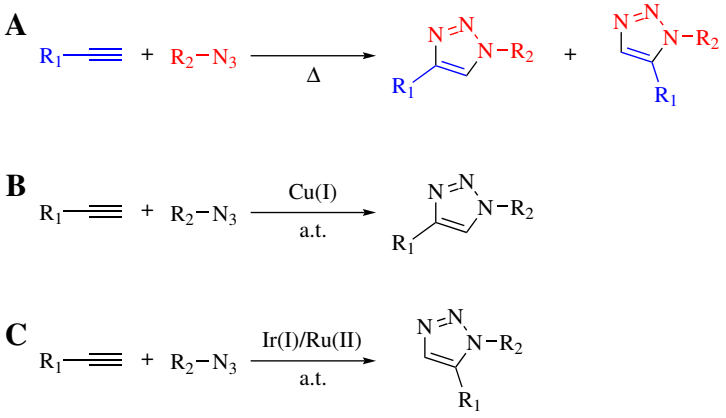

Scheme 2.7. While the Huisgen cycloaddition (**A**) requires elevated temperatures to afford 1,2,3-triazoles as a mixture containing the 1,4- and 1,5-isomer, the CuAAC (**B**) and Ru/IrAAC (**C**) provide selectively 1,4- and 1,5-substituted 1,2,3-triazoles at ambient temperature, respectively.[16, 165, 166, 168, 169]

Due to its outstanding characteristics, the CuAAC reaction was employed in a high number of applications in chemistry, and is extensively studied.[179–182] As a result, polymer chemistry makes intense use of the CuAAC as well.[150, 183–185] Especially diverse macromolecular architectures are accessible in a facile and efficient fashion.[186–188] Yet again, the success of the CuAAC lies in its reacting moieties, which are facilely introduced into chemical structures. On the one hand, while the azide unit tethered to either the monomer, initiator or CTA is stable under RDRP or ROMP conditions,[189–193] alkyne functionalities require protection. For instance, the trimethylsilyl (TMS) protecting group prevents the incorporation of the alkyne during polymerization, and is readily removed with tributylammonium fluoride (TBAF).[191, 193, 194] On the other hand, azido groups are readily introduced at the chain termini of ATRP polymers *via* substitution reactions.[91] The grafting of carbohydrates onto a PMMA-backbone for the synthesis of synthetic glycopolymers,[194] and the convergent construction of 1,2,3-triazole-based dendrimers utilizing various azide derivatives and dialkyne core molecules,[195] are merely two examples for the successful exploitation of the CuAAC ligation in polymer chemistry. However, not only the synthetic benefits of the cycloaddition are utilized for the synthesis of macromolecular architectures, the properties of the polymers are explored as well. For example, the analysis of the thermal and thermomechanical behavior of block copolymers with triazole linkages indicates that quaternization of the triazole occurs if the blocks are terminated with a bromine end group.[196]

Besides the CuAAC ligation, the photochemical generation of 1,3-dipoles has garnered much attention for the modification of functional polymers. For instance, nitrile imine and nitrile ylide species are rapidly generated upon the irradiation of tetrazoles and 2*H*-azirines, respectively. Due to their association to photochemistry, these ligation methods are covered in **Section 2.2.4**.

2.1.3.3 Thiol-X Chemistry

Thiols represent an important class of compounds since their derivatives are often commercially available, and they are reactive towards various substrates. Nevertheless, the latter point in combination with the occurrence of side reactions (which will be discussed in the following) prevent thiol-X chemistry to be completely included into the concept of *click* chemistry.[197] Even though, thiol-X chemistry proves its importance in polymer chemistry due to its versatility and practically quantitative yields.[150, 198–200]

The mechanism of the thiol-ene addition following a radical pathway is depicted in **Scheme 2.8A**.[201] Any radical source, either a heat- or photolabile initiator, is applicable to initiate the process by abstracting a H-atom from the thiol, forming a thiyl radical. Subsequently, the thiyl radical adds to the olefinic substrate followed by another H-atom abstraction from the parent thiol. As a consequence, a thioether as anti-Markovnikov product among another thiyl radical are generated. Due to the radical mechanism, common side reactions include termination *via* coupling and chain growth. The lacking orthogonality of thiols and olefinic substrates towards RDRP protocols limits the applicability of radical thiol-ene chemistry in the modification of well-defined macromolecular architectures. Nevertheless, a few methods exist to evade this issue, such as using non-polymerizable double bonds (*e.g.*, butenyloxyl moieties),[202] post-polymerization modification to introduce the desired functional group,[203] or aminolysis of the RAFT group affording thiol termini.[204] Clearly, the immense strength of the radical thiol-ene ligation lies in the possibility to functionalize non-polar double bonds, as in natural rubber or polybutadienes,[205, 206] presenting the reaction as a valuable extension in the toolbox of polymer chemistry. The sequential addition of two thiols to an alkyne is termed thiol-yne reaction.[207] Since two thiol derivatives are able to add to the alkyne, high functionalization densities can be obtained, compelling the thiol-yne reaction as a valuable tool for network formation.[208]

Employing bases as catalyst is a further possibility to promote the thiol-ene reaction. The latter is known as thio-Michael addition, although electron-deficient olefinic substrates are required for the reaction to succeed. The mechanism in **Scheme 2.8B** indicates the deprotonation of the thiol by the catalyst in the first step, followed by addition to the alkene in an anti-Markovnikov manner. The subsequent protonation delivers the final product in combination with another thiolate ion. The thio-Michael ligation chemistry suffers from the incompatibility of the functionalities in polymerization processes as well. Nevertheless, the protection of the thiol or the alkene moiety,[209, 210] aminolysis of the RAFT group,[211, 212] and dehydrohalogenation,[213] have resulted in the successful implementation of the functional groups of interest either as a repeating unit in the polymer backbone or as chain termini.

Beside the addition of thiols to unsaturated compounds, thiol moieties react with dibromomaleimides through a sequential conjugate addition followed by HBr elimination. Likewise, the thiol-disulfide exchange reaction has gained much attention in the interdisciplinary field of soft matter and biomedical therapeutics.[150]

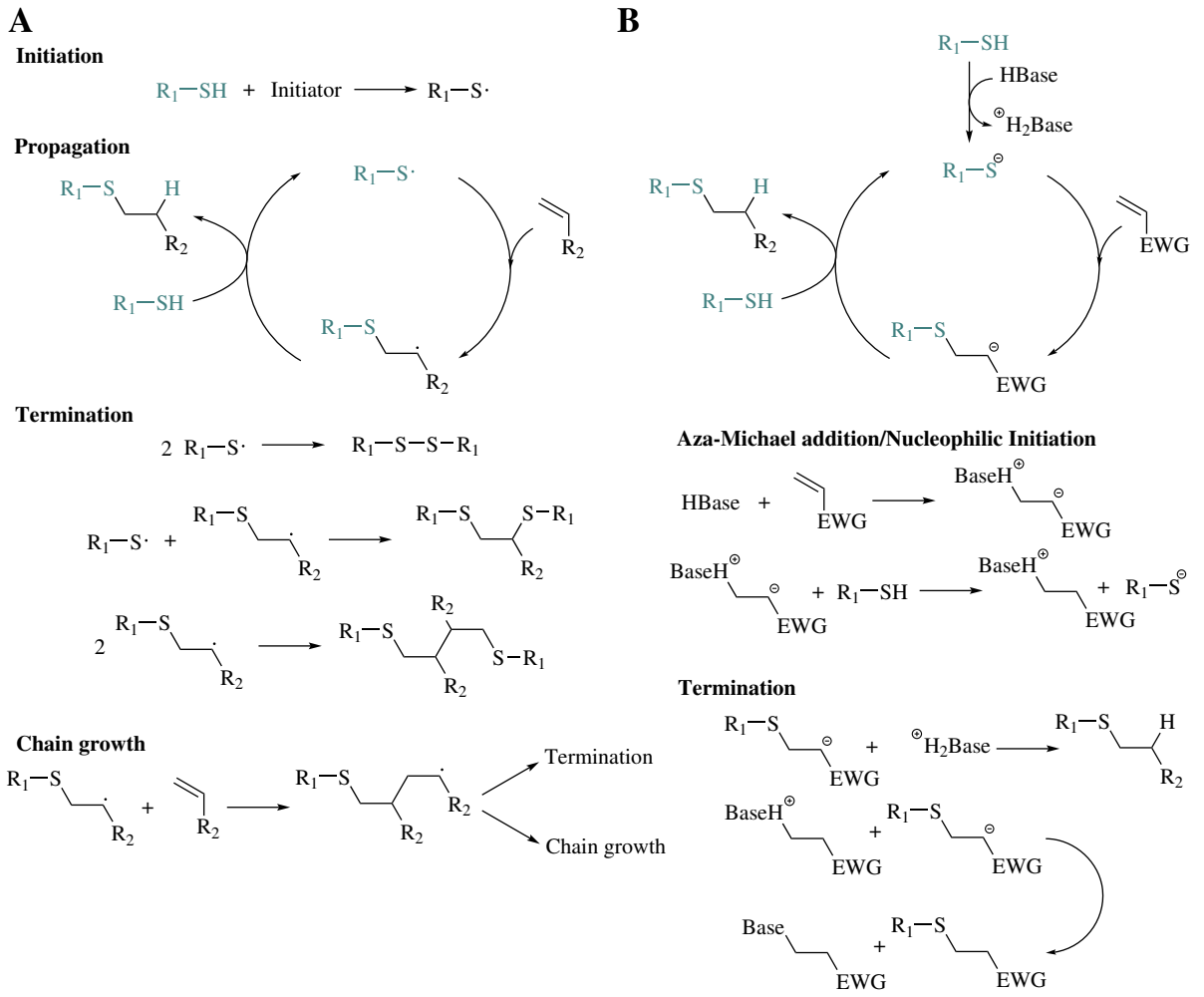

Scheme 2.8. Mechanism of the radical-induced thiol-ene addition (**A**) and of the thio-Michael conjugation (**B**). If a radical source - generated from either a heat-labile compound or a photoinitiator - is added to a thiol and an olefinic substrate, the addition of the thiol to the alkene follows a radical pathway (**A**), suffering from radical coupling processes as termination reactions alike to polymerizations. In contrast, the base-catalyzed version (**B**) proceeds *via* an ionic pathway. In this case, side reactions stem from aza-Michael reaction between the amine as the base and the electron-deficient olefinic compound, which can be reduced by employing non-nucleophilic bases such as 1,8-diazabicyclo(5.4.0)undec-7-ene (DBU).[198–201]

2.1.4 Polymer Architectures

Due to the advent of RDRP polymerization techniques and *click* chemistry, novel macromolecular architectures have been designed with unprecedented precision, that has never existed before. Furthermore, with efficient ligation methods in hands, various monomer species have been combined that could not be previously copolymerized. As a result, this opportunity has paved the way to merge the properties of a vast range of diverse polymers.

The following two subsections describe the synthesis and potential application of linear block copolymers and mikto-arm star polymers. In addition, single-chain nanoparticles and unimolecular micelles, as further unique polymer architectures, are discussed thereafter.

2.1.4.1 Linear Block Copolymers

Linear block copolymers are of particular importance due to their structural and compositional versatility. They consist of at least two distinct polymer blocks connected *via* their chain termini forming a linear polymer chain. In detail, this class of polymer is accessible in a facile fashion by the sequential polymerization of different monomers *via* RDRP techniques (refer to **Figure 2.1**).[99, 100, 214, 215] However, the sequence of the polymerization process is crucial, since the monomer forming the more stable radical needs to be polymerized first. Otherwise, the reinitiation of the propagation with the preliminary block is hindered.[101] Indeed, the ATRP technique offers the possibility to exchange the halogen in order to reverse the sequence of monomer polymerization.[85, 86] Nevertheless, a large library of block copolymer species has been obtained *via* NMP, ATRP, RAFT or combinations thereof.[216]

The coupling of two individual block copolymer segments *via* efficient ligation chemistry is an alternative approach for the synthesis of linear block copolymers (refer to **Figure 2.1**). The CuAAC ligation, (hetero)-Diels–Alder cycloaddition or thiol-ene reaction are prominent examples for the linkage of two distinct blocks as discussed in the preceding two sections. Especially appealing are the possibilities to convert the halogen end termini of ATRP polymers into an azide functionality,[91, 92] and the RAFT end group into a thiol termini,[211, 212] for subsequent block copolymer synthesis *via* CuAAC and thiol-ene reaction, respectively.[204, 217–219]

Depending on their properties, linear block copolymers have a broad range of applications. If the blocks are immiscible, self-assembly of block copolymer species in solid state results, forming do-

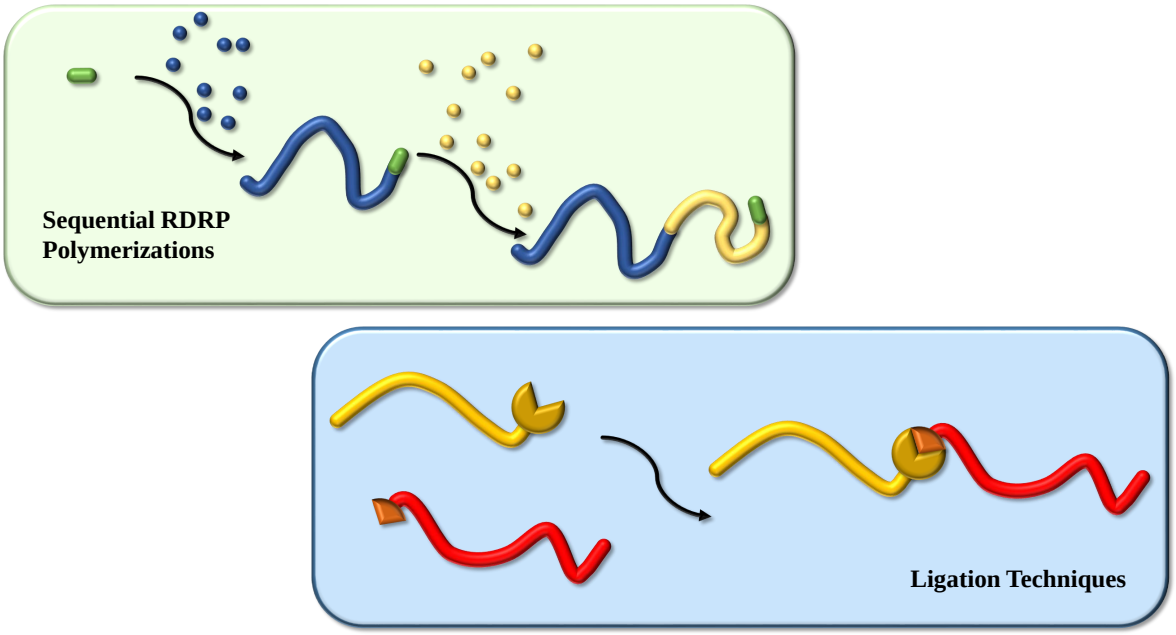

Figure 2.1. The synthetic strategies for linear block copolymers include the sequential polymerization of monomers *via* RDRP techniques (top part) and a modular approach using efficient ligation chemistry (bottom part).

mains with spheres, cylinders, gyroids or lamellae structures.[220–224] The feature size of these structures lies in the lower nanometer range (down to 3 nm) allowing their exploitation in soft lithography for microelectronics.[225–227]

Hydrophilic parts tethered to hydrophobic segments trigger the aggregation of linear block copolymer species in solution to form micelles. Herein, the shape depends on various factors including block copolymer composition and concentration, water and solvent content, additives and the so-called packing parameter. Spherical micelles, lamella, vesicles and tubules are exemplary shapes, which are obtained *via* the aggregation of block copolymers species in solution.[214] Due to the control over shape and the combination of a hydrophobic interior joint with a hydrophilic shell, the micelles are attractive agents for the encapsulation of drugs for medical drug delivery.[228, 229] Poly(ethylene glycol) (PEG) especially allows the formation of a tight shell in aqueous media, while resisting protein adsorption and cellular adhesion.[228] Furthermore, the micelles can be equipped with an external stimulus for targeted drug release, *e.g.*, with a thermo-responsive poly(*N*-isopropylacrylamide) block.[230]

Another appealing field for the application of block copolymers is the connection of a glassy polymer segment with a soft rubbery unit in order to afford thermoplastic elastomers. For example, polystyrene in

poly(styrene-*b*-isoprene-*b*-styrene) generates physically crosslinked, rigid domains, while the polyisoprene block contributes with its soft properties. Consequently, inject molding and melt extrusion are applicable to manufacture block copolymers.[214]

Finally, block copolymers are utilized for the synthesis of porous materials. The process includes the following steps: In the beginning, cooperative self-assembly of the network precursor (*e.g.*, metal oxides) and the amphiphilic block copolymer occurs. Subsequently, the porous material is formed *via* hardening of the precursor, and in the last step, the block copolymer in the pores is removed by washing or thermal decomposition.[214] As a result of the process, high surface areas are created (up to 1500 $m^2\ g^{-1}$) with uniform and adjustable cavities, promising a successful insert for water purification,[231] and gas sensoring.[232]

2.1.4.2 Mikto-Arm Star Polymers

A higher level of complexity in macromolecular architectures is achieved with star-shaped polymeric structures. First reports of the synthesis of such macromolecular structures date back to 1948, when Schaefgen and Flory used step-growth polymerization for the preparation and investigated the influence of the number of arms on the viscosity of the polymeric species.[233] Later in 1962, anionic polymerization allowed the synthesis of well-defined star-shaped polymers for the first time by employing polystyrene as arms, and silicon tetrachloride as core unit and termination agent for the polymerization.[234] Since then, the advantage of utilizing living polymerization or RDRP methods for the synthesis of uniform star-shaped polymers has become obvious, and many reports on the topic have followed.[235] In general, linear polymer chains connected to a center or core belong to the class of star-shaped architectures. Hereby, the core consists of either an atom, a small molecule or a macromolecule. As a consequence, star-shaped architectures with various arms are realized differing in length/molar mass (also termed heterogeneous or asymmetric stars) or chemistry. Macromolecular stars that possess chemically distinct arms are termed mikto-arm star polymers, which are covered in the presented section.[235–238]

The word mikto originates from the greek language and means *mixed*. Commonly, three different synthetic routes grant access to mikto-arm star polymers (refer to **Figure 2.2**):[235, 236]

- *arm-first approach*: Distinct functional polymer chains are individually tethered to the center *via* the application of a multifunctional linking agent as core. The number of arms depends on the number

of functional substituents attached to the core unit. The arm-first approach is highly demanding in synthetic terms, yet good control over the architecture is assured, and the arms can be independently analyzed.

- *core-first approach*: If a core species is equipped with several distinct initiating groups, the arms are obtained by chain growth from the core. The potential crosslinking of star units during radical polymerization, and no direct analytical access to the properties of the arms without cleavage are the main drawbacks of the core-first method.

- *difunctional monomers*: The addition of a difunctional monomer to RDRP polymerization results in the formation of nodules of crosslinked polymer species as center. Although the method presents a facile access to mikto-arm star polymers, no control over the number of arms is given affording stars with broad dispersities.

Due to its simplicity, various articles report the synthesis of mikto-arm star polymers by employing the core-first approach for ATRP or RAFT polymerizations,[239, 240] and even star-block copolymers *via* successive polymerization are accessible.[241, 242] Multifunctional cores with at least two types of initiators allow access to mikto-arm stars by sequential polymerization *via* ring-opening polymerization (ROP), NMP or ATRP process.[243, 244] Protecting group chemistry further supports the core first approach, for example by masking the alcohol unit of a multifunctional core for ROP initiation during radical polymerization.[245]

Because of the high dispersity of the synthesized macromolecular stars, the application of difunctional monomers for the preparation of mikto-arm star polymers is rare.[238] Nonetheless, mikto-arm star copolymers containing at least two chemically distinct arm species are afforded *via* the ATRP polymerization of two different linear macroinitiators and a divinyl crosslinker.[246] Moreover, the so-called in-out method is used to generate mikto-arm star polymers. After the formation of the core *via* ATRP polymerization analogous to the difunctional monomer approach, a subsequent ATRP process induces chain growth of a further monomer exploiting the pendant bromine substituents of the core.[247]

However, for the synthesis of mikto-arm star polymers by the arm-first approach, polymer ligation techniques based on *click* chemistry are required. For instance, an alkyne-bearing diinitiator for ROP polymerization is coupled to an azido-functional RAFT polymer after the polymerization process *via* CuAAC ligation yielding A_2B mikto-arm star polymers.[248] Analogously, the alkyne group of a combined ATRP and ROP initiator is employed for the linkage of the third arm *via* CuAAC reaction after

the polymerization,[249] or during polymerization process, since the copper catalyst is able to support ATRP process and CuAAC ligation simultaneously.[250] While most of the reports utilize the CuAAC cycloaddition, some examples for Diels–Alder reactions based on maleimide-anthracene are found as well.[251]

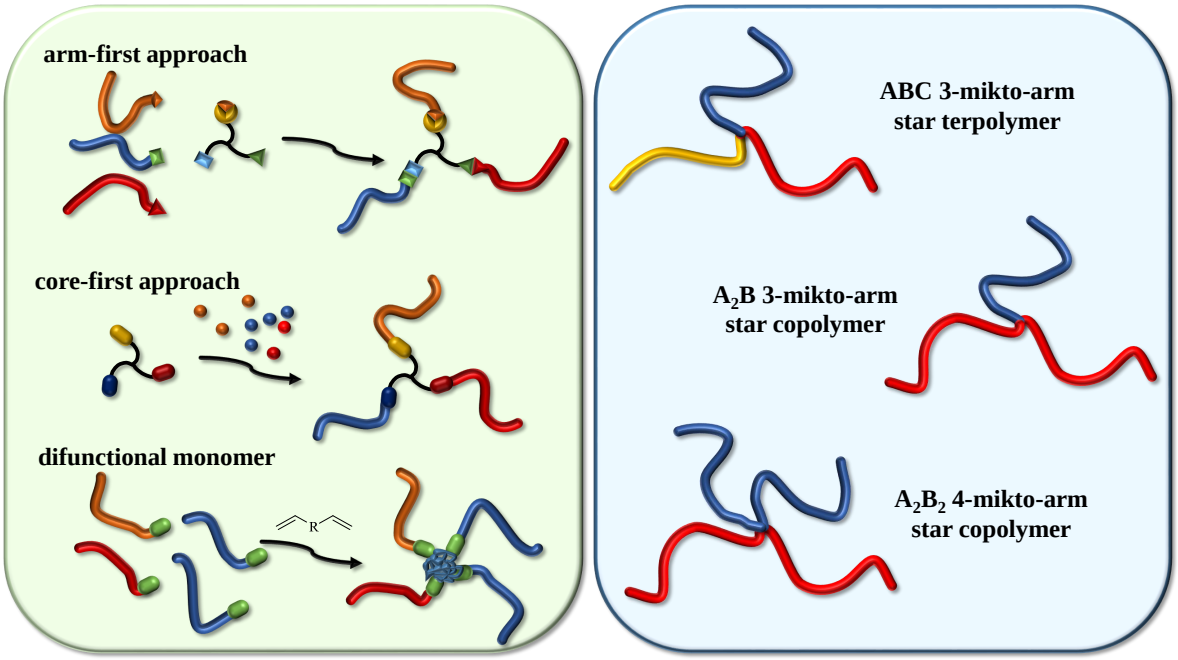

Figure 2.2. The synthetic approaches for mikto-arm star polymers are displayed in the left column. While in the arm-first approach polymer blocks are coupled to a multifunctional core, the polymer arms in the core-first approach are created *via* polymerization using core units with initiator moieties. The use of difunctional monomers in RDRP polymerization of macroinitiators leads to star-shaped polymers as well. The nomenclature of mikto-arm star polymers is explained in the right column. Herein, different colors indicate chemically distinct polymer strands.[235, 236, 238]

From an academic point of view, the changes in the morphology of mikto-arm star polymers induced by variable arm length or by an external trigger including light, pH, solvent or temperature changes are in-depth investigated.[238] As a result, the encapsulation of small molecules presents the main future application of mikto-arm star polymers. Hydrophobic dyes, including pyrene and 1-naphthyl perfluoroheptanyl ketone,[252] and drugs, *e.g.*, paclitaxel or doxorubicin hydrochloride,[253, 254] are successfully encapsulated into micelles of mikto-arm star polymers. Specifically, a loading of approximately 10 wt% of paclitaxel into mikto-arm star species is achieved in combination with a continuous drug release under biological conditions.[253]

2.1.4.3 Single-Chain Nanoparticles

Intramolecular crosslinking of individual polymer chains in highly diluted solution results in the formation of so-called single-chain nanoparticles (SCNPs). Herein, network formation *via* intermolecular reactions are prohibited due to the low concentration of polymer chains in solution. First described in 1956,[255] and re-explored in 2001,[256] the design of SCNPs has experienced a renaissance thanks to the development of RDRP polymerization techniques allowing the compaction of well-defined structures similar to proteins in nature. Indeed, the structure and functionality of proteins often serve as ultimate goal for SCNPs. However, the precise folding into secondary, tertiary or quaternary structures as seen in biomolecules (*e.g.*, deoxyribonucleic acid) has not been achieved yet with the present synthetic tools in polymer science.

In the realm of SCNPs, two distinct approaches for their synthesis exist: The 'repeating unit' and the 'selective point folding' approach (refer to **Figure 2.3**, left part). The former method presents a facile synthetic access route to SCNPs since the functionalities responsible for crosslinking are randomly placed along the polymer chain, either *via* copolymerization of a functional monomer or postpolymerization modification reactions. Nevertheless, no control over the location of the reactive groups results in random connections in the particle formation process. In contrast, the 'selective point folding' strategy includes defined tethering of orthogonal chemical units at selected points along the polymer chain. Although the latter approach is highly challenging in synthetic means, the obtained SCNPs exhibit high structural definition with the potential to mimic the structure of natural proteins.[257, 258] For example, cyclic and bicyclic motifs are realized utilizing well-defined polymer precursors.[259, 260] Nonetheless, recent advances in sequence defined macromolecules in combination with efficient ligation chemistries have created a novel milestone for the 'selective point folding' of macromolecules, one step further in the direction to the synthesis of artificial proteins.[258, 261]

Furthermore, the crosslinking process of polymer chains can be further classified by the origin and number of distinct chemical units participating in the chain compaction reaction (refer to **Figure 2.3**, right part). In the first case, a single chemical group able to crosslink (*via e.g.*, self-dimerization) is tethered to the polymer backbone.[262–264] Secondly, complementary functionalities along the backbone induce chain collapse.[265–267] External crosslinking agents are able to trigger SCNPs synthesis of homofunctional polymer chains as well.[268] The use of an external stimulus to induce chain collapse has the advantage to decrease the overall amount of solvent required for the particle synthesis. By the continuous addition of a

functional polymer solution to a solution containing the crosslinking agent, a substantial reduction of the necessary volume of solvent is accomplished.[264, 269]

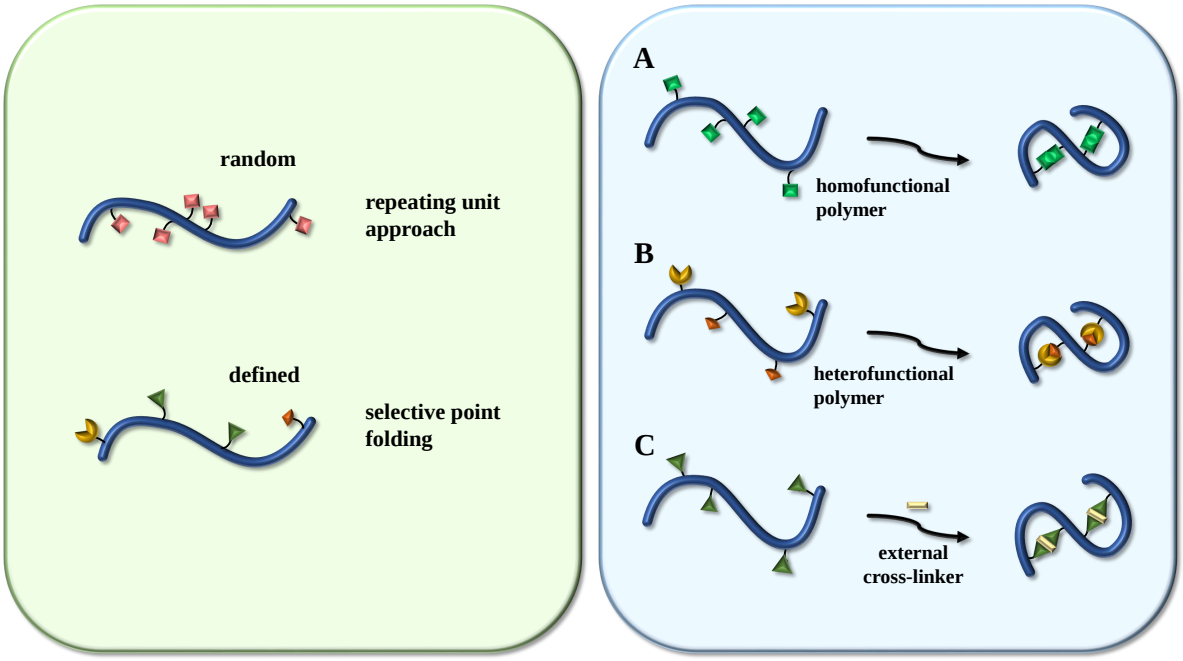

Figure 2.3. Schematic illustration of the diverse crosslinking technologies for the construction of SCNPs. The two different approaches - the 'repeating unit approach' and 'selective point folding' - are displayed on the left side, in which the reactive functionalities responsible for chain collapse are either randomly incorporated or selectively placed along the polymer chain. In comparison, the right part displays the different approaches classified by the origin and the number of distinct chemical groups participating in the chain compaction reaction. **A**: Homofunctional polymer chains are able to collapse *via e.g.,* dimerization reactions. **B**: In hetereofunctional polymer species, distinct chemical groups react to induce chain compaction, and **C**: External crosslinkers trigger SCNPs formation of homofunctional polymer chains.[257, 270, 271]

The chemistry leading to single chain collapse is categorized by the nature of the created crosslinks: Covalent and dynamic covalent as well as non-covalent bonds and crosslinks *via* metal complexation.[270, 271] For instance, covalent connections are formed if light is used for dimerization, or the generation of reactive species able to react with suitable functional groups.[36, 152, 264–267] Likewise, the addition of a catalyst induces covalent bond formation, such as alkyne coupling promoted by Cu(I) compounds.[272] Dynamic covalent bonds are either cleaved or regenerated upon an external trigger. For instance, disulfide and hydrazide bonds are cleaved by employing reducing agents and heat, and the links are reformed by oxidation and low temperatures, respectively.[273, 274] Furthermore, hydrogen bonds occurring in the dimerization of ureidopyrimidinone or in the interaction between Hamilton Wedge and cyanuric acid are examples for non-covalent crosslinks utilized for the synthesis of SCNPs.[263, 275] In the end, the

formation of stable metal complexes is utilized to intramolecularly crosslink polymer strands with suitable ligand-derived monomer units.[268, 269, 276]

In general, the size of the nanoparticles is influenced by the length of the pristine polymer chain and the crosslinking agent in addition to the density of the crosslinking points.[267, 277, 278] Special attention is directed to the characterization methods for SCNPs.[279] On the one side, the change in chemical structure as a concomitant phenomenon of chain collapse is readily observed *via* NMR spectroscopy,[269] mass spectrometry,[280] IR,[281] UV/Vis or fluorescence spectroscopy.[36, 266] On the other side, direct access to absolute values for the particle size of the SCNPs remains challenging. However, a relative decrease in the average hydrodynamic diameter is clearly evidenced by various characterization methods.[279] For instance, the concept of size exclusion chromatography (SEC) relies on the separation of polymer species by their hydrodynamic volumes. Long polymer chains with high hydrodynamic volumes are detected first, whereas shorter chains are visible at longer retention times.[282] Consequently, successful chain collapse is evidenced by a shift to higher retention times compared to the parent polymer. Concomitantly, species at shorter retention times indicate unintended intermolecular reactions. Access to absolute values for the hydrodynamic radius *via* SEC measurements is difficult since exact calibration parameters are missing due to the unknown shape and structure of the SCNPs. Hereby, dynamic light scattering (DLS) provides a remedy: By measuring the scattering intensity of a polymer solution at a constant angle over time, and analyzing the collected data *via* an autocorrelation function, diffusion coefficients D are obtained. The coefficients are translated into a distribution of hydrodynamic diameters D_h by employing the Stokes-Einstein relationship (refer to **Equation 2.4**) with k_b = Boltzmann constant, T = temperature, and η = viscosity of the solution.

$$D = \frac{k_b T}{3\pi\eta D_h} \tag{2.4}$$

However, a recent article describes a vast scattering of values at fixed molar masses beside extremely small hydrodynamic radii. The deviations might be caused by the unknown shape of the nanoparticles or by the too small particle size for reliable detection.[279] Similar to DLS, diffusion coefficients are determined *via* diffusion-ordered NMR spectroscopy (DOSY),[283] and converted into hydrodynamic radii applying the Stokes-Einstein equation as well.[36, 266, 269, 284] Nevertheless, merely an average value for the hydrodynamic radius of polymer or SCNPs samples is obtained *via* DOSY measurements. Additionally,

small-angle neutron scattering (SANS) and small-angle X-ray scattering (SAXS) give insights into the morphology of SCNPs in solution revealing information about the form factor and the radius of gyration.[270] Specifically, the work of Pomposo and coworkers revealed similar form factors for SCNPs and disordered proteins. As a consequence, SCNPs in solution are comparable to loosely crumpled coils than to globular, strongly folded nanoparticles.[285, 286] In contrast to the previously mentioned analytical methods, atomic force microscopy (AFM) and transmission electron microscopy (TEM) afford access to size and shape in solid state.[276, 277, 287]

Apart from the application of SCNPs as artificial protein mimics, their potential use in further areas is also evident.[257, 258, 270] For instance, the metal compound utilized for chain compaction is additionally utilized for the catalysis of chemical transformations.[288] The advantage of the metal-loaded SCNPs lies in the selectivity, which can be directed towards different reaction products compared to the free metal complex.[289] Furthermore, the separation and recyclability of the SCNP-bound catalyst from the reaction mixture is facile.[269] Besides, transient-binding nanocarriers are successfully synthesized and able to release vitamin B9 for potential application in drug delivery.[285] Finally, benzene-1,3,5-tricarboxamide-substituted SCNP species are reported to be efficient metal sensors by losing their fluorescence upon conformation changes through interaction between copper ions and bipy units.[290]

2.1.4.4 Unimolecular Micelles

In aqueous solution, amphiphilic molecules, *e.g.*, block copolymers, are able to self-assemble into multimolecular micelles with variable shapes. Yet, these supramolecular structures are highly labile towards dilution, therefore, they disaggregate into free polymer chains if the concentration falls under their critical micelle concentration (CMC). Beyond dilution, temperature or pH changes potentially destroy the structure of multimolecular micelles as well. The instability is the reason why multimolecular micelles are not applicable in certain fields including biomedical areas.[291] In order to overcome the fragile nature of multimolecular micelles, crosslinking reactions within the micelles yield chemical connections of the individual amphiphilic molecules. Thus, the disaggregation of micelles is prevented.[292] An alternative approach for the design of resilient micelles is the preparation of so-called unimolecular micelles. The covalent connection between a hydrophilic shell and a hydrophobic core affords monomolecular micelles, which maintain their structure upon environmental changes.

Various macromolecular architectures are able to form unimolecular micelles, *e.g.*, amphiphilic dendrimers.[293, 294] Their synthesis needs sequences with several steps, but the discrete size and precise structure allow the installation of multiple terminal groups in the shell suitable for further functionalization. In contrast, the synthesis of amphiphilic hyperbranched polymers provides facile access to unimolecular micelles on a large scale.[295, 296] In addition, brush-shaped and cyclic polymers are successfully investigated regarding their behavior as unimolecular micelles.[297, 298] Eventually, amphiphilic star polymers represent the last class of macromolecular architectures forming unimolecular micelles (refer to **Section 2.1.4.2**). The advantage of star-shaped polymers for unimolecular micelles lies in their customizable structure leading to different types of amphiphilic star architectures (refer to **Figure 2.4**). Structure A in **Figure 2.4** as an example is realized by employing a cyclodextrin core able to initiate the sequential ATRP polymerization of *tert*-butyl acrylate and styrene. After hydrolytic ester cleavage, a 21-arm star-like poly(acrylic acid)-*b*-poly(styrene) species is obtained, which forms unimolecular micelles in *N,N*-dimethylformamide.[299] Furthermore, amphiphilic A_4B_4 mikto-arm star polymers (refer to structure D in **Figure 2.4**) are obtained using a core-first approach. Hydrophilic PEG arms are polymerized utilizing the respective hydroxyl initiator units tethered to the core followed by the polymerization of the hydrophobic counterpart (either ϵ-caprolactone, *tert*-butyl acrylate or styrene) *via* an ATRP or ROP procedure.[300] More complex architectures for unimolecular micelles are illustrated in **Figure 2.2** including branched and dendrimer-like structures (B and C, respectively).

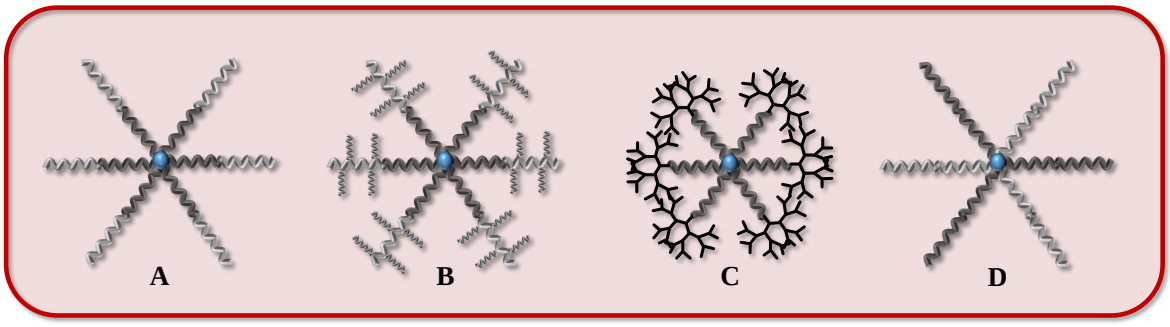

Figure 2.4. Structures of amphiphilic mikto-arm star polymers that are able to serve as unimolecular micelles. As soon as amphiphilic block copolymer species are deliberately tethered to a core unit, a behavior similar to unimolecular micelles can be achieved (refer to structure **A**). Branched and dendrimer-like structures as displayed in **B** and **C**, respectively, are able to reinforce the hydrophilic shell of unimolecular micelles. Structure **D** displays that mikto-arm star polymers of the A_4B_4-type might show properties of unimolecular micelles as well. Adapted with permission from [291]. Copyright (2016) Royal Society of Chemistry.

Unimolecular micelles are potential candidates for drug delivery agents. Compared to multimolecular micelles, they do not disassemble in the blood stream upon dilution, and they are stable upon temperature, pH and ionic strength changes.[301] The drug is either covalently linked to the micelle or physically encapsulated in the core. For example, an anticancer drug is efficiently released in an acidic tumor microenvironment while the unimolecular micelle is stable at pH 7.4 due to a zwitterionic polymer shell of poly[3-dimethyl(methacryloyloxyethyl)-ammonium propanesulfonate].[302] In order to enhance the biocompatibility, degradable unimolecular micelles as drug delivery agents are designed. Upon treatment with dithiothreitol, the disulfide bonds in the branches cleave resulting in a molar mass shrinkage from 20.000 to 2.000 g mol^{-1} as detected *via* SEC.[303] Besides drug delivery, unimolecular micelles are also able to encapsulate catalysts such as metal complexes. Herein, these micelles show a high metal loading capacity, and the substrate easily reaches the catalyst *via* diffusion. In comparison, the catalyst itself is not able to escape the micelle.[291, 304, 305] Specifically, a dendrimer containing triazole units accelerates the CuAAC ligation reaching turn-over-numbers of up to 510.000.[306] Eventually, the template synthesis of inorganic nanoparticles is accomplished with the aid of unimolecular micelles as well. For instance, gold nanoparticles are prepared *via* the reduction of $KAuCl_4$ in the hydrophilic core of a poly(ethylene glycol)-*b*-poly(ϵ-caprolactone) star-block copolymer.[307]

2.2 Photochemistry

For a chemical reaction to proceed, energy has to be provided in order to overcome the activation barrier. Traditionally, the required energy is supplied *via* heat. Yet, with the discovery of sunlight promoting chemical reactions by Ciamician and Silber near the end of the 19th and in the early 20th century,[308–310] the immense success of photochemistry for efficient chemical transformations began.

Photochemically driven reactions can be one step towards green chemistry.[18, 19] The demands for atom efficient, sustainable and environmental benign synthesis protocols are rising, and irradiation-induced reactions are especially economic by employing easily accessible light sources - sometimes even sunlight as straightforward, unlimited and inexpensive source of illumination. Therefore, light-triggered reactions directly address the spirit of the time in terms of environmental protection. Furthermore, the reactions can be controlled in a spatiotemporal manner, *i.e.*, not merely the reaction time is confined by the period of irradiation, but photochemistry also offers the ability to initiate the reaction on selected spots, *e.g.*, on surfaces. These benefits are essential for kinetic studies of polymerization processes and spatially resolved surface modification.[21, 311] Moreover, the intensity of the applied irradiation source regulates the reaction rate of photochemical reactions.

The following subsections cover the physical fundamentals of photochemistry (*e.g.*, Beer-Lambert's law, Franck-Condon principle, Jablonski diagram and molecular electronic transitions). The subchapter will be completed with photochemical transformations applied in polymer chemistry providing a manifold of macromolecular architectures and modified surfaces.

2.2.1 Beer-Lambert's Law

From a macroscopic point of view, the absorption of monochromatic light in a homogenous sample is governed by Beer-Lambert's law (refer to **Equation 2.5**). Herein, a linear dependency of the measured absorbance A on the concentration c and the path length l is assumed. The ability of a molecule to absorb light of a given wavelength is defined as molar extinction coefficient ϵ, which depends on the frequency of the incident light. High values of ϵ indicate allowed electronic transitions, whereas forbidden electronic transitions are characterized with low numbers for ϵ.[312, 313]

$$A = \epsilon l c \tag{2.5}$$

The transmittance T is defined as the fraction of the incident light leaving the sample, and hence it is utilized for experimental measurements. Absorbance and transmittance are inversely related (refer to **Equation 2.6**).

$$A = -log(T) = -log(I/I_0) \tag{2.6}$$

Consequently, the intensity of the incident light source decreases exponentially while passing through the sample as defined in **Equation 2.7** (refer to **Figure 2.5**).[314]

$$I = I_0 10^{-\epsilon l c} \tag{2.7}$$

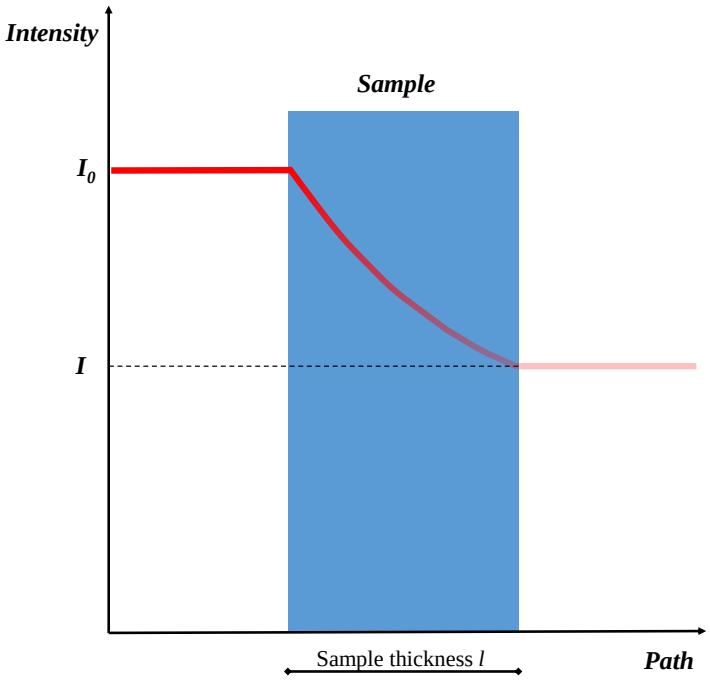

Figure 2.5. Illustration of the Beer-Lambert's law. When a monochromatic light beam with the intensity I_0 passes through a homogeneous sample solution with the sample thickness l, the molecules can absorb a fraction of the light. As a result, a light beam with lower intensity I is detected after traversing through the sample.[314]

2.2.2 Franck-Condon Principle and Jablonski Diagram

The Schrödinger equation describes the energetic properties of atoms including their rotational and vibrational motion. After solving the Schrödinger equation, the energy states of the molecules are

determined by wavefunctions, which predict a quantization of energy levels. A schematic representation of electronic states including vibrational states is presented in **Figure 2.6**.[315]

As soon as a molecule or atom is irradiated with a light source, electrons gain energy resulting in electronic transitions from the ground level to an excited state. Since only selected amounts of energies can be absorbed due to the quantization of the energy levels, only light of certain wavelengths is able to excite electrons into higher energy states. Here, the Franck-Condon principle predicates that in photochemical processes electronic transitions are fast (10^{-15} s) compared to the movement of heavy nuclei (10^{-12} s). As a consequence, electronic transitions occur vertically (ergo without change of the nuclear coordinates) in an energy vs. nuclear coordinates diagram (refer to the red arrow in **Figure 2.6**). The transition probability depends on the vibrational properties. A high value for the overlapping integrals of the vibrational wave functions of electronic states indicates a high probability for an electronic transition resulting in a high absorption intensity of a given wavelength. In contrast, low absorption intensities are found for the transitions with a poor overlap of the vibrational wave functions.[316, 317]

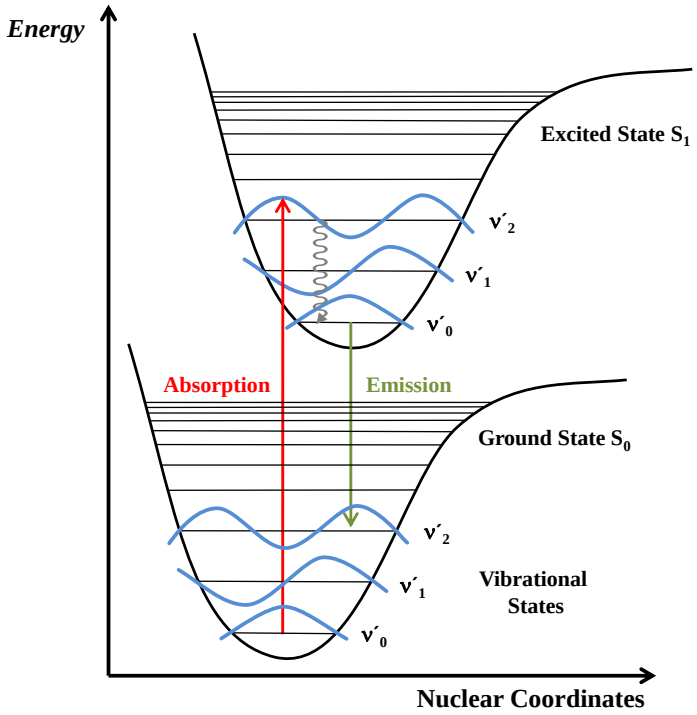

Figure 2.6. A plot of energy vs. nuclear coordinates illustrating the Franck-Condon principle. Electronic transitions appear as vertical transitions at fixed nuclear coordinates (red arrow), and their probability depends on the value of the overlapping integrals of the vibrational wave functions of electronic states (blue curves). Analogously after vibrational relaxation, the transition into the ground state S_0 follows the Franck-Condon principle as well.[316, 317]

After electronic excitation, the energy can be released by several distinct processes. In the presented case, the deactivation of the excited molecule is well described in a so-called Jablonski diagram (refer to **Figure 2.7**).[318] Herein, the energy is plotted on the y-axis, and the different states are represented as horizontal lines; electronic levels are described as bold lines, while vibrational states are displayed as thin lines. S_0 is assigned to the singlet ground state, and S_1 and S_2 represent the first and second energetically excited singlet states, respectively. In addition, T_1 indicates the first energetically excited triplet niveau. Furthermore, the arrows indicate various transitions between states including vibrational relaxations (curvy arrows), radiative transitions (colored, solid arrows) and non-radiative transitions (dashed arrows). All deactivation pathways of energetically excited electrons are competitive depending on the energy levels, which differ from one molecule to the other.

Thus, the following processes are displayed in the Jablonski diagram:

- **Absorption**: As discussed in the preceding paragraph, the absorption of light with a suitable wavelength leads to the transition of an electron from the singlet ground state S_0 with ν_0 (due to Boltzmann distribution function) to an electronically excited state S_n (with $n \geq 1$ and $\nu \geq 1$) according to the Franck-Condon principle. Therefore, the process occurs under preservation of spin. The electron possesses additional vibrational excitation beside the electronic excitation because the dependence on the overlapping integrals of the vibrational wave functions of electronic states leads to the population of electronic niveaus with $\nu \geq 1$. In general, the absorption of energy is a highly fast process (10^{-15} s).

- **Vibrational Relaxation (VR) and Internal Conversion (IC)**: While the vibrational relaxation proceeds within the same electronic state in order to reach the vibrational ground state ν_0, internal conversion is a non-radiative process to a vibrationally excited state of the next lower electronic state with the same spin multiplicity. The energy of vibrational relaxation is released as heat to the surrounding medium. Since the vibrational relaxation and internal conversion are fast (within 10^{-12} s), due to close spacing of the excited states and their distorted geometries, the vibrational ground state of S_1 is rapidly reached. Consequently, the rule of Kasha applies, which predicts that all emission processes after the absorption of light start from S_1.

- **Fluorescence**: The electron in the vibrational ground state of S_1 is deactivated by a radiative process reaching a vibrationally excited state of S_0. Yet again, the Franck-Condon principle governs which vibrational state is reached. With 10^{-9} to 10^{-5} s, the fluorescence is a rather slow process. The combination of losing energy by relaxation processes in electronically excited states and transitioning into vibrationally excited states of S_0 causes that the wavelength of emission is higher

than the wavelength of excitation. This phenomenon is termed Stokes shift. However, S_1 may also be deactivated by radiationless means (within 10^{-9} to 10^{-6} s).

- **Intersystem Crossing (ISC) and Phosphorescence**: Competitive to fluorescence, a transition to a vibrationally excited state of the triplet state T_1 is termed intersystem crossing. Thus, spin multiplicity is not preserved, and the time scale for ISC lies between 10^{-9} and 10^{-6} s. Strictly speaking, the process is formally forbidden. Nevertheless, spin-orbit interactions undermine the strict rule that transitions merely occur between states of the same multiplicity. After vibrational relaxation, phosphorescence can take place from the vibrational ground state of T_1 to a vibrational excited level of S_0 within 10^{-5} to 1 s. Therefore, phosphorescence occurs in combination with spin reversion, resulting in a long time span for T_1. The depopulation of the triplet state T_1 may proceed *via* radiationless deactivation as well.[315, 319–321]

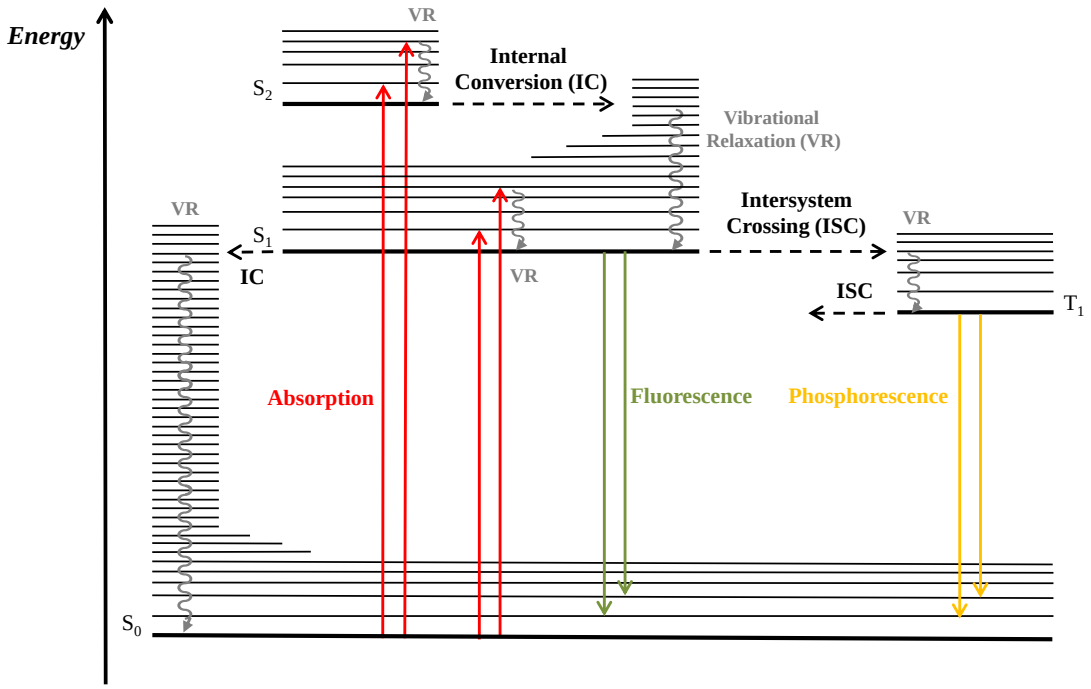

Figure 2.7. The modes of deactivation of energetically excited electrons are illustrated in a Jablonski diagram. Here, the energy is plotted on the y-axis, while the horizontal lines represent electronic (bold lines) and vibrational (thin lines) states. The rotational niveaus are not displayed. Furthermore, dashed arrows indicate transition processes (*e.g.*, internal conversion and intersystem crossing), curvy arrows represent vibrational relaxation, and energy absorbing or releasing processes are displayed as colored, solid arrows.[315, 319–321]

2.2.3 Molecular Electronic Transitions

The absorption of a photon with a suitable wavelength results in the excitation of an electron. To determine which type of electron of a molecule is excited, the corresponding molecular orbitals of the electrons have to be considered. In general, outer electrons in the 2s or 2p orbitals are preferentially promoted, abandoning their initial molecular orbital in order to occupy another orbital with higher energy. The following electronic transitions have to be considered when molecules are exposed to light sources:[52, 320–322]

- $\sigma \rightarrow \sigma^*$ **transitions**: Photons with high energy (100-200 nm) are required in order to excite an electron from a bonding σ orbital into an antibonding σ^* orbital. These transitions particularly occur in saturated hydrocarbons.

- $\pi \rightarrow \pi^*$ **transitions**: π-Electrons in conjugated systems including non-saturated or aromatic compounds are promoted in a $\pi \rightarrow \pi^*$ transition, whose trigger wavelength is simple to adjust by the expansion of the conjugated system (starting from 173 nm for acetylene). The molar extinction coefficients are high since $\pi \rightarrow \pi^*$ transitions are symmetry-allowed. Without the dissociation of a chemical bond, the cleavage of π bonds may lead to torsion as present in *cis-trans* isomerizations. The effect of solvatochromism results in a bathochromic shift of the absorption maximum in polar solvents due to a higher stabilization of the π^* orbital than of the π orbital.

- $n \rightarrow \pi^*$ **transitions**: A $n \rightarrow \pi^*$ transition is a symmetrically forbidden transition of free electrons in non-bonding orbitals of a heteroatom (*e.g.*, N, O, Cl or S) into non-bonding π^* orbitals, available in *e.g.*, carbonyl compounds, imines and azo moieties. Photons with wavelengths of approximately 300 to 380 nm are able to trigger the excitation. However, the transition displays low molar extinction coefficients, since it is quantum mechanically forbidden. The $n \rightarrow \pi^*$ transition is affected by solvatochromism as well. Polar solvents lower the energy of the non-bonding orbital *via* the solvation of the lone pair resulting in a hypsochromic shift of the absorption wavelength.

- $n \rightarrow \sigma^*$ **transitions**: For molecules containing σ-bonds and lone pairs (*e.g.*, water, alcohols and ethers), a $n \rightarrow \sigma^*$ transition is triggered by wavelengths between 150 and 250 nm leading to homolytic dissociation.

- **Charge-Transfer (CT) transitions**: CT transitions are found in polarized/push-pull systems with delocalized molecular orbitals. Upon irradiation, the energy is delocalized in the entire compound affording a strong absorption and a pronounced red-shift of the excitation wavelength.

Merely $\pi \rightarrow \pi^*$, $n \rightarrow \pi^*$ and CT transitions of electrons in conjugated systems are able to operate in the visible light range (above 400 nm), which will be subject of **Section 2.3**.[321]

2.2.4 Light-Induced Polymer Conjugation[1]

The outstanding feature of reactions triggered by light is the possibility to conduct a spatially and temporally resolved conjugation without the application of a catalyst or elevated temperatures. In the subsequent subchapters various photoreactive groups are described, which were successfully implemented in polymer chemistry. The discussed light-induced conjugation methods have in common that highly reactive substrates are formed as soon as the reaction mixture is irradiated by light of a suitable wavelength.

2.2.4.1 Photochemical Activation of *ortho*-Alkylbenzaldehydes and *ortho*-Alkylbenzophenones

Despite the possibility to generate *ortho*-quinodimethanes as highly reactive intermediates for Diels–Alder cycloadditions *via* the thermolysis of benzocyclobutenes,[323–325] the photochemical pathway with *ortho*-alkylbenzaldehydes or *ortho*-alkylbenzophenones as starting material benefits from the advantages of the employment of light. Thus, the mechanism for the light-triggered activation by taking the example of *ortho*-alkylbenzophenones is depicted in **Scheme 2.9** (top part).[326] The irradiation of the phenone derivative results in the population of a singlet-excited state of nπ^* character, followed by ISC reaching the triplet niveau, in which the intramolecular abstraction of a hydrogen atom yields a triplet diradical species.[327, 328] Subsequently, a rearrangement of bonds delivers the *E* and *Z* hydroxy-*ortho*-quinodimethanes, which are also termed photoenol.[327, 329–331] The *E* isomer is the long-lived diastereomere, and therefore, is able to either rearrange forming the starting material or to participate as diene in an irreversible Diels–Alder cycloaddition with electron-deficient dienophiles. The cycloaddition proceeds stereospecifically affording the *endo* product. In contrast, the short-lived *Z* isomer is unable to react due to a fast [1,5]-sigmatropic shift yielding the starting material.[331, 332] According to the Cahn-Ingold-Prelog rules, the irradiation of *ortho*-alkylbenzaldehydes affords the *Z* form as long-lived isomer, while the *ortho*-quinodimethane with *E* configuration exclusively rearranges to the aldehyde species. The *Z* form particularly isomerizes generating the short-lived *E* isomer upon exposure to light with higher wavelengths (440 nm). The

[1] The theoretical background for the subchapters concearning activation of tetrazoles, 2*H*-azirines and phenacyl sulfides is based on J. T. Offenloch, M. Gernhardt, J. P. Blinco, H. Frisch, H. Mutlu, C. Barner-Kowollik, *Chem. Eur. J.*, **2019**, *25*, 3700-3709. Adapted with permission from Wiley-VCH Verlag GmbH & Co. KGaA, Weinheim.

behavior as photoswitch is utilized for STED (stimulated emission depletion)-inspired laser lithography of structures below 100 nm. In general, the formation of the hydroxy-*ortho*-quinodimethane is fast and fully reversible at ambient temperature, therefore quenching and separation of the intermediate is not necessary. However, if no suitable reaction partner is present, dimerization *via* [4+2] or [4+4] cycloaddition reactions occurs.[323, 333]

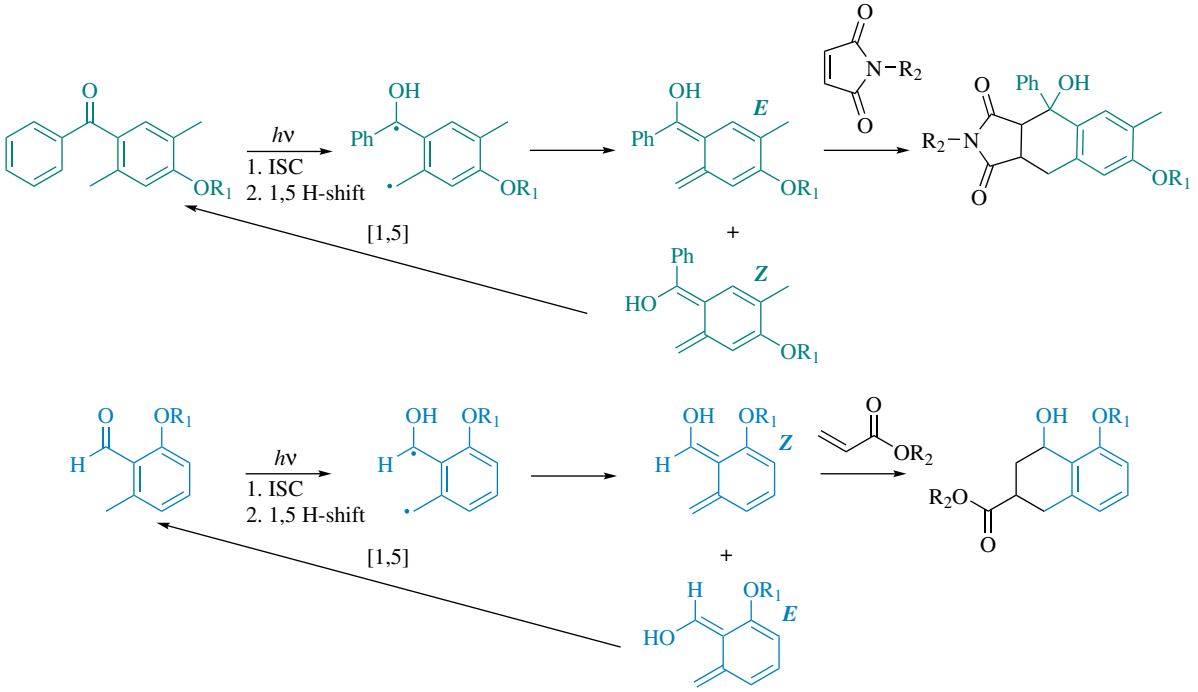

Scheme 2.9. Hydroxy-*ortho*-quinodimethanes (photoenols) as reactive species are obtained *via* the irradiation of *ortho*-alkylbenzophenones (occasionally referred to as 1st generation photoenol, top row) or *ortho*-alkylbenzaldehydes (2nd generation photoenol, bottom row) with UV light (320-365 nm). Particularly, one long-lived isomer is able to react with electron-deficient dienophiles in a Diels–Alder cycloaddition, while the other one is rapidly deactivated by a [1,5]-sigmatropic shift.[327]

Interestingly, the reactivity of *ortho*-alkylbenzaldehydes and *ortho*-alkylbenzophenones differs. Since *ortho*-quinodimethane derivatives originating from *ortho*-alkylbenzaldehydes with an *ortho*-ether are stabilized due to intramolecular hydrogen bond formation, the reactivity towards dienophiles is enhanced.[334] As a result, cycloadducts with various dienophiles including acrylates,[32, 335] acrylonitrile,[336] and electron-deficient C-S bonds[337] are formed in the presence of light-activated *ortho*-alkylbenzaldehydes. In comparison to the aldehyde species, for the light-triggered reaction of *ortho*-alkylbenzophenones highly electron-deficient reaction partners such as maleimides are necessary. Exploiting the difference in reactivity, a triblock polymer is synthesized in an orthogonal manner. In a one pot procedure, a polymer

strand tethered to an α-acrylate moiety and an ω-*ortho*-alkylbenzophenone unit reacts selectively upon irradiation with a maleimide-terminated PEG block by employing its photoactivable end group. The conversion of the acrylate chain end is achieved in the subsequent step utilizing a poly(ϵ-caprolactone) derivative end-capped with an *ortho*-methylbenzaldehyde functionality.[335]

The use of *ortho*-quinodimethanes as reactive intermediates has a great potential due to its outstanding characteristics resembling the nature of *click* reactions.[323, 338] Especially, the rapid, efficient and catalyst-free nature of this ligation technique is beneficial for the synthesis of macromolecular structures,[112, 151, 335, 339, 340] the curing of polymer films,[32] and the modification of surfaces and nanoparticles.[33, 334, 341–345] In addition, the stability of the cycloadducts is exploited for polymer end group protection, since the C-S double bond of RAFT polymers is susceptible towards nucleophilic attack (refer to **Section 2.1.2.2**).[112] Furthermore, the imine formation of *ortho*-methylbenzaldehydes presents another yet thermodynamically controlled pathway for the photoenol precursor. During the irradiation of the photoreactive moiety in the presence of *N*-ethyl maleimide as dienophile and an amine, the reaction proceeds selectively *via* the photochemical path, whereas the oxime is generated in the dark. As a result, light as external stimulus is able to switch between the two different reaction channels.[34] Moreover, the photoreactivity can be recovered *via* hydrolysis of the imine. Therefore, the amine is capable of acting as protecting group for the presented photoreactive unit, *e.g.*, in the wavelength-selective synthesis of star-shaped polymer species in case the photoreactive moiety (a tetrazole derivative) with a shorter activation wavelengths is addressed first.[340]

2.2.4.2 Nitrile Imine-Mediated Tetrazole-Ene Cycloaddition

Analogous to the *in situ* generation of reactive species *via* irradiation of *ortho*-methyl benzaldehydes, 2,5-diaryl tetrazoles are capable of forming reactive intermediates upon light exposure as well.[346, 347] The use of a light source with a wavelength of 300 nm results in the conversion of the 2,5-diaryl tetrazole into a highly reactive nitrile imine, a 1,3-dipole, along nitrogen release (refer to **Scheme 2.10**).[348] Here, the photolysis is extremely fast and efficient due to high quantum yields (0.5 to 0.9), and therefore, commercially available light sources are suited to initiate the photoligation.[349] Subsequently, the intermediate is able to react with various substrates. If an activated or non-activated olefinic substrate, *e.g.*, methyl methacrylate, acrylnitrile, styrene, or maleimide, as dipolarophile is present, a highly fluorescent pyrazoline adduct

is formed in a 1,3-dipolar cycloaddition, also termed nitrile imine-mediated tetrazole-ene cycloaddition (NITEC).[152, 348, 350, 351] Importantly, the pyrazoline unit exhibits diverse biologically relevant properties including antidepressant activity.[352] In addition, the cycloadduct possesses a broad fluorescence band in the visible light region upon excitation with wavelengths larger than 400 nm, and consequently, the pyrazoline derivative is suitable for applications as fluorescent marker.[353, 354] Furthermore, in the nitrile imine carboxylic acid ligation (NICAL), carboxylic acid moieties react with nitrile imines followed by a 1,4-acyl transfer yielding hydrazine compounds.[355] Indeed, various nucleophiles are able to react with the intermediate including alcohols,[355] amines,[355] and thiols.[356] However, the latter pathways have gained limited attention compared to the NITEC reaction. Lastly, if no reaction substrate is present, the dimerization of two nitrile imine species occurs.[348] Critically, the broad range of possible reaction partners forbids the photochemically-driven reaction of tetrazoles to be termed *click*. However, this drawback can be neglected due to the fast, versatile and efficient nature of the NITEC reaction without the help of any external catalyst. Additionally, the reaction is highly tolerant towards the solvent medium since it has been successfully tested with various solvents and mixtures including water.[348]

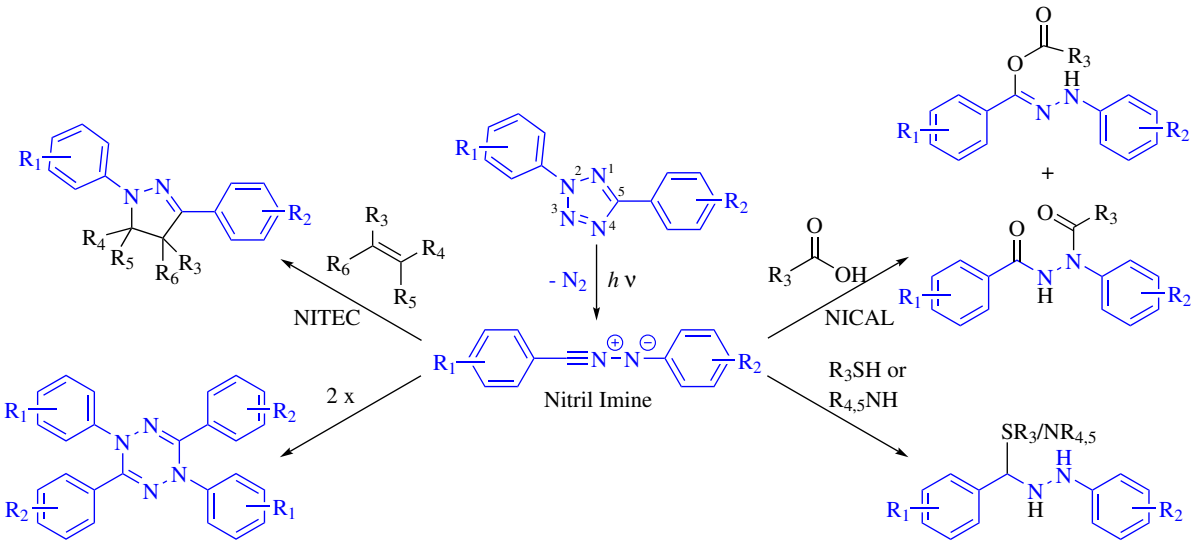

Scheme 2.10. The irradiation of a 2,5-diaryl tetrazole results in the formation of a highly reactive nitrile imine, which is able to react with olefinic substrates in a nitrile imine-mediated tetrazole-ene cycloaddition (NITEC) or with various nucleophiles including carboxylic acids (nitrile imine carboxylic acid ligation, NICAL), amines and thiols. If no reaction partner is present, the dimerization of two nitrile imine species occurs. The wavelength required to generate the 1,3-dipole strongly depends on the substitution pattern of the tetrazole compound.[354, 355, 357, 358]

The substitution pattern has substantial impact on the reactivity of the nitrile imine. *Para*-substitution of the *N*-phenyl ring with auxochromic substituents shifts the reactivity to higher wavelengths, while

the same substitution in *ortho*- or *meta*-position has no influence on the trigger wavelength.[354] The enlargement of the conjugated system changes the trigger wavelength to higher values as well, yet only in case of the phenyl group in N2 position.[354, 355, 357, 358] Further investigations reveal that EWG units attached to the C5 phenyl ring substantially decrease the reaction rate, while EDG moieties show no significant effect. In comparison to the substitution of the C5 phenyl group, the presence of an EDG unit increases the reaction rate if it is placed on the N2 phenyl ring, and an EWG moiety decelerates the reaction in the same position. Nevertheless, the reaction rate, and therefore the (regio)selectivity is most affected by altering the electron density of the π-system attached to the C5 atom.[359]

Due to thoughtful choice of substituents, control over the reaction path is gained, and as a result, the NITEC reaction is successfully implemented into various fields. In soft matter science, block copolymer formation,[351] and the crosslinking of polymer chains forming a fluorescent network are established *via* NITEC ligation.[35] In detail, the number of pyrazoline units as cross points in polymer networks are quantified *via* fluorescence spectroscopy measurements.[360] In addition, individual polymer chains are collapsed upon light exposure forming either water soluble or degradable fluorescent nanoparticles – ideal candidates for imaging application and cell transport.[36, 266] By exploiting the spatio control of the NITEC reaction, cellulose and silicon surfaces are successfully patterned with polymer strands,[351, 361] or functional molecules.[362] The NITEC reaction is successfully implemented into a λ-orthogonal macromolecular ligation protocol. Two polymer strands, one end-capped with an *ortho*-methyl benzaldehyde and the other one tethered to a tetrazole moiety, react with diverse reaction rates at different wavelengths. At lower wavelengths (λ = 270-310 nm), the NITEC reaction is faster, while at higher wavelengths (λ = 310-350 nm), the formation of *ortho*-quinodimethanes and following cycloaddition have higher reaction rates.[363] Subsequently, the λ-orthogonal concept was expanded for the synthesis of macromolecular star architectures.[340]

2.2.4.3 2*H*-Azirine Ligation

Closely related to the NITEC ligation, the light-induced reaction of 2*H*-azirines proceeds in two steps. In the first step, the 2*H*-azirine releases its ring strain by heterolytic cleavage of the C-C bond generating a highly reactive nitrile ylide upon light irradiation. The reactive species acts as 1,3-dipole in the following cycloaddition with electron-deficient alkene units or alkyne groups affording Δ^1 pyrrolines (refer to

Scheme 2.11).[364–366] Due to the efficient nature of the cycloaddition, the photolysis of 2*H*-azirines is frequently employed for the synthesis of nitrogen-containing five-membered rings.[367–369] However, if the dipolarphilic character of the reaction partner is particularly low, dimerization of the nitrile ylide occurs depending on the structure.[370, 371]

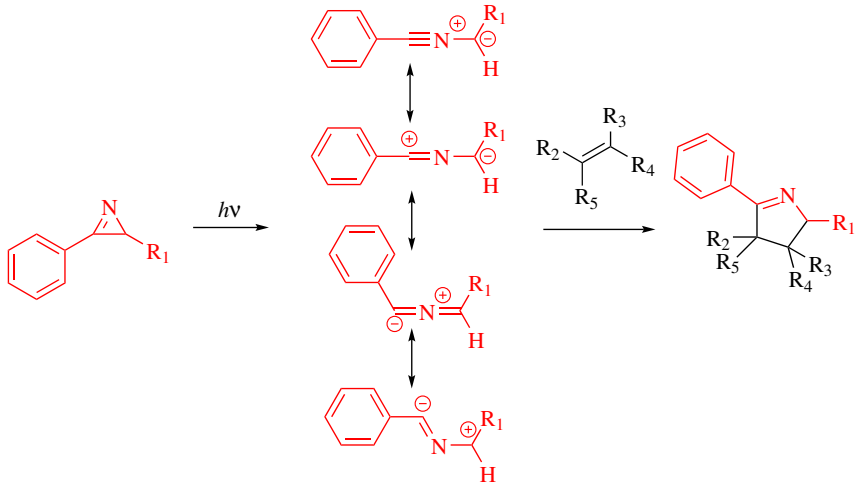

Scheme 2.11. Similar to the photochemistry of diaryl tetrazoles, the irradiation of 2*H*-azirines generates nitrile ylides as reactive 1,3-dipoles, which react with electron-deficient olefin substrates to form nitrogen-containing five-membered heterocycles.[364–366]

Both nucleophiles and electrophiles are capable of attacking the 2*H*-azirine,[372] which additionally participates in [4+2] cycloaddition reactions as dienophilic or dipolarophilic partner.[373–375] As a result of its instability towards different chemical groups, the interest in the photochemistry of 2*H*-azirines is limited, and examples of successful implementation into soft matter science or bio-medical application are rare. Hence, only the rapid and selective peptide conjugation using 2*H*-diarylazirines in combination with a UV light source (λ = 302 nm) in aqueous media is reported.[376]

2.2.4.4 Irradiation-Induced Decay of Phenacyl Sulfides

Thioaldehydes are valuable and highly reactive compounds, yet they have not been present in synthetic chemistry for a long time due to their high reactivity and tendency to oligomerize.[377] However, they are excellent dienophiles for hetereo-Diels–Alder cycloaddition reactions in the presence of dienes including buta-1,3-diene, cyclobutadiene and derivatives.[377, 378] Access to these reactive intermediates can be tedious and harsh. Either flash thermolysis of allyl sulfides at 600-800 °C,[379] or thermolysis

of alkyl thiosulphinates at 100 °C are reliable methods to synthesize thioaldehydes.[380] The irradiation of phenacyl sulfides with light (λ = 355 nm) clearly presents the most facile and mildest pathway to generate thioaldehydes.[377, 378] Upon UV light exposure, phenacyl sulfides fragment into thioaldehydes releasing acetophenone as side product (refer to **Scheme 2.12**). The subsequent [4+2] cycloaddition forming dihydrothiopyrans was in-depth studied. While thioaldehydes substituted with electron-acceptor groups react with various diene species, intermediates with aliphatic character need a higher stoichiometry of the diene in order to prevent the self-polymerization.[378] Furthermore, thioaldehydes also undergo [2+2] and [3+2] cycloaddition with terpenes and phenyl allenes, respectively.[380, 381] Additionally, several adducts are feasible if a suitable nucleophile is present. With amines as reaction partner, imines are generated as product, which are prone to oxidation. Analogously, hydroxylamines and thioaldehydes form oximes, and in the presence of thiolates, disulfide bonds are formed (refer to **Scheme 2.12**).[382] Nevertheless, thioaldehydes are tolerant towards carboxylic acids, esters, amides, ethers and hydroxy groups, enabling the application of thioaldehydes in various fields,[377, 378, 383] including end group modification of polymers,[382, 383] and patterning of surfaces with nucleophilic moieties,[382] polymer chains,[383] or metal complexes.[384]

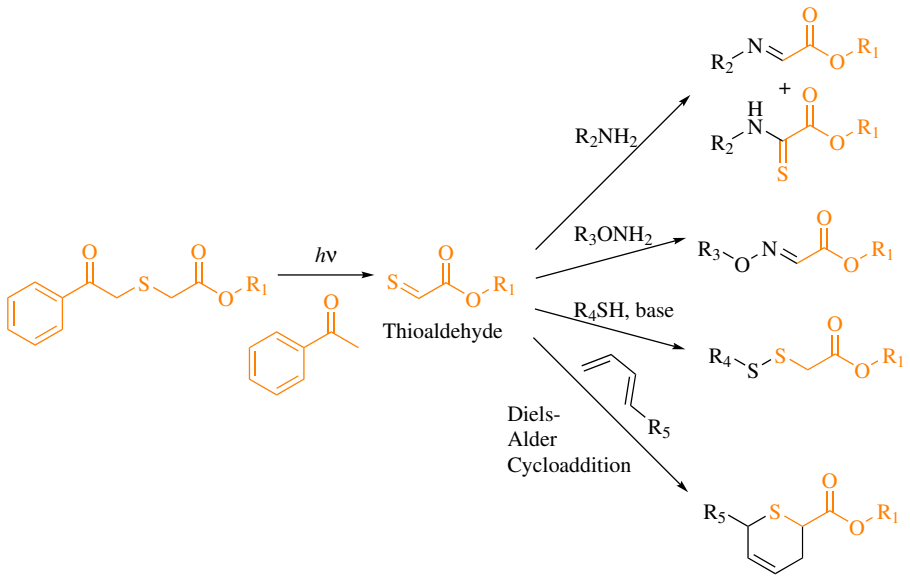

Scheme 2.12. The phenacyl sulfide generates a highly reactive thioaldehyde upon UV light irradiation releasing acetophenone as side product. Subsequently, the thioaldehyde is able to react with various nucleophiles including amines, aminoxys and thiols. If a diene is present, the reactive species acts as dienophile in a hetero-Diels–Alder cycloaddition.[377, 378, 382]

2.3 Methods for a Bathochromic Shift of the Excitation Wavelength in Photochemistry[2]

The interest in chemical transformations driven by light activation has grown over the last years due to the gain of spatiotemporal control in combination with the economic impact of light (*e.g.*, sustainability, availability and non-toxicity at ambient temperature) over other analogous methods in polymer and material science. Indeed, some of these light-activated synthetic protocols fulfill the criteria of *click* reactions specified by Kolb, Finn and Sharpless in 2001 (for details refer to **Section 2.1.3**).[16] However, the implemented light source has been a tremendous drawback for many light-triggered reactions as irradiation with high energy UV light (100-380 nm) readily led to the desired reaction products. Because of the high energy profile of the applied light, damage to the irradiated molecules and the reaction media (*e.g.*, solvent, polymer material and biological tissue) cannot be avoided; decomposition and undesired side reactions are the result of the utilization of harsh UV light.[385, 386] In addition, the penetration depth of UV light in solution or material is rather low preventing efficient application in dental curings and related material science.

Consequently, photochemists have been investigating ways to circumvent the harmful UV light in order to utilize either light from the visible (400-800 nm) or NIR (800-1400 nm) light range possessing lower energies than UV irradiation sources. In general, photochemical reactions include bond breaking processes. Despite the fact that the energy of visible or NIR light is too low to break these bonds, mainly four complementary approaches have been successfully established. Each method displays its own benefits and drawbacks, and they are discussed in the following subsections including their principles and potential application fields.

2.3.1 Modification of the Photoreactive Species Employing Pyrene

A bathochromic shift of the photochemical reactivity *via* the modification of the photoreactive species displays an elegant, and occasionally an intricate, approach to prevent the application of UV light. The avoidance of additives (*e.g.*, catalysts) or advanced experimental setups (*e.g.*, high intensity laser

[2] The theoretical background for the presented chapter and its subsections is based on J. T. Offenloch, M. Gernhardt, J. P. Blinco, H. Frisch, H. Mutlu, C. Barner-Kowollik, *Chem. Eur. J.*, **2019**, *25*, 3700-3709. Adapted with permission from Wiley-VCH Verlag GmbH & Co. KGaA, Weinheim.

systems) are the dominant advantages for the approach, which is linked to the idea of altering the molecule's structure to achieve a shift of the trigger-wavelength to higher values. In general, UV/Vis spectra of photoreactive compounds provide information about the wavelength regimes, which lead to electronic excitation of the molecule. Hereby, careful studies revealed that the plot of educt conversion *vs.* wavelength (at a constant photon count) does not necessarily follow the absorption spectrum of a specific compound.[387, 388] Therefore, the irradiation with $\lambda_{abs.max}$, based on spectroscopic determination, does not have to result in efficient photoinitiation of a reaction. Indeed, a suitable excitation wavelength for phototriggering might be presented as subtle absorbance, or even not visible, in the UV/Vis spectrum. However, approximate assessments on the reactivity of photoreactive species based on the absorption spectrum are still feasible.

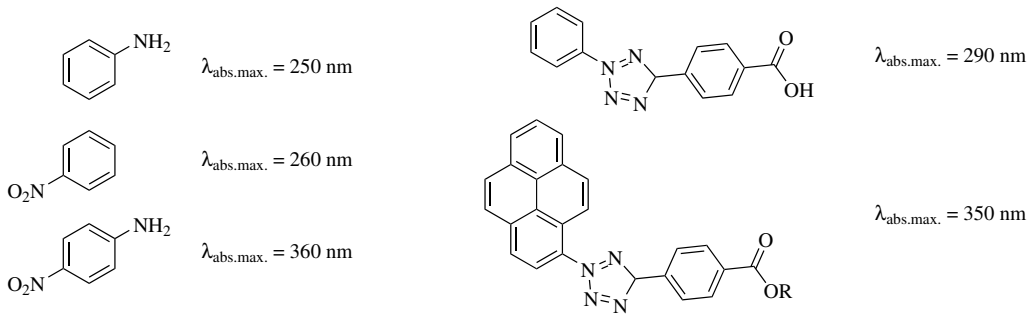

Scheme 2.13. Two different strategies for a bathochromic shift in the absorption spectrum of compounds. Electron donor (*e.g.*, amino groups) and electron acceptor (*e.g.*, nitro groups) substituents in a push-and-pull configuration have an immense impact on the absorption spectrum as depicted on the left side. In contrast, the bathochromic shift in the absorption spectrum caused by expansion of the aromatic system as displayed on the right side is less pronounced. The values of the absorption maxima $\lambda_{abs.max.}$ are taken from [340, 357, 389].

Two different strategies for a successful bathochromic shift in the absorption spectrum of photoreactive compounds are established (refer to **Scheme 2.13**). The first approach includes the installation of electron-withdrawing (or electron-donating) substituents on a conjugated framework.[390] Substantial effects on the absorption spectrum are achieved if the conjugated system is end-capped with electron donor and electron acceptor groups in a push-and-pull configuration, *i.e.*, the electron-donating and -withdrawing units are each located on different ends of the conjugated system.[389] Expanding the conjugated system *via* the enlargement of condensed aromatic systems or conjugation is the second option for a bathochromic shift of the excitation wavelength of photoreactive molecules.[391–393] With both approaches the risk of altering the reactivity of the parent compound exists potentially leading to a loss of selectivity.[391, 392] Furthermore, the intended modification should not reduce the quantum yield for ISC, *i.e.*, the excited

species of the light-sensitive moiety requires to reach a triplet state for reacting.[394] For a successful photoinduced reaction the chromophore additionally has to perform as a photosensitizer, which is capable of transporting energy efficiently.

Pyrene as chromophore exhibits an established chemistry with regard to synthesis and modification in both organic synthesis and polymer science, in addition to its well-documented properties including a long singlet lifetime and high fluorescence quantum yields.[395–397] Indeed, the absorption spectrum of the unsubstituted aromatic compound displays an absorption band reaching to 350 nm (refer to **Figure 2.8**). The properties of pyrene will be discussed in the following excursus with the emphasis on the application of the chromophore in polymer chemistry. Eventually, the additional benefits of utilizing pyrene as light harvesting unit in photochemical reactions will be highlighted by demonstrating pyrene-based visible light-induced reactions.

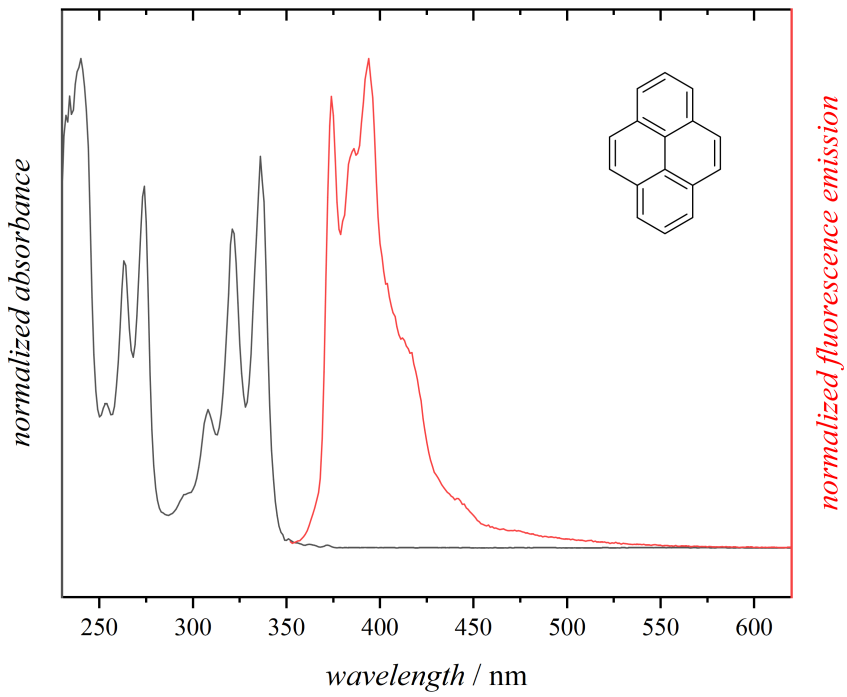

Figure 2.8. Absorption (black trace) and emission spectra (red trace, $\lambda_{exc.}$ = 344 nm) of pyrene in DCM at ambient temperature (UV/Vis: c = $7.37 \cdot 10^{-5}$ mmol mL^{-1}, fluorescence: c = $3.68 \cdot 10^{-5}$ mmol mL^{-1}).

In 1837 the destructive distillation of coal tar by Laurent led to the discovery of pyrene in the residue of the process. As a result, he termed this polycyclic compound "pyrene" - the greek word for "fire" - since he assumed that pyrene was formed by burning organic compounds.[395] However,

the polycyclic compound is formed in various processes including the catarol process, a special distillation of mercury,[395] and the pyrolysis of acetylene and hydrogen.[398] Today, the commercial production of pyrene mainly proceeds *via* destructive hydrogenation of hard coal as well as modified distillation of coal tar.[395]

Most of the applications of pyrene in polymer chemistry stems from its optical properties. Its absorption spectrum (refer to the black trace in **Figure 2.8**) displays an absorbance reaching up to 350 nm, which is not interfering with the absorbances of any common polymeric species. As a consequence, SEC systems coupled to UV detection, which is set to a wavelength that only the pyrene moiety absorbs, enable the selective recording of polymer chains coupled to the chromophore.[204, 399]

The fluorescence properties of pyrene are particularly outstanding (refer to the red trace in **Figure 2.8**), and therefore this aromatic compound is the most frequently used dye in organic synthesis and polymer chemistry. Remarkably, one pyrene unit in an excited singlet state and another unit in the ground state form an excimer dimer in close proximity, which reveals a fluorescence maximum in the range of 480 to 500 nm, whereas the fluorescence for dissociated pyrene species lies in the area between 380 and 420 nm.[400, 401] This excimer formation is applied in various fields, *e.g.*, polymer dynamics including association. In fact, valuable results of the efficiency of the intra- or intermolecular excimer formation of the pyrene moieties are obtained *via* the comparison of the intensity of the monomer fluorescence (I_M) to the intensity of the excimer (I_E).[400] For example, fluorescence measurements of polymer chains modified with pendant pyrene units reveal constant values for I_E/I_M at low concentrations due to intramolecular excimer formation along the chain. In contrast, with increasing polymer concentration, the generation of intermolecular excimers is detected, and I_E/I_M increases.[402] Additionally, external changes affect the optical properties of pyrene functionalized stimuli-responsive (*i.e.*, temperature) polymers. For instance, under the lower critical micellization temperature (LCMT), excimer emission is pronounced due to stable aggregates formed between polymer and pyrene units. Nevertheless, above the LCMT the aggregates of the chromophore are destructed resulting in more intense and sharper absorption bands in combination with a more intense monomer emission in the fluorescence spectrum.[403]

The polarity of the environment of the chromophore in general also affects its fluorescence spectrum. Thus, the polarity is determined by the intensity ratio of the first (I_1) to the third vibronic

band (I_3) of monomer emission (*i.e.*, pyrene).[400, 404, 405] As a result, variances in the environment of pyrene upon altering the concentration of a polymer give access to the dynamics of the polymers chains in solution depending on the concentration. By tracing the progression of I_1/I_3 when changing the concentration, direct access to the critical aggregation concentration of polymer chains is received.[402] Besides, due to the affinity of pyrene towards hydrophobic environment such as interiors of micelles,[406] the fluorescence intensity of the chromophore increases when it is encapsulated in micelles.[406, 407] Therefore, pyrene is a suitable fluorescence probe for detecting the CMC of amphiphilic polymeric species. Relying on the optical properties of pyrene, extensive studies in solution of poly(*N*-isopropylacrylamide),[402, 403] hydroxypropylcellulose,[408] poly(ethylene glycol),[408] poly(acrylic acid),[409, 410] poly(methyl meth-acrylate),[411] and block copolymers thereof, as well as of side chains,[412] are realized.[408]

The fluorescence properties of pyrene are quenched by radicals such as nitroxide derivatives, *e.g.*, 2,2,6,6-tetramethylpiperi-dinyloxyl (TEMPO), because of the ability of the free radical to quench excited singlet, triplet and excimeric states inter- and intramolecularily *via* electron-interchange interactions.[413] As a result, the fluorescence of pyrene- and nitroxide-functional polymers is silenced, and subsequently restored upon heat- and light-induced release of pyrene as a self-reporting system.[37, 414]

Another application of pyrene-functionalized polymers is accomplished in optical recordings *via* the combination of its optical properties and pyrene's ability for π-π stacking. Photoinduced heating of films consisting of polylactide species end-capped with pyrene units results in local melting, and subsequent photo-induced arrangement of the pyrene end groups to form dimers, which are retained after cooling. Afterwards, excimer fluorescence exhibits the written structures.[415, 416]

Well-ordered nanopore films with fluorescent character are accessible *via* drop-casting of a copolymer with pyrene moieties along the backbone, which are useful for various optoelectronic and biomedical applications.[417] Additionally, nanorods and nanotubes of PS-*b*-PMMA with pendant pyrene end groups as further examples for nanostructures were prepared and in-depth characterized.[418]

Highly conjugated polymers possessing pyrene units incorporated into their backbone are of great interest as well. Indeed, carbon dioxide from air is converted into CO driven by visible light using an ionic liquid for gas absorption in combination with a conjugated, pyrene-substituted polymer

as catalyst.[419] Analogously, the conjugation of pyrene and benzothiadiazole provides polymeric material capable of transforming water into hydrogen gas.[420]

Notably, the magnetic resonances arising from the aromatic protons of pyrene in ^{1}H NMR spectra are located separately in highfield supporting the facile identification of the success of modification reactions.[401]

Apart from the great success of pyrene in polymer chemistry, this aromatic compound gained attention in dye industry for the synthesis of pyranthrones.[421] In addition, π-conjugated materials based on pyrene are promising candidates for future semiconductor devices including light-emitting diodes (LEDs) and organic photovoltaics.[396]

The first visible light-induced reaction employing pyrene as chromophore was published in 2015, where our team introduced a pyrene-substituted 2*H*-azirine (refer to **Figure 2.14A**).[422] Upon irradiation with a blue LED light source (410-420 nm), the ring strain of the three-membered ring is released by generating a reactive 1,3-dipole, the nitrile ylide. The selective reaction of the nitrile ylide with electron-deficient olefin species in 1,3-dipolar cycloadditions is proven, resulting in nitrogen-containing five-membered heterocycles as products. In general, the reaction proceeds very fast (within one minute) and without the requirement of any catalyst. Nonetheless, the chemical stability of 2*H*-azirines is limited, and thus preventing the attachment of anchoring groups for further application until today.

One year later, our team described a novel visible light-reactive compound combining pyrene and tetrazole chemistry.[357] Based on preliminary reactivity studies of tetrazoles,[390–393] a pyrene-functionalized aryl tetrazole (PAT, refer to **Figure 2.14B**) was designed, not only allowing efficient 1,3-dipolar cycloadditions *via* formation of reactive nitrile imines upon irradiation with a light source (410-420 nm), but it also supports the further attachment to various relevant molecules in esterification reactions for subsequent application. In addition, the fluorescence of the cycloadduct with olefinic substrates, the pyrazoline, possesses a broad fluorescence band with a tailing in the NIR region suitable for biomedical issues, *e.g., in vivo* imaging. Therefore, the PAT compound is applied in various fields, *e.g.*, for the quantitative block copolymer formation using either an LED light source,[357] or NIR light in combination with upconversion nanoparticles (UCNPs).[423] Moreover, PAT- and diaryl tetrazole-functionalized surfaces are synthesized exploiting the λ-orthogonality of the utilized tetrazole species.[424] Furthermore, visible light-reactive latex

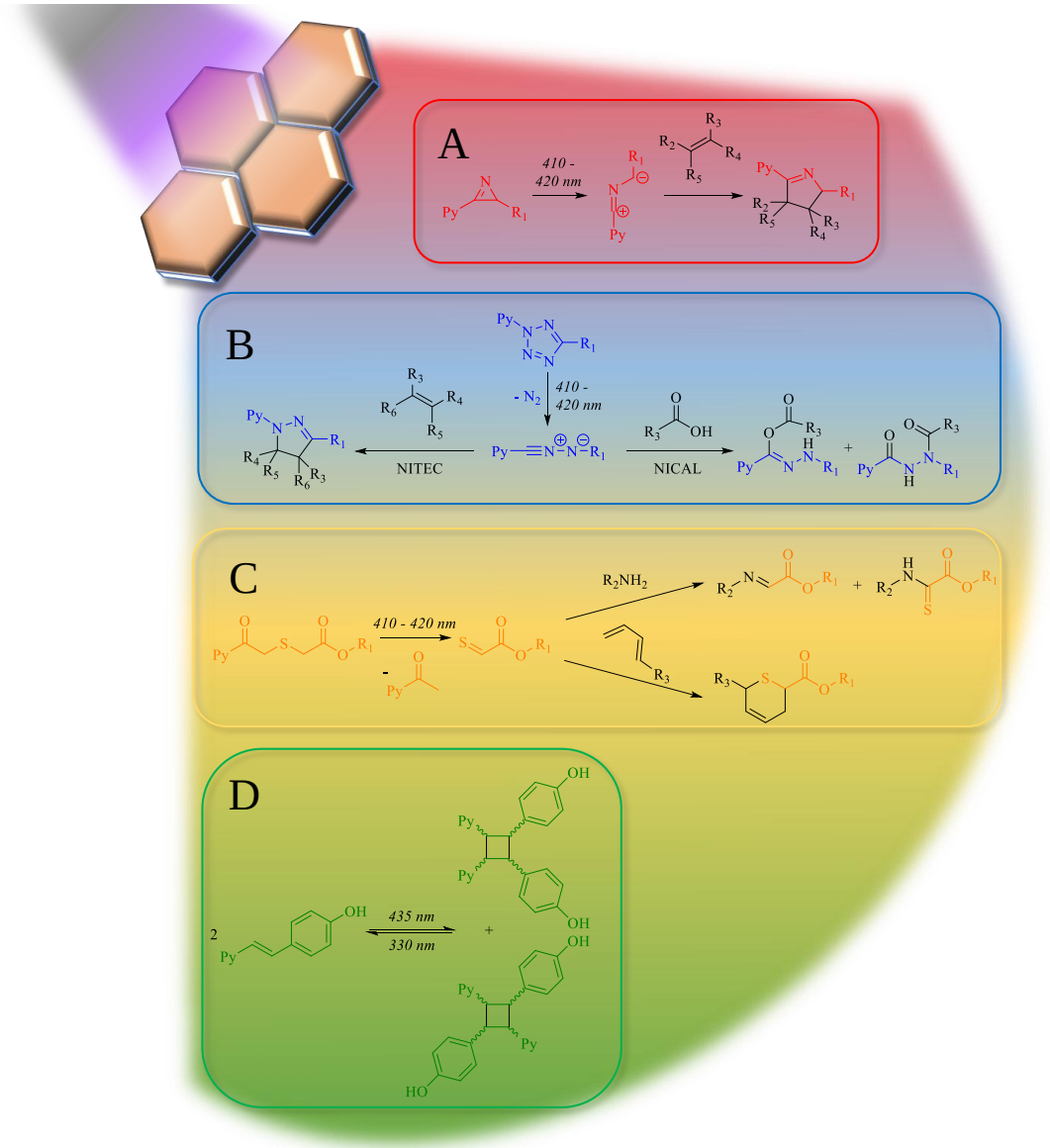

Scheme 2.14. Through the utilization of pyrene as chromophore, the trigger wavelengths of four different photochemically induced reactions are successfully shifted to higher values (Stokes shift). Thus, the reaction schemes **A** - **D** indicate the red-shifted chemical transformations arranged by the year of publication. **A**: 2*H*-azirine ligation, **B**: Tetrazole activation, **C**: Light-induced fragmentation of pyreneacyl sulfide and **D**: Dimerization and cycloreversion of styryl pyrene and its dimer, respectively.

particles have been successfully prepared.[425] Last but not least, the photochemistry of the PAT moiety allows the yet mildest approach to form single-chain nanoparticle based on the collapse of PAT-functional polymer strands *via* NITEC and NICAL reaction.[267]

Subsequently, the successful transfer of the UV light-triggered photochemistry of phenacyl sulfides to the visible light range has been reported.[426] Upon irradiation with a blue LED light source (410-420 nm), pyreneacyl sulfides (refer to **Figure 2.14C**) react analogously to its UV light-triggerable counterpart with diverse nucleophiles, *e.g.*, amines, aminoxyls and thiols, as well as dienes in hetero-Diels–Alder reactions. A poly(methyl methacrylate) species decorated with pyreneacyl sulfide acting as photoreactive fluorophore alongside TEMPO as fluorescence quencher is realized for the detection of the visible light-triggered release of 1-acetylpyrene. The nitroxide radical suppresses the fluorescence of pyrene in the polymer due to the close proximity. Upon release of the pyrene, the fluorescence is restored as indicated by the fluorescence measurements.[37]

Pyrene is also successfully introduced in the field of visible light-induced reversible [2+2] cycloadditions.[427, 428] The self-dimerization and the cycloreversion of styryl pyrene (refer to **Figure 2.14D**) are fully λ-orthogonal: While the cycloaddition is accomplished at a wavelength of 435 nm, the ideal wavelength for the dissociation lies in the UV range with 330 nm.[427] Therefore, styryl pyrene displays the most orthogonal and mildest reversible conjugation approach in terms of applied wavelengths. Consequently, styryl pyrene was employed for the reversible block copolymer formation based on a functional PEG block, and for the synthesis of a photodynamic hydrogel, which is able to change its mechanical properties upon irradiation with a certain wavelength.[427, 428]

Finally, the following example underlines that conjugation of pyrene with suitable chromophores is important in order to reach an excitation wavelength in the visible light regime. Compounds possessing aryl methyl moieties with a leaving group $ArCH_2LG$ (LG = RCO_2) undergo either homolytic or heterolytic fragmentation upon irradiation with a suitable wavelength (*e.g.*, Ar = Ph: λ = 254 nm). Coupling/disproportionation and substitution products are the result of this cleavage reaction.[429] Despite the implementation of pyrene as chromophore, a light source of the UV light regime (365 nm) is required for the reaction indicating the importance of a suitable substitution of pyrene for a visible light-induced transformation. Nevertheless, this reaction pathway was exploited for the synthesis of amphiphilic block copolymers for micelle formation. In fact, upon a UV light trigger, the micelles collapse due to the

transformation of the hydrophobic, light-sensitive pyrene block into a hydrophilic segment with carboxylic acid functionalities.[430]

The above mentioned examples for visible light-induced reactions unambiguously demonstrate the versatility of pyrene as efficient chromophore for a bathochromic shift of the reactivity of chemical groups activated by light. The following question may arise: Why was the reactivity shift to higher wavelengths not yet achieved with *ortho*-methylbenzaldehydes, an excellent photoreactive moiety for light-induced Diels–Alder cycloaddition? Indeed, various structures based on pyrene are realized, yet they remain inactive upon visible light exposure. This observation illustrates that shifting of the photoreactivity might not be a trivial task. However, a recent study from our team reveals the successful red-shifting of the excitation wavelength of *ortho*-methylbenzaldehydes *via* the substitution of the ether unit into a thioether group.[431] Nevertheless, additional investigations, *e.g.*, DFT calculations, are necessary to deliver insights into the different electronic transitions and their excitation wavelengths of diverse photoactive compounds. In this regard, a careful study on the photochemistry of tetrazoles indicates that for a successful photoreaction an effective ISC from the singlet S_1 to the triplet state T_1 presents a precondition. In addition, relaxation occurring either by vibrational deactivation caused by the non-planar conformation of the singlet states S_0 and S_1 or by charge recombination needs to be avoided. As a result, an amino-substituted diphenyl tetrazole is not able to undergo visible light activated cycloadditions, although its absorption spectrum shows absorption bands in similar ranges compared to PAT.[394]

In summary, a bathochromic shift of the photoreactivity can present a delicate task, yet this method does not require an advanced experimental setups or any additives.

2.3.2 Photoredox Catalysis

Visible light photoredox catalysis (VLPC) is a rapidly growing research field embedded between diverse areas of chemistry. Substrates are transformed *via* photoinduced single electron-transfer processes assisted by a suitable catalyst.[432, 433] Generally, polypyridyl complexes of ruthenium or iridium are utilized as catalysts, *e.g.*, [$Ru(bipy)_3^{2+}$], capable of absorbing visible light to generate a long-lived excited species for bimolecular electron-transfer reactions. Thus, by the judicious choice of a catalyst diverse chemical transformations including oxidations,[434] reductions,[435] and cycloadditions,[436, 437] are triggered *via* the application of visible light. The mechanism of the VLPC reaction is well studied and illustrated in

Figure 2.9 on the basis of the prototypical catalyst [Ru(bipy)$_3$$^{2+}$].[432] The absorption of a photon leads to the excitation of an electron situated within a metal-centered t_{2g} orbital into a ligand-centered π^* orbital. This process is called a metal-to-ligand charge transfer (MLCT), and it is followed by a rapid ISC to the lowest energy triplet state. Due to the forbidden relaxation to the S_0 niveau, the long-lived photoexcited triplet species are capable to participate in electron-transfer processes. Hence the activated species can either receive an electron in its half occupied t_{2g} orbital, or provide an electron *via* the π^* orbital. As a consequence, the photocatalyst may participate in oxidative quenching as well as reductive quenching processes (refer to **Figure 2.10**). In the oxidative quenching cycle, the triplet species expels an electron to an oxidative quencher (*e.g.*, viologens and polyhalomethanes) in order to receive it one more time from the substrate. In contrast, [Ru(bipy)$_3$$^{2+}$] accepts an electron originating from a reductive quencher (*e.g.*, tertiary amines) in order to donate it to the substrate in the reductive quenching cycle. Which reaction pathway will proceed depends on the redox potentials of each species that in turn is correlated to the substitution pattern of the ligands.[432, 433]

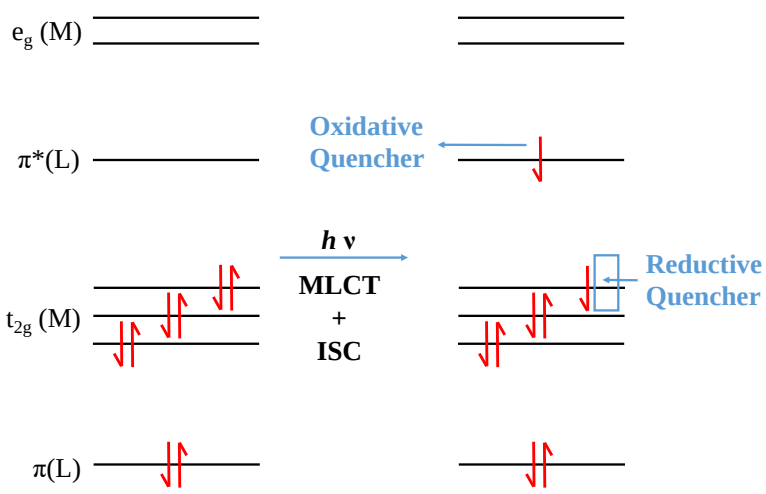

Figure 2.9. Photoinduced activation of [Ru(bipy)$_3$]$^{2+}$ illustrated by means of the orbital energy levels. In the oxidative quenching cycle, the high energy electron available in the π^* orbital is transferred to an oxidative quencher, while the vacant electron position in the t_{2g} orbital is available for an electron from a reductive quencher. Adapted with permission from [432]. Copyright (2013) American Chemical Society.

The tunability of the reaction conditions with regard to the substrates and the adjustment of the employed wavelength are the vast benefits of the VLPC. Nevertheless, the removal of the catalyst can display a disadvantage for *in situ* experimental setups. In addition, careful inspection of the catalyst system has

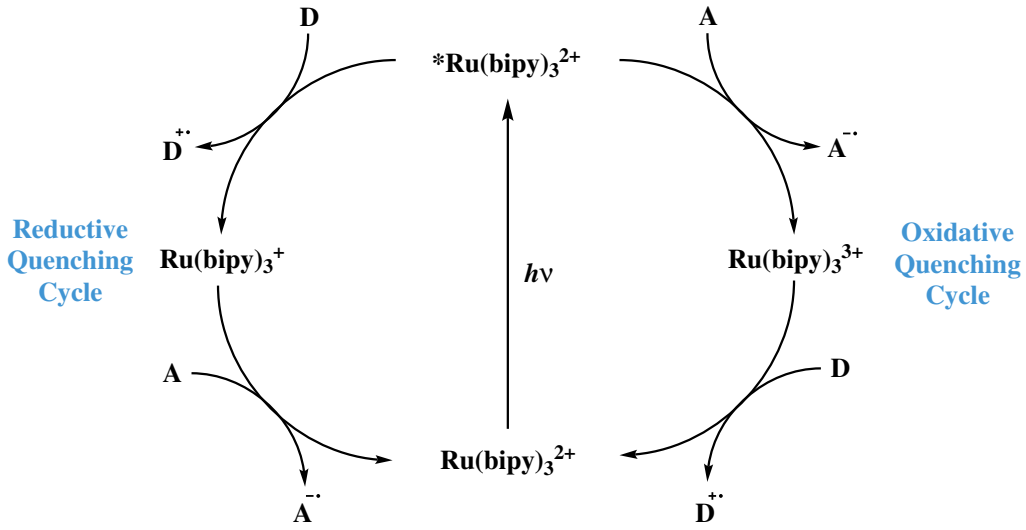

Figure 2.10. The oxidative and reductive quenching cycles illustrate the dual nature of the excited [$Ru(bipy)_3^{2+}$] species. The excited metal compound expels an electron to an oxidative quencher in the first step of the oxidative quenching cycle in order to receive it one more time from the substrate in the second step. In the reductive quenching cycle, [$Ru(bipy)_3^{2+}$] accepts an electron originating from a reductive quencher, and subsequently donate it to the substrate. Electron-acceptors and -donors are abbreviated as A and D, respectively. Adapted with permission from [432]. Copyright (2013) American Chemical Society.

to be conducted in order to avoid side reactions between the catalyst and additionally present functional groups. Besides, the potential toxicity of the metal poses a threat to biomedical applications. In fact, the organic photoredox catalysis holds the potential to avoid this problem, it nonetheless faces issues such as the lack of highly reducing catalysts and the urgency to identify more robust chromophores.[438]

2.3.3 Simultaneous Two-Photon Absorption

With the improvement and the commercialization of high intensity laser systems, a further strategy to induce photochemical reactions with visible or NIR light has gained attention: The simultaneous two-photon absorption (TPA). At first merely described in principle,[439] 30 years had to pass until the TPA process was experimentally verified in the 1960's.[440, 441] The TPA is a non-linear optical process in which a simultaneous absorption of two photons is necessary to reach the excited state. Therefore, a virtual level between the ground and the excited state exists, which lifetime is limited to 1 to 10 femtoseconds (refer to **Figure 2.11**).[442] Hence longer wavelengths are applied in TPA processes in comparison to common one-photon absorption. However, considering the simultaneous absorption of two photons is scarce, the spatiotemporal density of photons demands to be high. As a consequence, exclusively focused high-intensity laser systems fulfill the requirements to exploit the TPA effect.

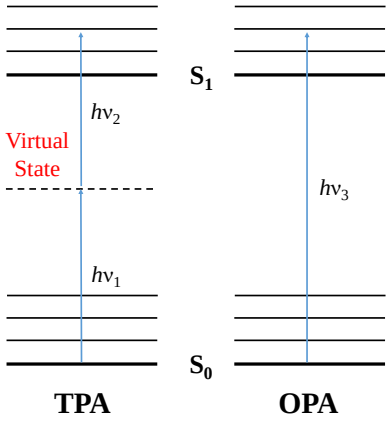

Figure 2.11. Schematic comparison between the two-photon absorption (TPA, left) and the one-photon absorption (OPA, right).[440–442]

Since the absorption of the TPA increases with the square of the light intensity, the excitation occurs only at the focal point, whereas conventionally one-photon excitation is triggered along the light beam due to the linear dependency on the light intensity.[443]

The spatial control of excitation at the focal point combined with the shift of the applied wavelength to higher values as main benefits of the TPA process resulted in the successful implementation of this phenomenon in diverse fields,[444] *e.g.*, fluorescence microscopy and spectroscopy,[445, 446] and also sensors for ions,[447–449] and pH changes.[450] Particularly biomedical applications, *e.g.*, drug delivery,[451–453] and photodynamic therapy,[454] exploit the large Stokes shift associated with TPA processes. In contrast, the fabrication of 3D structures with features in the hundred nm range,[455–457] profits from the focused excitation site, ultimately enabling superior data storage for future application.[458, 459]

Chemical reactions that can be triggered by TPA processes include cycloadditions,[460, 461] as well as isomerizations,[462–464] decarbonylation,[465] and the initiation of polymerizations.[466] For instance, *ortho*-methylbenzaldehyde derivatives display particularly valuable compounds due to their ability to be activated by light of one wavelength (*via* TPA with 700 nm), while the deactivation can be triggered with light of another wavelength (440 nm). Therefore, this molecular switch can be implemented in sub-diffraction laser lithography for the attachment of soft matter on a glass surface with a feature size down to 60 nm.[467]

In the absence of additives, the TPA process is capable to shift the excitation wavelengths of chemical transformations to higher values. Nevertheless, advanced experimental setups are required in combination

with a high intensity laser source. Moreover, 3D lithography yet forbids the mass production of novel data storage systems.[444]

2.3.4 Upconversion Nanoparticles

Particles of lanthanide- or actinide-doped transition metals capable of photon upconversion are known as upconversion nanoparticles (UCNPs).[468–471] These particles convert two or more incident photons into one emitted photon with combined energy. The effect of photon upconversion was first experimentally verified by Auzel in 1966.[472] However, over 40 years had to pass until UCNPs were introduced to photochemistry with the aim to assist light-triggered transformation *via* the enhancement of the applied wavelength.[468]

Three different processes for photon upconversion are identified in **Figure 2.12**: Excited state absorption (ESA), photon avalanche (PA) and energy transfer upconversion (ETU, the most common pathway).[469, 470, 472] Long lifetimes of the excited states and an arrangement of energy levels with similar spacings are preconditions for efficient upconversion. In these processes, the sequential absorption of photons occurs reaching higher energy levels.[469] For ESA, the consecutive absorption of two photons leads to the population of the second excited metastable E_2, and the subsequent upconversion emission triggers the relaxation. Whereas, in the ETU process two neighboring ions absorb each one photon of the same energy reaching the metastable level E_1, followed by a non-radiative energy transfer from one ion relaxing to the ground state to the other ion being promoted to the emitting state E_2. From there, upconversion emission promotes the population of the ground state as well. In contrast, E_1 is populated *via* non-resonant absorption in PA. Subsequently, the promotion to E_2 is accomplished *via* resonant ESA, followed by a cross-relaxation energy transfer with a neighboring ground state ion. Accordingly, both ions now occupy E_1. The repetitive cycles of ESA and energy transfers amplify the E_2 population exponentially resulting in a strong upconversion emission.

Merging photochemistry and UCNPs opens the possibility to induce chemical transformations of photosensitive compounds utilizing mild NIR light.[471] For instance, azobenzene motifs,[473] spiropyran derivatives,[474] and dithienylethene[468] are successfully tested in UCNPs-assisted photoisomerizations. Furthermore, photolysis presents the second main class of photoreactions that can be supported by UCNPs. *Ortho*-nitro benzyl,[475, 476] coumarin,[477, 478] 3',5'-di(carboxymethoxy)benzoin acetate,[479] and

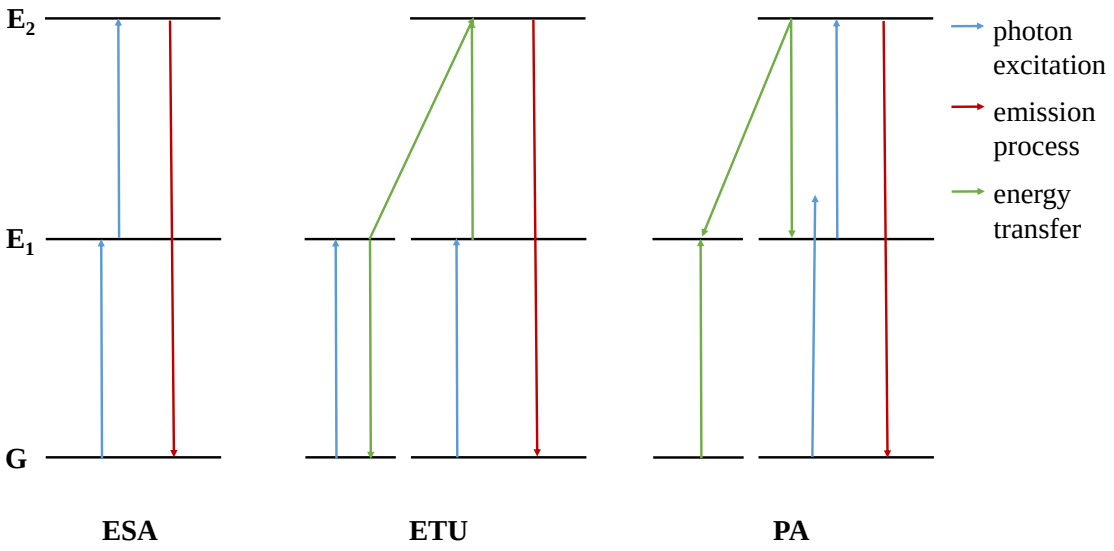

Figure 2.12. Three different processes for photon upconversion: Excited state absorption (ESA, left), energy transfer upconversion (ETU, middle) and photon avalanche (PA, right). Adapted with permission from [470]. Copyright (2009) Royal Society of Chemistry.

ruthenium complexes,[480, 481] take part in photolysis reactions upon irradiation in the presence of UCNPs. In addition, photopolymerizations,[482, 483] and photocoupling reactions,[423] proceed efficiently with the aid of the photon upconversion process.

UCNPs are customizable substrates; their wavelength for photon upconversion can be altered by structural changes of the particles (*e.g.*, passivation or modification of the surface), size and choice of the employed lanthanide.[470] An additional advantage of UCNPs is the excitation intensity, which is significantly lower for the utilization of these particles than for TPA processes.[471] Finally, the use of light sources with high penetration depths results in dental applications in which the curing of the material can be accomplished in a single step with the help of UCNPs instead of single layer curing.[482] Similar to the application of catalysts in VLPC, the presence of the nanoparticles reveals a disadvantage for *in situ* experiments, as well as additional interactions or side reactions between the substrates and the UCNPs have to be excluded.

CHAPTER 3

AZIRINES AS VERSATILE AND FUNCTIONAL HANDLE FOR THE SYNTHESIS OF MACROMOLECULAR ARCHITECTURES

3.1 Visible Light-Induced Ligation Chemistry *via* Azirines

Upon irradiation, 2*H*-azirines release their ring-strain *via* cleavage of the C-C bond and generation of a reactive 1,3-dipole, the nitrile ylide. Depending on the structure of the conjugated chromophore, the excitation wavelengths differ: While 2*H*-phenylazirines can be triggered with wavelengths stemming from the UV light regime (302 nm),[376] visible light (410-420 nm) is able to generate the reactive species of the pyrene derivative.[422] Whereas, the former substance was successfully employed for light-induced conjugation of proteins with small molecules,[376] the latter moiety was merely utilized for polymer end group conversion and in the synthesis of small molecule cycloadducts, since it lacks functionality to form conjugates in a non-photochemical way, *e.g.*, 2*H*-pyrenylazirine-functional polymerization initiators or transfer agents. The employment of 2*H*-azirines for photochemical-induced ligation is advantageous in various ways: The cycloaddition is extremely fast (within 2 min) and it proceeds without the need of any

catalyst. Furthermore, no detectable side product formation has been observed. As a result, it is highly desirable to install a functional group tethered to the pyrene-substituted 2*H*-azirine in order to expand its field of application. Functional groups may include carboxylic acids or hydroxyl groups as handle for esterification, azides and alkyne groups for CuAAC ligation, along double bonds, thiols or halogen groups for thiol-ene addition or substitution. On this account, the following sections cover strategies and the respective results for the synthesis of a functional pyrene-substituted 2*H*-azirine, among the challenges related to the modification and purification of these mentioned pyrene compounds.

3.1.1 Investigation of the Synthesis Routes of Functional Azirines

An overview of the synthesis routes resulting in functional 2*H*-azirines is given in **Scheme 3.1**. Due to the vast number of experiments, the description of experiments contains exclusively the most important aspects as well as merely the most relevant NMR spectroscopic results.

A: 2*H*-azirines as intermediates in Neber rearrangements

The Neber arrangement is a facile synthesis route for the preparation of α-aminoketones from tosyl ketoximes. The treatment of tosyl ketoximes with bases results in deprotonation of the α-proton followed by cyclization forming 2*H*-azirines. Acidic hydrolysis of the three-membered ring leads to ring-opening and formation of α-aminoketones.[484–486] According to a reported synthesis protocol of phenyl-substituted 2*H*-azirines obtained as intermediates in a Neber rearrangement,[487] the reaction steps in **Scheme 3.1A** leading to a 2*H*-azirine functionalized with a methyl ester were proposed (with X=COOMe).

The first step comprises the α-arylation of 1-acetylpyrene based on a modified procedure from the literature.[488] 2 mol% of Pd_2(dba) and 1,1'-bis(di-tert-butylphosphino)ferrocene (D*t*BPF) as catalytic system in addition to 2.2 eq. of NaO*t*Bu as base were loaded in a Schlenk tube at ambient temperature, and the tube was degassed by three vacuum/argon refill cycles. Subsequently, 1.0 eq. of 1-acetylpyrene and methyl 4-bromobenzoate, dissolved in 1,4-dioxane were added, and the resulting mixture was stirred at 100 °C for 22 h. The targeted compound was obtained after purification *via* column chromatography (for ^{1}H NMR spectrum, refer to **Figure 3.3**, top spectrum). The subsequent formation of the oxime was carried out *via* refluxing 1.0 eq. of the ketone derivative in the presence of 5.00 eq. of hydroxylamine hydrochloride and 4.00 eq. of sodium hydroxide in a mixture of MeOH:1,4-dioxane:H_2O (15:7:1) for

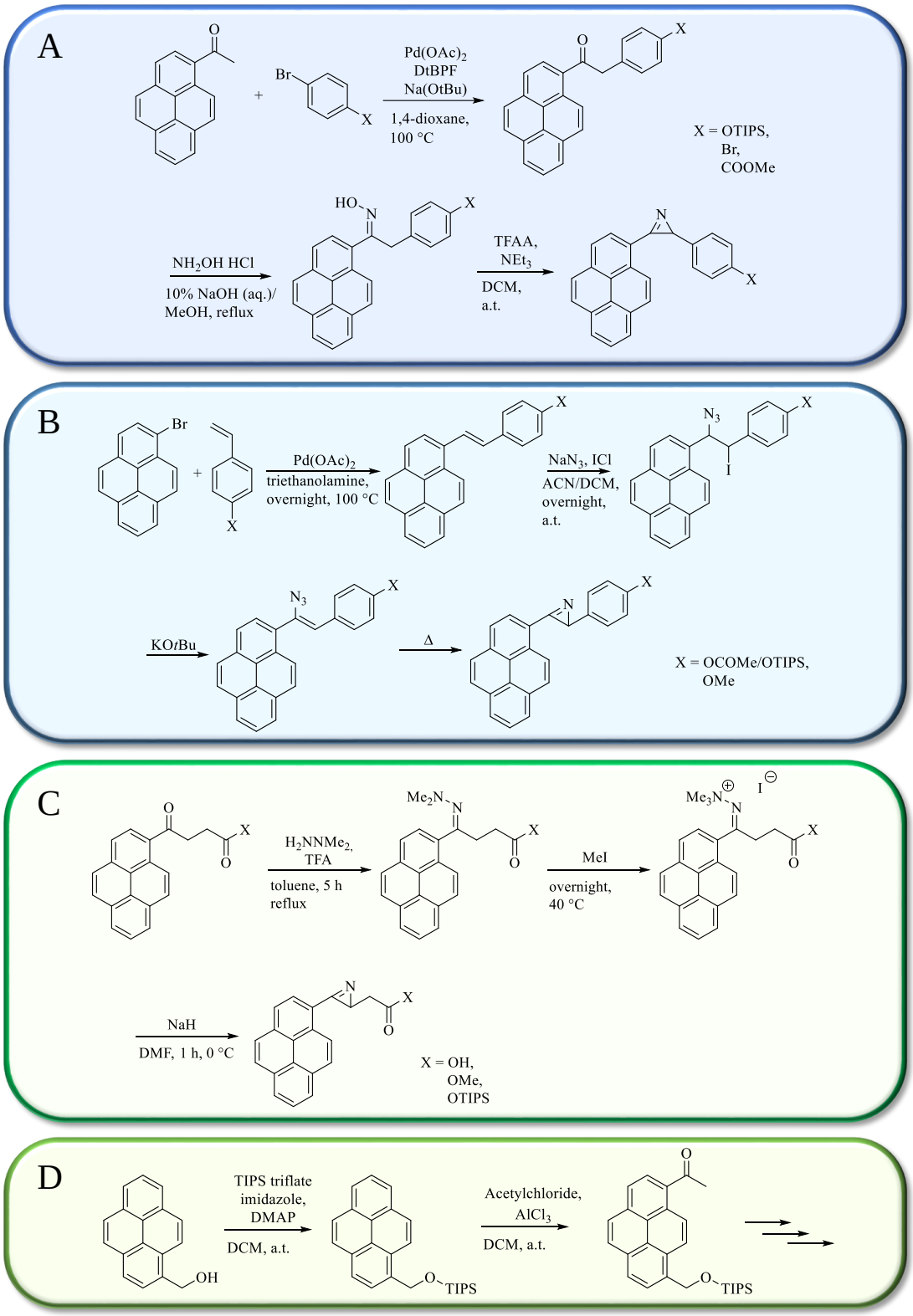

Scheme 3.1. Routes investigated for the synthesis of functional 2*H*-azirines (first part). **A**: 2*H*-azirines as intermediates in Neber rearrangements. **B**: 2*H*-Azirines *via* double elimination of iodoazides **C**: Employment of commercially available functional keto-pyrene derivatives **D**: Separate attachment of the 2*H*-azirine moiety and the functionalization unit to the pyrene core.

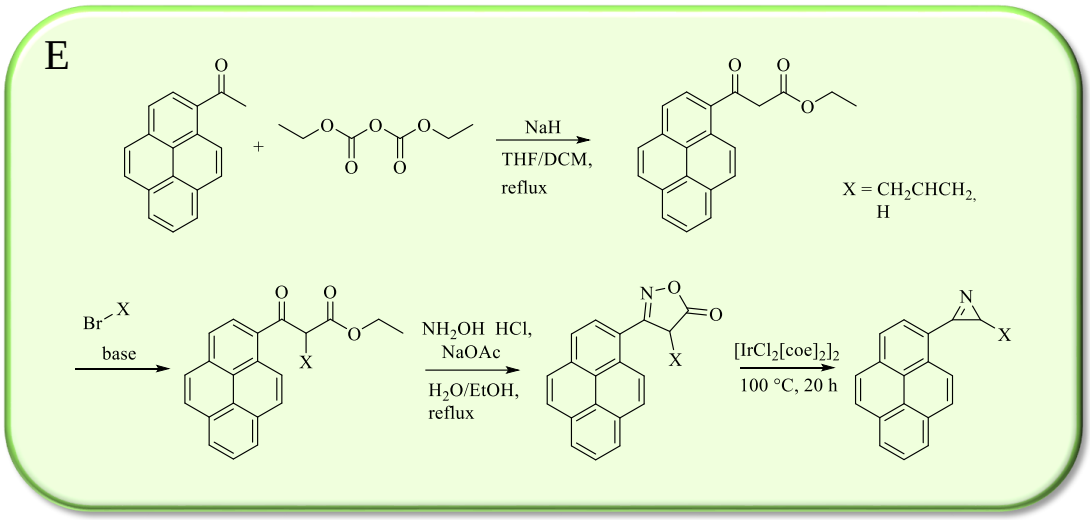

Scheme 3.2. Routes investigated for the synthesis of functional 2*H*-azirines (second part). **E**: 2*H*-Azirines *via* iridium-catalyzed ring contraction of isoxazol-5(4*H*)-ones.

22 h. After the product was purified *via* column chromatography (for the ^{1}H NMR spectrum, refer to **Figure 3.3**, bottom spectrum), the oxime was introduced in the 2*H*-azirine formation step. Trifluoroacetyl anhydride, tosyl chloride and mesityl chloride were employed in order to convert the hydroxyl group of the oxime derivatives into a good leaving group, and supposedly the respective *O*-sulfonyl (or *O*-acyl) ketoxime derivative rearranges into the 2*H*-azirine in the presence of a base (such as DBU or triethylamine). However, none of the noted derivatives (*O*-sulfonyl and *O*-acyl ketoxime) resulted in the desired 2*H*-azirine formation. In order to exclude an unfavorable electronic influence in the step of the 2*H*-azirine generation, the substitution of the phenyl moiety was varied (depicted as X in **Scheme 3.1A**). Still, the formation of the targeted 2*H*-azirine was observed for any of the substances. After all, although the mechanistic details of the Neber reaction remain ambiguous, it can be presumed that the stereochemistry of the oxime derivative causes the failure: For the rearrangement to the 2*H*-azirine, the hydroxyl group requires to be in *syn*-position in regard to the pyrene unit. However, according to ^{1}H NMR analysis, merely one isomer could be detected, which is apparently the *anti*-isomer incapable of ring formation.

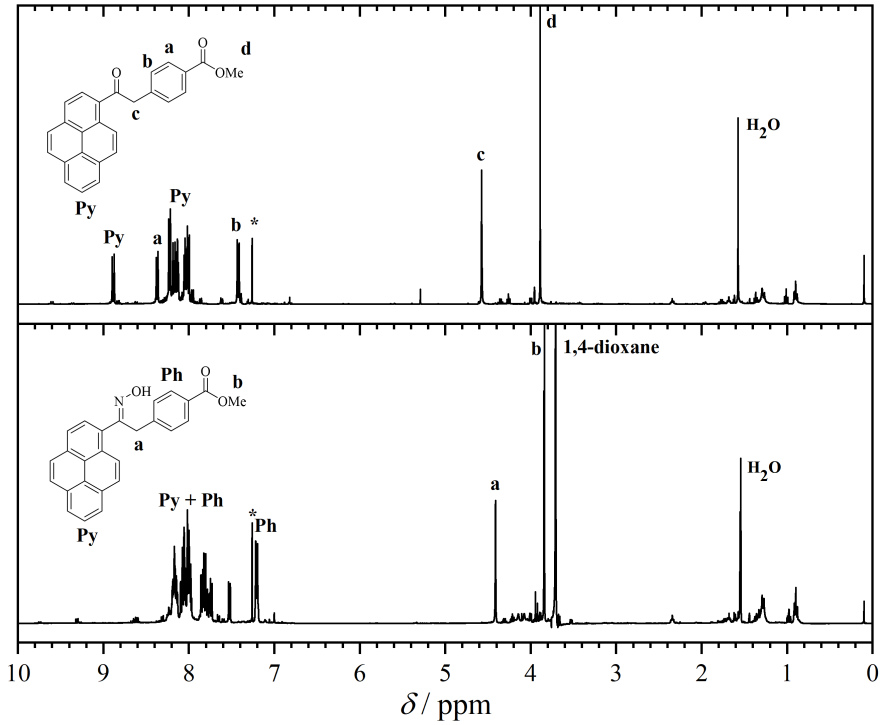

Scheme 3.3. ^{1}H NMR spectra (400 MHz, $CDCl_3$, 298 K) of methyl 4-(2-oxo-2-(pyren-1-yl)ethyl)benzoate (top spectrum) and of methyl 4-(2-(hydroxyimino)-2-(pyren-1-yl)ethyl)benzoate (bottom spectrum). Likely, the hydroxyl group of the oxime unit is in *anti*-position in regard to the pyrene unit and therefore prohibits the formation of the targeted 2*H*-azirine. The magnetic resonance marked with an asterisk is assigned to $CHCl_3$.

B: 2*H*-azirines *via* double elimination of iodoazides

Access to 2*H*-azirines is also accomplished through a four-step procedure. In summary, the Mizoroki-Heck coupling of 1-bromo pyrene and styrene moieties affords styrylpyrene derivatives in the first step. In the second step, the iodoazidation of the double bond of the stilbene derivative by the treatment with iodine monochloride and sodium azide is performed followed by subsequent base-induced elimination of hydrogen iodide with potassium *tert*-butoxide to yield initially a vinyl azide derivative, which upon exposure to heat releases N_2 and cyclizes to the targeted 2*H*-azirine (refer to **Scheme 3.1B**).[376]

To assess the suitability of the above mentioned procedure, 1-bromopyrene (1.2 eq.) and 4-acetoxy-styrene (1.0 eq.) were selected as components for the coupling reaction. 0.05 eq. of $Pd(OAc)_2$ were utilized as catalyst to yield the styrylpyrene derivative with a functional ester group. After stirring the mixture at 100 °C in triethanolamine overnight, water was added as a quencher followed by extraction with ethyl acetate. Nevertheless, after the purification *via* column chromatography, the desired product could not be obtained as was stated in the literature.[376] Instead, the ester moiety was cleaved during

the process, which in turn yielded a styrylpyrene moiety functionalized with a hydroxyl group as main product.

Regardless, the proposed synthetic path was assessed further with a slight modification: The alcohol derivative was protected after the Mizoroki-Heck coupling reaction. Since aryl alcohols require rather stable silyl protecting groups, triisopropyl-silyl trifluoromethanesulfonate (TIPS triflate) was identified as suitable reagent for the introduction of the TIPS protecting group.[489] By stirring 1.0 eq. of the stilbene derivative and 1.2 eq. of TIPS triflate in DCM at ambient temperature overnight in the presence of 2.0 eq. of imidazole as base and 0.1 eq. of DMAP as co-catalyst, the desired protected compound was isolated after aqueous work up and subsequent column chromatography (for ^{1}H NMR spectrum, refer to **Figure 3.4**, top spectrum).

Eventually, 1.0 eq. of the protected styrylpyrene derivative and 3.5 eq. of sodium azide were dissolved in a mixture of acetonitrile and DCM (1:1). At 0 °C, 1.2 eq. of iodomonochloride were added dropwise, and the reaction mixture was thawed to ambient temperature overnight. Afterwards, the reaction was quenched by the addition of water and extracted with DCM (3×). The combined organic phases were washed with aq. $Na_2S_2O_3$ solution and brine, subsequently dried over magnesium sulfate and concentrated under reduced pressure. However, the ^{1}H NMR spectrum of the raw product (refer to **Figure 3.4**, bottom spectrum) depicts a broad spectrum of products. Presumably, the mixture of products comprised the kinetically and thermodynamically most stable derivatives, which in turn lead to the synthesis of 2*H*-azirines in conjugation with the pyrene moiety and the phenyl unit, respectively. The latter one, however, is not photoreactive in the visible light range. Eventually, column chromatography was conducted to separate the products. Although various conditions were implemented, the separation of the kinetic and thermodynamic product was not feasible. It was concluded that the path presented in **Scheme 3.1B** is not suitable for the synthesis of a functional pyrene-substituted 2*H*-azirine. Alternatively, the product resulting from step 1 was successfully utilized for the reversible [2+2] cycloaddition for polymer ligation. Herein, visible light with wavelengths of 435 nm was most effective in the cycloaddition reaction whereas light of 330 nm supports the cycloreversion in an orthogonal fashion.[427]

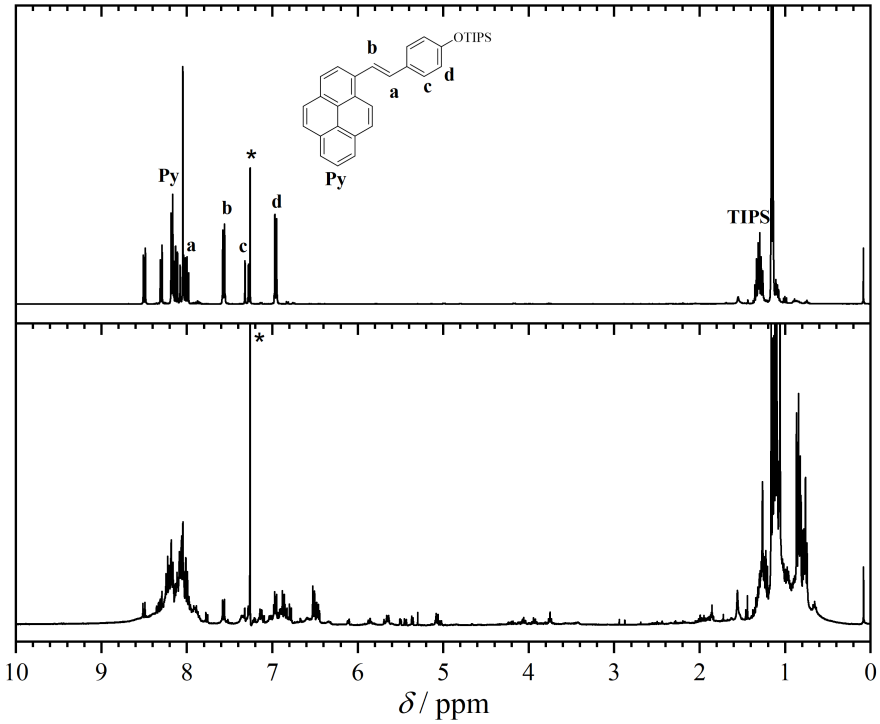

Scheme 3.4. ^{1}H NMR spectra (400 MHz, $CDCl_3$, 298 K) of the TIPS-protected styryl pyrene (top spectrum) and of the same substance after addition of iodomonochloride and sodium azide (bottom spectrum). The magnetic resonances of a broad range of different products are detectable in the bottom spectrum that prevent the purification of the targeted compound. The magnetic resonance marked with an asterisk is assigned to $CHCl_3$.

C: The employment of commercial available functional keto-pyrene derivatives

The range of commercially available pyrene compounds is quite limited. Monosubstituted derivatives of pyrene are available, yet in specific cases at considerable expense, whereas difunctional pyrene moieties are rarely accessible. It is noteworthy that the γ-oxo-1-pyrenebutyric acid is a product that is commercially acquired. This compound features two distinct chemical groups: A carboxylic acid and a keto group. While the keto group can be readily transformed into an 2*H*-azirine according to a known literature procedure,[422] the carboxylic acid serves as an anchor for tethering other functional molecules.

Therefore, the reaction sequence shown in **Scheme 3.1C** was suggested for the synthesis of a functional pyrene-substituted 2*H*-azirine. The first step of the approach involved the hydrazine formation by employing 3.0 eq. of *N,N*-dimethylhydrazine in the presence of trifluoroacetic acid as catalyst in toluene. The product was obtained after washing with water, and removing the solvent under reduced pressure. For

the second step, the isolated crude product was dissolved in iodomethane, and the reaction mixture was stirred overnight at 40 °C. After the precipitation in diethyl ether, the methylated product was received, and immediately employed for the next step. Dissolving in DMF and addition of 1.2 eq. of sodium hydride at 0 °C induces the rearrangement of the methylated hydrazone species to the targeted 2*H*-azirine, which in turn was isolated *via* column chromatography. Concomitantly, the reaction sequence was applied for three different pyrene derivatives: The commercially available γ-oxo-1-pyrenebutyric acid as well as the methyl ester and the triisopropylsilyl ester derivatives (depicted as X in **Figure 3.1C**). While the keto functionality of the carboxylic acid and methyl ester derivative was readily converted into the hydrazone moiety without any side reactions occurring, the triisopropylsilyl unit was cleaved. Thus, an additional step was required to reinstall the silyl group. The subsequent methylation was successfully carried out for all derivatives. Nevertheless, the ring closure of the reactive species in the presence of NaH, which supposed to yield the 2*H*-azirine, was not successful for any of the targeted functionalized derivatives. The latter result could be explained by the fact that the carbon skeleton between the original keto group and the functionality appears to be particularly short for efficient formation of the 2*H*-azirine derivatives.

D: Separate attachment of the 2*H*-azirine moiety and the functionalization unit to the pyrene core

The ketone as functional group, essential in the synthetic procedure for 2*H*-azirine described in part C, is facilely introduced *via* Friedel-Crafts acylation.[486] Therefore, it is possible to propose a synthetic route towards functional pyrene-substituted 2*H*-azirines by employing a pyrene derivative with a functional group able for coupling reactions. 1-Pyrenemethanol depicted in **Scheme 3.1D** possesses a hydroxyl moiety suitable for further esterification reactions. Subsequent, acylation with acetyl chloride introduces the functional group required for 2*H*-azirine synthesis. The succeeding hydrazone formation, methylation and ring closure steps give access to the desired photoactive group.

In order to avoid side reactions during Friedel-Crafts acylation and consequent base-induced ring formation stemming from the deprotonated alcohol, it is necessary to install an efficient and suitable protecting group for the alcohol. Similarly, the protecting group needs to be easily removed in a mild fashion without cleavage of the 2*H*-azirine. Ideally, TIPS fulfills the requirements for the efficient protection of the alcohol unit due to its stability against acids and bases in addition to its mild cleavage with tributylammonium fluoride (TBAF). Stirring 1.2 eq. of TIPS triflate, 1.0 eq. of 1-pyrenemethanol and

2.0 eq. of imidazole in the presence of 0.1 eq. of DMAP in DCM overnight, followed by aqueous work up and column chromatography led to a product, which was insoluble in all conventional organic solvent. As a result, further reactions could not be executed.

E: Iridium-catalyzed ring contraction of isoxazol-5(4*H*)-ones

Recently, a novel method was investigated, which generates 2*H*-azirines upon iridium-catalyzed ring contraction of isoxazol-5(4*H*)-ones. This approach was tested on a wide range of substrates with various functional groups including keto groups, internal alkynes and divers substituted alkenes.[490] Since the latter functionality presents an excellent handle for thiol-X reactions, the synthetic route in **Scheme 3.2E** was proposed. The synthesis of a β-keto ester derivative is presented in the first step followed by the introduction of the alkene functionality *via* nucleophilic substitution. Isoxazol-5(4*H*)-one formation and metal-catalyzed ring contraction are described in the third and fourth step, respectively.

The preparation of the β-keto ester was conducted according to the literature:[491] Under inert atmosphere, 2.1 eq. of sodium hydride were dispersed in dry THF followed by the addition of 2.0 eq. of diethyl carbonate. Upon reaching the temperature for refluxing, 1-acetylpyrene dissolved in DCM was added in a dropwise manner. The resulting reaction mixture was refluxed for additional 5 h, and subsequently poured into a mixture of ice-water:glacial acetic acid (6:1). The organic layer was separated, and the aqueous phase was extracted with DCM. Combination of the organic phases, drying over $MgSO_4$ and removal of the solvent led to a crude product, which was further purified *via* column chromatography (for ^{1}H NMR spectrum, refer to **Figure 3.5**, top spectrum).

In order to test the presented synthetic procedure for the synthesis of 2*H*-azirine derivatives without any functionality, the second step was initially skipped, and the product from the first step was directly employed for the isoxazol-5(4*H*)-one formation. Hereby, 1.0 eq. of hydroxylamine hydrochloride and 3.0 eq. of sodium acetate were utilized. After refluxing in a mixture of ethanol:water (5.3:1) for 22 h, the solvent was removed, and the crude product was dissolved in a mixture of DCM:water (1:1). The phases were separated and the aqueous phase was extracted with DCM. Drying of the combined organic phases and removal of the solvent afforded the desired product (for ^{1}H NMR spectrum, refer to **Figure 3.5**, bottom spectrum).

Thereafter, the ring contraction was performed by utilizing 1.5 mol% of $[IrCl(coe)_2]_2$ in cyclopentyl methyl ether. The reaction mixture was stirred at 100 °C for 22 h followed by removal of the solvent. Prior to further purification, the ^{1}H NMR analysis of the crude product did not reveal any characteristic magnetic resonances of the 2*H*-azirine derivative. Therefore, the reaction was not successful. In contrast, the literature solely describes synthetic procedures for 2*H*-azirines with isoxazol-5(4*H*)-one substituted in 4-position as starting material for the ring contraction.[490] To ensure that the missing substituent is not the reason for the failure of the last reaction, a propargyl group was installed by employing a nucleophilic reaction. For this purpose, 1.1 eq. of the pyrene β-keto ester dissolved in dry DCM were added dropwise to a suspension mixture of 1.1 eq. of sodium hydride and propargyl bromide in dry THF at 0 °C. After stirring at ambient temperature for 16 h, the product was isolated *via* aqueous work up and subsequently purified *via* column chromatography. The isoxazol-5(4*H*)-one formation step was executed according to the procedure described for the non-functionalized β-keto ester derivative. Nevertheless, the chemical transformation was not successful, and the reasons for the latter were unclear. Accordingly, it can be concluded that the iridium-catalyzed ring contraction of isoxazol-5(4*H*)-one does not present a suitable pathway for the synthesis of functional 2*H*-azirines.

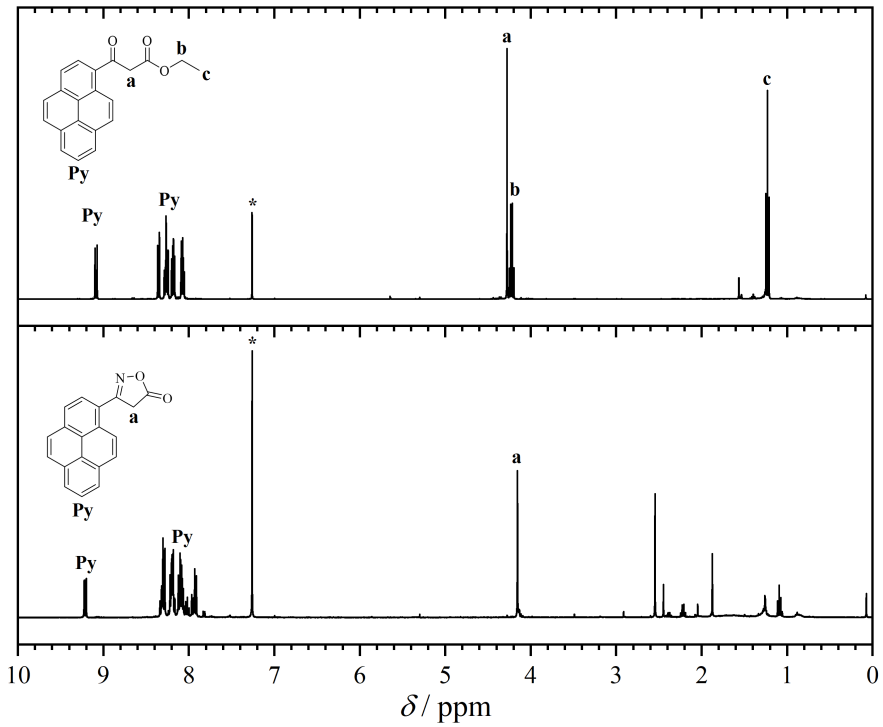

Scheme 3.5. ^{1}H NMR spectra (400 MHz, $CDCl_3$, 298 K) of ethyl 3-oxo-3-(pyren-1-yl)propanoate (top spectrum) and of 3-(pyren-1-yl)isoxazol-5(4*H*)-one (bottom spectrum). The iridium-catalyzed contraction of the isoxazol-5(4*H*)-one derivative yielding the 2*H*-azirine was not successful due to unknown reasons. The magnetic resonance marked with an asterisk is assigned to $CHCl_3$.

3.1.2 Employing Different Monomers in the Hydrazone Route for the Synthesis of Functional Azirines

The preceding paragraph clearly displays the challenges associated with the synthesis of a functional 2*H*-azirine. On the one hand, 2*H*-azirines are sensitive chemical groups that react under various conditions. On the other hand, pyrene incorporation into substrates ultimately results in tedious purification approaches leading to low yields and solubility issues. In order to address the issue concerning the difficult purification, it was concluded that the synthesis route proceeding *via* a hydrazone species depicted in **Scheme 3.1C** is worth to be investigated in-depth since purification *via* column chromatography is only required after the last step, while crude products can be directly employed in all other reaction steps. A variation of possible monomers, which are accessible from commercially available starting materials by one step procedures for the requested synthesis route, is displayed in **Scheme 3.6**.

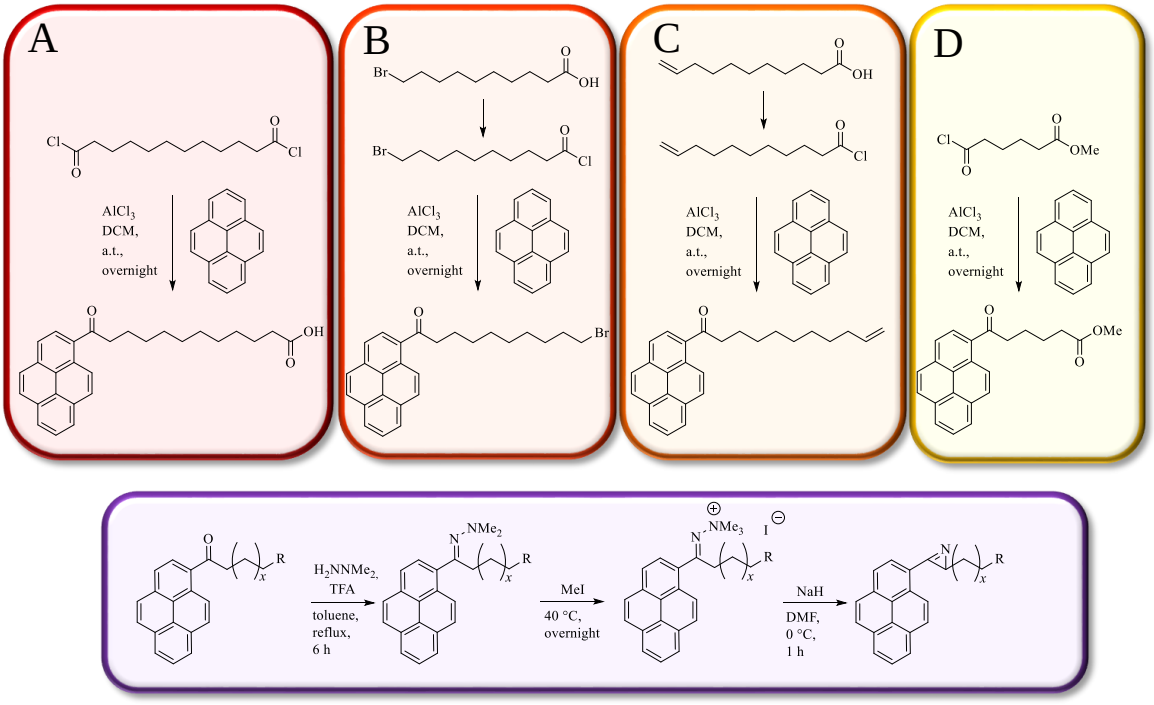

Scheme 3.6. In-depth investigation of the synthesis of functional pyrene-substituted 2*H*-azirines proceeding *via* hydrazones as intermediates. In part **A** to **D** different keto-pyrene species equipped with distinct functional groups are displayed, which are accessible *via* one step procedures of commercially available compounds.

The synthesis of all different keto pyrene derivatives proceeds analogously according to literature.[492] 1.0 eq. of the acyl chloride species and 1.2 eq. of pyrene were dissolved in dry DCM followed by the addition of 1.2 eq. of $AlCl_3$ at -10 °C. The addition of $AlCl_3$ was performed in a portion-wise manner over

20 minutes. After stirring overnight at ambient temperature, the reaction was quenched by the addition of ice. The resulting reaction mixture was saturated with NaCl followed by separation of the phases. The organic layer was washed with brine, and dried over $MgSO_4$. Removal of the solvent led to the crude product, which was further purified *via* column chromatography using mixtures of hexane and ethyl acetate or pure chloroform. The eluent was chosen depending on the functional group of the acyl chloride derivative.

A keto pyrene species bearing a carboxyl acid at the ω-end is accessible by the utilization of dodecanedioyl dichloride as the acyl chloride component in the Friedel-Crafts acylation of pyrene (refer to **Scheme 3.6A**). The hydrazone formation and the methylation reaction were performed according to the procedure described in the preceding section. Due to the presence of a carboxylic acid, the amount of sodium hydride as base in the 2*H*-azirine forming step was doubled from 1.2 to 2.4 eq. However, no ring formation could be observed *via* ^{1}H NMR analysis. The interference of the deprotonated carboxylic acid as nucleophile after the ring closure might result in opening of the three-membered ring of the 2*H*-azirine derivative.

The transformation of the commercially available 10-bromo-decanoic acid into its carboxylic chloride derivative, and its utilization in the Friedel-Crafts acylation resulted in a keto pyrene species possessing a functional ω-bromo group (refer to **Scheme 3.6B**). Nonetheless, TFA as the acidic catalyst during the hydrazone formation step inevitably induced alkylation of the aromatic system leading to insoluble polymeric material.

If 10-undecenoic acid is transformed into a carboxylic chloride, the acylation of pyrene (refer to **Scheme 3.6C**) results in polymeric material as well due to the fact that the ω-double bonds are also able to alkylate aromatic systems under the optimized Friedel-Crafts acylation conditions.

Friedel-Crafts acylation of pyrene with methyl adipoyl chloride results in a keto pyrene derivative with a methyl ester (namely, methyl 4-(3-(pyren-1-yl)-2*H*-azirin-2-yl)butanoate, for ^{1}H and ^{13}C NMR spectra refer to **Figures B.1** and **B.2**). In contrast to the previously described pyrene-substituted keto compounds, the transformation of the keto group into a 2*H*-azirine moiety *via* the three step synthesis depicted in the bottom part of **Scheme 3.6** was successful with an overall yield of 50 %. The ^{1}H NMR spectrum in **Figure 3.1** features a magnetic resonance arising from the proton of the CH group of the three-membered ring at 2.45 ppm overlapping with the magnetic resonance of the methylene protons adjacent to the ester

unit. Concomitantly, the proton of the aromatic system in the closest proximity to the photoreactive group is displayed as doublet at 9.19 ppm, while the methoxy group of the ω-ester is detected at 3.67 ppm.

To ensure that the structural changes of the pyrene-substituted 2*H*-azirine do not affect its reactivity in the targeted light-triggered reaction, a model reaction using the freshly synthesized 2*H*-azirine derivative and 5.0 eq. of *N*-ethyl maleimide as dienophile was carried out. The irradiation of the both compounds dissolved in DCM for 1 hour with an LED setup (410-420 nm, refer to **Figure A.2** for the emission spectrum), and subsequent removal of the solvent under reduced pressure results in a product mixture, which was analyzed *via* NMR spectroscopy. The ^{1}H NMR spectrum in **Figure 3.2** represents a comparison between the 2*H*-azirine derivative and the results after the irradiation process. Characteristic magnetic resonances for the protons of the five-membered heterocycle, which is formed during the light-induced cycloaddition, are detectable at 4.99, 4.85 and 3.81 ppm. Similarly, the cycloadduct possesses a stereocenter, which gives arise to a doublet of the methoxy group at 3.70 ppm (instead of a singlet for achiral substances). For the same reason, the doublet of the aromatic proton closest to the photoreactive unit at 9.12 ppm appears as a triplet. In addition, the magnetic resonances of the structural unit of the dienophile appears at 3.48 and 1.10 ppm. Consequently, the reactivity of the functionalized pyrene-substituted 2*H*-azirine proceeds analogously to the non-functional counterpart.

After having successfully established a route for the synthesis of a ω-methyl ester functionalized α-pyrene 2*H*-azirine in combination with the positive results from the test photoreaction, the subsequent step involved the transformation of the methyl ester. Generally, ester groups are mostly cleaved or transesterified for the following synthesis steps. As a result, the methods described in the subsequent section were applied for the functionalization of the newly synthesized 2*H*-azirine derivative.

The cleavage of the ester functionality of the methyl ester functionalized pyrene-substituted 2*H*-azirine was performed under refluxing in a mixture of water:THF (1:1) by employing either 2.0 eq. of sodium carbonate or sodium hydroxide as base to induce alkaline hydrolysis. While no transformation was detected analytically with sodium carbonate, sodium hydroxide induced the destruction of the 2*H*-azirine moiety.

Consequently, diverse mild transesterification protocols as alternative methods were utilized to functionalize the ω-end of the α-pyrene-substituted 2*H*-azirine. For instance, in order to enhance the effectiveness of the transesterification reaction, molecular sieves (4 $\AA$) were employed, which facilitates the removal

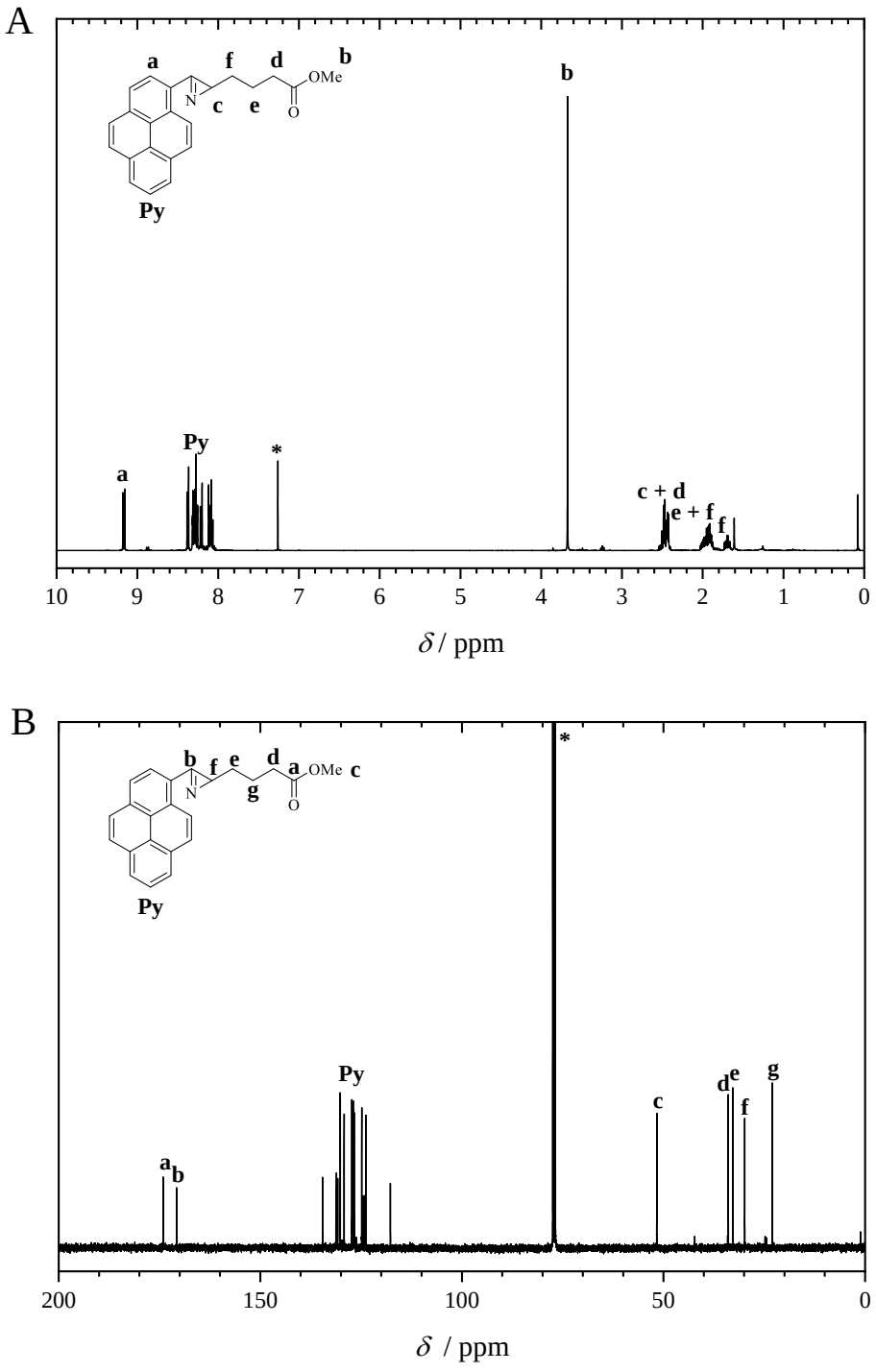

Figure 3.1. A: ^{1}H NMR spectrum (400 MHz, $CDCl_3$, 298 K) and **B**: ^{13}C NMR spectrum (100 MHz, $CDCl_3$, 298 K) of the methyl ester functionalized pyrene-substituted 2*H*-azirine, respectively. The magnetic resonance marked with an asterisk is assigned to $CHCl_3$.

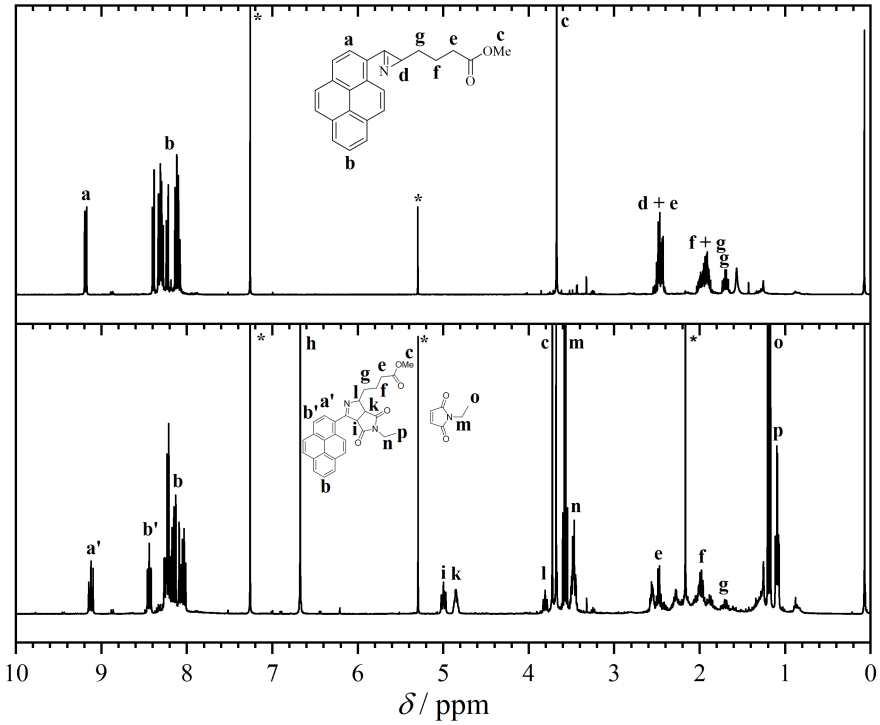

Figure 3.2. ^{1}H NMR spectra (400 MHz, $CDCl_3$, 298 K) of the methyl ester functionalized pyrene-substituted 2*H*-azirine before (top spectrum) and after the light-induced cycloaddition with *N*-ethyl maleimide (bottom spectrum). The magnetic resonance marked with an asterisk is assigned to $CHCl_3$.

of MeOH generated during the process. In addition, 3.0 eq. of DoPAT-OH (synthesized *via* a previously described method[493]) as alcohol component ensured high conversion of the transformation. First tests were conducted with catalytic amounts of TFA and sulfuric acid in THF at 40 °C. The analysis of the crude reaction mixtures after stirring for 24 h *via* ^{1}H NMR spectroscopy revealed the degradation of the 2*H*-azirine moiety in case of sulfuric acid, whereas novel magnetic resonances in the ^{1}H NMR spectrum arose when TFA was used as catalyst. A conversion of approximately 30 % was determined by ^{1}H NMR spectroscopy. As a result, the latter experiment was repeated with different reaction time (*i.e.*, three days). Yet, the analysis *via* ^{1}H NMR spectroscopy indicated that the photoreactive moiety of the 2*H*-azirine was destroyed. Increasing the reaction temperature to 50 °C, in contrast, did not yield better results. Hence, amberlyst 15 - a mild acidic solid catalyst - was tested for the transesterification reaction. In a similar way to previous attempts, no product formation was detected in this case. Therefore, the strategy was modified and non-nucleophilic base derivatives were used. For example, 1,8-diazabicyclo[5.4.0]undec-7-ene (DBU) as a strong non-nucleophilic base was utilized in catalytic amounts for the transesterification reaction. In this case, no conversion of the methyl ester was detected in the ^{1}H NMR spectrum as well.

It can be concluded that conventional methods adopted for the functionalization of the ω-methyl ester end of the 2*H*-azirine derivative were not successful. The latter mainly results from the susceptibility of the 2*H*-azirine group towards acids, nucleophiles and bases.

3.2 Access to Fluorescent Labeled Three Armed Mikto Star Polymers *via* Interrupted CuAAC Ligation

Organic reactions play an important role in polymer chemistry, specifically for the functionalization of polymer chains or the construction of complex macromolecular architectures. Due to the difficult purification of polymer samples, these reactions require to fulfill important parameters such as high yields, selectivity and any side products. Ideally, polymer modification reactions fall in line with the philosophy of *click* chemistry, in which the copper(I)-catalyzed azide-alkyne cycloaddition (CuAAC) is the most prominent representative example.[16] Similarly, multicomponent reactions (MCRs) play an increasingly important role in polymer science. The high atom efficiency of MCRs and the possibility to introduce a high number of diverse functional groups in a single synthetic step are the causes for the constant increase in literature articles since 2011 covering these highly efficient reactions.[150, 494, 495]

Accordingly, a variation of the CuAAC reaction is introduced into polymer science and discussed in-depth within the section. In the light of multicomponent reactions, this transition metal-catalyzed approach, namely the interrupted CuAAC reaction, involves the rapid transformation of azide and alkyne derivatives into 1,2,3-triazoles in the presence of 2*H*-azirines (refer to **Figure B.3** for the mechanism). Intriguingly, this reaction offers a facile route for the incorporation of an enamine group on the C5 position of the 1,2,3-triazole *via* vinyl nitrene transfer; the latter vinyl group being addressable as reactive handle for further modifications (*e.g.*, thiol-ene addition). In fact, by employing the approach of CuAAC interrupted by 2*H*-azirines, a facile two step synthesis of mikto-arm star polymers is established. Furthermore, this method allows the simultaneous tethering of a fluorescent label to the midpoint of block copolymers or to the core of mikto-arm star polymers in case a pyrene-substituted 2*H*-azirine is employed. As a result, the herein presented polymeric species are in-depth investigated *via* their optical properties as well as NMR spectroscopy, SEC, ATR-IR and DSC. Last but not least, DLS studies indicated the formation of micelles in water, which further possess robust characteristics in the aqueous medium in analogy to unimolecular micelles.

Parts of the current chapter are reproduced from J. T. Offenloch, H. Mutlu, C. Barner-Kowollik, *Macromolecules* **2018**, *51*, 2682-2689 with permission from the American Chemical Society.

3.2.1 Block Copolymer Formation *via* Interrupted CuAAC Ligation

Similar to conventional CuAAC ligation, the Cu(I)-catalyzed azide-alkyne cycloaddition interrupted by 2*H*-azirines enables the reaction of terminal alkynes and azides. As a result, polymer strands with those functional groups at their respective chain termini are required for block copolymer formation. Since the coupling efficiency of functional end groups decreases with increasing chain length, polymer blocks with low molar masses were targeted, *i.e.*, the ARGET ATRP polymerization of methyl methacrylate afforded a hydrophobic and monodisperse PMMA derivative (**PMMA-alkyne**) bearing an alkyne end group with a $M_{n,SEC}$ of 4000 g mol^{-1} and $Đ$ of 1.1 (refer to **Scheme 3.7** as well as **Figure 3.3B** for ^{1}H NMR spectrum and **Figure 3.3C** for SEC trace). For the polymerization, $CuBr_2$ and an excess of 1,1,4,7,10,10-hexamethyltriethylenetetramine (HMTETA), which serves simultaneously as ligand and reducing agent, were employed.[84] Furthermore, an alkyne-functional initiator installed the desired functionality as end group. As counterpart, a readily available poly(ethylene glycol)methyl ether azide (**PEG-N_3**) with a $M_{n,SEC}$ of 2800 g mol^{-1} and $Đ$ of 1.03 was selected (for the ^{1}H NMR spectrum and SEC trace, refer to **Figure 3.3B** and **Figure 3.3C**, respectively).

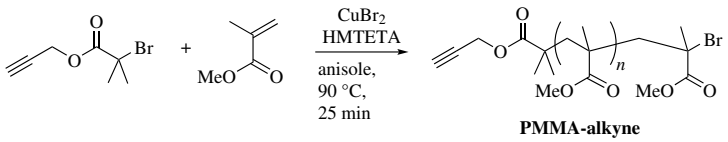

Scheme 3.7. ARGET ATRP of MMA which yields **PMMA-alkyne**. HMTETA was employed as ligand to solubilize $CuBr_2$ as well as the reducing agent to deliver the Cu(I) species for the polymerization.

Thereupon, the interrupted CuAAC ligation was carried out with the functional polymer blocks under conditions adopted from the literature.[178] 0.1 eq. of copper(I) iodide and 1.4 eq. of *N,N*-diisopropylamine (DIPEA) were employed as catalytic system in dichloromethane, while 1.2 eq. of a pyrene-substituted 2*H*-azirine served as fluorescence marker for the block copolymer formation as well as the source for the vinyl functionality at the junction point. The reactants were mixed at 0 °C, and the reaction mixture was thawed to ambient temperature after 1 h. After an additional reaction time of 23 h, an azide-functional resin was added to the mixture in order to remove the small excess of **PMMA-alkyne** which was employed to ensure high yields and high purity of the block copolymer (molar ratio: alkyne:azide = 1.1:1). After further 24 h at ambient temperature, the resulting block copolymer **PMMA-*b*-PEG** was isolated *via* precipitation in ice-cold hexane. The ^{1}H NMR spectrum of the block copolymer species depicted in

Figure 3.3B indicates no residual magnetic resonances for the alkyne group as they are detected at 4.64 and 2.46 ppm in the ^{1}H NMR spectrum of **PMMA-alkyne** in the same figure. A magnetic resonance for the protons of the methylene group adjacent to the azide terminus at 3.43 ppm is not visible as well for **PMMA-*b*-PEG**. However, novel magnetic resonances in the area between 5.35 to 4.99 ppm and at 4.52 ppm can be assigned to the successful triazole formation. Importantly, the magnetic resonances of the enamine are detectable at 4.57 and 4.05 ppm. Further features of the ^{1}H NMR spectrum of **PMMA-*b*-PEG** are the magnetic resonances located in the range of 9.00 and 8.00 ppm, which are stemming from the aromatic protons of the pyrene unit. Besides, the magnetic resonances of the PMMA backbone are visible between 3.62 and 3.57 ppm adjacent to the magnetic resonances of the PEG backbone in the area of 3.66 to 3.62 ppm. The evaluation of the SEC trace of the block copolymer obtained by RI detection in **Figure 3.3C** reveals a monomodal distribution at lower retention time compared to the pristine polymer blocks (shift of approximately 1 and 2 minutes compared to the retention time of the SEC trace of **PMMA-alkyne** and **PEG-N_3**, respectively). The subsequent assessment of the molar mass based on a PMMA calibration suggests a value of 1.1 for $Đ$ and a $M_{n,SEC}$ of 6500 g mol^{-1}, the latter corresponding to an increase in the molar mass of 2500 g mol^{-1} compared to **PMMA-alkyne**. On the account that the UV/Vis spectrum of pyrene is characterized by strong absorption bands at 334, 320 and 307 nm, SEC measurements coupled with UV detection enable the recording of pyrene-functionalized species such as **PMMA-*b*-PEG**. Correspondingly, the SEC traces resulting from the UV detection (at 320 nm, shown in **Figure 3.3D**), indicate a polymer distribution for the block copolymer stemming from the attached chromophore. In contrast, no signals for the parent polymer species can be detected due to the absence of pyrene.

3.2.2 Modification of the Block Copolymer *via* Radical Thiol-Ene Addition

It was assumed that the vinyl function of the enamine group at the junction point of the two polymer blocks in **PMMA-*b*-PEG** can further undergo thiol-ene addition, hence serving as handle for the further modification of the block copolymer in order to synthesize mikto-arm star polymers. In this way it was possible to report the synthesis of mikto-arm star polymers with pyrene as fluorescent marker attached to their core. With the aim of screening and optimizing the conditions for the modification reaction, 1-dodecanethiol (**Dode-SH**) was selected as a model thiol counterpart. Since the nature of olefin group

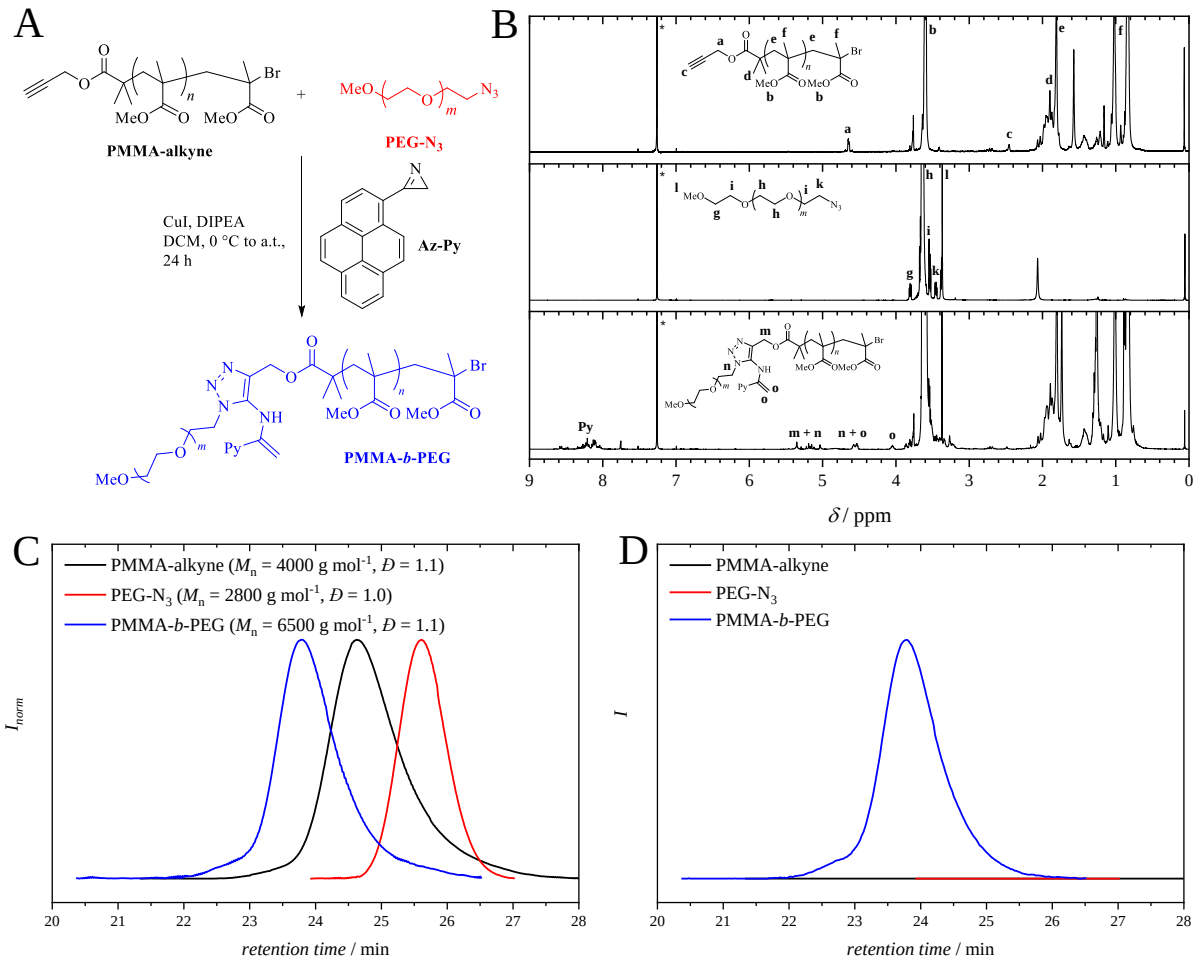

Figure 3.3. **A**: Reaction scheme of the block copolymer formation *via* interrupted CuAAC ligation. **B**: ^{1}H NMR spectra (400 MHz, $CDCl_3$, 298 K) of **PMMA-alkyne** (top spectrum) and **PEG-N$_3$** (middle spectrum) as parent polymers, and the block copolymer **PMMA-*b*-PEG** (bottom spectrum). The magnetic resonance marked with an asterisk is assigned to $CHCl_3$. **C**: SEC (THF, 30 °C, RI) and **D**: SEC (THF, 30 °C, UV) traces of the same polymer species. Adapted with permission from reference [204]. Copyright (2018) American Chemical Society.

of the enamine is rather electron-rich and conventional Michael thiol-ene reaction requires alkenes of electron-deficient character (refer to **Section 2.1.3.3**), the thiol-ene reaction based on a radical pathway was employed for the ligation of the thiol to the block copolymer species. Therefore, the block copolymer and the thiol were dissolved in 1,4-dioxane in the presence of 1.5 eq. of azobis(isobutyronitrile) (AIBN) as radical source. After 29 h at 60 °C, the modified polymer species was isolated *via* precipitation in ice-cold hexane and further characterized. A comparison of the ^{1}H NMR spectra before and after the modification with **Dode-SH** depicted in **Figure 3.4B** illustrates that the magnetic resonances associated with the enamine group at 4.57 and 4.05 ppm have disappeared. However, the magnetic resonances associated to the newly formed thio-ether are not visible due to the plausible overlap of these specific magnetic resonances with the magnetic resonances stemming from the methoxy backbone of the PMMA block as well as with the magnetic resonances of the repeating unit of the PEG chain. In contrast, the SEC traces of the modified block copolymer species (refer to **Figure 3.5B1** and **3.5B2**) clearly evidence the successful thiol-ene ligation: The traces obtained by RI and UV detection both indicate a clear shift to lower retention times as well as an increase in molar mass while retaining a narrow molar mass distribution. The in-depth evaluation of the RI data based on a PMMA calibration results in an increase of molar mass of 1200 g mol^{-1}. Compared to the molecular weight of **Dode-SH**, which is approximately 200 g mol^{-1}, this shift appears to be excessively high. However, it is assumed that the increase in hydrophobicity in the center of the modified block copolymer species induces the stretching of the polar polymer blocks, especially of the highly hydrophilic PEG segment, resulting in a higher hydrodynamic volume.

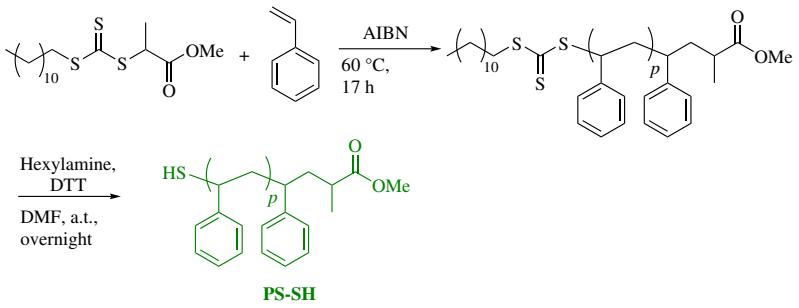

Scheme 3.8. RAFT polymerization of styrene followed by aminolysis in the presence of hexylamine afforded **PS-SH** as macromolecular thiol for the synthesis of mikto-arm star polymers. In the aminolysis step, dithiothreitol (DTT) was added to prevent the oxidation to disulfide derivatives.

After the successful modification of **PMMA-*b*-PEG** with a model thiol derivative, thiol-terminated polymer blocks were employed in the modification step, hence aiming for the synthesis of mikto-arm star

polymers. Therefore, styrene was polymerized *via* RAFT polymerization and a subsequent aminolysis reaction with hexylamine afforded **PS-SH** with $M_{n,SEC}$ of 2600 g mol^{-1} and $Đ$ of 1.1 (refer to **Scheme 3.8** as well as **Figure 3.4C** for the ^{1}H NMR spectrum and **Figure 3.5C1** and **3.5C2** for SEC results). In analogy to the modification of the block copolymer species with **Dode-SH**, **PS-SH** was utilized for the synthesis of a mikto-arm star polymer of the ABC type under the optimized reaction conditions. The SEC trace obtained by RI detection in **Figure 3.5C1** indicates that the distribution of **PS-SH** disappeared after the radical thiol-ene reaction. Supplementary SEC data of the raw polymer mixture before and after the ligation process (refer to **Figure B.4A**) supports the consumption of the thiol termini upon attachment of the PS block to the midpoint-reactive block copolymer species. The evaluation of the SEC data delivers a $M_{n,SEC}$ of 6600 g mol^{-1} and a $Đ$ of 1.2 for the polymer after thiol-ene reaction. The complementary SEC trace obtained by UV detection in **Figure 3.5C2** reveals a shift to lower retention time. This small increase in the molar mass is in excellent agreement with previous studies on mikto-arm star polymers: The additional segment of mikto-arm star polymers has an insignificant effect on the hydrodynamic radius compared to the block copolymers.[249, 496–499] Thus, SEC measurements merely provide insights into the size of star polymers instead of the actual molar masses. Furthermore, styrene units are able to show affinity to form sandwich-like excimers *via* the interaction of excited and non-excited moieties along the polymer chain leading to coiling of the polymer chain in solution.[500–504] Further evidence of the successful synthesis of a mikto-arm star polymer species is provided by ^{1}H NMR data. **Figure 3.4C** indicates the disappearance of the magnetic resonances associated with the enamine protons while the novel magnetic resonances arising from the thioether bond are overlapping with the magnetic resonances of the polymeric backbone, analog to the ^{1}H NMR spectrum of **PMMA-*b*-PEG-Dode**. Therefore, COSY spectra of the block copolymer and the star polymer were recorded, and the results are displayed in **Figure 3.6**. While cross signals stemming from the protons of the enamine are visible in the 2D NMR spectrum for **PMMA-*b*-PEG** (a zoom-in of this area is presented in the upper inset), they are no longer present in the 2D NMR spectrum of **μ-PMMA-PEG-PS** (a zoom-in is presented in the dashed boxed area). Consequently, the NMR results further underline the successful synthesis of the mikto-arm star polymer derivative.

An alternative mikto-arm AB_2 star polymer was synthesized by employing a commercially available thiol-terminated PEG (**PEG-SH**). Since the SEC trace of the pristine PEG species indicated a bimodal

distribution, which may result from the oxidation of the thiols to disulfides, the respective cleavage of the disulfides with DTT as reducing agent in the presence of triethylamine as base was performed. However, a monomodal distribution could not be obtained and complete removal of any residual DTT was not possible (for the ^{1}H NMR spectrum and SEC trace, refer to **Figure 3.4D** and **3.5D1**, respectively). Nevertheless, **PEG-SH** ($M_{n,SEC}$ = 2600 g mol^{-1}, $Đ$ = 1.1) was used for the synthesis of a mikto-arm star polymer adopting the optimized reaction conditions. The ^{1}H NMR spectrum of the resulting polymer species in **Figure 3.4D** displays the same characteristics as **PMMA-*b*-PEG-Dode** and **μ-PMMA-PEG-PS**. Moreover, the SEC trace obtained by RI detection (refer to **Figure 3.5D1**) indicates a shift to higher retention time for the star polymer compared to its linear analogue ($M_{n,SEC}$ = 6300 g mol^{-1}, $Đ$ = 1.2). This decrease in molar mass is consistent with the star-shaped architectures which possess a smaller hydrodynamic radius due to their geometry in comparison to the pristine block copolymer.[505] A comparison of the SEC traces of the polymer mixture before and after radical thiol-ene reaction is shown in **Figure B.4B** underpinning the successful ligation by the complete consumption of the **PEG-SH** derivative after the reaction. Nonetheless, a tailing in the SEC trace of **μ-PMMA-PEG-PEG** was detected, which can be caused by two factors: The anchoring of the PEG arms in the pores of the SEC columns or inappropriate analysis conditions *via* SEC. Indeed, the latter point is frequently reported in the literature for various polymer systems measured on a range of different SEC systems.[249, 497, 499, 505–509]

3.2.3 In-Depth Characterization of the Polymer Species

3.2.3.1 ATR-IR

The ATR-IR measurements of selected polymer derivatives are presented in **Figure 3.7**. Hereby, the spectra of the relevant components for the block copolymer formation are shown in part **A**. The spectrum of **PMMA-*b*-PEG** features all relevant peaks stemming from the pristine polymer blocks, *i.e.*, the C=O and C-O stretching vibrations of the backbone in **PMMA-alkyne** are detectable at 1724 cm^{-1} and 1148 cm^{-1}, respectively. Moreover, the spectrum of the block copolymer exhibits the C-O-C stretch of the PEG backbone at 1100 cm^{-1}. Concurrently, the peaks of the reactive groups of the parent polymers including the weak band of the characteristic C-H stretching vibration of the terminal alkyne at 3250 cm^{-1} (refer to the zoom-in of the spectrum of **PMMA-alkyne**) as well as the absorption for azides at 2100 cm^{-1} are no longer detectable for the block copolymer. Meanwhile, weak absorptions at 3042 cm^{-1} and 1585 cm^{-1}

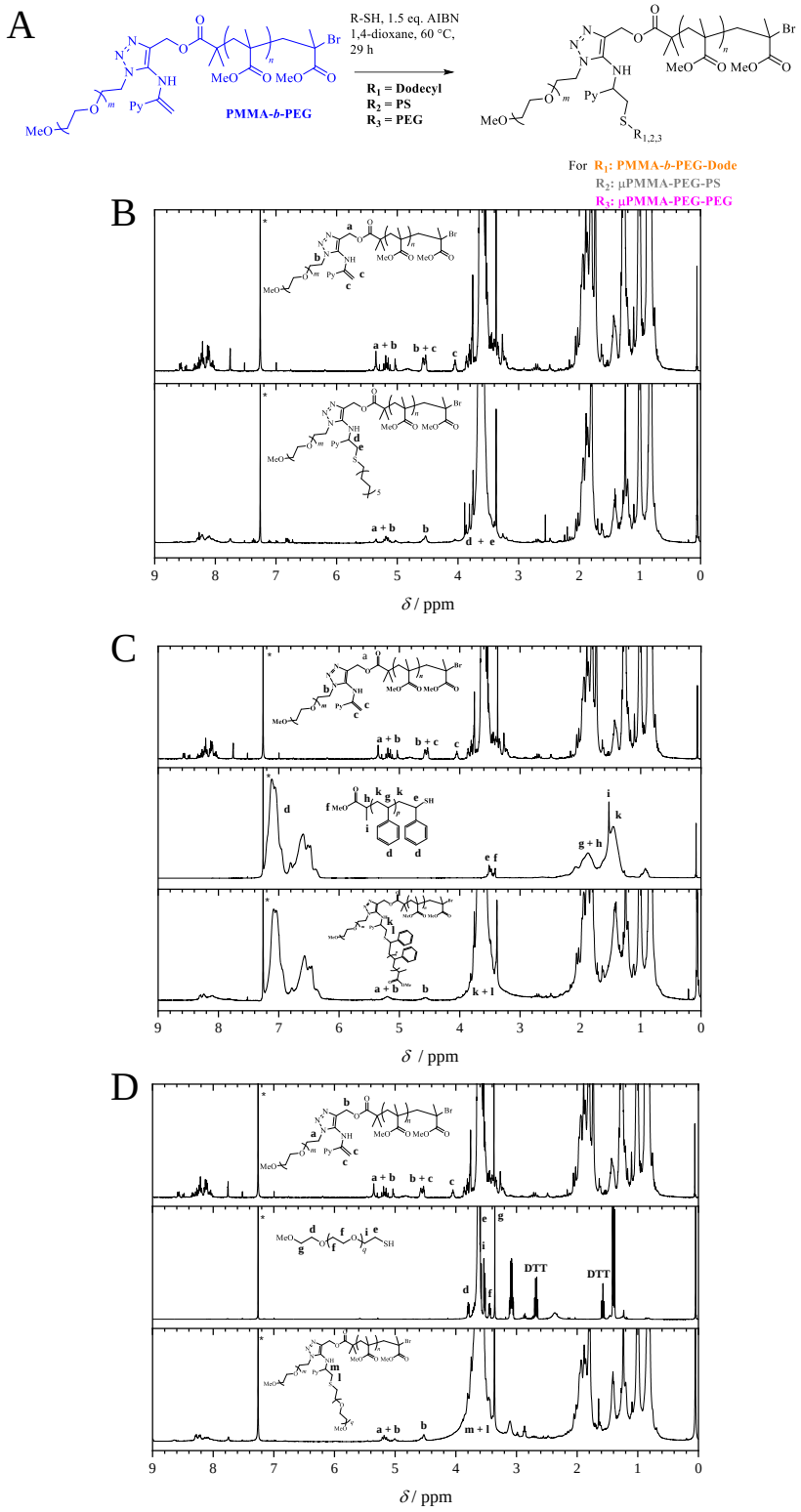

Figure 3.4. Modification of **PMMA-*b*-PEG** *via* the radical thiol-ene addition of various thiol derivatives (first part). **A**: Reaction scheme of the modification of **PMMA-*b*-PEG** *via* the radical thiol-ene addition of various thiol derivatives. **B**, **C** and **D**: ^{1}H NMR spectra (400 MHz, $CDCl_3$, 298 K) of **PMMA-*b*-PEG** (top spectrum) and the modified block copolymer species (bottom spectrum). In case of the synthesis of the mikto-arm star polymers, the ^{1}H NMR spectra of the thiol-terminated polymers are presented in the middle. The magnetic resonance marked with an asterisk is assigned to $CHCl_3$. Adapted with permission from reference [204]. Copyright (2018) American Chemical Society.

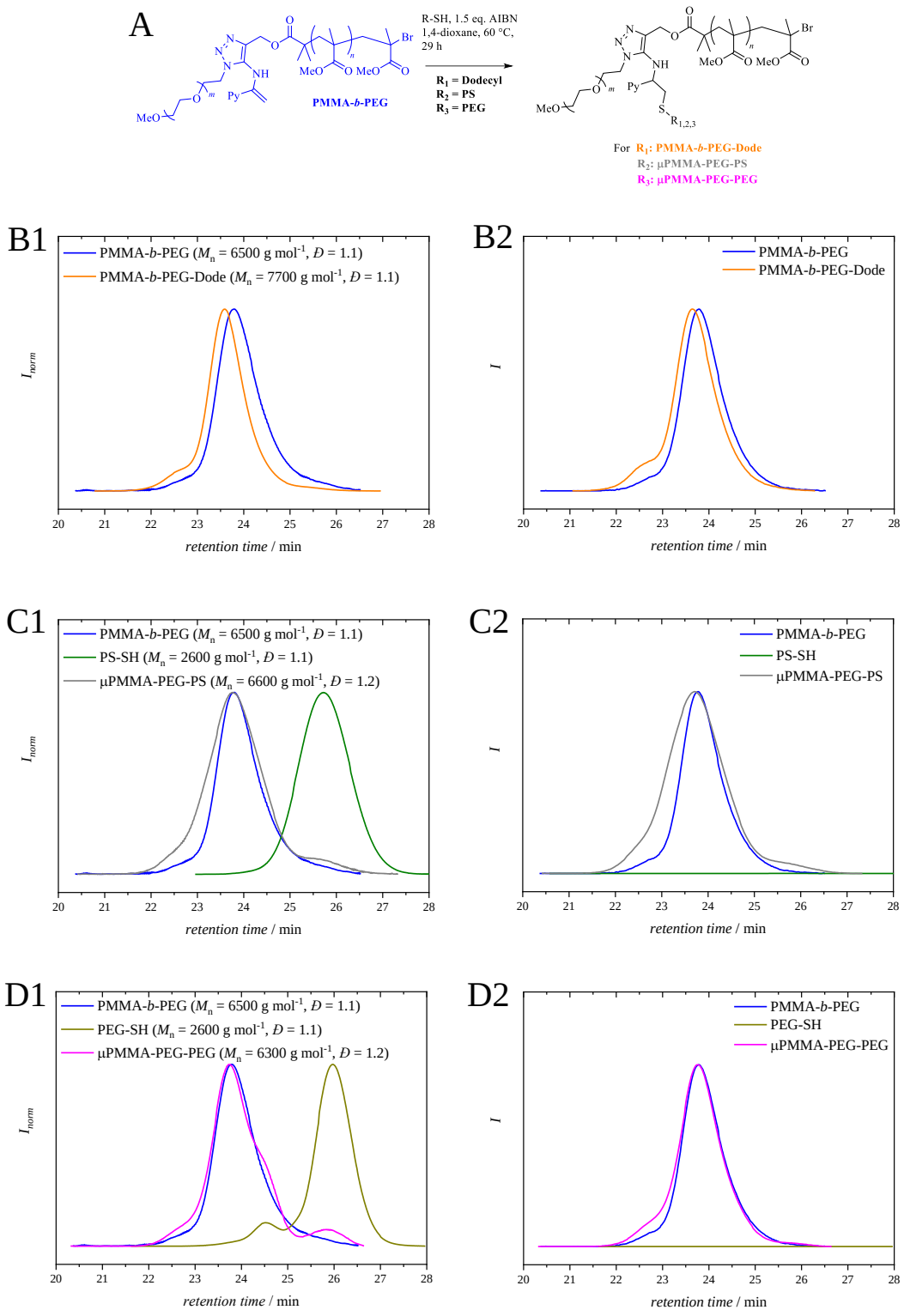

Figure 3.5. Modification of **PMMA-*b*-PEG** *via* the radical thiol-ene addition of various thiol derivatives (second part). **A**: Reaction scheme of the modification of **PMMA-*b*-PEG** *via* the radical thiol-ene addition of various thiol derivatives (part 2). **B1**, **C1** and **D1**: SEC (THF, 30 °C, RI), and **B2**, **C2** and **D2**: SEC (THF, 30 °C, UV) traces of **PMMA-*b*-PEG** and the modified block copolymer species. Adapted with permission from reference [204]. Copyright (2018) American Chemical Society.

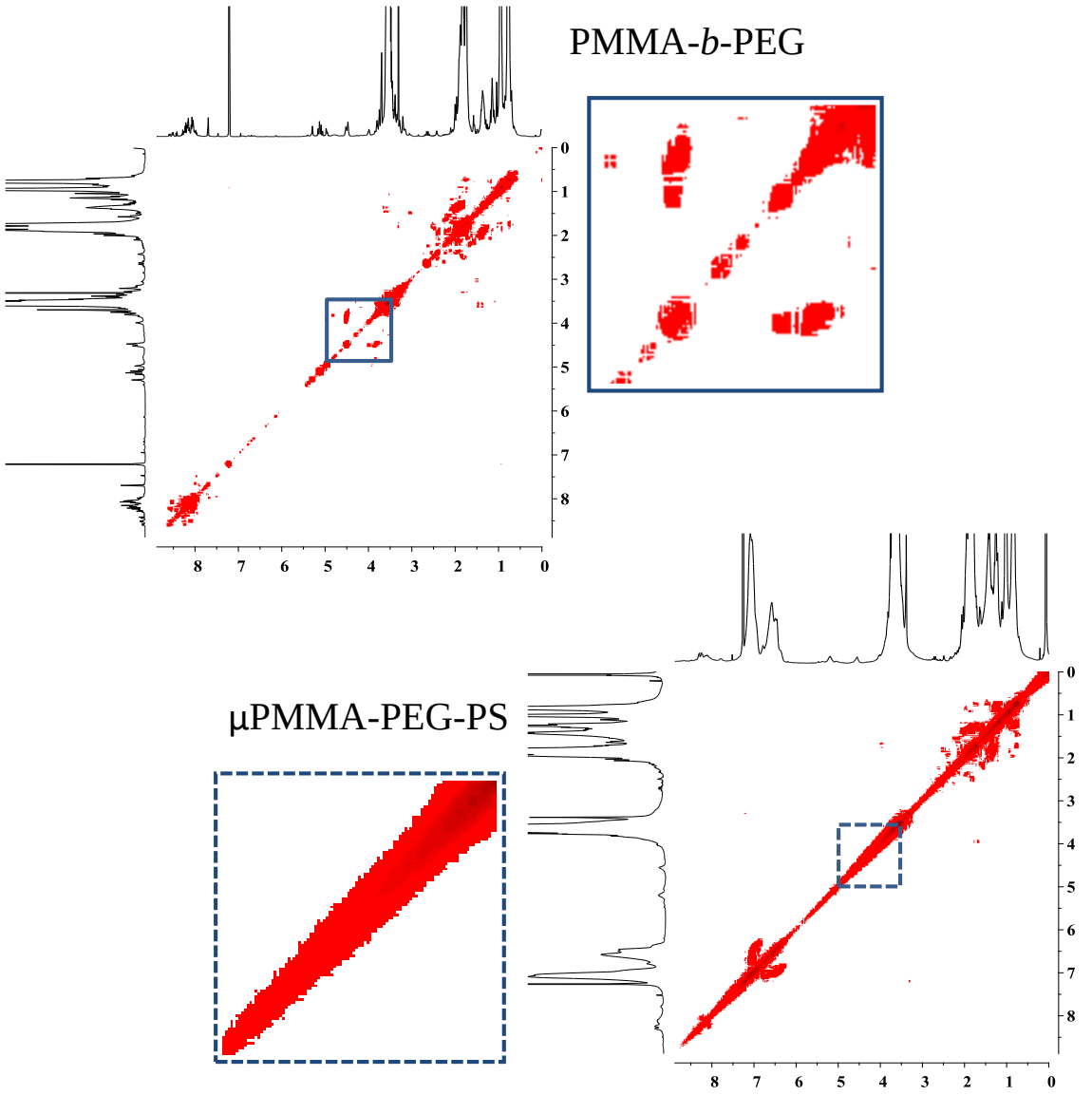

Figure 3.6. 2D NMR (COSY, 400 MHz, $CDCl_3$, 298 K) spectra of **PMMA-*b*-PEG** (top spectrum) and **μ-PMMA-PEG-PS** (bottom spectrum) indicating the successful modification of the block copolymer species *via* radical thiol-ene addition. Zoom-in of the relevant areas of the cross peaks stemming from the enamine protons are highlighted in a box for **PMMA-*b*-PEG** and a dashed box for **μ-PMMA-PEG-PS**. Adapted with permission from reference [204]. Copyright (2018) American Chemical Society.

which are stemming from the pyrene unit appear, whereas another weak peak at 1640 cm^{-1} can be assigned to the C=C stretching vibration of the newly formed enamine group.

The cumulative results of the ATR-IR measurements after the modification of the block copolymer are presented in **Figure 3.7B**. The spectrum of **μ-PMMA-PEG-PS** displays novel peaks for the characteristic aromatic C-H stretches of the introduced polystyrene block at 2922 cm^{-1} and 697 cm^{-1}, while the relevant absorbances of the backbone of PMMA and PEG are still present at 1724 cm^{-1} and 1100 cm^{-1}, respectively. In contrast, the weak peak for the enamine at 1640 cm^{-1} disappeared upon formation of a novel C-S bond. The weak peak of the thioether bond is visible at 628 cm^{-1}. The spectrum of **PMMA-*b*-PEG-Dode** also reveals the appearance of the peaks of the PMMA and PEG backbone while no signal for the enamine can be detected. In addition, a weak peak for stretching of a long CH_2 chain is visible at 726 cm^{-1}.

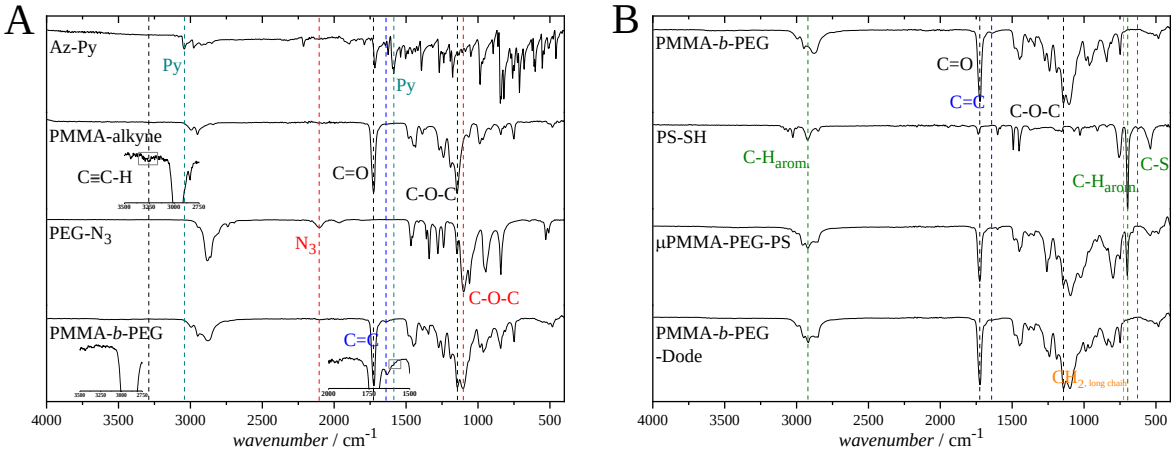

Figure 3.7. ATR-IR measurements of **A**: **Az-Py**, **PMMA-alkyne**, **PEG-N_3**, **PMMA-*b*-PEG**, and **B**: **PS-SH**, **μPMMA-PEG-PS** and **PMMA-*b*-PEG-Dode** at ambient temperature, respectively. All spectra were recorded in bulk without solvent. Adapted with permission from reference [204]. Copyright (2018) American Chemical Society.

3.2.3.2 DSC

PMMA-alkyne, **PMMA-*b*-PEG** and **μPMMA-PEG-PS** were investigated *via* DSC measurements in order to investigate their behavior in the solid state and the corresponding architectural changes. For DSC analysis, it is important to erase the prehistory of polymers, which is influenced by various factors including the isolation method and storage conditions. Therefore, it is necessary to perform two heat scans: In the first scan the polymer sample requires to melt in order to subsequently crystallize or/and solidify under defined conditions. As a result, glass transitions and melting temperatures can be accessed

in the second heat scan. To display the discrepancies between the first and second heat scan, both scans are shown in **Figure 3.8**, in which part **A** and **B** depict the first and the second heat scan, respectively.

In **Figure 3.8B**, **PMMA-alkyne** reveals a glass transition point at approximately 102 °C, showing amorphous characteristic without a melting point. In contrast, PEG is a crystalline polymer. Indeed, PEG derivatives with molar masses of 2000 g mol^{-1} exhibit a melting point in the range of 45 to 50 °C. However, the content of PMMA affects the chain organization of PEG. Environments with 60 w% or more PMMA can even inhibit the crystallization of the PEG chains.[510] As a result, the second heat scan of **PMMA-*b*-PEG** does not display any melting temperature for the PEG block. Merely, a weak glass transition of the PMMA block at approximately 50 °C is detected. The reduction of the glass transition of PMMA can be attributed to the influence of the soft PEG block. The investigation of the second heat scan for **μ-PMMA-PEG-PS** displays glass transition temperature at 104 °C and 156 °C for the PS and PMMA block, respectively. Any melting temperature for the PEG block is detectable due to the high content of PMMA and PS.

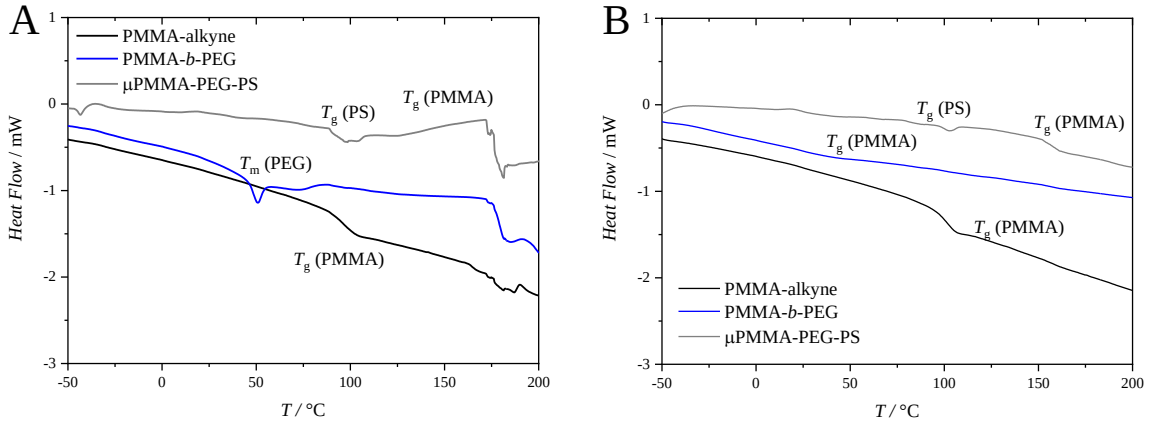

Figure 3.8. DSC measurements of **PMMA-alkyne**, **PMMA-*b*-PEG** and **μPMMA-PEG-PS** obtained with a heating rate of 20 K min^{-1}. **A**: First heat scan and **B**: Second heat scan. Adapted with permission from reference [204]. Copyright (2018) American Chemical Society.

3.2.3.3 UV/Vis and Fluorescence Spectra

The optical properties of the herein presented polymer species are clearly dependent on the pyrene unit, which was introduced at the junction point of the block copolymer synthesized *via* the CuAAC ligation interrupted by a pyrene functionalized 2*H*-azirine derivative. The UV/Vis and fluorescence spectra of

the polymer species which are involved in the formation of **PMMA-*b*-PEG** as block copolymer are displayed in **Figure 3.9**. While the UV/Vis spectra of **PMMA-alkyne** and **PEG-N_3** do not show any relevant absorption bands between 200 and 800 nm in **Figure 3.9A** (due to the lack of any chromophore), the spectrum of **PMMA-*b*-PEG** indeed exhibits a broad absorbance between 200 and 450 nm, which is caused by the presence of pyrene as chromophore. Compared to the absorption spectrum of pyrene, which shows distinct strong absorption maxima at 337, 321 and 308 nm in DCM, the maxima in the spectrum of the block copolymer species are less defined due to the polymer segments that surround the chromophore at the midpoint of the block copolymer, and therefore influence the absorption spectrum depending on their polarity.[400, 404, 405] In addition, the absorbance of the pyrene tethered to the block copolymer is red-shifted compared to isolated pyrene. The substitution of the pyrene in general has an influence on the location on the absorption maxima. Therefore, the enamine group, which is directly attached to the chromophore, shifts the absorption of pyrene to higher wavelengths.

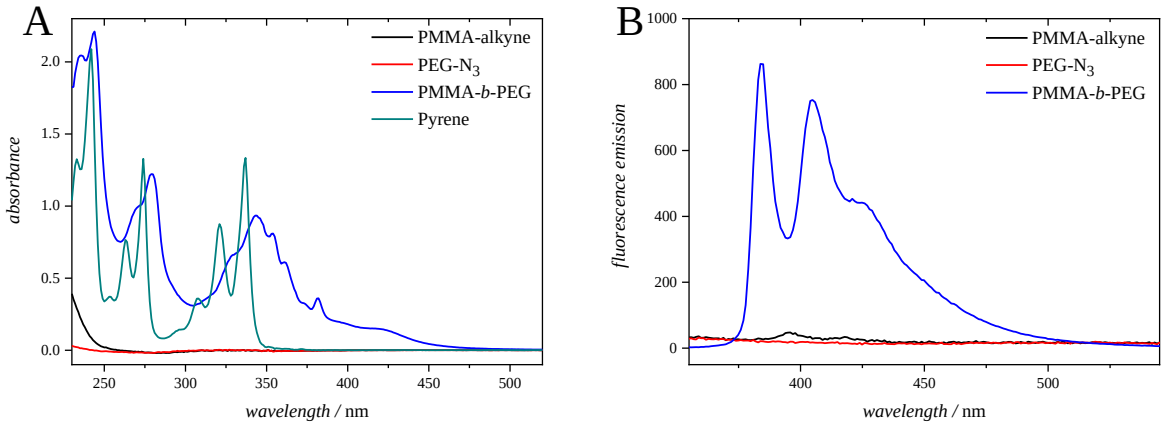

Figure 3.9. A: UV/Vis and **B**: fluorescence ($\lambda_{exc.}$ = 344 nm) spectra of **PMMA-alkyne**, **PEG-N_3** and **PMMA-*b*-PEG** in DCM at ambient temperature. Concentrations of $7.22 \cdot 10^{-5}$ mmol mL^{-1} and of $1.81 \cdot 10^{-5}$ mmol mL^{-1} were employed for UV/Vis and fluorescence measurements, respectively. Adapted with permission from reference [204]. Copyright (2018) American Chemical Society.

Concomitantly, the fluorescence spectra of **PMMA-alkyne**, **PEG-N_3** and **PMMA-*b*-PEG** are presented in **Figure 3.9B**. Analogous to the results of the UV/Vis measurements, the fluorescence measurements of **PMMA-alkyne** and **PEG-N_3** do not display any fluorescence emission upon excitation with a wavelength of 344 nm. However, for **PMMA-*b*-PEG** a characteristic fluorescence of pyrene monomers between 350 and 500 nm is detected. Due to the fact that the chromophore unit is located at the junction point of the block copolymer species, and is therefore spatially separated from other pyrene moieties, the fluorescence emission of the excited dimers (between 400 and 600 nm) is not seen.

The UV/Vis and fluorescence spectra of the modified block copolymer and the mikto-arm star polymers are depicted in **Figure B.5**. Herein, the UV/Vis spectra in **A1** to **A3** display a particularly inexplicit devolution of the absorption bands as detected for **PMMA-*b*-PEG**. Consequently, the attached thiol derivatives further influence the absorption bands of the pyrene unit by making them less sharp. Hereby, the nature of the thiol is insignificant since the absorption spectra for **PMMA-*b*-PEG-Dode**, **μ-PMMA-PEG-PS** and **μ-PMMA-PEG-PEG** are approximately superimposable. Merely, **PS-SH** adds an absorption band between 250 and 275 nm to the spectrum of **μ-PMMA-PEG-PS**. Moreover, the intensity of the fluorescence emission of the modified block copolymer and the mikto-arm star polymers (refer to **Figures B.5B1** to **B.5B3**) is decreased by approximately a factor of 10. Yet again, the nature of the attached thiol is irrelevant since the fluorescence emission spectra are superimposable. The effective shielding of the fluorescence of pyrene due to the attachment of the third component onto the core of the star polymer presents a plausible explanation for this decrease in fluorescence intensity.

3.2.3.4 DLS studies

Direct access to hydrodynamic radii of (self-assembled) polymer chains or other objects in the nm range in solution is provided by dynamic light scattering (DLS). The aim of the DLS studies was to investigate the impact of dilution and temperature on the particle size of **PMMA-*b*-PEG-Dode**, **μ-PMMA-PEG-PS** and **μ-PMMA-PEG-PEG** in water due to the fact that these polymer species exhibit a unique structure. In other words, they consist of a highly hydrophobic core (*e.g.*, pyrene) as a fluorescent marker, and possess arms of different polarity, *i.e.*, from highly hydrophobic (PS) to highly hydrophilic (PEG). Therefore, the herein introduced structures are suited for self-assembly in water.

Due to the high hydrophilicity, **μ-PMMA-PEG-PEG** could be directly dispersed in water while aqueous samples of **PMMA-*b*-PEG-Dode** were prepared by a nanoprecipitation procedure. However, both methods were not applicable for the formation of stable micelles of **μ-PMMA-PEG-PS** in water because of the high impact of the hydrophobic PMMA and PS arms. Therefore, merely the former polymer species were investigated *via* DLS. At 25 °C and with a concentration of 1 mg mL^{-1}, **PMMA-*b*-PEG-Dode** and **μ-PMMA-PEG-PEG** form stable particles in water with an average hydrodynamic radius (D_H) of 42.7 and 18.3 nm, respectively. The reason why the latter species forms smaller micelles than the former might be the polarity of each individual structure: Since **PMMA-*b*-PEG-Dode** is more hydrophobic,

more amphiphilic segments (PEG units) are necessary in order to form a hydrophilic shell around the hydrophobic arms (PMMA and the dodecyl chain). As a result, micelles of **PMMA-*b*-PEG-Dode** are rather bigger in size. While the two PEG arms of **μ-PMMA-PEG-PEG** are capable of forming a more effective hydrophilic shell around the PMMA block alone, leading to a smaller value of D_H.

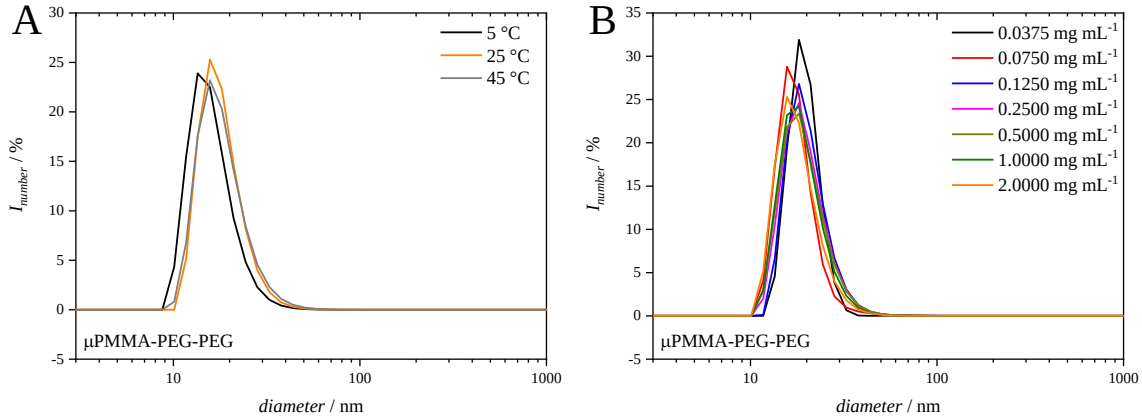

Figure 3.10. DLS studies of **μ-PMMA-PEG-PEG** in water. The temperature-dependent measurements in part **A** were conducted with a concentration of 1 mg mL^{-1}, while the concentration-dependent studies in part **B** were performed at 25 °C. Additional DLS results are presented in **Figures B.6** and **B.7**. Adapted with permission from reference [204]. Copyright (2018) American Chemical Society.

In biomedical applications, for the long-term stability and applicability of the micelles it is important to retain their structure at different temperatures. As a result, the values for D_H of the micelles were determined at three different temperatures: 5 °C, 25 °C and 45 °C. The outcomes are displayed in **Figures 3.10** and **B.6**. By varying the temperature by 20 °C, the micelles of **μ-PMMA-PEG-PEG** depicted deviations in size by 0.2 nm (1 %) for 5 °C and by 2.0 nm (11 %) for 45 °C. In contrast, increasing the ambient temperature for the micelles of **PMMA-*b*-PEG-Dode** results in deviations for D_H of 1.8 nm (4 %), while decreasing the temperature leads to deviations of up to 24.7 nm (58 %). Consequently, micelles of **μ-PMMA-PEG-PEG** are stable upon temperature changes, while particles of **PMMA-*b*-PEG-Dode** loose their structural integrity likely due to rising interactions between the hydrophobic PMMA and dodecyl chain at the lower temperatures.

Another essential characteristic of micelles as potential drug nanocarrier for biomedical applications is the stability upon dilution. Intravenous injection of drugs leads to a drastic dilution in the bloodstream. As a result, the initial particles in water were diluted by a factor of 50. The DLS studies in **Figures 3.10** and **B.7** display maximal derivations of 1.2 nm (7 %) for **μ-PMMA-PEG-PEG** and of 2.1 nm (5 %) for

PMMA-*b*-PEG-Dode, respectively. As a result, concentration changes do not influence the micelles of both block copolymer species.

Since the DLS studies demonstrated that the particles of μ**-PMMA-PEG-PEG** and of **PMMA-*b*-PEG-Dode** in water maintain their structural integrity upon temperature and concentration changes, it can be concluded that their micelles consist of single molecules without dissociation at a critical micelle concentration (CMC). Similar to unimolecular micelles, they exhibit increased stability due to their covalent nature enabling them to be suitable candidates as carrier for drug delivery in the biomedical field. In other words, the core of the micelles is highly hydrophobic due to the presence of the pyrene moiety, and therefore facilitates the encapsulation of drugs. Last but not least, the pyrene chromophore enables tracking of the drug *via* fluorescence measurements.

3.3 Summary

The synthesis of a functional pyrene-substituted 2*H*-azirine compound revealed various challenges. On the one hand, the stability of the photoreactive moiety itself is quite limited since any nucleophile readily attacks the three-membered ring. Furthermore, the synthetic access to 2*H*-azirines consists of multiple step sequences with a minimum of three stages. On the other hand, the pyrene itself exacerbates the purification process, and thus prohibits the large-scale synthesis and reduces reaction yields. Furthermore, the aromatic unit lowers the solubility of the targeted chemical compounds to a substantial extent, and the commercial availability of its derivatives is quite limited. As a result, the reaction pathway employing hydrazones as intermediates was successful and reasonable in the synthesis of a functional pyrene-substituted 2*H*-azirine since it requires the least purification steps in terms of column chromatography.

Nevertheless, the access to the ester functionality of the methyl ester functionalized pyrene-substituted 2*H*-azirine still presents a barrier since the stability of the 2*H*-azirine is quite low, while mild methods for ester cleavage or transesterification were not successful.

However, the copper(I)-catalyzed azide-alkyne cycloaddition interrupted by 2*H*-azirines presents a versatile tool for the construction of advanced macromolecular structures including mikto-arm star polymers as depicted in the current chapter. By elevating the conventional CuAAC reaction to an advanced multicomponent reaction, the construction of midpoint reactive block copolymers is feasible while the reaction holds the potential to incorporate an additional marker (such as pyrene) as fluorescent probe at the junction point. Furthermore, the incorporated vinyl function is a readily available handle to further introduce either a small molecule or macromolecular arm to the core of the block copolymer.

On the one side, the herein introduced modified block copolymer and mikto-arm star polymer species are readily accessible. On the other side, DLS studies revealed micelle formation in water, which are stable against temperature and concentration changes. Amphiphilic mikto arm star polymer based on PEG are widely investigated in the biomedical field,[511] as a result the herein presented structures possess potential application as drug carriers. In other words, the micelles hold a hydrophobic core for drug encapsulation besides the hydrophilic shell, which solubilizes the drug in the blood stream. Last but not least, the pyrene unit as fluorescent marker allows the tracking *via* fluorescence detection.

CHAPTER 4

PHOTOCHEMISTRY AT ELEVATED TEMPERATURES: POLYETHYLENE LIGATION

For a long time, polyolefins have been the most widely employed commodity polymers with the largest volume produced worldwide. The reason behind their dominant position is the combination of outstanding properties from both physical and chemical point of view, such as mechanical strength, flexibility, superior processability, ductility, insulator properties and chemical resistance. In addition, polyolefins can be produced and processed at low cost.[131] Among thermoplastics, polyethylene and its related fabrication techniques (*e.g.*, Ziegler-Natta or high pressure processes) offer a broad range of products for everyday life. However, it presents an on-going research topic for industry and academia as well. Due to the catalyzed chain grow (CCG) concept (refer to **Section 2.1.2.3**), well-defined blocks of polyethylene *via* the pseudo-living polymerization of ethylene are accessible, and the facile introduction of various polar end groups is possible. Therefore, well-defined polyethylene species have been utilized in the synthesis of block and graft copolymers, or as polymerization initiator for example. Consequently, polyethylene has lost its main drawback related to its incompatibility caused by non-polar characteristics. [131–133]

Parts of the current chapter are reproduced from J. T. Offenloch, S. Norsic, H. Mutlu, M. Taam, O. Boyron, C. Boisson, F. D'Agosto, C. Barner-Kowollik, *Polym. Chem.* **2018**, *9*, 3633-3637 with permission from the Royal Society of Chemistry.

The introduction of polyethylene into photochemistry provides a new perspective for the employment of polyolefins. The spatiotemporal control over the reaction site is a substantial benefit of light-induced ligation techniques. Therefore, polyethylene strands may be photochemically patterned onto surfaces using (laser) lithography techniques,[361] or they may be implemented into photoresist systems during 3D laser lithography.[512]

Herein, the basis for future photochemical application of polyethylene is established. While the first subchapter covers the design and synthesis of a photoreactive polyethylene derivative, light-driven end group modification and block copolymer formation are presented in the second one. Finally, the last subchapter describes the modification of silicon surfaces with polyethylene strands tagged with iodine *via* light-triggered cycloaddition.

4.1 Synthesis of a Photoreactive Polyethylene Derivative

Short chain polyethylene (PE) derivatives ($\leq M_n = 5000\,g\,mol^{-1}$) are merely soluble at high temperatures, *i.e.*, above 90 °C, in a limited range of solvents including benzene, toluene, trichlorobenzene and tetrachloroethylene. Thus, the modification reactions and the analysis of the reaction products require to be performed in selected solvents at elevated temperatures. For a light-triggerable PE species, the long-term thermal stability of the attached photoreactive group in solution is a necessary characteristic as well.

Ortho-alkylbenzaldehydes present the ideal photoreactive moiety for PE derivatives, since they are composed of thermally stable chemical units including aromatic systems, ether bonds and carboxylic ester connections (refer to **Section 2.2.4.1**). In contrast, tetrazoles are known for nitrogen release at elevated temperatures,[347] 2*H*-azirines suffer from ring-strain resulting in ring opening,[513] and phenacyl sulfides possess a weak C-S bond with a bond-dissociation energy of $272\,kJ\,mol^{-1}$ (in comparison, a bond-dissociation energy of 335 and $347\,kJ\,mol^{-1}$ for C-O and C-C bonds is found,[514] respectively). Initially, readily accessible end groups for PE species in combination with efficient ligation techniques, anchoring the *ortho*-alkylbenzaldehyde at the chain termini, should be considered. For instance, hydroxyl- and azide-terminated PE derivatives offer the possibility to tether an end group functionality *via* efficient esterification reaction and CuAAC ligation (refer to **Section 2.1.3.2**), respectively. The synthesis of a carboxylic acid-functional *ortho*-alkylbenzaldehyde derivative is in-depth described in the literature,[334, 337, 515] whereas the alkyne unit is facilely introduced *via* the esterification of the carboxylic acid species with propargyl

alcohol. As a result, two distinct methods for the incorporation of the photoreactive unit into the polyolefin species were assessed.

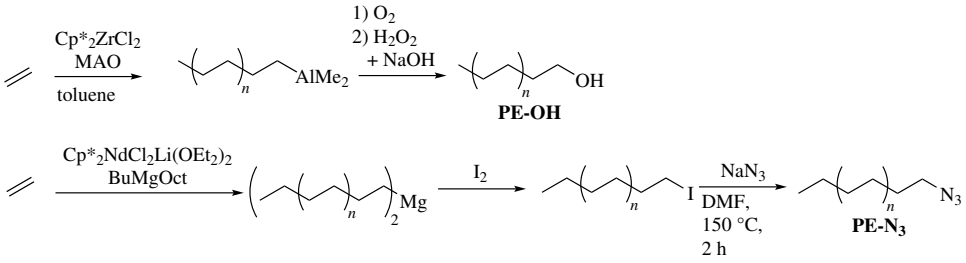

Scheme 4.1. The CCG polymerization of ethylene delivers on the one hand the hydroxyl functional PE species (**PE-OH**) *via* oxidative work up. On the other hand, the addition of iodine after the polymerization enables the synthesis of iodo end-capped PE chains, which are transformed into azido-functional polymer species *via* nucleophilic substitution.

On the one side, the synthesis of the PE derivatives was accomplished at Lyon University according to previously described strategies.[125, 128] The pseudo-living polymerization of ethylene followed by oxidative work-up affords the hydroxyl-terminated PE species, and the azide-capped PE derivative is obtained *via* the addition of iodine after the polymerization followed by substitution reaction with NaN_3 (refer to **Scheme 4.1**, **PE-OH**: $M_{n,SEC(TCB)}$ = 700 g mol^{-1}, $Đ$ = 1.30, **PE-N$_3$**: $M_{n,SEC(TCB)}$ = 1100 g mol^{-1}, $Đ$ = 1.28). On the other side, the carboxylic acid and alkyne derivative of the *ortho*-alkylbenzaldehyde, **Ph-OH** and **Ph-alkyne**, were obtained *via* a consequent four- and five-step synthesis (refer to **Scheme 4.2**), respectively. According to literature, 2,3-dimethylanisole was converted into 2-methoxy-6-methylbenzaldehyde by employing copper(II) sulfate ($CuSO_4$) and potassium persulfate ($K_2S_2O_8$) as oxidizing agent in the first step.[515] The ether bond was cleaved in the subsequent step,[337] and the newly formed hydroxyl group was etherified with methyl 4-(bromomethyl)benzoate,[334] whose ester unit was cleaved under basic conditions affording **Ph-OH** in the fourth step.[334] Finally, the fifth step entailed the esterification of **Ph-OH** with propargyl alcohol in THF utilizing 1-ethyl-3-(3-dimethylaminopropyl)carbodiimide hydrogenchloride (EDC·HCl) as coupling agents and 4-dimethylaminopyridine (DMAP) as catalyst. To ensure high conversion of **Ph-OH**, propargyl alcohol was predried over sodium sulfate, and 10 eq. of the alcohol were used. After aqueous work-up, the targeted compound was obtained in very good yields, *i.e.*, 97 %, without further purification. The ^{1}H and ^{13}C NMR spectrum in **Figure C.1** and **C.2**, respectively, and high resolution ESI-MS measurements (refer to the Experimental Section) confirmed the successful formation of **Ph-alkyne**.

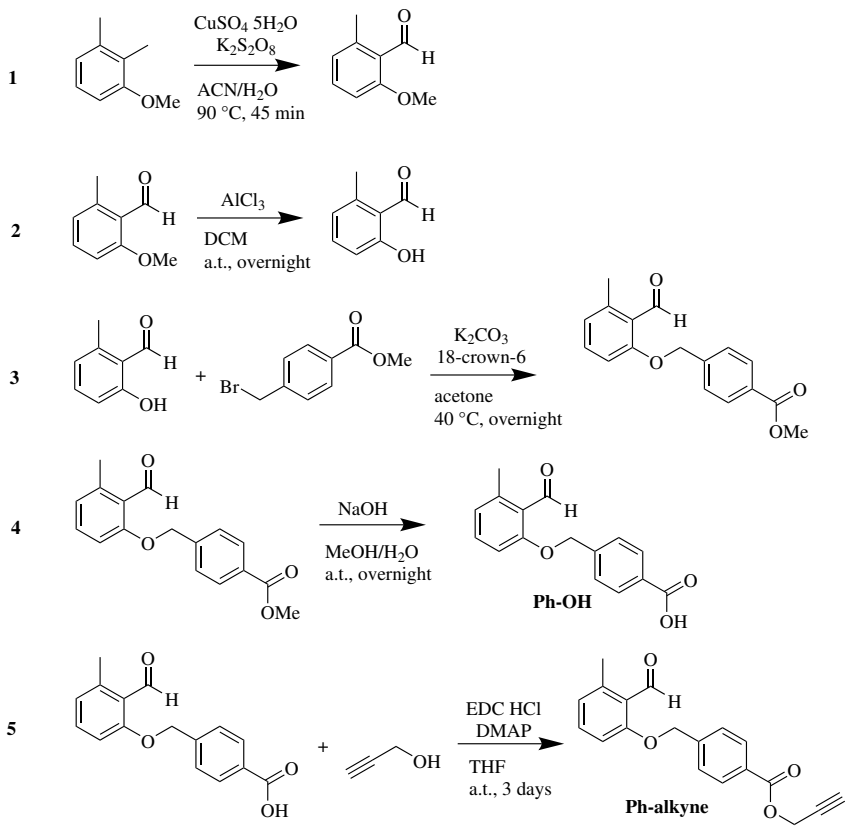

Scheme 4.2. The synthesis of **Ph-OH** and **Ph-alkyne** entails four and five steps, respectively. In the first step, a methyl group of 2,3-dimethylanisole is oxidized to an aldehyde unit. The ether cleavage is performed in the second step, followed by the attachment of a benzyl ester *via* etherification reaction. **Ph-OH** is received after base-catalyzed ester hydrolysis in the fourth step. The esterification of **Ph-OH** with propargyl alcohol affords **Ph-alkyne**. Adapted with permission from reference [151]. Copyright (2018) Royal Society of Chemistry.

The attachment of the photoreactive *ortho*-alkylbenzaldehyde to the chain termini of the PE derivatives was tested *via* two distinct approaches. One approach included the esterification of **PE-OH** with **Ph-OH** in a mixture of toluene and DMF (7:3) at 100 °C. The reaction was executed with 1.29 eq of the acid derivative and a combination of EDC·HCl and DMAP, or tosyl sulfonic acid as catalyst. However, with neither of the two reagents any conversion of the hydroxyl end group of **PE-OH** could be detected. Nevertheless, the ligation approach relying on the CuAAC reaction was successful. Indeed, $CuSO_4$ and sodium ascorbate (0.08 eq. and 0.10 eq., respectively) were effectively converting the azide end group of the PE species under the same conditions as the esterification experiments (*i.e.*, a mixture of toluene and DMF (7:3), 100 °C, 1.29 eq. of **Ph-alkyne**). After three days, the polymer was precipitated by adding methanol to the reaction mixture, collected by filtration and dried. The subsequent analysis was performed in a mixture of benzene and tetrachloroethene (TCE, 1:2) at 90 °C for high temperature (HT) ^{1}H NMR spectra, and in trichlorobenzene at 150 °C for HT SEC measurements. The comparison of the ^{1}H NMR spectra of the parent polymer **PE-N$_3$** and the modified polymeric species **PE-Ph** in **Figure 4.1B** indicates that the magnetic resonances associated with the methylene group adjacent to the azide unit at 3.00 ppm vanished for **PE-Ph**. Instead, a novel magnetic resonance at 3.96 ppm is assigned to the protons of the CH_2 group next to the triazole linkage. The magnetic resonance of the proton of the newly formed aromatic system is visible as a singlet at 7.25 ppm. Further relevant magnetic resonances associated with the *ortho*-alkylbenzaldehyde are detectable at 5.35 and 10.67 ppm arising from the protons next to the ether bond and from the aldehyde proton, respectively. In addition, the HT SEC trace of the modified PE species **PE-Ph** in **Figure 4.1C** is similar to the trace of the pristine polymer. As a result, non-desired side reactions during modification reaction are excluded, and the efficient nature of the ligation technique is confirmed. The analysis of the HT SEC data based on a PE calibration affords a $M_{n,SEC(TCB)}$ of 1200 g mol^{-1} and a dispersity $Đ$ of 1.25.

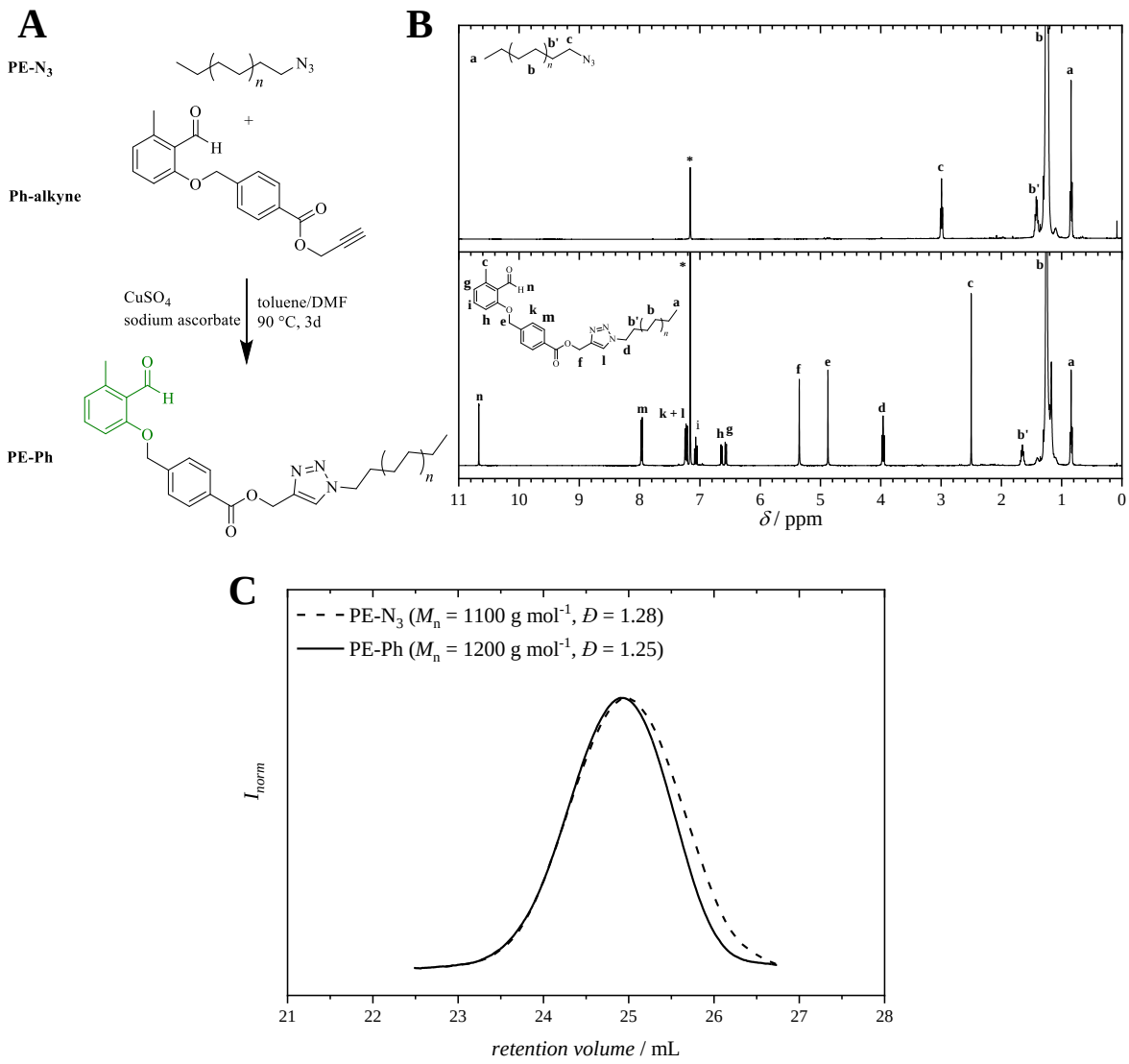

Figure 4.1. **A**: Reaction scheme of the modification of **PE-N$_3$** with a photoreactive *ortho*-alkylbenzaldehyde utilizing CuAAC ligation. **B**: HT ^{1}H NMR spectra (400 MHz, C_6D_6/TCE, 90 °C) of **PE-N$_3$** as parent polymer (top spectrum) and of **PE-Ph** (bottom spectrum) indicating the successful modification. The magnetic resonance marked with an asterisk is assigned to C_6H_6. **C**: HT SEC (TCB, 150 °C, RI) traces of the same polymer species. Adapted with permission from reference [151]. Copyright (2018) Royal Society of Chemistry.

4.2 UV Light-Induced Polyethylene Ligation

After paving the way for the synthesis of a PE derivative functionalized with a photoreactive end group, the reactivity upon irradiation was investigated. The energy supply *via* UV light irradiation of *ortho*-alkylbenzaldehyde results in the formation of highly reactive *ortho*-quinodimethanes, which serve as dienes for subsequent Diels–Alder cycloaddition with electron-deficient dienophiles (refer to **Section 2.2.4.1**). Therefore, 1.0 eq. of **PE-Ph** and 5.0 eq. of *N*-ethyl maleimide as small molecule test system were dissolved in a mixture of acetonitrile and toluene (1:1). The overall concentration of reactants was $4 \cdot 10^{-5}$ mol L^{-1}. In order to solubilize the PE species, the reaction mixture was heated to 100 °C prior to irradiation in a custom-built photoreactor. For this purpose, a compact lamp (Philips PL-L cleo, 36 W) with an emission maximum at 365 nm was employed as light source (refer to **Figure A.1**). After one hour of light exposure, the mixture was again heated to 100 °C in order to redissolve the PE species, and subsequently irradiated for another hour in the photoreactor. All in all, the mixture underwent five heating-irradiation cycles. Since toluene displays a solvent cut-off wavelength of 286 nm,[516] a prolonged reaction time was selected compared to existing irradiation protocols of *ortho*-alkylbenzaldehydes.[335, 339] After 90 % of the solvent was removed, the modified polymer was precipitated *via* addition of methanol, collected by filtration and dried for following characterization. The comparison of HT ^{1}H NMR spectra before and after UV light irradiation in the presence of the maleimide species in **Figure 4.2B** clearly confirms the successful light-induced cycloaddition. In the ^{1}H NMR spectrum of the modified polymer species **PE-Et**, the magnetic resonance of the proton of the aldehyde unit at 10.67 ppm vanished upon consumption. Concomitantly, novel magnetic resonances in the range between 3.13 and 2.59 ppm appear, which are assigned to the protons of the newly formed cyclohexane ring. Importantly, the magnetic resonance of the proton of the secondary alcohol is detected at 5.80 ppm. However, the evaluation of the HT SEC data in **Figure 4.2C** does not indicate an increase in apparent molar mass ($M_{n,SEC(TCB)}$ = 1200 g mol^{-1}, $Đ$ = 1.38) compared to the pristine polymeric species. A particularly small influence of the newly formed cycloadduct on the hydrodynamic radius of the polymer in solution, and non-adequate SEC conditions for the end group, present two plausible causes for the same molecular mass after light-induced cycloaddition with *N*-ethyl maleimide.

After the optimization of the conditions for successful photocycloaddition, the efficiency of the reaction was tested. Therefore, the synthesis of block copolymer species was targeted under equimolar ratios of the

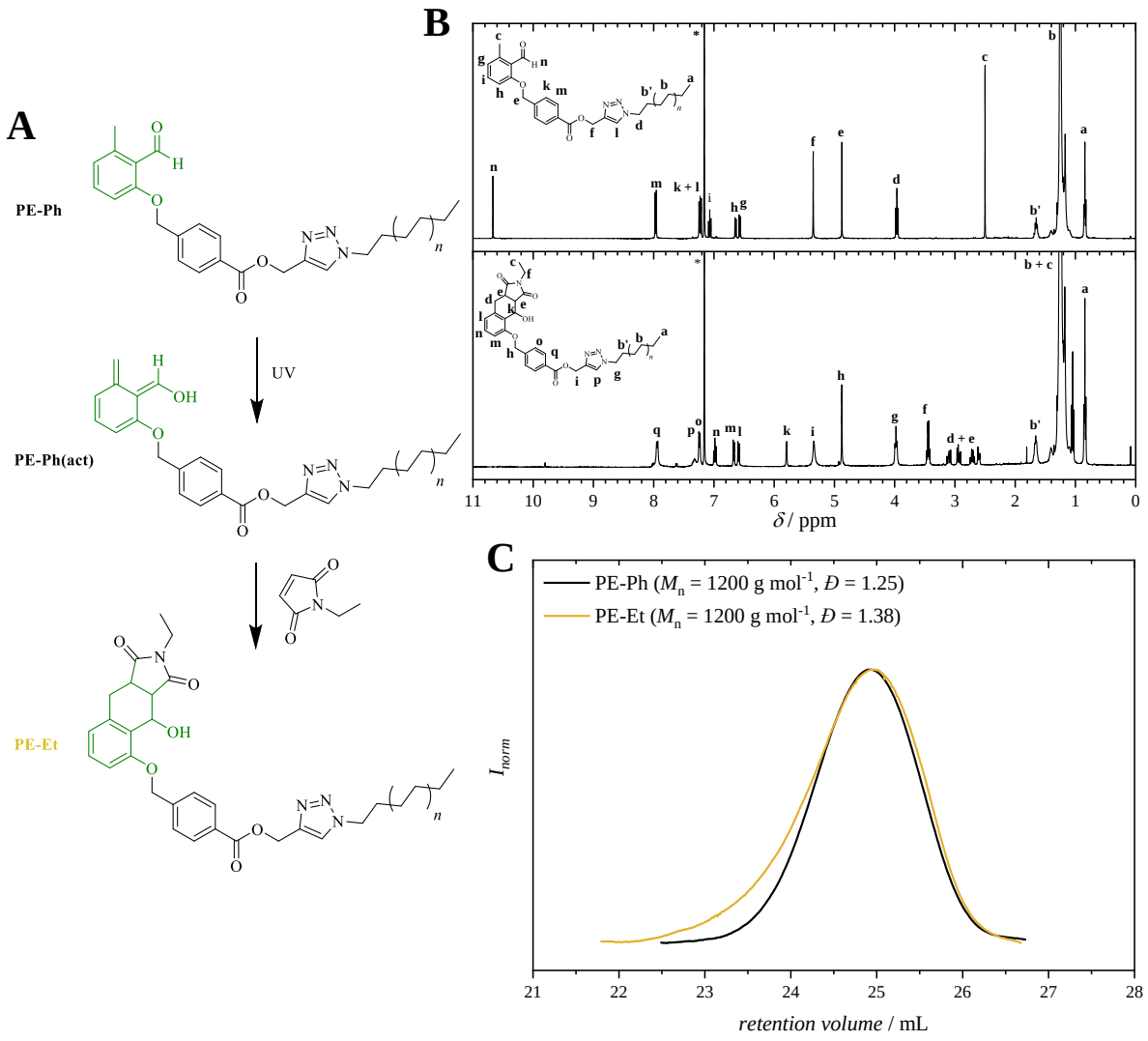

Figure 4.2. A: Reaction scheme of the light-induced cycloaddition of **PE-Ph** using *N*-ethyl maleimide as model dienophile. **B**: HT ^{1}H NMR spectra (400 MHz, C_6D_6/TCE, 90 °C) of **PE-Ph** as parent polymer (top spectrum) and of **PE-Et** (bottom spectrum) indicating the successful cycloaddition. The magnetic resonance marked with an asterisk is assigned to C_6H_6. **C**: HT SEC (TCB, 150 °C, RI) traces of the same polymer species. Adapted with permission from reference [151]. Copyright (2018) Royal Society of Chemistry.

reactive units. For the second block, a polystyrene and a poly(methyl methacrylate) block were synthesized *via* ARGET ATRP polymerization to ensure high end group fidelity. In order to incorporate the maleimide end group as dienophilic partner for the DA reaction, an initiator bearing a furan-protected maleimide was employed for the process. The deprotection of the maleimide termini during the polymerization was avoided *via* a low reaction temperature, *i.e.*, 30 °C. Moreover, the ARGET ATRP process was conducted with $CuBr_2$ and tris[2-(dimethylamino)ethyl]amine (Me_6TREN) as catalytic system, and Fe(0) powder as reductant. The chain growth was stopped after 22 h and 5 h for **PS-Mal** and **PMMA-Mal**, respectively, *via* dilution with THF. The copper catalyst was removed by filtration through neutral aluminium oxide. Subsequently, the polymer species were received by two-fold precipitation in ice-cold methanol. The ^{1}H NMR spectrum of **PS-Mal** in **Figure C.3** indicates magnetic resonances of the protected maleimide end group at 5.22 and 2.79 ppm as well as broad magnetic resonances of the aromatic protons of the polymeric backbone in the range between 7.40 and 6.25 ppm. Analogously for the ^{1}H NMR spectrum of **PMMA-Mal** in **Figure C.4**, the magnetic resonance associated with the protons of the methoxy group is detected at 3.60 ppm next to the end group resonances at 6.54, 5.27 and 2.91 ppm. Moreover, the ambient temperature SEC(THF) analysis in **Figure C.5** reveals narrow dispersities and low molar masses (**PS-Mal (pro)**: $M_{n,SEC(THF)}$ = 5000 g mol^{-1}, $Đ$ = 1.08, **PMMA-Mal (pro)**: $M_{n,SEC(THF)}$ = 5500 g mol^{-1}, $Đ$ = 1.23), which are ideal to visualize block copolymer formation with short PE species. With the aim to remove furan as protecting group of the maleimide termini, both polymer species were heated to 110 °C in bulk under reduced pressure in a drying oven, and characterized without additional purification steps. The analysis of the ^{1}H NMR spectrum of **PMMA-Mal** in **Figure C.4** reveals the disappearance of the aforementioned end group resonances. Instead, a novel magnetic resonance associated with the unsaturated protons of the maleimide is visible at 6.76 ppm. For **PS-Mal**, the end group resonances of the furan protected maleimide in **Figure C.3** cannot be detected anymore. However, the magnetic resonance of the unsaturated protons of the maleimide is superimposed with the magnetic resonances of the aromatic protons of the backbone. The concomitant SEC analysis of the deprotected polymer species on a THF-based system in **Figure C.5** displays the successful prevention of non-desired transesterification reactions - resulting in crosslinking - caused by prolonged exposure of the polymeric substances to elevated temperatures (**PS-Mal**: $M_{n,SEC(THF)}$ = 5000 g mol^{-1}, $Đ$ = 1.10, **PMMA-Mal**: $M_{n,SEC(THF)}$ = 5300 g mol^{-1}, $Đ$ = 1.20).

The next step consisted in the block copolymer formation of **PE-Ph** and the dienophilic polymeric species **PS-Mal** and **PMMA-Mal**. The same conditions as for the cycloaddition with *N*-ethyl maleimide were utilized for the modular ligation of two distinct polymer blocks. The analysis of the ^{1}H NMR spectra of the potential block copolymers in **Figure 4.3B** yields similar results compared to the cycloaddition with the small molecule. While the magnetic resonance of the proton of the aldehyde at 10.67 ppm cannot be detected for the block copolymer species **PE-*b*-PS** and **PE-*b*-PMMA**, novel magnetic resonances are visible between 3.14 and 2.54 ppm stemming from the Diels–Alder cyclohexane adduct. Furthermore, the magnetic resonance of the proton of the secondary alcohol is present at 5.78 ppm for **PE-*b*-PS** and at 5.90 ppm for **PE-*b*-PMMA**. The comparative integration of these magnetic resonances is in good agreement with the integrals of the backbone magnetic resonances (refer to **Table 4.1**). The successful block copolymer formation is also confirmed by the analysis of the HT SEC data (refer to **Figure 4.3C** and **4.3D**). A clean shift to lower retention volumes compared to the newly synthesized, starting **PE-Ph** (**PE-Ph**: $M_{n,SEC(TCB)}$ = 850 g mol^{-1}, $Đ$ = 1.22) is visible for both block copolymers. The evaluation based on a PE calibration results in an increase of molar mass of 2300 g mol^{-1} for **PE-*b*-PS** (**PE-*b*-PS**: $M_{n,SEC(TCB)}$ = 3200 g mol^{-1}, $Đ$ = 1.08), which perfectly corresponds to the HT SEC analysis of **PS** based on the same calibration (**PS**: $M_{n,SEC(TCB)}$ = 2300 g mol^{-1}, $Đ$ = 1.08). For **PE-*b*-PMMA** (**PE-*b*-PMMA**: $M_{n,SEC\ (TCB)}$ = 1800 g mol^{-1}, $Đ$ = 1.34), an increase in apparent molar mass of 900 g mol^{-1} is determined. Compared to the results for **PMMA-Mal** based on a PE calibration (**PMMA-Mal**: $M_{n,SEC(TCB)}$ = 1500 g mol^{-1}, $Đ$ = 1.38), the increase for **PE-*b*-PMMA** is still in good agreement. Further evidence for the successful light-induced cycloadditions was provided by solubility tests. Whereas **PE-Ph** was hardly soluble in solvents including THF and chloroform, the block copolymers were fully solubilized in these solvents enabling NMR recording at ambient temperature in $CDCl_3$. A comparison of ^{1}H NMR spectra at ambient and at elevated temperature is presented in **Figure C.6** for **PE-*b*-PS** as an example.

The validation of the HT SEC data for the block copolymer species was obtained by temperature stability tests. **PE-*b*-PS** was dissolved in TCB at different temperatures and analyzed *via* HT SEC after different periods of time. **Figure C.7** shows three similar monomodal SEC traces for **PE-*b*-PS**, even after 24 h at 150 °C. As a result, the synthesized PE species as well as the block copolymers do not degrade during analysis, confirming the above presented SEC results.

As demonstrated before, UV light-induced block copolymer formation of a photoreactive PE block and the analysis of the ligation products at high temperatures are effective. However, since the value of the refractive index increment *dn/dc* of PE is -0.104 in TCB, and the value for PS is 0.052 in the same solvent, the resulting RI signal for **PE-*b*-PS** is positive.[517] Consequently, the ligation of a PE block with a molar mass of approximately 1000 g mol^{-1} with a PS block of 2300 g mol^{-1} (**PS2-Mal**) results in a block copolymer species with a *dn/dc* value of approximately 0. Hence, no RI signal associated with the polymeric species is recorded in HT SEC analysis by employing RI detection. Nevertheless, the ^{1}H NMR results in **Figure C.8D** unambiguously indicate the successful block copolymer formation of **PE-*b*-PS2** upon the disappearance of the magnetic resonance of the aldehyde proton next to the detection of the magnetic resonances of the newly formed cyclohexane motif at 6.80 ppm and between 3.80 and 2.50 ppm. Furthermore, no *dn/dc* values for PMMA in TCB are found in the literature. In contrast to **PS-Mal**, the measured RI signal for **PMMA-Mal** in TCB is negative (analogous to the RI signal of PE), therefore no issues with the detection of PE-PMMA block copolymers are encountered.

Table 4.1. Summary of the results for the light-induced modification of **PE-Ph** listed in tabular form. In general, $M_{n,SEC(TCB)}$ is based on a PE calibration while for $M_{n,SEC(THF)}$ either a PS calibration (**PS-Mal**) or a PMMA calibration (**PMMA-Mal**) was employed. For **PE-Et**, the integral of the backbone resonances between 1.40 and 1.10 ppm was compared to the end group magnetic resonance at 4.88 ppm. For **PE-*b*-PS** and **PE-*b*-PS2**, referencing the magnetic resonance of the same proton at 4.87 ppm to either the aromatic backbone resonances of PS between 7.20 and 6.20 ppm or the backbone resonances of PE in the area of 1.35 to 1.10 ppm results in $M_{n,\,NMR}$ for the PS and PE block, respectively. In the case of **PE-*b*-PMMA**, the magnetic resonance between 5.12 and 4.90 ppm was compared to the magnetic resonance of the methoxy group of PMMA at 3.44 ppm and to the backbone resonance of PE stemming from the saturated alkyl chain between 1.30 and 1.15 ppm in order to assess the $M_{n,\,NMR}$ values of the individual blocks. The addition of the values for the distinct polymer blocks results in $M_{n,\,NMR}$ for the block copolymers. Reprinted with permission from reference [151]. Copyright (2018) Royal Society of Chemistry.

Species	**Block**	$M_{n,SEC(TCB)}$ / g mol^{-1}	$Đ$ /	$M_{n,SEC(THF)}$ / g mol^{-1}	$Đ$ /	$M_{n,NMR}$ / g mol^{-1}
PE-Et		1200	1.38	-	-	2000
	PE-Ph	1200	1.25	-	-	1600
PE-*b*-PS		3200	1.08	-	-	7500
	PE-Ph	850	1.22	-	-	1400
	PS-Mal	2300	1.10	5000	1.10	6100
PE-*b*-PMMA		1800	1.34	-	-	6100
	PE-Ph	850	1.22	-	-	1200
	PMMA-Mal	1500	1.38	5300	1.20	4900
PE-*b*-PS2		X	X	-	-	4000
	PE-Ph	1200	1.25	-	-	1800
	PS2-Mal	1000	1.15	2300	1.15	2200

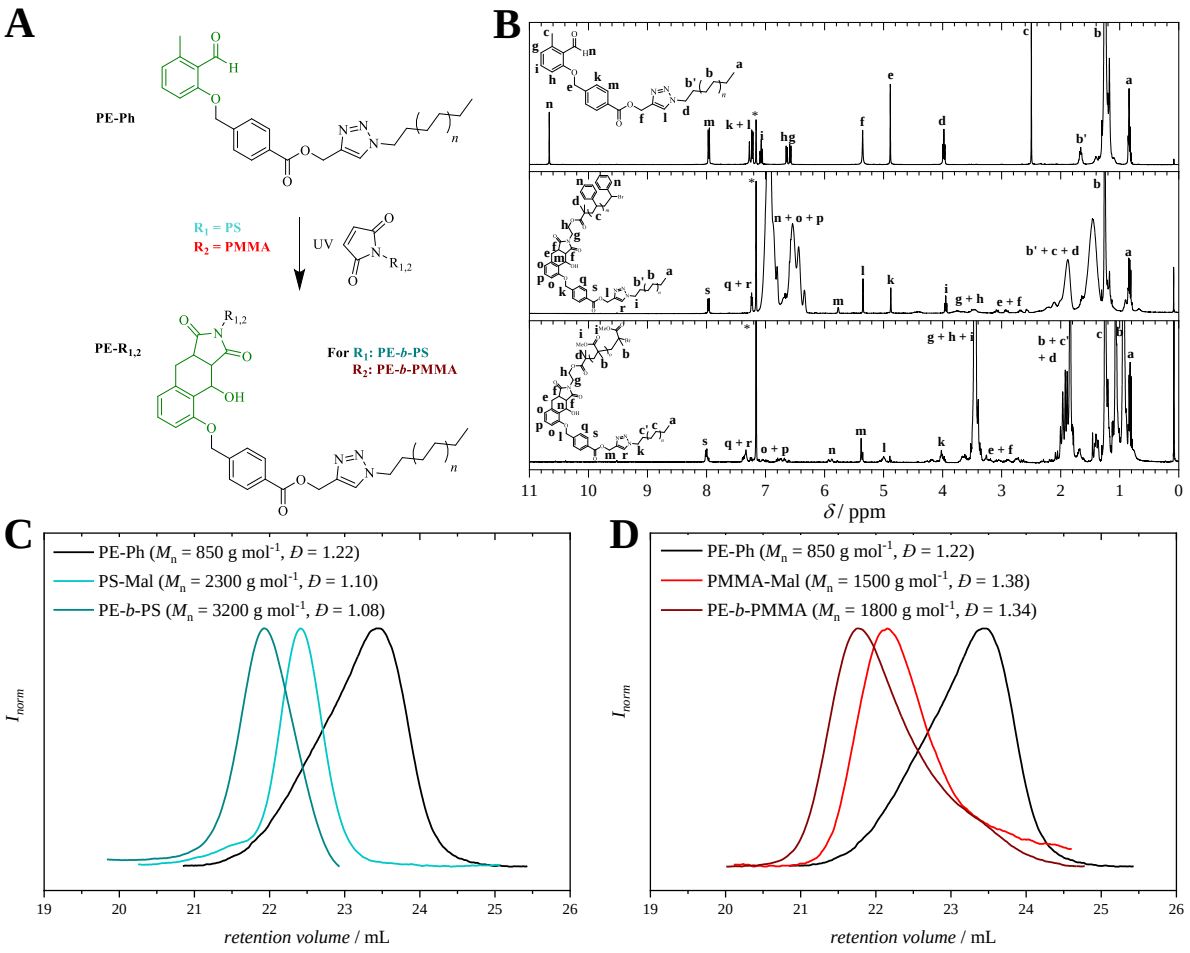

Figure 4.3. **A**: Reaction scheme of the light-induced block copolymer formation of **PE-Ph** and the maleimide-terminated PS and PMMA species. **B**: HT ^{1}H NMR spectra (400 MHz, C_6D_6/TCE, 90 °C) of **PE-Ph** as parent polymer (top spectrum) and of the block copolymers **PE-*b*-PS** (middle spectrum) and **PE-*b*-PMMA** (bottom spectrum) indicating the successful synthesis of the block copolymers. The magnetic resonance marked with an asterisk is assigned to C_6H_6. **C** and **D**: HT SEC (TCB, 150 °C, RI) traces of the same polymer species. Adapted with permission from reference [151]. Copyright (2018) Royal Society of Chemistry.

4.3 UV Light-Induced Generation of Hydrophobic Surfaces

Surfaces covered with a hydrophobic layer are an intriguing research field due to their water-repellent properties. In this context, PE - as one of the most hydrophobic polymer species - presents the ideal candidate to modify surfaces in order to achieve higher hydrophobicity of surfaces. Light-induced anchoring of the herein introduced photoreactive PE blocks might allow to implement hydrophobic properties onto a surface in a spatially resolved fashion.[21]

Time-of-flight secondary ion mass spectrometry (ToF-SIMS) is a powerful tool to detect fragment ions of molecules attached to surfaces in combination with their lateral distribution. However, the polymeric species **PE-Ph** does not feature a characteristic mass fragment for ToF-SIMS measurements. As a consequence, the synthesis route was modified receiving an iodo-substituted triazole linkage *via* interrupted CuAAC ligation.[172, 518] 2.0 eq. of $Cu(ClO_4)_2$, 4.0 eq. of KI, 1.0 eq. of NEt_3 and 10 mol% of tris(benzyltriazolylmethyl)amine (TBTA) as ligand were employed to trigger the ligation reaction between **PE-N_3** and **Ph-alkyne** as light-sensitive termini (refer to **Scheme 4.4**). The reaction mixture was heated to 100 °C for three days followed by the addition of methanol to precipitate the product. **Figure C.9** displays the ^{1}H NMR spectrum of the resulting polymer after filtration and drying. Analogously to the ^{1}H NMR spectrum of **PE-Ph**, no magnetic resonance associated with the methylene group adjacent to the azide unit at 3.00 ppm is detected in the ^{1}H NMR spectrum of **PE-Ph-I**. Instead, a magnetic resonance at 4.18 ppm is assigned to the CH_2 adjacent to the triazole linkage. Additionally, relevant magnetic resonances of the *ortho*-alkylbenzaldehyde unit are detectable at 5.35 and 10.67 ppm arising from the protons of the methylene group next to the ether bond and from the aldehyde, respectively. However, a careful examination of the aldehyde resonance displays two magnetic resonances instead of one (refer to the enlargement of the ^{1}H NMR spectrum in **Figure C.9**). Furthermore, a magnetic resonance at 7.64 ppm is visible stemming from the protonated triazole system. Therefore, the targeted photoreactive **PE-Ph-I** and **PE-Ph** as side product are received. Nevertheless, due to the high sensitivity of ToF-SIMS analysis, the mixture of iodinated and non-iodinated polymeric species was subjected to surface modification.

The synthesis pathway of silicon surfaces functionalized with highly hydrophobic PE species includes three steps (refer to **Figure 4.5**): The activation of the silicon surfaces yielding an amino-functionalized substrate is performed in the first step, followed by anchoring of a suitable dienophilic compound in the subsequent step. Finally, the last step comprises light-induced ligation of the PE block in a grafting-to

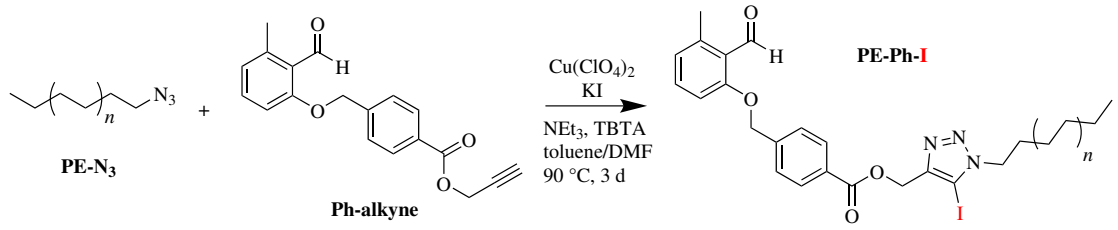

Figure 4.4. For ToF-SIMS measurements, a novel photoreactive PE species was synthesized bearing a 5-iodo-1,2,3-triazole linkage, whose iodine group is suitable for precise detection of surface-bound polymer chains.

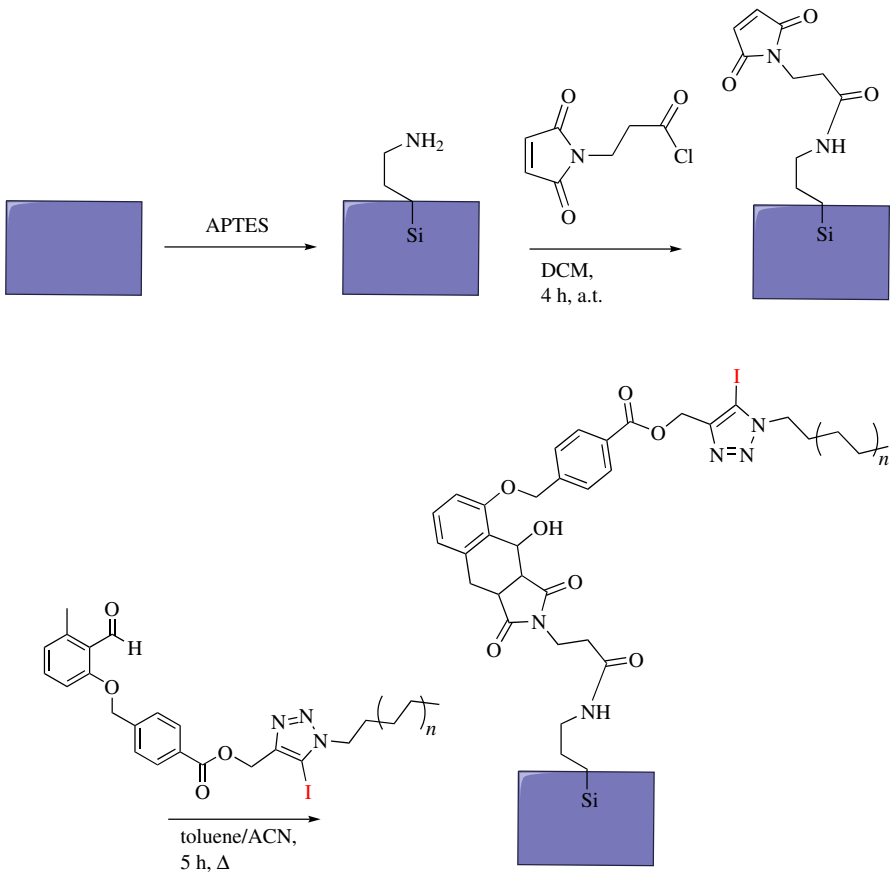

Figure 4.5. General reaction pathway for the functionalization of silicon surfaces with **PE-Ph-I**. In the first step, the silicon wafer is activated *via* air plasma followed by treatment with APTES. The attachment of the dienophilic compound for light-induced Diels–Alder cycloaddition is depicted as the second step. Finally, surfaces modified with hydrophobic PE are obtained *via* light-induced ligation of the PE derivative in a grafting-to approach.

approach. In the beginning, a silicon wafer was cut into squares. Prior to air plasma activation, residual particles were removed *via* rinsing with isopropanol and subsequent drying in a nitrogen stream. After the activation step, the respective substrates lying on a petri dish were immediately placed in a desiccator among a separate glass vial filled with (3-aminopropyl)triethoxysilane (APTES). Evacuating the system for 2 h, followed by annealing at 130 °C for 4 h in a vacuum oven, and rinsing with various solvents (sequence of rinsing: toluene, acetone water, acetone and water), provided the substrates possessing amino groups chemically tethered to the surface area. Without further characterization, the APTES-functionalized surfaces were immersed in dry DCM solution containing 55 mM of NEt_3 for the second step. After 5 minutes, 4-maleimidobutyroyl chloride in dry DCM was added and the reaction was allowed to proceed for 4 h at ambient temperature. Subsequently, the surfaces were rinsed with DCM, MeOH and water, and left in MeOH overnight before rinsing with MeOH, DCM, acetone, water acetone and water, and drying under a nitrogen flow. The ToF-SIMS spectrum in **Figure 4.6A** of a respective surface sample indicates a signal at 96.01 *m/z* corresponding to the chemical formula of the ion $C_4H_2O_2N^-$, which presents a characteristic mass fragment for a maleimide group.

Thereupon, a surface functionalized with maleimide groups was placed in a head-space vial containing **PE-Ph-I** (c = 2 mg mL^{-1}) dispersed in a mixture of ACN and toluene (1:1). Prior to photoreaction, the solution was degassed with nitrogen for 10 min. In order to solubilize the PE species, the vial was placed in an oil bath at 100 °C for 10 min before the irradiation in a photoreactor with the same UV lamp as the one utilized for the end group modification and block copolymer formation. Analogously, the mixture underwent five heating-irradiation cycles followed by rinsing with toluene and water, and drying under a stream of nitrogen. For the blank sample, a maleimide-containing surface was also placed in the solution comprising **PE-Ph-I**. The sample was degassed with nitrogen and heated as well. However, the blank sample was not irradiated. The ToF-SIMS results in **Figure 4.6B** indicate a signal for the iodine I^- fragment with a *m/z*-value of 126.90 and the characteristic mass fragment for the maleimide group at a *m/z*-value of 96.01 in **Figure 4.6A**. The intensity of the signal for the mass fragment of the maleimide group is reduced for the irradiated surface as well as for the blank sample. Furthermore, the spectrum of the irradiated surface unambiguously indicates a signal for the iodine fragment stemming from the polymeric species, while the spectrum of the blank surface shows a signal at the same *m/z*-value with half of the intensity. Consequently, the blank sample exhibited a large amount of adsorbed **PE-Ph-I**, and

therefore, it was necessary to optimize the rinsing procedure. Since PE is merely soluble in toluene at elevated temperatures, two freshly prepared samples - one was irradiated the other not - were immersed two times in vials containing toluene at 100 °C, and left overnight in a third vial with toluene at 100 °C. Subsequently, the surfaces were rinsed with toluene and water, and dried in a stream of nitrogen. Different than expected, the signal for the iodine fragment in the ToF-SIMS spectrum in **Figure 4.6D** possesses a weaker intensity for the irradiated surface than for the blank sample after the optimized rinsing procedure. Concomitantly, the intensity of the fragment ion of the maleimide group decreases in both cases (refer to **Figure 4.6C**). As a result, it was not possible to functionalize surfaces with PE species since either APTES or the maleimide group attached to the surface were not resistant to elevated temperatures required for solubilizing the PE species.

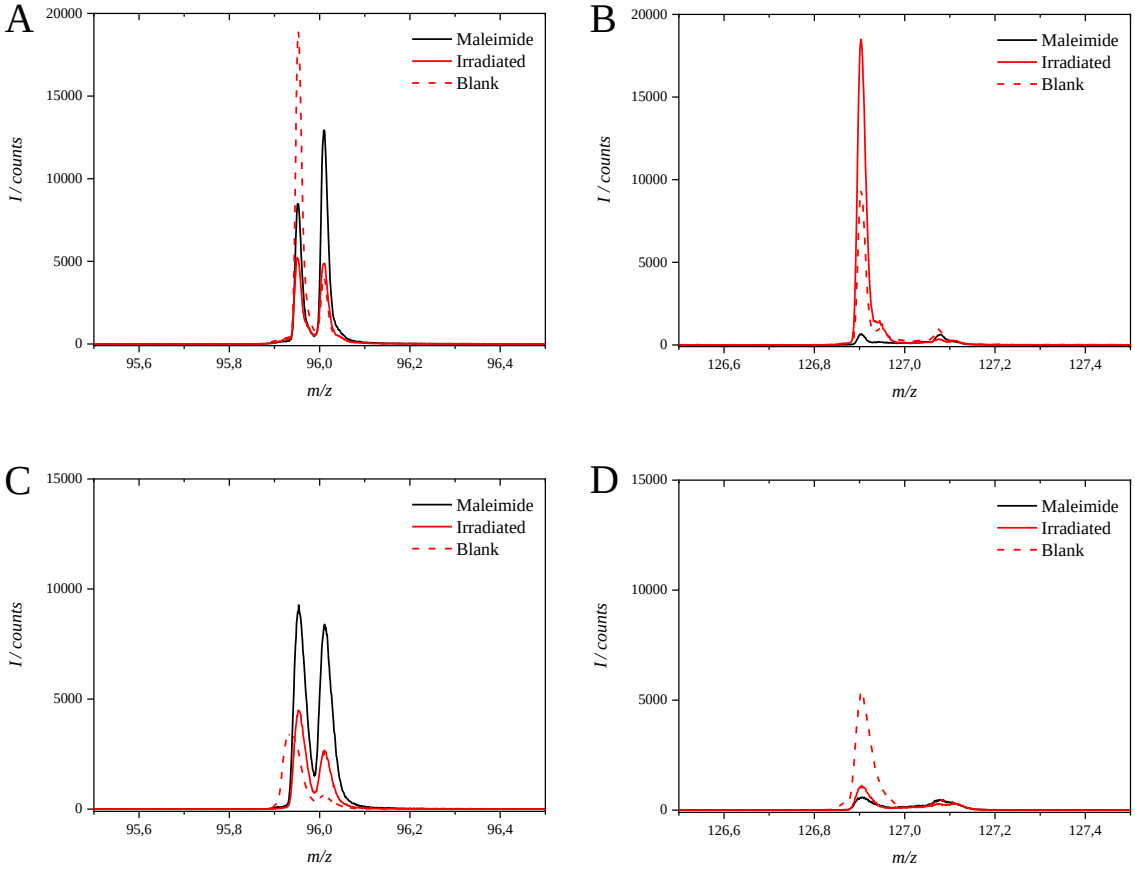

Figure 4.6. ToF-SIMS spectra of the surface modification experiments. On the one side, the signal at a *m/z*-value of 96.01 in part **A** and **C** is assigned to the mass fragment with the chemical formula of $C_4H_2O_2N^-$, which presents a characteristic mass fragment ion for a maleimide group. On the other side, the iodine I^- fragment in part **B** and **D** is detected at a *m/z*-value of 126.90. The black traces indicate the TOF-SIMS results for the surfaces functionalized with dienophilic maleimide groups, while the ToF-SIMS results of the maleimide surfaces after irradiation in the presence of a solution containing **PE-Ph-I** are represented as red traces. The control experiment, in which the maleimide functionalized surfaces have been in contact with the polymer solution without light exposure, are visualized as red dashed lines. **A** and **B**: Results of the first experiment. **C** and **D**: Results for the improved rinsing procedure (refer to text).

4.4 Summary

The herein described results clearly demonstrates the compatibility of photochemistry and the chemistry of highly unpolar polyolefins, *i.e.*, polyethylene. The elevated temperatures required to solubilize polyethylene species in combination with the limited choice of suitable solvents do not prevent the successful synthesis of a photoreactive polyethylene derivative, **PE-Ph**. Furthermore, UV light-induced modification and block copolymer formation are as effective as conventional ambient temperature polymer ligation based on *ortho*-methylbenzaldehydes. In addition, the polymer species received by light-triggered coupling of polyethylene at high temperatures exhibit a robust ligation point that is proven to be stable up to 150 °C. However, the modification of silicon surfaces was not successful since either the APTES coating or the maleimide groups attached to the surface degrade under elevated temperatures.

The presented concept of light-induced polyethylene ligation provides a platform for the synthesis of advanced polyethylene-containing macromolecular architectures utilizing a photochemical pathway. Moreover, the application of PE species during 3D laser lithography and further advanced applications based on light is within reach.

CHAPTER 5

MILD PHOTOCHEMICAL ACTIVATION OF CHLORO OXIMES AND OXIME ESTERS

5.1 Introduction of Photochemical Properties for Chloro Oximes

The demand for shifting the excitation wavelength to higher values in photochemistry is rationalized with the favored application of mild energetic sources. In addition, light with higher wavelengths has a greater penetration depth into soft matter materials in comparison to harsher UV irradiation. On the one hand, as described in **Section 2.3**, pyrene has demonstrated itself as an established chromophore for triggering photochemical transformations in the violet visible light regime between 400 and 450 nm. The facile substitution of phenyl moieties with pyrene units enables a distinct shift of the excitation wavelength of various photoreactive groups including tetrazoles, 2*H*-azirines, acyl sulfides and stilbene derivatives.[357, 422, 426, 427] On the other hand, pyrene as fluorescent probe is extremely useful for the deduction of various properties of polymeric species, *e.g.*, the nature and distance of specific binding sites, or the polarity of the environment of the chromophore. Based on spectroscopic examination, the utilization of pyrene also assists to determine the behavior of polymer chains in solution, such as the critical micelle concentration (CMC) and the lower critical micellization temperature (LCMT).[519]

Parts of the current chapter are reproduced from J. T. Offenloch, S. Bastian, H. Mutlu, C. Barner-Kowollik, *ChemPhotoChem* **2019**, *3*, 66-70 with permission from Wiley-VCH Verlag GmbH & Co. KGaA, Weinheim.

In organic synthesis, chloro oximes are key structures for the generation of nitrile oxides utilized in 1,3-dipolar cycloaddition reactions. The thermally induced reaction of these highly reactive 1,3-dipoles with olefinic substrates and alkyne groups affords 4,5-dihydroisoxazoles (isoxazolines) and isoxazoles, respectively, which play an important role in synthetic reactions due to their transformability into miscellaneous chemical motifs (*e.g.*, hydroxyl ketones,[520] amino alcohols,[521] and themselves).[522, 523] Furthermore, isoxazoline and isoxazole derivatives indicate bioactivity in pharmaceutical and therapeutical fields.[524, 525]

The following sections describe the facile synthesis of a pyrene-substituted chloro oxime, which generate a highly reactive nitrile oxide derivative upon light exposure. Hence the light-induced cycloaddition was investigated with regard to its orthogonality towards various reactive groups enabling a novel approach for the introduction of pyrene as fluorescence marker unit.

5.1.1 Synthesis of the Chloro Pyrene Oxime

Nitrile oxides are commonly generated *via* the rearrangement of chloro oximes in the presence of moderate bases (*e.g.*, $NaHCO_3$ or NEt_3),[522, 526, 527] or metal catalysts (*e.g.*, Cu(I) and Ru(II), in specific cases in combination with bases).[528–530] In addition, elevated temperatures trigger the formation of the 1,3-dipole.[531] In analogy to previously reported red-shifting protocols,[357, 422, 426, 427] the chloro oxime unit was equipped with pyrene as light-harvesting chromophore in order to address the harsh limitations faced during the preparation of nitrile oxides (refer to **Scheme 5.1**).

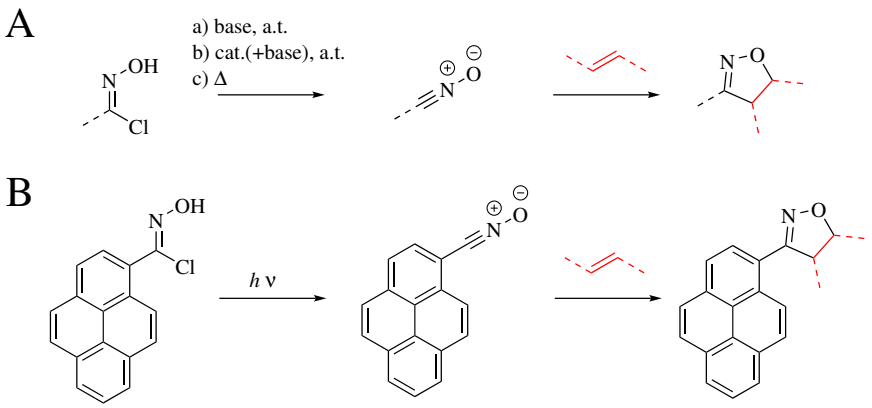

Scheme 5.1. **A**: Conventional methods to generate nitrile oxides for subsequent 1,3-dipolar cycloaddition with dipolarophiles. **B**: Proposed mechanism of the photochemical activation of chloro oximes with the aid of pyrene as chromophore. Adapted with permission from reference [532]. Copyright (2019) Wiley-VCH Verlag GmbH & Co. KGaA, Weinheim.

The pyrene-substituted chloro oxime (**PyOCl**) was synthesized in a two-step procedure including oxime formation in the first step followed by chlorination. Starting from 1-pyrenecarbaldehyde, the aldehyde group was converted into an oxime unit by stirring 1.0 eq. of the pyrene derivative in the presence of 3.0 eq. of each hydroxylamine hydrochloride and sodium acetate in a mixture of DCM and MeOH (1:1) for 24 h at ambient temperature (refer to **Scheme 5.2**). Subsequently, the solvent was removed under reduced pressure, and the residue was dissolved in a mixture of DCM and 1N HCl solution (1:1). The organic phase was separated and washed with 1N HCl solution. Drying over $MgSO_4$ and removal of the solvent afforded the targeted compound without further purification in excellent yields (96 %). The ^{1}H NMR spectrum of the reaction product (refer to appendix **Figure D.1**) indicates complete conversion upon shifting the magnetic resonance of the proton of the aldehyde from 10.70 to 9.15 ppm for the respective oxime derivative. Furthermore, the magnetic resonances associated with the aromatic protons are visible in the range between 8.60 and 8.02 ppm. Concomitantly, the ^{13}C NMR spectrum (refer to appendix **Figure D.2**) indicates a novel magnetic resonance at 149.67 ppm, which is attributed to the carbon atom of the oxime. In contrast, the magnetic resonance stemming from the carbon atom of the aromatic aldehyde at 192.91 ppm is not detectable. A complementary ESI-MS measurement confirms the successful product formation as well (refer to the Experimental Section).

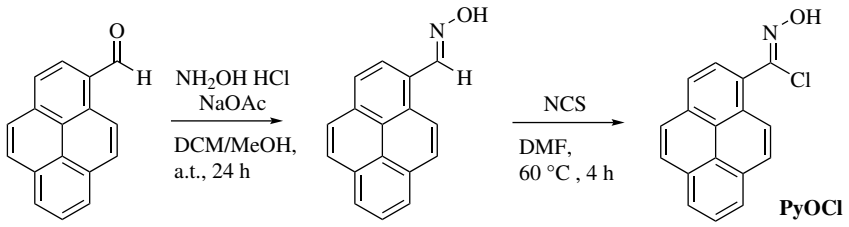

Scheme 5.2. Two step synthesis of **PyOCl**: Starting from 1-pyrenecarbaldehyde, the oxime moiety is generated by employing hydroxylamine and sodium acetate as base. The subsequent treatment with *N*-chlorosuccinimide (NCS) yields the targeted compound, **PyOCl**.

1-Pyrenecarbaldehyde oxime was further converted into the targeted chloro pyrene oxime *via* chlorination with *N*-chlorosuccinimide (NCS). An excess of NCS was avoided in order to prevent substitution of the aromatic structure. Therefore, the pyrene compound was dissolved in DMF followed by the addition of 1.0 eq. of the chlorination agent. The solution was stirred at 60 °C for 4 h. Subsequently, the crude reaction mixture was directly subjected to column chromatography (cyclohexane:DCM = gradient from 3:1 to 1.5:1) affording the product in reasonable yields (44 %). While the ^{1}H NMR spectrum of **PyOCl** in

Figure 5.1 merely shows magnetic resonances between 8.20 and 7.60 ppm stemming from the aromatic pyrenyl protons, the ^{13}C NMR spectrum of the compound in **Figure 5.2** features key information on the structure of the product. The magnetic resonance of the carbon atom of the oxime unit at 149.67 ppm is not detectable anymore. Instead, a singlet at 106.76 ppm is assigned to the carbon atom of the chloro oxime moiety, and the magnetic resonances associated with the aromatic carbon atoms are visible in the area between 132.69 and 123.40 ppm. Importantly, the lack of magnetic resonances at approximately 34 ppm, stemming from a potential fragmentation of the chloro oxime into the nitrile oxide species,[533] underpins the stability of the targeted product in the absence of reaction partners. Additional elemental analysis confirms the successful synthesis of **PyOCl**. The experimentally obtained values (N: 4.69, C: 73.96, H: 3.79) are in good agreement with the theoretical ones (N: 5.01, C: 73.00, H: 3.60), and accordingly, this information excludes the nitrile oxide derivative as possible structure (theoretical values for the nitrile oxide derivative: N: 5.76, C: 83.94, H: 3.73). Further confirmation of the successful synthesis of the targeted compound was obtained *via* ESI-MS measurement (refer to the Experimental Section).

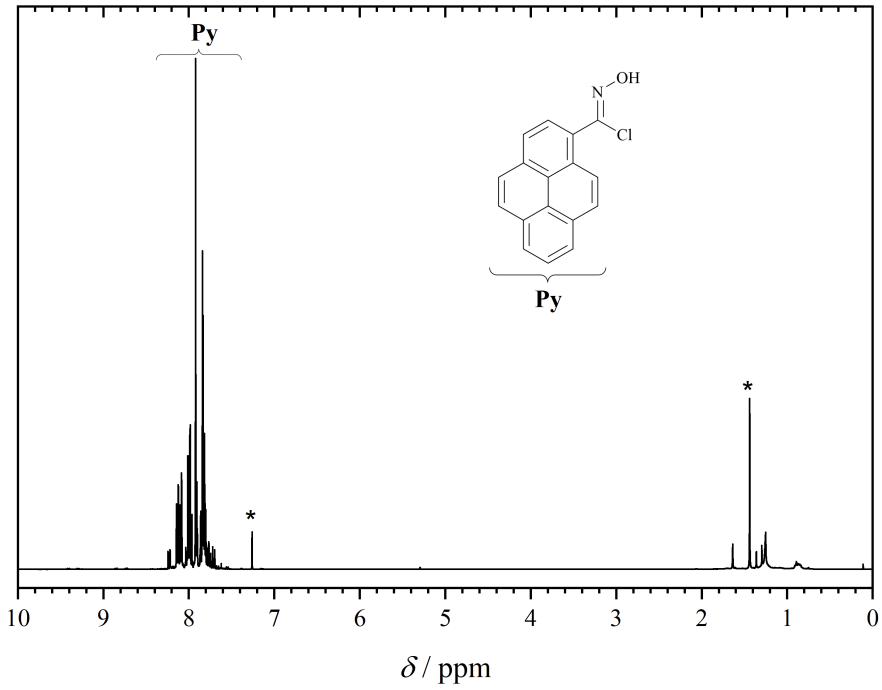

Figure 5.1. ^{1}H NMR spectrum (400 MHz, $CDCl_3$, 298 K) of **PyOCl**. The magnetic resonances marked with an asterisk is assigned to $CHCl_3$ and cyclohexane. Adapted with permission from reference [532]. Copyright (2019) Wiley-VCH Verlag GmbH & Co. KGaA, Weinheim.

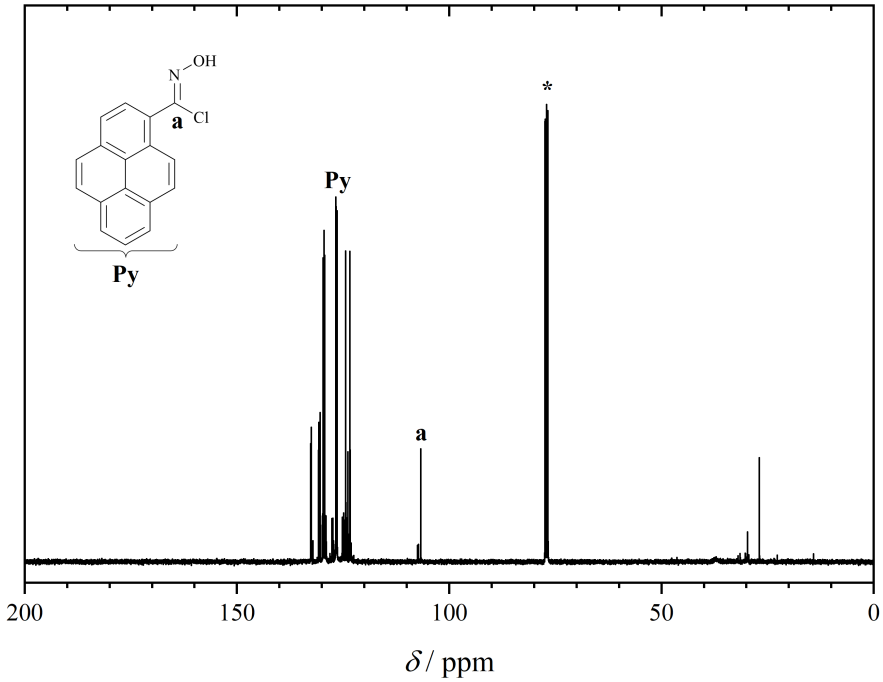

Figure 5.2. ^{13}C NMR spectrum (100 MHz, $CDCl_3$, 298 K) of **PyOCl**. The magnetic resonance marked with an asterisk is assigned to $CHCl_3$. Adapted with permission from reference [532]. Copyright (2019) Wiley-VCH Verlag GmbH & Co. KGaA, Weinheim.

5.1.2 Assessing the Reactivity of the Chloro Pyrene Oxime upon Exposure to Light

As the synthesic route to the chloro pyrene oxime derivative was successfully established, the following task included the extensive evaluation of the behavior of the respective compound upon light exposure. Initially, the influence of the light source – using either an LED setup with an emission wavelength of 410 to 420 nm (3x, 3 W, for the emission spectrum refer to **Figure A.2**) or ambient laboratory light – on the potentially photoreactive pyrene derivative was explored. Therefore, *N*-ethyl maleimide was used as the dienophile for 1,3-dipolar cycloaddition in DCM as solvent. The irradiation of the starting material with the LED setup or ambient light for one hour followed by removal of the solvent resulted in crude reaction mixtures, which were directly analyzed *via* ^{1}H NMR spectroscopy (refer to **Figure 5.3B**). As reference for the light source-dependent reactivity experiments, a comparison between the ^{1}H NMR spectra of **PyOCl** and the purified cycloadduct is presented in **Figure 5.3A**. In the ^{1}H NMR spectrum of the reaction product, the doublets at 5.57 and 5.15 ppm are characteristic magnetic resonances associated with the protons of the generated isoxazoline moiety. Moreover, a magnetic resonance at 9.05 ppm is detectable stemming from the aromatic proton of the pyrene unit, which is in close proximity to the reactive group. As a

consequence, the magnetic resonance of the before mentioned proton is significantly affected during the light-induced reaction. With the idea to compare the impact of the different light sources on the reaction (depicted in **Figure 5.3B**), the ^{1}H NMR data was examined, which revealed the characteristic magnetic resonances associated with the cycloadduct in each case. In fact, the integration of those resonances yields identical results for the experiments with the light sources. Consequently, the comparison between the irradiation sources was repeated with two further dipolarophiles in order to eliminate the influence of the reactivity of the dipolarophile on the reaction. The ^{1}H NMR spectra are presented in **Figures D.3** and **D.4**. The ^{1}H NMR spectra that display the crude reaction mixture after exposure to LED or ambient light, also exhibit perfectly matching integrals of the relevant magnetic resonances (which were identified by the ^{1}H NMR spectra of the purified compounds in **Figures D.9** and **D.13**). As a result, even a low flux of light as ambient laboratory light is adequate to trigger the 1,3-dipolar cycloaddition of the chloro pyrene oxide.

Further reactivity studies entailed control experiments in the absence of any light source. Therefore, 1.0 eq. of **PyOCl** and 0.7 eq. of *N*-ethyl maleimide were dissolved in $CDCl_3$ and a ^{13}C NMR spectrum of the reaction mixture was immediately recorded (refer to **Figure 5.4**). Analogous to the ^{1}H NMR spectra comparing the results of the cycloaddition induced by two different light sources, the two ^{13}C NMR spectra in part A of **Figure 5.4** display the starting material and the purified reaction product. Further in part B, the ^{13}C NMR spectra recorded in the dark or after LED irradiation are presented. The magnetic resonance at 106.76 ppm associated with the carbon atom of the chloro oxime unit represents the relevant feature of the photoreactive group, and therefore, it was assigned as the reference to monitor the process of the reaction. The chloro oxime moiety is present after mixing the reactants as clearly evidenced *via* the detection of the above noted magnetic resonance in the immediately recorded ^{13}C NMR spectrum. After additional 20 minutes in entire darkness at ambient temperature, the magnetic resonance at 106.76 ppm is still detectable (refer to the middle spectrum in **Figure 5.4B**). In contrast, the ^{13}C NMR spectrum, which was recorded after LED irradiation of the same mixture for 20 minutes at ambient temperature, depicts no signal of the magnetic resonance associated with the chloro oxime motif (refer to the bottom spectrum in **Figure 5.4B**). Consequently, the 1,3-dipolar cycloaddition of the chloro pyrene oxime is substantially faster upon light irradiation.

To validate the orthogonality of the light-sensitive moiety towards different reaction partners, the cycloaddition with selected dienophiles shown in **Scheme 5.3** was additionally studied. In particular,

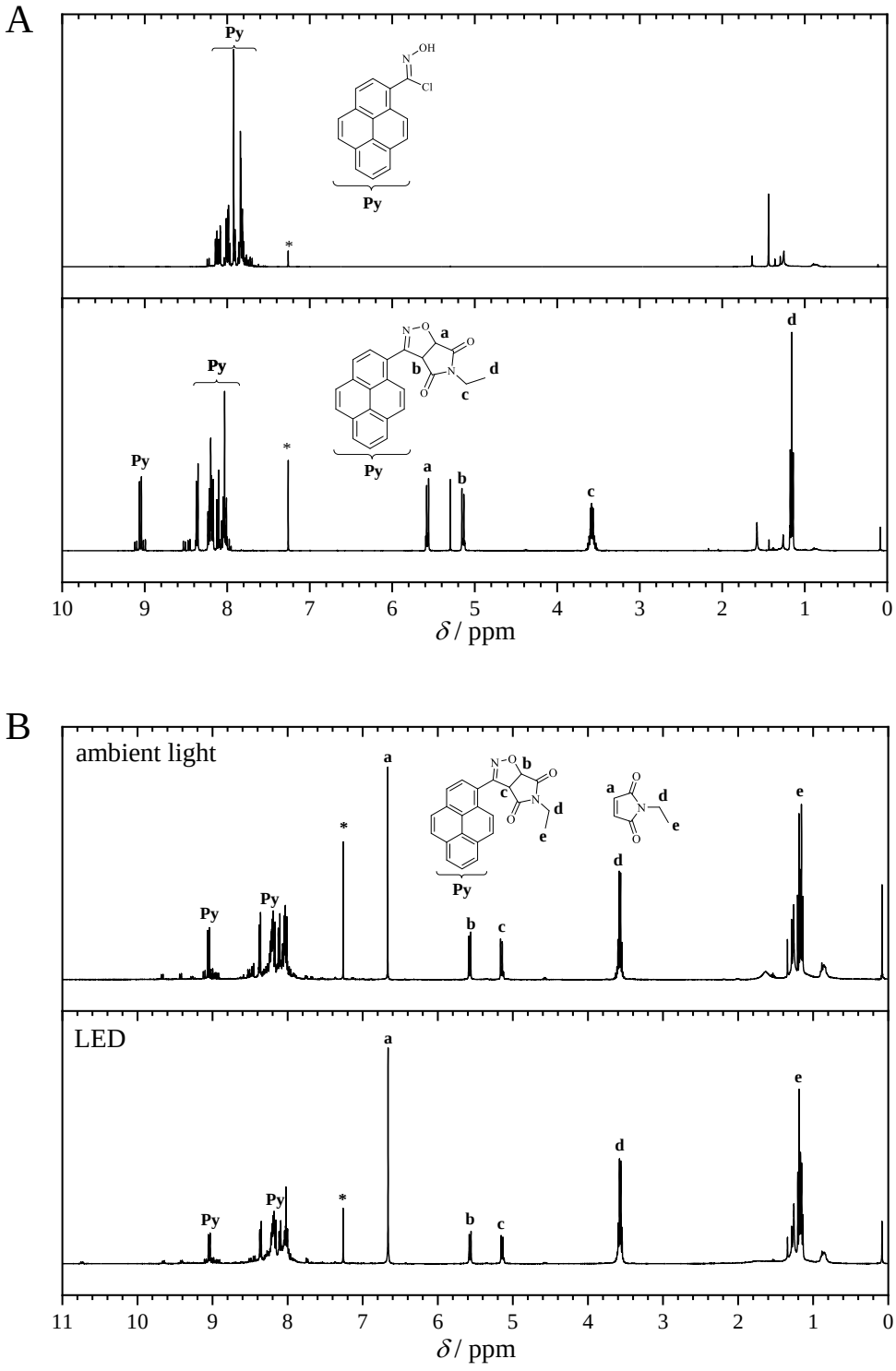

Figure 5.3. **A**: ^{1}H NMR spectra (400 MHz, $CDCl_3$, 298 K) of **PyOCl** (top spectrum) and the purified adduct with *N*-ethyl maleimide (bottom spectrum) as a reference for **B**: Comparison of the ^{1}H NMR spectra (400 MHz, $CDCl_3$, 298 K) of the crude reaction mixtures thereof after exposure to ambient light (top spectrum) or LED irradiation (bottom spectrum). The magnetic resonance marked with an asterisk is assigned to $CHCl_3$. Adapted with permission from reference [532]. Copyright (2019) Wiley-VCH Verlag GmbH & Co. KGaA, Weinheim.

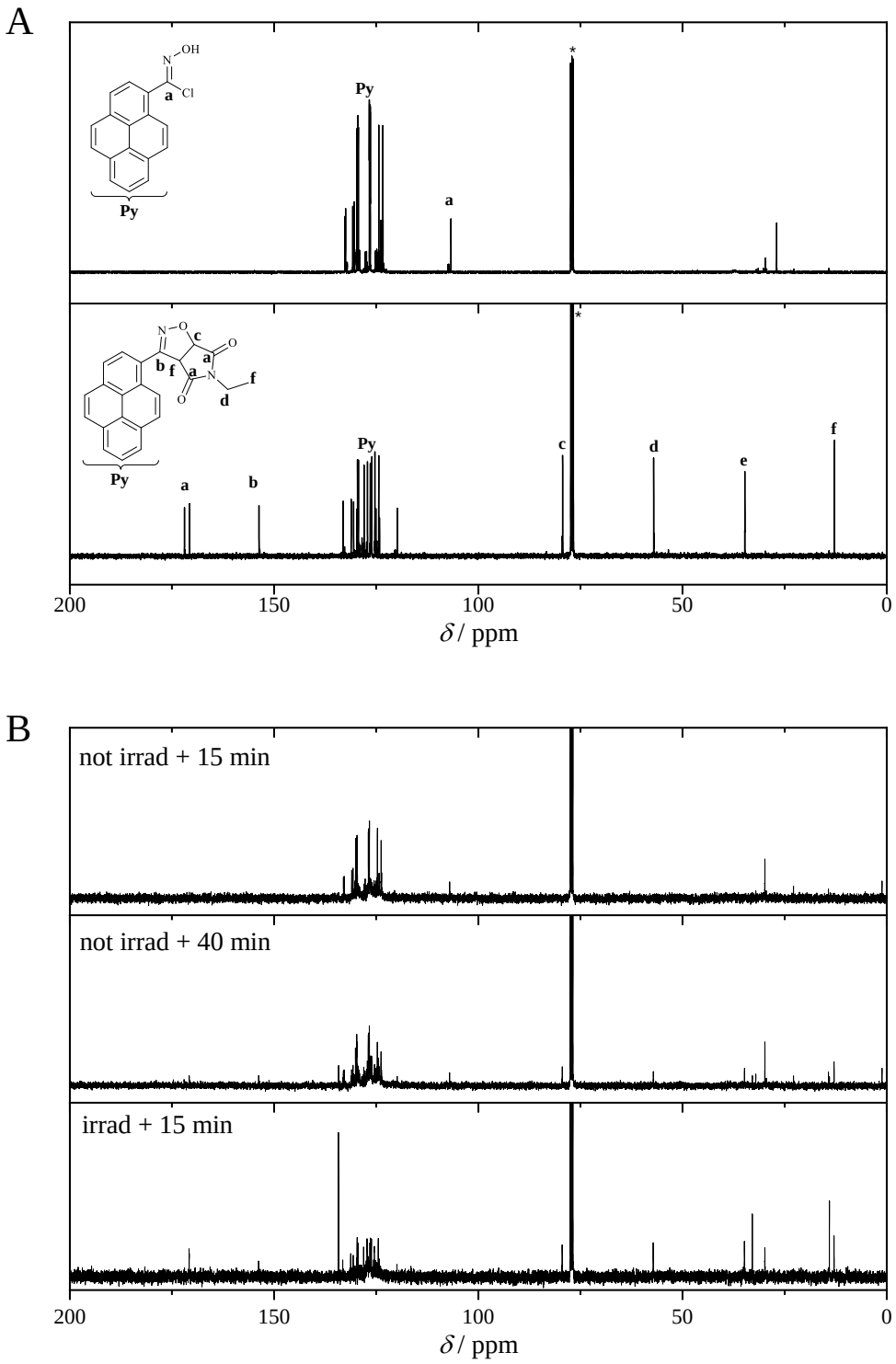

Figure 5.4. **A**: ^{13}C NMR spectra (100 MHz, $CDCl_3$, 298 K) of the **PyOCl** (top spectrum) and the purified adduct with *N*-ethyl maleimide (bottom spectrum) as a reference for **B**: Comparison of the ^{13}C NMR spectra (100 MHz, $CDCl_3$, 298 K) of the crude reaction mixtures thereof after mixing in the absence of light or LED irradiation. The magnetic resonance marked with an asterisk is assigned to $CHCl_3$. Adapted with permission from reference [532]. Copyright (2019) Wiley-VCH Verlag GmbH & Co. KGaA, Weinheim.

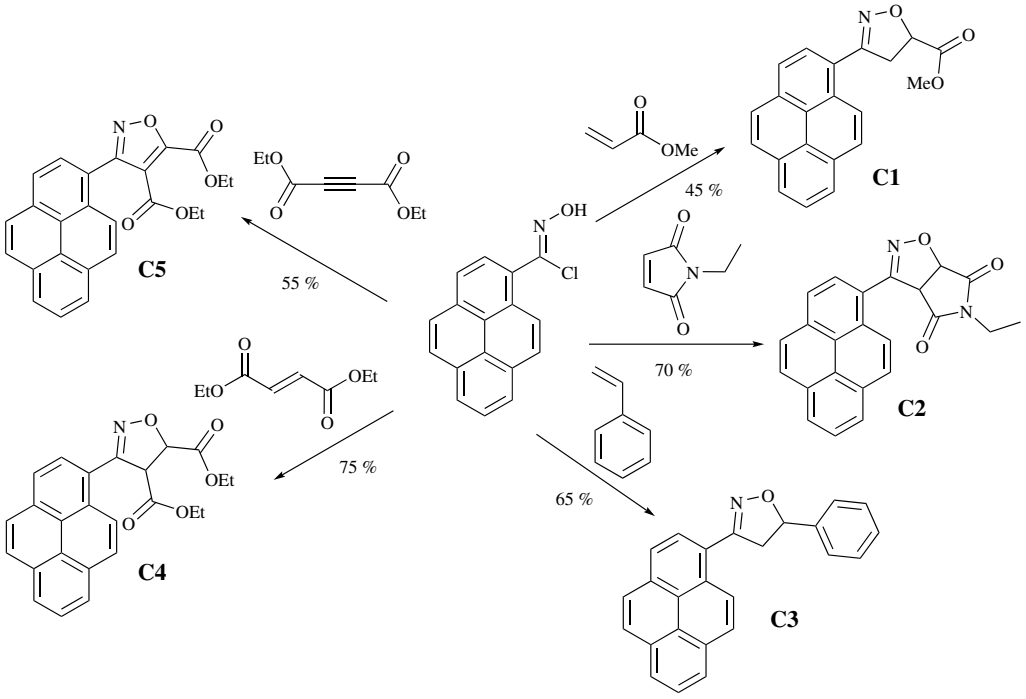

Scheme 5.3. Employed dienophiles and their resulting cycloadducts upon irradiation in the presence of **PyOCl**. The gravimetrically obtained reaction yields after purification are additionally indicated. Adapted with permission from reference [532]. Copyright (2019) Wiley-VCH Verlag GmbH & Co. KGaA, Weinheim.

different electronic and steric properties of olefin moieties and alkyne units potentially have an influence on the cycloaddition reaction. As a result, the range of the dienophilic partners for the light-induced cycloaddition of the pyrene-substituted chloro oxime included methyl acrylate, *N*-ethyl maleimide, styrene, diethyl fumarate and diethyl acetylenedicarboxylate. 1.0 eq. of the photoreactive moiety dissolved in DCM was irradiated in the presence of 5.0 eq. of the olefinic reaction partner. Results of equivalent quality were obtained *via* a constant flux of light, and therefore, an LED setup (410-420 nm) was selected as irradiation source. In the next step, the raw reaction mixtures were purificed *via* column chromatography to yield the respective cycloadducts (refer to **Scheme 5.3**). The united analysis of the ^{1}H and ^{13}C NMR spectra of the reaction products (refer to **Figures D.5** to **D.14** in the Appendix) and the ESI-MS results (refer to the Experimental Section) confirms the successful cycloaddition of each dienophile derivative.

Specifically, enantiostereomeric mixtures were obtained after the cycloaddition with non-symmetric dienophiles (such as methyl acrylate and styrene), considering that a stereocenter is formed in 5-position of the isoxazoline unit. As a result, two doublets at 4.01 ppm for **C1**, and two magnetic resonances at 5.87 and 4.14 for **C3** are distinguishable in the ^{1}H NMR spectra in **Figures D.5** and **D.9**, respectively.

Here, the formed isoxazoline moieties are substituted in 3,5-position, which is in agreement with the reported regioselectivity of nitrile oxides.[534, 535] The ^{1}H NMR spectrum of the irradiated crude reaction mixture containing the chloro pyrene oxime and styrene in **Figure D.4** does not indicate any magnetic resonances attributed to the 3,4-isomer. Consequently, the herein presented light-induced ligation is highly regioselective. Similar to the ^{1}H NMR spectrum of **C2**, the magnetic resonance of the proton in closest proximity to the isoxazoline ring is shifted downfield to 9.21 and 9.30 ppm in the ^{1}H NMR spectra of **C1** and **C3**, respectively. For both cycloadducts, the magnetic resonances associated with the protons of the pyrene unit are detected between 8.26 and 7.99 ppm. In the ^{1}H NMR spectrum of **C3** in **Figure D.9** the phenyl protons are visible as a multiplet in the range of 7.56 to 7.34 ppm, and the singlet stemming from the protons of the methoxy group is present at 3.89 ppm in the ^{1}H NMR spectrum of **C1** in **Figure D.5**. For the cycloadduct **C4**, the magnetic resonances, which are assigned to the protons of the isoxazoline ring, are present at 5.62 and 5.22 ppm in the ^{1}H NMR spectrum in **Figure D.11**. Similar to the ^{1}H NMR spectra of the previously mentioned cycloadducts **C1** and **C3**, the magnetic resonances stemming from the pyrenyl protons are located at 8.84 ppm, and between 8.25 and 8.01 ppm. Additionally, the multiplets between 4.43 and 4.35 ppm, and in the region from 4.05 to 3.95 ppm are assigned to the methylene protons. Concomitantly, the magnetic resonances at 1.41 and 0.87 ppm appear as triplets originating from the protons of the CH_3 groups. In contrast to the ^{1}H NMR spectra of the before discussed cycloadducts **C1** to **C4**, the ^{1}H NMR spectrum of **C5** in **Figure D.13** indicates no distinguishable magnetic resonance for the aromatic proton in the range of 9.00 ppm. Instead, all magnetic resonances associated with the pyrenyl protons appear between 8.28 and 8.03 ppm. Furthermore, the quartets at 4.56 and 4.05 ppm, and the triplets at 1.49 and 0.86 ppm are assigned to the protons of the ethoxy moieties of **C5**.

Subsequently, the optical properties of **PyOCl** and the corresponding cycloadducts were investigated *via* UV/Vis and fluorescence spectroscopy (refer to **Figure 5.5**). Two main absorbances in similar regions of the absorption spectra in **Figure 5.5A** are identified for all molecules in DCM as solvent. While one band is evident between approximately 260 and 300 nm with an absorption maximum at ca. 280 nm, the other band is located in the area of 300 to 400 nm with a maximum between 347 (*e.g.*, **C4**) and 366 nm (*e.g.*, **PyOCl**). Compared to the absorption spectrum of unsubstituted pyrene (refer to **Figure 2.8**), the absorbance values of the currently presented compounds are shifted by 50 nm to higher wavelengths. Based on Beer-Lambert's law in **Equation 2.5**, the molar extinction coefficients ϵ were

calculated (refer to **Figure 5.5B**). Here, an ϵ value of 42000 L mol^{-1} cm^{-1} for 1-pyrenecarbaldehyde oxime is determined. The chloro pyrene oxime and the corresponding cycloadducts exhibit ϵ values between 36000 and 31000 L mol^{-1} cm^{-1}.

Furthermore, the fluorescence spectra were recorded in DCM by employing an excitation wavelength of 344 nm (refer to **Figure 5.5C**). Similar to the emission spectra of non-functional pyrene (refer to **Figure 2.8**), 1-pyrenecarbaldehyde oxime, **C1** and **C3** indicate a narrow emission band between 380 to 460 nm with an emission maximum at ca. 415 nm. In contrast, the fluorescence emission of **C2** and **C4** is broader by approximately 20 nm extending to higher wavelengths, and indicating an emission maximum at around 422 nm. However, the emission spectrum of the photoreactive species has a strong tailing. In this instance, fluorescence emission is detected up to 550 nm. Surprisingly, the intensity of the fluorescence in the emission spectra of **C5** is remarkably low, whereas the reason for the latter remains unclear.

In addition to the reactivity study towards small molecules, the photoinduced cycloaddition of **PyOCl** was applied in post-polymerization modification functionalization of polymer chain termini (refer to **Scheme 5.4**). Due to the elaborate purification methods present in the synthesis of polymer-based materials, the criteria for polymer modification reactions are strict. Therefore, chemical reactions in polymer science presents an excellent measure to indicate the effectiveness of transformations. For quantitative analysis, sensitive detection methods are required including ESI-MS measurements. Due to its high ionization ability in the ESI process, poly(ethylene glycol) (PEG) was selected as the polymer for end group post-polymerization modification. Moreover, a broad variety of commercially available PEG derivatives coupled to distinct functional units exists. Consequently, 1.0 eq. of a commercially available maleimide-terminated PEG polymer **P1** as well as a synthesized pentene-capped species **P2** with potentially lower reactivity towards 1,3-dipoles were added to a solution containing 5.0 eq. of **PyOCl** in DCM, and the reaction mixtures were irradiated with the LED setup for 4 hours. The crude reaction mixtures were directly analyzed *via* ESI-MS, while for ^{1}H NMR analysis **PC1** was precipitated twice in ice-cold diethyl ether.

The full ESI-MS spectra including zoom-ins are presented in **Figure 5.6** for **P1** and **PC1**, and in **Figure D.15** for **P2** and **PC2**. For all four polymeric species, the experimental *m/z*-values perfectly match with the theroetical ones (with $\Delta m/z$-values between 0.0000 and 0.0009, refer to appendix **Table D.1**), revealing the successful (light-induced) preparation of **P2**, **PC1** and **PC2**. Whereas the ESI-MS spectrum of the

A

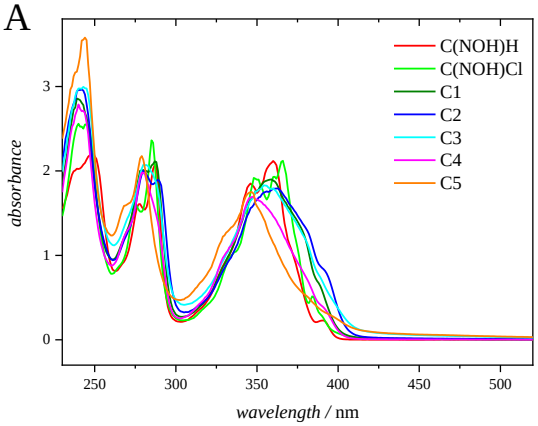

B

Species	$\lambda_{abs.max}$ / nm	ε / L mol^{-1} cm^{-1}
C(NOH)H	360	42000
	346	
	287	
	278	
C(NOH)Cl	366	36000
	348	
	285	
	275	
C1	359	35000
	287	
	280	
C2	363	32000
	289	
	280	
C3	354	33000
	280	
C4	347	31000
	279	
C5	347	32000
	279	

C

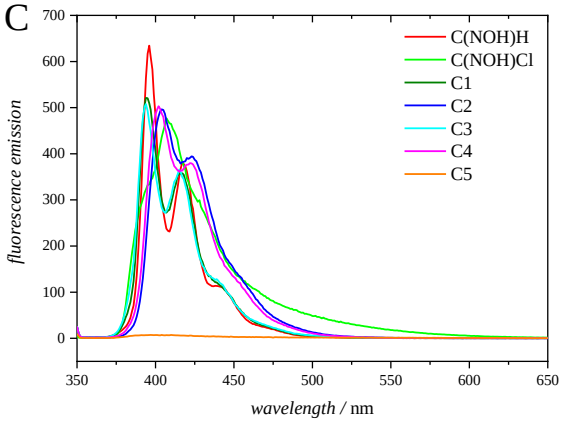

D

Species	$\lambda_{em.max}$ / nm
C(NOH)H	417
	396
C(NOH)Cl	407
C1	417
	394
C2	423
	404
C3	415
	394
C4	422
	394
C5	-

Figure 5.5. A: UV/Vis spectra of 1-pyrenecarbaldehyde oxime, **PyOCl** and the small molecule adducts **C1** to **C5** in DCM at ambient temperature (c = 4.52·10^{-5} mmol mL^{-1}). **B**: Corresponding table with the absorption maxima $\lambda_{abs.max}$ and the molar extinction coefficient ϵ. **C**: Fluorescence spectra ($\lambda_{exc.}$ = 344 nm) of **PyOCl** and the small molecule adducts **C1** to **C5** in DCM at ambient temperature (c = 1.13·10^{-5} mmol mL^{-1}). **D**: Corresponding table displaying $\lambda_{em.max}$. Adapted with permission from reference [532]. Copyright (2019) Wiley-VCH Verlag GmbH & Co. KGaA, Weinheim.

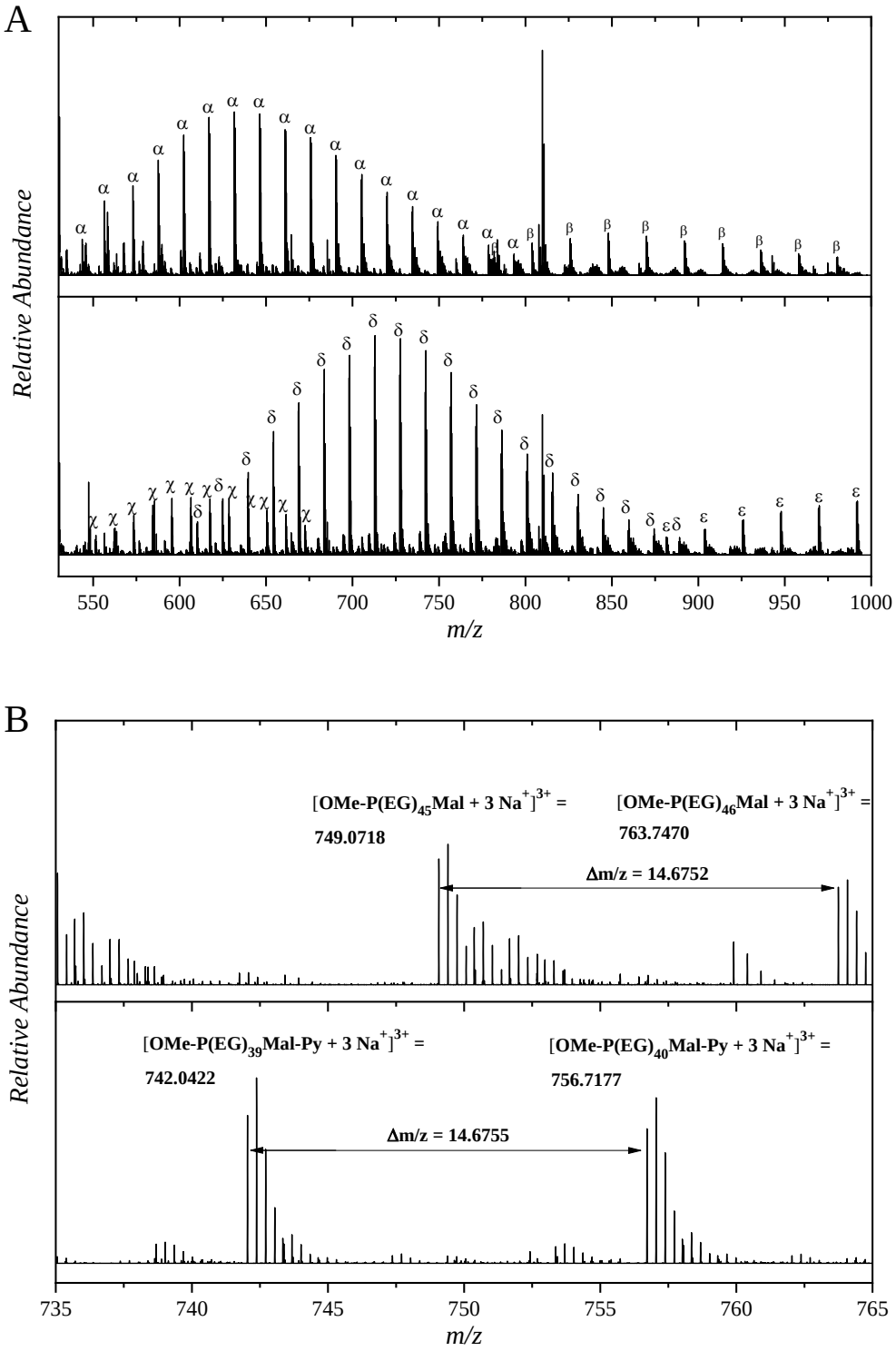

Figure 5.6. **A**: Full ESI-MS spectrum of **P1** and **PC1**. Tripel- and four-times-charged species are identified for **P1** (α: triple-charged, β: four-times-charged), whereas double-, tripel- and four-times-charged polymer distributions are visible for **PC1** (χ: double-charged, δ: triple-charged, ϵ: four-times-charged). **B**: Zoom-in into the tripel-charged species of the ESI-MS spectra of **P1** and **PC1**. Adapted with permission from reference [532]. Copyright (2019) Wiley-VCH Verlag GmbH & Co. KGaA, Weinheim.

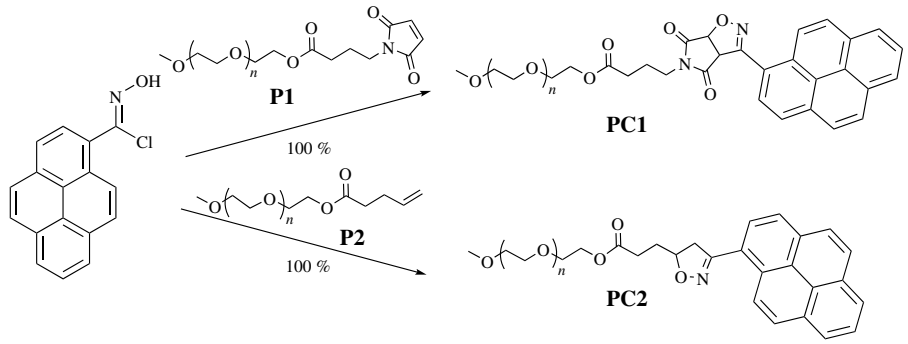

Scheme 5.4. Light-induced end group modification of two functional poly(ethylene glycol) derivatives. The conversion was determined *via* ESI-MS measurements. Adapted with permission from reference [532]. Copyright (2019) Wiley-VCH Verlag GmbH & Co. KGaA, Weinheim.

maleimide-terminated PEG species in **Figure 5.6A** indicates two polymer distributions (α: triple-charged, β: four-times-charged), the ESI-MS spectrum of **PC1** shows three differently charged polymer species (χ: double-charged, δ: triple-charged, ϵ: four-times-charged). All main distributions are ionized by sodium cations as counter ion. Therefore, the tendency for lower charged species of the modified polymeric species is caused by the pyrene unit, which has a low ionization ability with sodium ions. The enlargement of the ESI-MS spectrum in **Figure 5.6B** displaying the triple-charge species reveals $\Delta m/z$-values, which perfectly match with the theoretical value of the repeating unit ($\Delta m/z_{\text{theo.}}$ =14.6754) for both **P1** and **PC1**. Importantly, no residual ions stemming from **P1** are detectable in the enlargement of the ESI-MS spectrum of **PC1**. Since the ionization ability of the starting material and the modified polymeric species are expected to be comparable, the maleimide end group was fully converted during the photoreaction.

The ESI-MS spectrum of **P2** in **Figure D.15A** depicts three differently charged polymer distributions (ϕ: double-charged, γ: triple-charged, η: four-times-charged), while merely double(ι)- and triple(κ)-charged species are identified in the spectrum of **PC2**. Similar to the ESI-MS analysis of **P1** and **PC1**, the pyrene unit suppresses the higher charged species of **PC2**. The evaluation of the enlargement of the ESI-MS spectra of **P2** and **PC2** proceeds analogous to the preceding polymer sample **P1** and **PC1**. The experimentally obtained $\Delta m/z$-values (**P2**: $\Delta m/z$ =14.6756, **PC2**: $\Delta m/z$ =14.6752) perfectly match with the theoretical value of the repeating unit ($\Delta m/z$ =14.6754), and no residual signals of **P2** are visible in the ESI-MS spectrum of **PC2**. In the presented case, full conversion was obtained as well. Moreover, it can be assumed that even less activated double bonds are suitable reaction partners for the light-induced post-polymerization modification of polymeric species with **PyOCl**.

Complementary to ESI-MS analysis, **PC1** was characterized *via* ^{1}H NMR spectroscopy (refer to appendix **Figure D.16**). In agreement to the ^{1}H NMR spectrum of the small molecule adduct **C2** in **Figure D.7**, the ^{1}H NMR spectrum of the end group modified polymeric species yields magnetic resonances associated with the protons of the isoxazoline ring at 5.63 and 5.26 ppm in addition to the magnetic resonances between 8.46 and 8.02 ppm, which are assigned to the protons of the pyrene moiety. The aromatic proton which is influenced most during the photoreaction is distinguishable as a doublet at 9.11 ppm. Moreover, no magnetic resonances in the area between 7.00 and 6.00 ppm stemming from the olefinic protons of the maleimide end group are detectable. Furthermore, the protons of the polymer backbone are visible as a broad magnetic resonance at 3.65 ppm. As a result, the analysis of the ^{1}H NMR spectrum also confirms the successful end group modification of **PC1**.

Next, the light-induced cycloaddition of **PyOCl** was further tested with a maleimide-functionalized biotin compound (biotin-mal) as a representative for a biologically relevant derivative, which features the most complex chemical structure of all tested dienophiles. For solubility reasons, the photoreaction was performed in a mixture of DCM and DMSO (1:1), and an equimolar amount of reactants was employed. Similar to the preceding experiments, the reaction mixture was irradiated with the LED setup (410-420 nm) for one hour. After removal of the solvent, residual **PyOCl** was dissolved in DCM and subsequently removed from the insoluble cycloadduct. The ^{1}H NMR spectra of the pyrene-modified biotin compound and biotin-mal are depicted in **Figure 5.7**. The magnetic resonances of the protons of the isoxazoline ring as representative signal for a successful photo-induced cycloaddition are visible as doublets at 5.75 and 5.62 ppm. Furthermore, the multiplet in the region between 8.50 and 8.10 ppm and the separate doublet at 8.74 ppm can be correlated with the protons of the pyrene moiety. Moreover, no magnetic resonance associated with the olefinic protons of the maleimide is detected. Instead, side products are obtained, which are formed by the addition of water to the maleimide group, and the latter cause the appearance of three new magnetic resonances at 7.25, 7.12 and 6.99 ppm. As a result, the analysis of the ^{1}H NMR spectrum unambiguously evidence the successful photoaddition of **PyOCl** and biotin-mal, a paradigm for a complex dienophile.

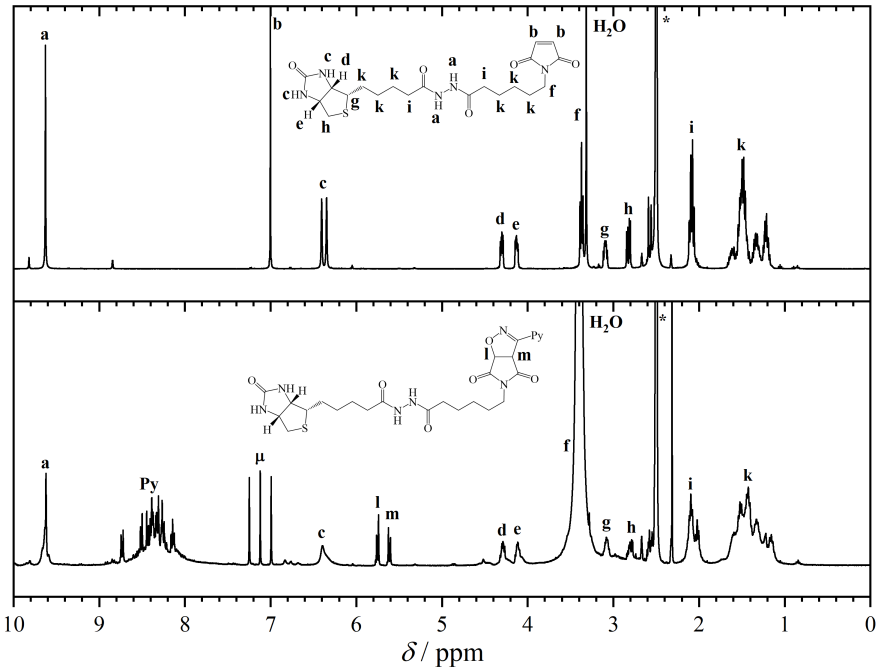

Figure 5.7. ^{1}H NMR spectra (400 MHz, DMSO, 298 K) of biotin-mal (top spectrum) and of the cycloadduct of biotin-mal and **PyOCl** (bottom spectrum). The presence of water in the commercially available product of biotin-mal causes addition to the olefin group of the maleimide during photoactivation of **PyOCl**. The magnetic resonances stemming from the side reaction are marked with μ. The magnetic resonance marked with an asterisk is assigned to DMSO. Adapted with permission from reference [532]. Copyright (2019) Wiley-VCH Verlag GmbH & Co. KGaA, Weinheim.

5.2 Visible Light-Induced Fragmentation of Oxime Esters

Since the photochemistry of oxime ester (also referred to *O*-acyl oxime) was first reported in the beginning of the 20th century,[536] its fragmentation into radicals *via* Norrish Type I reaction or in bimolecular photoinitiator systems was examined in detail and utilized to initiate polymerizations by photochemical means.[537–541] *O*-acyl oxime derivatives have found further application in polymer science as photodegradable units. Indeed, Delzenne *et al.* reported polymeric species possessing oxime ester groups as degradable pendant functionality.[539] Moreover, in practical applications Reichmanis and colleagues investigated the potential of this kind of polymers as positive-type photoresists.[542] For advanced application including tissue engineering and coatings, the initiation of polymerizations with visible light is highly advantageous.[543–545] Indeed, by the judicious choice of substituents, the excitation wavelength of the homolytic cleavage of oxime esters can be adjusted in a facile fashion. However, the commercially available OXE 1 and OXE 2 initiators have been the first examples of photoreactive moieties, for which an in-depth study revealed that the plot of educt conversion *vs.* wavelengths at a constant photon (*i.e.*, the so-called action plot) count does not follow the absorption spectrum.[388] As a result, the red-shifting of the trigger-wavelength of photoreactive moieties is not a trivial task as it may seem.

The following subsections underpin the outstanding properties of pyrene as light-harvesting group in the visible light regime by designing a novel oxime ester, which is conjugated with a pyrene unit. Specifically, a straightforward reaction platform for the radical fragments of the oxime ester moiety is presented, namely radical coupling for intramolecular polymer crosslinking as indicated *via* SEC and diffusion-ordered spectroscopy (DOSY) NMR experiments.

5.2.1 The Design of a Visible Light-Cleavable Monomer

In order to incorporate the pyrene-substituted oxime ester motif into the polymer backbone, a synthetic procedure for a novel styrene derivative substituted with the photolabile group was proposed (refer to **Scheme 5.5**). The synthesis comprised two steps including oxime formation and subsequent esterification reaction.

The preparation of 1-pyrenecarbaldehyde oxime was performed according to the procedure described in **Section 5.1**. The following step entailed esterification reaction between the hydroxyl group of the oxime and 4-vinylbenzoic acid in order to introduce the polymerizable olefin moiety. Therefore, 1.0 eq. of

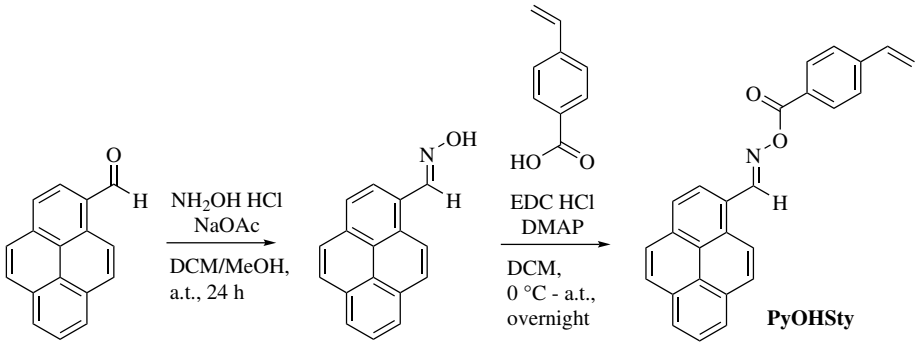

Scheme 5.5. Two-step synthesis of a novel styrene derivative functionalized with a photolabile pyrene-substituted oxime ester (**PyOHSty**). The pyrene-substituted oxime is received *via* the reaction between hydroxylamine hydrochloride and 1-pyrenecarbaldehyde by employing sodium acetate as base. Subsequently, facile esterification reaction with 4-vinylbenzoic acid grants access to the targeted compound.

1-pyrenecarbaldehyde oxime, 1.1 eq. of the styrene derivative and DMAP as catalyst were dissolved in a mixture of DCM and THF (1:1). After cooling to 0 °C, 1.2 eq. of EDC·HCl as coupling agent were added, and subsequently the reaction mixture was stirred at ambient temperature overnight. The solvent was removed under reduced pressure, and the residue was dissolved in DCM. Afterwards, the organic phase was washed with sat. $NaHCO_3$, 1H HCl, water and brine, and dried over $MgSO_4$. The removal of the solvent afforded the crude product, which was further purified *via* column chromatography (cyclohexane: DCM = 1:4). Thereafter, the targeted compound (**PyOHSty**) was isolated in excellent yields (95 %), and its structural composition was confirmed *via* NMR spectroscopy (refer to **Figures 5.8** and **5.9**). In the ^{1}H NMR spectrum in **Figure 5.8**, a characteristic magnetic resonance associated with the aldehyde proton can be identified at 9.55 ppm, and the protons of the olefin unit give rise to magnetic resonances at 6.81, 5.93 and 5.45 ppm. Furthermore, the magnetic resonances at 8.76 and 8.62 ppm and in the range between 8.29 and 8.05 ppm are assigned to the aromatic pyrenyl protons, whereas the doublets associated with the protons of the phenyl unit are detectable at 8.19 and 7.56 ppm. Concomitantly, the ^{13}C NMR spectrum in **Figure 5.9** indicates a characteristic magnetic resonance for oxime units at 164.06 ppm. Moreover, the magnetic resonances stemming from the carbon atoms of the double bond are located at 136.13 and 117.07 ppm.

Consequently, the optical properties of **PyOHSty** were explored, which are displayed in **Figure 5.10**. Herein, the absorption spectrum in DCM indicates a broad absorption band in the region between 320 and 420 nm with two maxima at 365 and 395 nm. In comparison to the UV/Vis spectrum of non-functionalized pyrene in **Figure 2.8** and of **PyOCl** in **Figure 5.5**, the absorption band of **PyOHSty** is red-shifted by

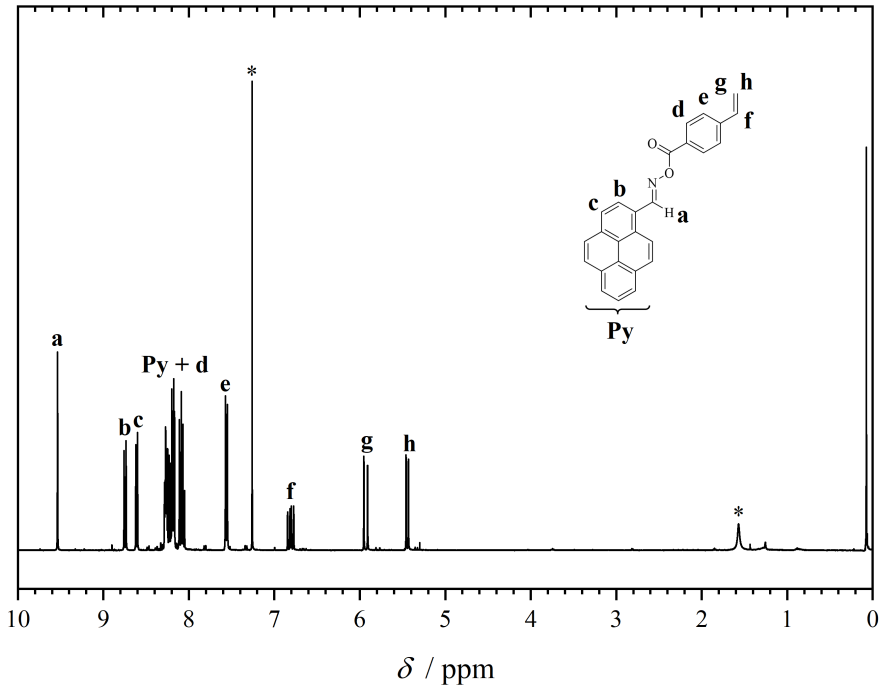

Figure 5.8. ^{1}H NMR spectrum (400 MHz, $CDCl_3$, 298 K) of **PyOHSty**. The magnetic resonance marked with an asterisk is assigned to $CHCl_3$.

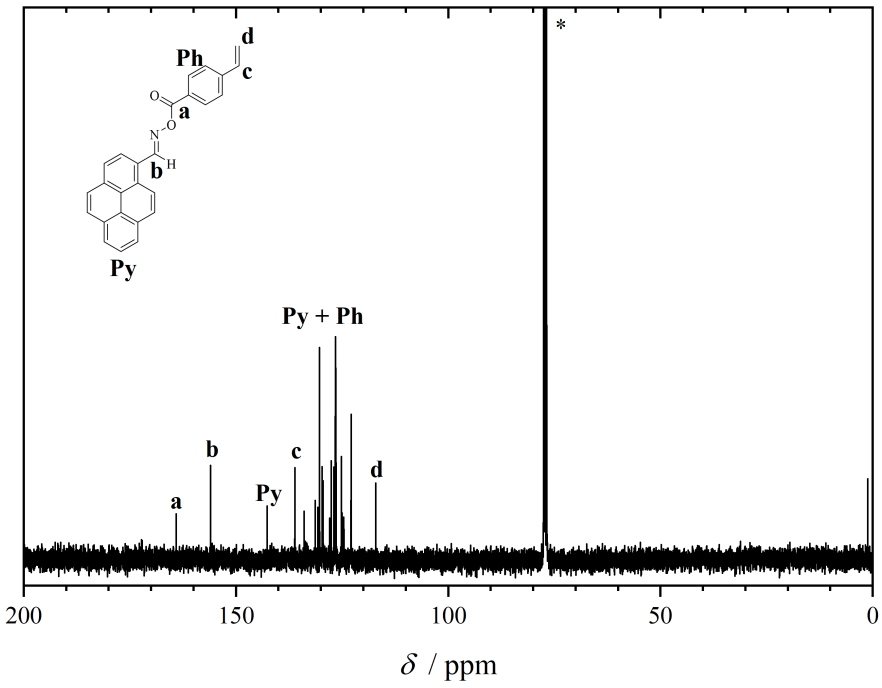

Figure 5.9. ^{13}C NMR spectrum (100 MHz, $CDCl_3$, 298 K) of **PyOHSty**. The magnetic resonance marked with an asterisk is assigned to $CHCl_3$.

approximately 70 nm and 20 nm, respectively. Since the wavelength-dependent reactivity screening of photoreactive groups reveals either a congruent evolution of photochemical reactivity and absorption, or a shift of the reactivity to higher wavelengths,[31] it is anticipated that wavelengths between 400 to 450 nm might be suitable to trigger the fragmentation of **PyOHSty**. The molar extinction coefficients of the absorption maxima lie between 60.000 and 160.000 L mol^{-1} cm^{-1}. Upon excitation with a wavelength of 344 nm, **PyOHSty** emits fluorescence between 400 and 520 nm with a maximum at 409 nm (refer to **Figure 5.10C**). In contrast, the fluorescence of non-functionalized pyrene moieties is detected between 380 and 440 nm, and compared to the preceding photoreactive moiety, the chloro pyrene oxime, any reasonable tailing of the emission is noticable in the spectrum of the monomer derivative.

A

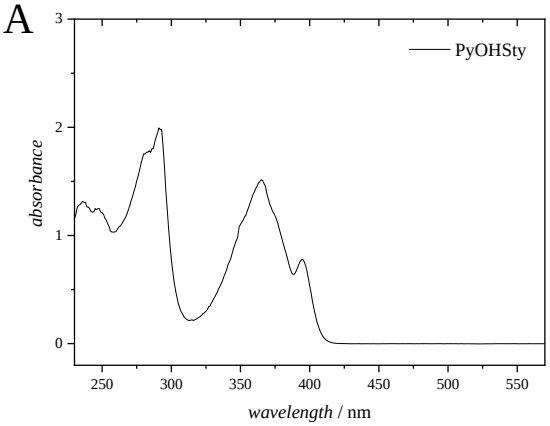

B

Species	$\lambda_{abs.max}$ / nm	ε / L mol^{-1} cm^{-1}
PyOHSty	395	63.000
	365	120.000
	291	160.000

C

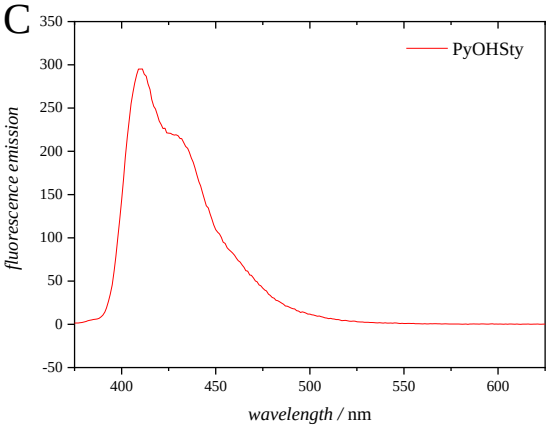

D

Species	$\lambda_{em.max}$ / nm
PyOHSty	409

Figure 5.10. **A**: UV/Vis spectrum of **PyOHSty** in DCM at ambient temperature (c = 1.23·10^{-5} mmol mL^{-1}). **B**: Corresponding table with the absorption maxima $\lambda_{abs.max}$ and the molar extinction coefficient ϵ. **C**: Fluorescence spectrum ($\lambda_{exc.}$ = 344 nm) of **PyOHSty** in DCM at ambient temperature (c = 3.98·$^{-7}$ mmol mL^{-1}). **D**: Corresponding table displaying $\lambda_{em.max}$.

5.2.2 Copolymerization of the Light-Sensitive Monomer and Irradiation Experiments

Inter- or intramolecular crosslinking reactions of polymer chains accompanied with changes in the hydrodynamic volume can be readily detected by SEC, dynamic light scattering (DLS) or DOSY NMR measurements. Therefore, molar masses exceeding 10.000 g mol^{-1} using reversible-deactivation radical polymerization techniques were targeted in order to display potential changes in hydrodynamic radii of well-defined polymer chains in solution. Styrene as comonomer facilitates the homogeneous incorporation of distinct monomer units due to its similar structure and hydrophobic character compared to **PyOHSty**. Consequently, cumyl dithiobenzoate (**CDB**) was selected as chain transfer agent (CTA), since it enables the access to high molar masses for the RAFT polymerization of styrene (refer to **Scheme 5.6**).[546] As the solubility of **PyOHSty** is limited in styrene, *o*-chlorobenzene utilized as solvent. In summary, the polymerization conditions are depicted in **Table 5.1**.

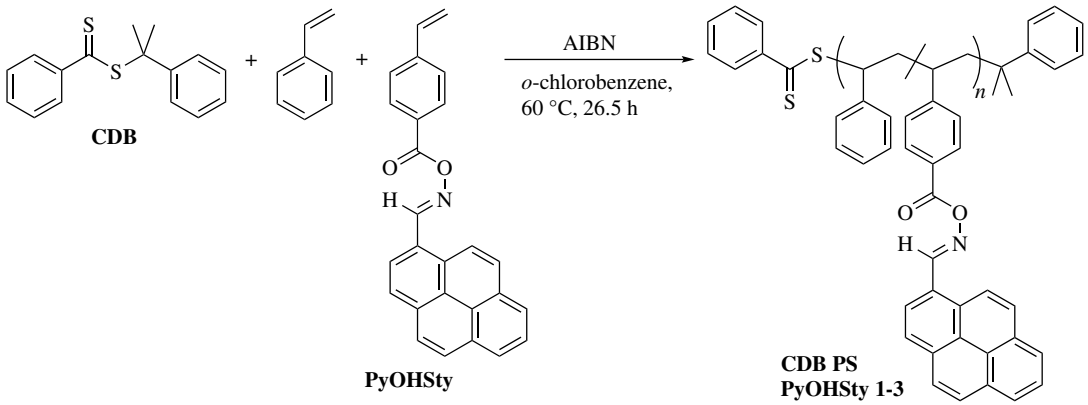

Scheme 5.6. RAFT copolymerization of styrene and **PyOHSty** by employing cumyl dithiobenzoate (**CDB**) as chain transfer agent. The initiation step proceeds thermally *via* fragmentation of AIBN, and *o*-chlorobenzene is required for solubilizing **PyOHSty** during the polymerization process.

In detail, 1.0 eq. of azobisisobutyronitrile (AIBN) and 4.0 eq. of **CDB** were dissolved in 3.00 g of destabilized styrene (3154 eq.). For a conventional RAFT polymerization, the concentration ratio of CTA to initiator is quite low. However, preliminary polymerization experiments suggested to employ higher amounts of initiator due to the observation that pyrene-functional monomers inhibit polymerization processes. Furthermore, the quantity of **PyOHSty** was varied for the distinct polymerization procedures in order to investigate the influence of the concentration of the photoreactive moiety along the polymer backbone upon irradiation. Consequently, either 146.0, 88.0 or 30.0 eq. of the pyrene-containing monomer were added to the polymerization mixture followed by degassing with argon for 30 min. Each polymer-

ization reaction was conducted at 60 °C for 26.5 h, and quenched *via* cooling with liquid nitrogen. The final polymer derivatives were purified *via* precipitation in ice-cold methanol. The higher the amount of **PyOHSty**, the more times a polymeric species required to be precipitated due to the fact that the light-sensitive monomer is merely poorly soluble in methanol. In average, the polymer samples were precipitated three times in order to remove residual unreacted monomer. In summary, the results of the polymerization procedures are presented in **Table 5.1**.

Table 5.1. Summary of the results of the RAFT-mediated copolymerization of **PyOHSty** using **CDB** as chain transfer agent. Every polymerization reaction was conducted at 60 °C for 26.5 h utilizing *o*-chlorobenzene as solvent. $M_{n,\,SEC(THF)}$ was calculated by employing a PS calibration.

Species	**AIBN:CTA:Sty:PyOHSty**	**yield /** g	$M_{n,\,SEC(THF)}$ / g mol^{-1}	$Đ$
1	1:4:3154:146	0.45	17.000	1.22
2	1:4:3154:88	0.35	12.000	1.15
3	1:4:3154:30	0.30	13.000	1.20

The SEC results of the isolated polymer derivatives based on a polystyrene (PS) calibration in **Table 5.1** and the SEC traces in **Figure 5.12** suggest a good control over the polymerization processes. The values for $Đ$ lie between 1.15 and 1.22, indicating narrow distributions of molar masses, which present a precondition for successful RDRP processes. Furthermore, $M_{n,\,SEC(THF)}$ values lie in the range of 17.000 to 12.000 g mol^{-1}, which are suitable to monitor inter- or intramolecular crosslinking reactions upon light-induced fragmentation of the oxime ester moieties *via* SEC, DLS or DOSY NMR. The analysis of the ^{1}H NMR spectra in **Figures 5.11**, **D.17** and **D.18** indicates characteristic magnetic resonances associated with the protons of the phenyl moiety of the polymer backbone between 7.40 and 6.20 ppm, as well as magnetic resonances in the area of 2.30 and 1.20 ppm, which stem from the polystyrene backbone. In addition, an indicator for pyrene moieties tethered to a polymeric species is the presence of broad magnetic resonances between 8.80 and 7.50 ppm. Specifically, the magnetic resonance assigned to the proton of the aldehyde unit is detectable between 9.60 and 9.20 ppm.

With the successful copolymerization of **PyOHSty**, the behavior of the light-sensitive polymer derivatives **CDB PS PyOHSty 1** to **3** upon light irradiation was examined. To avoid crosslinking and therefore solubility issues, the copolymers were dissolved in DCM under highly diluted conditions (c = 0.02 mg mL^{-1}). It is well known that the fragmentation process of oxime ester results in the generation

of radical species, therefore the polymer solutions were deoxygenated *via* purging with argon in order to avoid the formation of any peroxy derivatives. Subsequently, the dissolved polymeric species were irradiated with an LED setup (430-435 nm, 3 × 3 W, refer to **Figure A.2** for the emission spectrum) for 2.5 h. Small molecule fragments, which result from the photolysis reaction, were removed *via* precipitation in ice-cold methanol before further analysis.

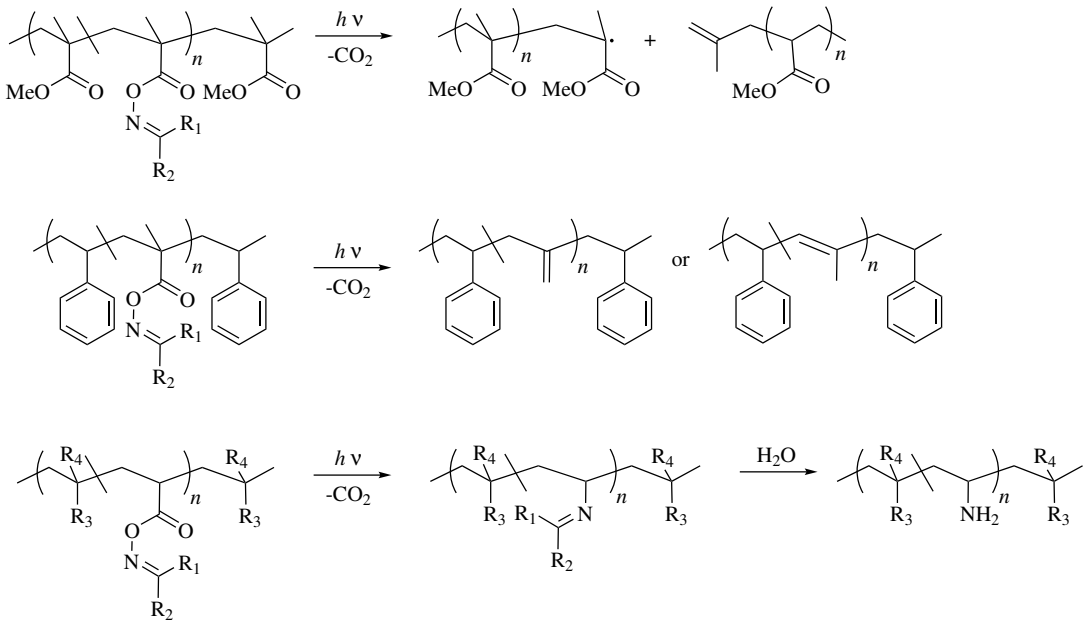

Scheme 5.7. The process of the light-induced fragmentation of oxime ester units along a polymer backbone depends on the structural environment of the reactive group. Whereas the irradiation of *O*-methacryloyl oximes species tethered to PMMA derivatives mainly affords chain scission (top row),[539, 547, 548] olefinic groups are predominantly obtained when the same oxime unit is incorporated into a polystyrene backbone.[549] However, *O*-acryloyl oxime moieties release CO_2 upon light exposure affording imine species after radical coupling, which can be cleaved *via* hydrolysis (R_1,R_2 = aliphatic or aromatic substituents, R_3,R_4 = styrene or methyl methacrylate).[550, 551]

Prior to the discussion of the results, which are obtained after the irradiation of the currently presented polymeric derivatives, selected literature studies need to be reviewed. Indeed, the light-induced fragmentation of oxime ester units along a polymer chain is an in-depth studied process (refer to **Scheme 5.7**).[547–550, 552] For example, *O*-methacryloyl oximes groups incorporated into a methyl methacrylate backbone are able to initiate graft polymerization upon light irradiation, or degrade in the absence of monomers.[539] The degradation mechanism starts with the release of CO_2 generating a tertiary radical in the polymer backbone. Subsequent bond scission results in two polymer derivatives: One species is equipped with an unsaturated chain end, and the radical species is located at the termini of the other chain.[547, 548] Furthermore, copolymers containing *O*-methacryloyl oxime and styrene units are more

stable when they are exposed to light since in this case main chain radicals prefer to abstract hydrogen atoms of methyl groups or methylene units in the polymer backbone instead of chain scission. As a result, double bonds are predominantly formed, which provide characteristic broad magnetic resonances at approximately 4.40 ppm in ^{1}H NMR spectra.[549] In contrast, the irradiation of pendant *O*-acryloyl oxime moiety followed by hydrolysis provides amino-functional copolymers.[550, 551]

Switching the focus to the current study, the comparison of the ^{1}H NMR spectra in **Figures 5.11** and **D.17** clearly indicates a substantially reduced intensity of the magnetic resonances associated with the pyrene moiety between 8.80 and 7.50 ppm after the irradiation of the polymer derivatives. The broad magnetic resonance of the aldehyde proton between 9.60 and 9.20 ppm is not detectable anymore as well. In contrast, the polystyrene backbone remains intact as evidenced by magnetic resonances between 7.40 and 6.20 ppm and in the area of 2.30 to 1.20 ppm. Hence, the evaluation of the ^{1}H NMR spectra confirms the fragmentation of the light-sensitive monomer unit along the polymer chain, and in addition, a subsequent combination of an iminyl and a carboxyl or phenyl radical species as main process after light-induced bond cleavage can be excluded.

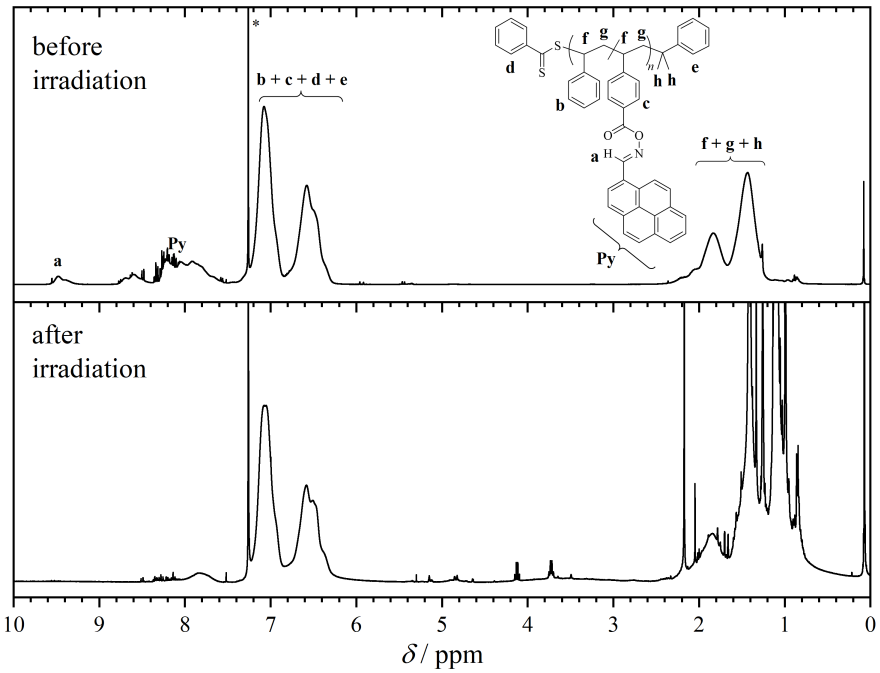

Figure 5.11. ^{1}H NMR spectra (400 MHz, $CDCl_3$, 298 K) of **CDB PS PyOHSty 1** before (top spectrum) and after exposure to LED light (430-435 nm, bottom spectrum). The magnetic resonance marked with an asterisk is assigned to $CHCl_3$.

Table 5.2. Comparison of the SEC results for **CDB PS PyOHSty 1 - 3** before and after LED irradiation (430-435 nm). $M_{n,\,SEC(THF)}$ was calculated by employing a PS calibration. The number of photoreactive units per chain was provided *via* ^{1}H NMR analysis.

Species	$M_{n,\,SEC(THF)}$ / before irradiation g mol^{-1}	$Đ$	$M_{n,\,SEC(THF)}$ / after irradiation g mol^{-1}	$Đ$	**Reduction /** %	**photoreactive units per chain**
1	17.000	1.22	8.000	1.37	50	15
2	12.000	1.15	7.000	1.56	40	7
3	13.000	1.20	13.000	1.29	0	2

Concomitantly, the SEC results are shown in **Figure 5.12** and **Table 5.2**. An important parameter for the evaluation of the SEC data is the amount of photoreactive groups for the individual polymeric species. **CDB PS PyOHSty 1** and **CDB PS PyOHSty 2** possess approximately 15 and 7 units of the light-sensitive monomer per chain, respectively. As a result, potential pathways after irradiation include inter- or intramolecular coupling and chain scission (refer to **Scheme 5.7**). Only intermolecular radical combination processes or chain breakage events are possible for **CDB PS PyOHSty 3** as approximately two units are incorporated per chain, which have a low probability to react with each other. On the one side, the SEC traces of **CDB PS PyOHSty 1** and **CDB PS PyOHSty 2** after irradiation shift to higher retention times, which can be either caused by intramolecular crosslinking or chain scission. On the other side, the SEC trace of the third polymer derivative, **CDB PS PyOHSty 3**, retained its shape after irradiation despite showing a small population at lower retention time, which is supposedly caused by intermolecular reaction. Furthermore, the SEC trace of **CDB PS PyOHSty 3** after irradiation excludes chain scission events as main process since the SEC trace is not shifted to higher retention times. As a result, intramolecular crosslinking is the predominant reaction after irradiation of **CDB PS PyOHSty 1** and **CDB PS PyOHSty 2**. The apparent molar masses of **CDB PS PyOHSty 1** and **CDB PS PyOHSty 2** decrease by 9000 and 5000 g mol^{-1}, respectively, indicating a reduction of 50 and 40 %. However, due to interaction of the column material of the SEC system and the carboxyl groups which are potentially generated *via* cleavage of the oxime followed by combination with a hydrogen atom as side reaction (refer to **Figure 5.13**), the SEC traces of the first and second polymeric species feature tailing into the small molar mass area. Consequently, the calculated values for $Đ$ of the polymer samples exposed to light are higher in comparison to their corresponding parent polymers.

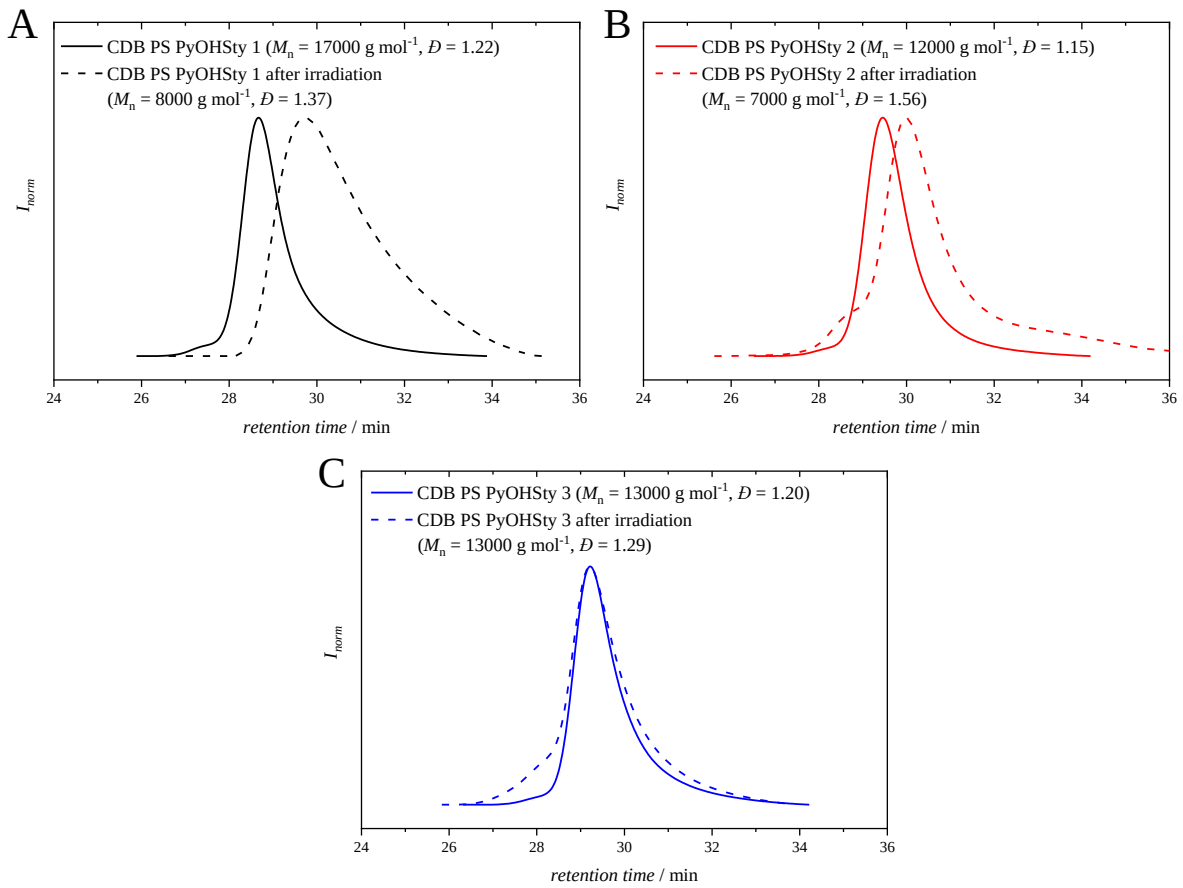

Figure 5.12. SEC (THF, 35 °C, RI) traces of **A**: **CDB PS PyOHSty 1**, **B**: **CDB PS PyOHSty 2** and **C**: **CDB PS PyOHSty 3**. The SEC traces of **CDB PS PyOHSty 1** and **CDB PS PyOHSty 2** after irradiation indicate a shift to higher retention time, which is either caused by intramolecular crosslinking or chain scission. In contrast, no shift is visible for the SEC trace of **CDB PS PyOHSty 3** after irradiation.

Consequently, the combined SEC and ^{1}H NMR analysis suggests one main reaction pathway for the copolymer derivatives featuring light-sensitive **PyOHSty** units, namely intramolecular coupling of radicals. This observation is in contrast to the reactions depicted in **Scheme 5.7**. Since either a phenyl or a carboxyl radical is formed, no main chain scission can occur as the generated radical is not located in the aliphatic backbone. In principle, the radical species is able to abstract a hydrogen atom from the chain, and in turn, a hydrogen atom can be transferred to another radical species providing unsaturated groups along the polymer backbone. Nevertheless, the olefinic moiety of the latter process is readily detected *via* ^{1}H NMR spectroscopy as magnetic resonances at approximately 6.00 ppm. It needs to repeatedly emphasized in the current context that the ^{1}H NMR spectra after irradiation of the polymeric species exclude the combination of a polymer chain and an iminyl radical as main process.

Therefore, the proposed crosslinking chemistry is envisaged in **Figure 5.13**. The light-induced fragmentation of pyrene-substituted oxime moieties results in the formation of iminyl and carboxyl radicals (part A of the current figure). The latter radical species is able to decompose further *via* CO_2-release, hence forming a phenyl radical. Therefore, three chemically distinct crosslinking motifs are feasible. The coupling of two radical carboxyl derivatives results in a peroxyanhydride bond, whereas a biphenyl linkage is formed by the reaction of two phenyl species. Furthermore, the coupling of a phenyl radical and a carboxyl species yields a phenyl ester motif. In case of the iminyl radical, either combination forming azine units, or addition of oxygen during work-up followed by rearrangement into the aldehyde moiety among release of nitric oxide are potential reaction processes.[547, 552]

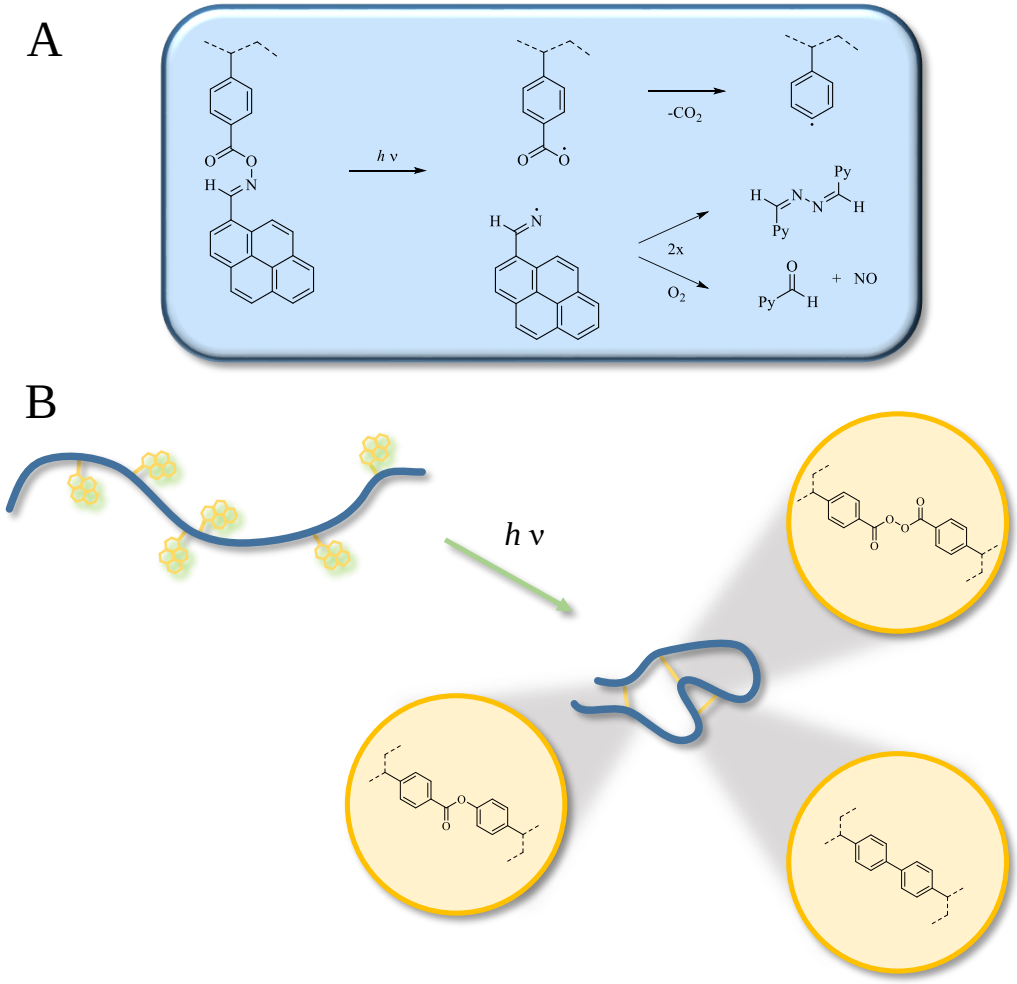

Figure 5.13. The light-induced fragmentation of the pyrene-substituted oxime moiety is depicted in part **A** of the current figure. Consequently, different intramolecular radical coupling products may be identified as the cause for reduced hydrodynamic volume during SEC measurements (part **B**). The combination of two radical carboxyl and two phenyl species results in a peroxyanhydride and a biphenyl bond, respectively. A phenyl ester connection is generated upon coupling of a carboxyl and a phenyl radical (with Py = pyrene).

Complementary evidence of the chain collapse is provided *via* DOSY NMR since the presence of pyrene in the pristine polymeric species excludes analytical methods based on light scattering. Consequently, NMR samples of **CDB PS PyOHSty 2** before and after LED light exposure with a concentration of 8.9 mg mL^{-1} in $CDCl_3$ were prepared. The measurements were performed with the standard Bruker pulse program, ledbpgp2s. After Fourier transformation and phase correction, the diffusion dimension of the 2D DOSY NMR spectra was processed with the Bruker Topspin software package, and the diffusion coefficients were obtained by employing the Bruker Dynamic Center software. Subsequently, the diffusion coefficients were translated into hydrodynamic diameters *via* the Stokes-Einstein equation in **Equation 2.4**. The DOSY NMR results of three selected magnetic resonances in the ^{1}H NMR spectra of the polymeric species before and after irradiation are presented in **Table 5.3**, while the DOSY fit data is collected in **Figure D.19**. The diffusion coefficients of the pristine polymer derivatives are in very good agreement to each other, providing a mean diameter of 4.3 nm. The light exposure of **PS PyOHSty 2** induced a reduction in hydrodynamic diameter of 30 % affording a value of 2.9 nm. In addition, the values of the diffusion coefficient of the irradiated polymeric species are consistent. The DOSY NMR results are supported by the DOSY NMR fit data in **Figure D.19**, which indicates the conformity between the experimental and theoretical fit data.

Table 5.3. DOSY NMR (400 MHz, $CDCl_3$, 298 K) results of **CDB PS PyOHSty 2** before and after LED irradiation. The diffusion coefficient of a selected magnetic resonance is translated into the diameter of the polymeric species in solution *via* the Stokes-Einstein relationship in **Equation 2.4** with η = 0.536 mPa s for chloroform.

Species	**Diffusion Coefficient /** m^2s^{-1}	**Signal /** ppm	**Diameter /** nm
CDB PS PyOHSty 2	$1.95 \cdot 10^{-10}$	7.11	4.18
	$1.88 \cdot 10^{-10}$	6.60	4.33
	$1.91 \cdot 10^{-10}$	1.45	4.26
CDB PS PyOHSty 2 (irrad)	$2.83 \cdot 10^{-10}$	7.11	2.88
	$2.76 \cdot 10^{-10}$	6.61	2.95
	$2.80 \cdot 10^{-10}$	1.45	2.91

5.2.3 Investigation of the Optical Properties

Upon light irradiation of the pyrene-substituted oxime ester moieties along the polymer backbone, radical pyrene-substituted iminyl species are released from the polymer chain. As a result, absorbance and fluorescence emission measurements of the individual polymer samples reveal important details on the light-induced fragmentation process. Only **CDB PS PyOHSty 1** and **CDB PS PyOHSty 2** were investigated due to their exceptional crosslinking behavior.

The UV/Vis spectra of the pristine polymeric species in **Figure 5.14A** and **5.14C** indicate similar features as the absorption spectrum of the light-sensitive monomer unit in **Figure 5.10**. A broad absorbance is located between 320 and 420 nm possessing two maxima at 365 and 395 nm. The intensity thereof is higher in the spectrum of **CDB PS PyOHSty 1** than in the spectrum of **CDB PS PyOHSty 2** since the content of the functional monomer is lower in the latter one. In contrast, the fluorescence spectra of the polymers in part **B** and **D** recorded with an excitation wavelength of 344 nm differ from the spectrum of the monomer unit. While a strong band between 375 and 460 nm is detected analogously to the spectrum of **PyOHSty** in **Figure 5.10**, an additional broad fluorescence emission is visible between 460 and 675 nm. The latter emission is attributed to excimer formation of two pyrene moieties, which are located in close proximity to each other in the polymer backbone. Therefore, the fluorescence emission, which arises due to excimer formation, is more pronounced in the spectrum of **CDB PS PyOHSty 1** than for **CDB PS PyOHSty 2** due to the fact that the content of the pyrene-substituted monomer along the polymer backbone is higher in the first case than for the second species. Consequently, the value of I_E/I_M is 0.54 for **CDB PS PyOHSty 1** while the spectrum of **CDB PS PyOHSty 2** suggests a value of 0.29.[400] The emission maxima of the excimer dimers are located at 524 nm for **CDB PS PyOHSty 1** and at 517 nm for **CDB PS PyOHSty 2**.

Last but not least, the successful cleavage of the pyrene moiety after irradiation is confirmed by the investigation of the optical properties. The UV/Vis spectra of the irradiated polymer derivatives (dashed lines) do not reveal any typical absorbances related to the presence of pyrene. Only a weak absorbance between 240 and 300 nm is visible, which stems from the polystyrene backbone. Furthermore, the fluorescence spectra of the same polymeric species indicate a substantial decrease in the intensity of the fluorescence emission. As a result, it can be anticipated that radical coupling between iminyl radicals and polymer chains does not occur, and consequently, the light-induced fragmentation of pyrene-substituted

oxime ester can be readily monitored by observing the optical properties *via* UV/Vis and fluorescence spectroscopy.

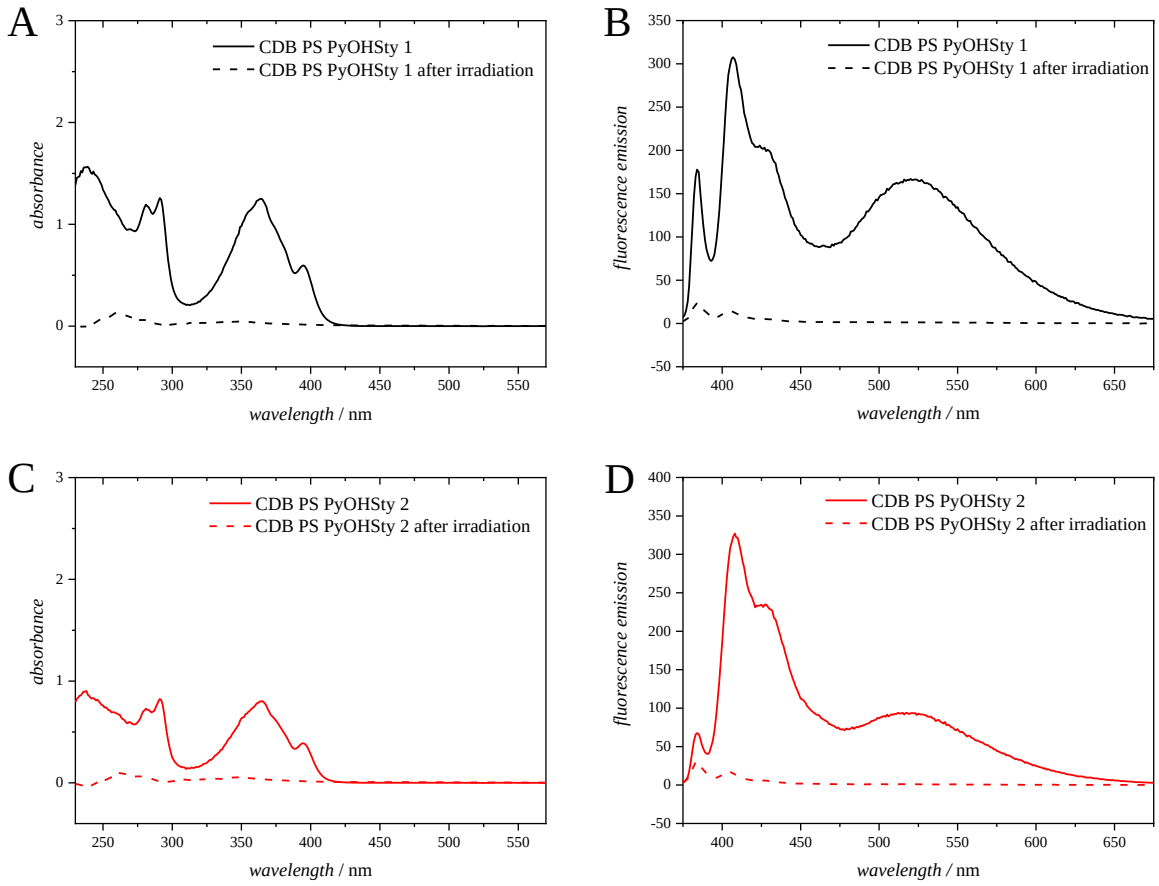

Figure 5.14. UV/Vis spectra of **A**: **CDB PS PyOHSty 1** and **C**: **CDB PS PyOHSty 2** in DCM at ambient temperature ($c = 6.25 \cdot 10^{-2}$ mg mL^{-1}), and fluorescence spectra ($\lambda_{exc.} = 344$ nm) of **B**: **CDB PS PyOHSty 1** and **D**: **CDB PS PyOHSty 2** in DCM at ambient temperature ($c = 1.04 \cdot 10^{-2}$ mg mL^{-1}).

5.3 Summary

The current chapter explores the first light-induced cycloaddition of chloro oximes and further emphases the outstanding role of pyrene as light-harvesting unit for photochemical transformations. The synthesis of the chloro pyrene oxime as light-sensitive compound is straightforward. A two-step synthesis starting from commercially available 1-pyrenecarbaldehyde delivers the desired compound, which is not only activated by LED light, but also by employing ambient laboratory light. Hereby, the generated 1,3-dipole is reactive towards a broad range of dienophiles including olefinic compounds and alkyne moieties, while showing a high regioselectivity and excellent tolerance towards functional groups. In addition, the conjugation of a biologically relevant molecule of high chemical complexity was successfully investigated. Particularly, the results for the end group transformation indicate the importance of the light-induced addition of the chloro pyrene oxime in polymer chemistry for the introduction of fluorescent marker units.

Furthermore, the light-triggered fragmentation of pyrene-substituted oxime ester groups along the polymer backbone is introduced. Therefore, a novel light-sensitive monomer was synthesized in two consecutive steps, and it was copolymerized with styrene in a RD radical polymerization process utilizing a chain transfer agent. The results of the irradiation of the polymer samples with various content of the light-sensitive oxime ester indicate the efficient fragmentation upon light exposure followed by radical coupling, which finally results in the formation of single-chain nanoparticles as proposed by SEC and DOSY NMR measurements. Due to the optical properties of the pyrene unit, the process can be readily monitored *via* UV/Vis and fluorescence spectroscopy, hence implying the self-reporting properties of the material. Whereas the linear precursors have high absorbances as well as pronounced fluorescence emission of pyrene monomers and excimers, the particles exhibit neither of them. The concept of light-sensitive oxime esters provides an in-depth look into the crosslinking behavior of polymer chains, and adds a new methodology into the toolbox for the mild photochemically induced synthesis of SCNPs.

CHAPTER 6

EXPERIMENTAL SECTION

6.1 Materials

6.1.1 Materials for Instrumentation

For ^{1}H and ^{13}C NMR spectra and DOSY NMR measurements, chloroform-d_1 ($CDCl_3$, Sigma Aldrich, 99.8 % D) and dimethyl sulfoxide-d_6 (DMSO-d_6, eurisotop, 99.8 % D) were employed as deuterated solvents.

Polymer samples dissolved in tetrahydrofuran (THF, VWR, 99.7 %, stabilized with BHT for SEC) (c = 2 mg mL^{-1}) were subjected to SEC measurements ((THF, 30 °C, RI/UV) or (THF, 35 °C, RI)). For high temperature SEC measurements (TCB, 150 °C, RI), a polymer concentration of 5 mg mL^{-1} dissolved in trichlorobenzene (TCB, stabilized with butylhydroxytoluene) at 150 °C was used.

Dichloromethane (DCM, Carl Roth, ROTISOLV HPLC ultra gradient grade), tetrahydrofuran (THF, Scharlau, stabilized with BHT) and methanol (MeOH, Carl Roth, ROTHISOLV HPLC ultra gradient grade) were utilized as solvents for ESI-MS measurements in combination with sodium trifluoroacetate (NaTFA, 98 %, Aldrich) as doping agent.

For UV/Vis and fluorescence spectroscopy dichloromethane (DCM, VWR, normapur) was used as received.

Deionized water was employed for the DLS studies.

6.1.2 Materials for Synthesis

Materials for Chapter 3

Unless otherwise stated all chemicals were used as received. 1-Acetyl pyrene (Acros, 97 %), aluminium trichloride ($AlCl_3$, Roth, $\geq$ 98 %, anhydrous, sublimated), basic aluminium oxide (Al_2O_3, Acros, Brockmann I for chromatography), neutral aluminium oxide (Al_2O_3, Acros, Brockmann I for chromatography), anisole (Acros, $\geq$99 %, extra dry), copper (II) bromide ($CuBr_2$, Sigma-Aldrich, 99+ %, extra pure), copper(I) iodide (CuI, Sigma Aldrich, 98 %), cyclohexane (VWR, normapur), dichloromethane (DCM, VWR, normapur), dichloromethane (DCM, Acros, 99.8 %, extra dry), *N,N*-diisopropylamine (DIPEA, Acros, 99.5 %), *N,N*-dimethylhydrazine (Merck, $\geq$ 98 %), 1,4-dioxane (Acros, 99+ % extra pure), diethyl ether (VWR, normapur), 4-dimethylaminopyridine (DMAP, Acros organics, 99 %), *N,N*-dimethylformamide (DMF, Acros, 99.8 %, extra dry), dithiothreitol (DTT, AppliChem Panreac, molecular biology grade), 1-dodecanethiol (Alfa Aesar, 98 %), ethyl acetate (VWR, normapur), 1-ethyl-3-(3-dimethylaminopropyl)-carbodiimide hydrogenchloride (EDC·HCl, Roth, $\geq$99 %), 1,1,4,7,10,10-hexamethyltriethylenetetramine (HMTETA, Sigma Aldrich, 97 %,), hexane (VWR, normapur), hexylamine (Merck, $\geq$99 %), iodomethane (Alfa Aesar, 99 %, stabilized with copper), magnesium sulfate ($MgSO_4$, Roth, $\geq$99 %), methanol (MeOH, VWR, normapur), methanol (MeOH, Acros, 99.9 %, extra dry), methyl adipoyl chloride (Sigma Aldrich, 97 %), poly(ethylene glycol)methyl ether azide (PEG-N_3, Sigma Aldrich, M_n = 2000 g mol^{-1}), poly(ethylene glycol)methyl ether thiol (PEG-SH, Sigma Aldrich, M_n = 2000 g mol^{-1}), pyrene (Alfa Aesar, 98 %), silica gel (Merck, Genduran SI60, 0.063 - 0.200 mm), sodium azide (Sigma Aldrich, $\geq$99.5 %), sodium hydride (Sigma Aldrich, 95 %, dry), tetrahydrofuran (THF, Acros, 99.5 %, extra dry, stabilized), triethylamine (Merck, for synthesis), trifluoroacetic acid (Alfa Aesar, 99 %), tris(2-carboxyethyl)phosphine hydrochloride (TCEP, Roth, >98.0 %), toluene (VWR, normapur).

Azobisisobutyronitrile (AIBN, Fluka, 98 %) was recrystallized from MeOH. 2-((Dodecylsulfanyl)-carbonothioyl)sulfanyl propanoic acid (DoPAT) was obtained from Lanxess Deutschland GmbH. Styrene (Merck, $\geq$99 %) and methyl methacrylate (MMA, Sigma Aldrich, 99 %) were passed over a column of basic aluminium oxide prior to polymerization. Az-Py,[422] and prop-2-ynyl 2-bromo-2-methylpropanoate were synthesized according to literature.[553] Resin-N_3 (1.8 mmol of N_3 functionality per mg) was synthesized by stirring chloromethyl polystyrene (Resin cross-linked with 1 % DVB, TCI) with sodium azide in DMF at ambient temperature overnight followed by filtration und drying.

Materials for Chapter 4

Unless otherwise stated all chemicals were used as received. Acetone (VWR, normapur), acetonitrile (ACN, Acros, 99.9 %, extra dry), aluminium chloride (Roth, $\geq$ 98 %, anhydrous, sublimated), basic aluminium oxide (Al_2O_3, Acros, Brockmann I for chromatography), neutral aluminium oxide (Al_2O_3, Acros, Brockmann I for chromatography), (3-aminopropyl)triethoxysilane (APTES, Sigma Aldrich, 99%), 2-bromo isobutyric bromide (Alfa Aesar, 97 %), 4-bromomethyl benzoate (Alfa Aesar, 98 %), copper (II) bromide ($CuBr_2$, Sigma-Aldrich, 99+ %, extra pure), copper (II) perchlorate hexahydrate ($Cu(ClO_4)_2 \cdot (H_2O)_6$, Acros, $\geq$ 98 %), copper (II) sulfate pentahydrate ($Cu_2SO_4 \cdot (H_2O)_5$, Merck, analytical grade), 18-crown-6 (Acros, 99 %), cyclohexane (VWR, normapur), dichloromethane (DCM, VWR, normapur), dichloromethane (DCM, Acros, 99.8 %, extra dry), 4-dimethylaminopyridine (DMAP, Acros organics, 99 %), *N,N*-dimethylformamide (DMF, HPLC Biosolve), dimethylsulfoxide (DMSO, Acros, 99.7 %, extra dry), ethanol (Acros, 99.7 %, extra dry), ethanolamine (Acros, 99 %), 1-ethyl-3-(3-dimethylaminopropyl)carbodiimide hydrogenchloride (EDC·HCl, Roth, $\geq$99 %), *N*-ethyl maleimide (Sigma Aldrich, 98 %), furan (Acros, 99+ %, stabilized), iron powder (Fisher, general purpose grade), magnesium sulfate ($MgSO_4$, Roth, $\geq$99 %), maleic anhydride (Acros, 99 %), methanol (MeOH, VWR, normapur), poly(ethylene glycol)methyl ether azide (PEG-N_3, Sigma Aldrich, M_n = 2000 g mol^{-1}), poly(ethylene glycol)methyl ether thiol (PEG-SH, Sigma Aldrich, M_n = 2000 g mol^{-1}), potassium carbonate (K_2CO_3, Alfa Aesar, 99 %, anhydrous), potassium iodide (Sigma Aldrich, $\geq$ 99 %), potassium peroxodisulfate ($K_2S_2O_8$, Sigma Aldrich, 97 %), propargyl alcohol (Acros, 99 %), silica gel (Merck, Genduran SI60, 0.063 - 0.200 mm), sodium ascorbate (Na asc., Sigma-Aldrich, 98 %), sodium azide (Sigma Aldrich, $\geq$99.5 %), sodium hydroxide (NaOH, Roth, $\geq$99 %), tetrahydrofuran (THF, VWR, normapur), tetrahydrofuran (THF, Acros, 99.5 %, extra dry, stabilized), tris(benzyltriazolylmethyl)amine (TBTA, TCI, $\geq$97 %), toluene (VWR, normapur), triethylamine (Merck, for synthesis), tris(2-(dimethylamino)ethyl)amine (Me_6TREN, Alfa Aesar, 99+ %).

Azobisisobutyronitrile (AIBN, Fluka, 98 %) was recrystallized from MeOH. Styrene (Merck, $\geq$99 %) and methyl methacrylate (MMA, Sigma Aldrich, 99 %) were passed over a column of basic aluminium oxide prior to polymerization. 2-Bromo-2-methyl propionic acid 2-(3,5-dioxo-10-oxa-4-azatricyclo-[5.2.1.02,6]-dec-8-en-4-yl) ethyl ester (PG-Mal initiator) was synthesized according to literature.[554] Ph-OH was synthesized according to a consecutive four-step synthesis (step 1,[515] step 2,[337] step 3,[334] step 4.[334])

Materials for Chapter 5

Unless otherwise stated all chemicals were used as received. Biotin maleimide (Sigma, ≥95 %), *N*-chlorsuccinimide (NCS, Aldrich, 98 %), cyclohexane (VWR, normapur), 1,2-dichlorobenzene (Acros, 99 %, extra pure), dichloromethane (DCM, VWR, normapur), dichloromethane (DCM, Acros, 99.8 %, extra dry), diethyl acetylenedicarboxylate (TCI, ≥95.0 %), diethyl fumarate (Alfa Aesar 98 %), 4-dimethylaminopyridine (DMAP, Acros organics, 99 %), *N,N*-dimethylformamide (DMF, Acros, 99.8 %, extra dry), dimethylsulfoxide (DMSO, Acros, 99.7 %, extra dry), 1-ethyl-3-(3-dimethylaminopropyl)-carbodiimide hydrogenchloride (EDC·HCl, Roth, ≥99 %), *N*-ethyl maleimide (Sigma Aldrich, 98 %), hydroxylamine hydrochloride (Alfa Aesar, 99 %), magnesium sulfate ($MgSO_4$, Roth, ≥99 %), methanol (MeOH, VWR, normapur), methanol (MeOH, Acros, 99.9 %, extra dry), methyl acrylate (Aldrich, 99 %, stabilized), 4-pentenoic acid (Alfa Aesar, 98 %), poly(ethylene glycol)methyl ether (PEG-OH, Alfa Aesar, M_n = 1900 g mol^{-1}), poly(ethylene glycol)methyl ether maleimide (PEG-Mal, Sigma Aldrich, M_n = 2000 g mol^{-1}), 1-pyrenecarboxaldehyde (Alfa Aesar, 99 %), sodium acetate (Roth, ≥98.5 %, pure, anhydrous), styrene (Merck, ≥99.0 %, stabilized), 4-vinylbenzoic acid (TCI, ≥97.0 %, stabilized with BHT).

Pentene-endcapped polyethylene glycol was synthesized according to literature.[422] Azobisisobutyronitrile (AIBN, Fluka, 98 %) was recrystallized from MeOH. Styrene (Merck, ≥99 %) and 1,2-dichlorobenzene (Acros, 99 %, extra pure) were passed over a column of basic and neutral aluminium oxide prior to polymerization, respectively.

6.2 Characterization

6.2.1 Size Exclusion Chromatography (SEC)

THF, 30 °C, RI/UV (Chapter 3)

The apparent number average molar mass (M_n) and the molar mass distribution [$Đ$ (dispersity) = M_w/M_n] of the polymers were determined *via* SEC measurements, which were performed on a TOSOH Eco-SEC HLC-8320 GPC System, comprising an autosampler, a SDV 5 µm bead-size guard column (50 × 8 mm, PSS) followed by three SDV 5 µm columns (300 × 7.5 mm, subsequently 100 Å, 1000 Å and 105 Å pore

size, PSS), and Waters 2487 dual wavelength absorbance detector (analysis at 254 nm) in series with a refractive index detector using tetrahydrofuran (THF) as the eluent at 30 °C with a flow rate of 1 mL min^{-1}. The SEC system was calibrated using linear polystyrene standards ranging from 266 to $2.52 \cdot 10^6$ g mol^{-1}. Calculation of the molecular weight proceeded *via* the Mark-Houwink-Sakurada (MHS) parameters for polystyrene (PS) in THF at 30 °C, i.e., $K = 13.63 \cdot 10^{-3}$ mL g^{-1}, $\alpha = 0.714$ and for poly(methyl methacrylate) in THF at 30 °C, $K = 12.8 \cdot 10^{-3}$ mL g^{-1}, $\alpha = 0.69$.[555] For poly(ethylene glycol), SEC calculations were carried out relative to a PMMA calibration.

THF, 35 °C, RI (Chapter 4 and 5)

The apparent number average molar mass (M_n) and the molar mass distribution [$Đ$ (dispersity) = M_w/M_n] of the polymers were determined *via* SEC measurements, which were performed on a Polymer Laboratories (Varian) PL-GPC 50 Plus Integrated System, comprising an autosampler, a PLgel 5 mm bead-size guard column (50 × 7.5 mm), one PLgel 5 mm Mixed E column (300 × 7.5 mm), three PLgel 5 mm Mixed C columns (300 × 7.5 mm) and a differential refractive index detector using tetrahydrofuran (THF) as the eluent at 35 °C with a flow rate of 1 mL min^{-1}. The SEC system was calibrated using linear polystyrene standards ranging from 476 to $2.5 \cdot 10^6$ g mol^{-1} and linear poly(methyl methacrylate) standards ranging from 700 to $2.0 \cdot 10^6$ g mol^{-1}. Calculation of the molecular weight proceeded *via* the Mark-Houwink-Sakurada (MHS) parameters for polystyrene (PS) in THF at 35 °C, i.e., $K = 13.63 \cdot 10^{-3}$ mL g^{-1}, $\alpha = 0.714$ and for poly(methyl methacrylate) in THF at 35 °C, $K = 12.8 \cdot 10^{-3}$ mL g^{-1}, $\alpha = 0.69$.[555]

TCB, 150 °C, RI (Chapter 4)

The high temperature SEC measurements were performed on a triple detection unit from Viscotek - Malvern Instrument. The system is equipped with a refractive index detector, static light scattering RALS (90 °) and LALS (7 °) and a viscometer detector. The set is equipped with a combination of three columns (Polefin 300 mm × 8 mm I.D porosity of 1 000, 100 000 and 1 000 000 Å) from Polymer Standards Service. The mobile phase is 1,2,4-trichlorobenzene (TCB) at 150 °C at a flow rate of 1 mL min^{-1}. The solvent is stabilized by butylhydroxytoluene at 0.2 g L^{-1} in order to prevent oxidative degradation of the polymer. The samples were dissolved in TCB at a concentration of 5 mg mL^{-1} at 150 °C for about one hour. Samples were injected through a 200 µL loop and filtered in-line before separation on the columns.

A conventional calibration curve, obtained with linear polyethylene standards (Polymer Standard Service) in the range of 338 to 78 000 g mol^{-1} was used for the calculation of the molar mass and the molar mass distribution of the samples. The results were acquired and processed using the software "OmniSEC" version 5.12 from Malvern Instrument.

6.2.2 Nuclear Magnetic Resonance Spectroscopy (NMR)

Ambient temperature NMR measurements (Chapter 3, 4 and 5)

NMR measurements were performed on a Bruker AM 400 spectrometer (^{1}H: 400 MHz, ^{13}C: 100 MHz) for hydrogen and carbon nuclei. The δ-scale was referenced to the respective solvent signal of chloroform-d_1, dimethylsulfoxide-d_6 or benzene-d_6 which were employed as deuterated solvent. Abbreviations used in the description of the materials synthesis include singlet (s), doublet (d), triplet (t), quartet (q), quintet (quin), and multiplet (m).

In Chapter 4, $M_{n,NMR}$ was received by comparing the integral of the magnetic resonances of the backbone with the integral of a magnetic resonance of a chain termini. For details, refer to the descriptions of the individual tables.

In Chapter 5, the number of photoreactive **PyOHSty** unit per chain was calculated by comparing the integral of the magnetic resonance of the aldehyde proton between 9.60 and 9.20 ppm with the value of the integral associated with the magnetic resonance of the aromatic backbone in the region of 7.40 to 6.20 ppm minus the number of protons of **PyOHSty**, which appear in the same area. $M_{n,SEC}$ was taken as the molecular weight of the polymeric species as $M_{n,NMR}$ cannot be obtained due to overlap of the magnetic resonances of the backbone and the protons of the end group.

High temperature NMR measurements (Chapter 4)

High-resolution liquid NMR spectroscopy was carried out with a Bruker DRX 400 spectrometer operating at 400 MHz for the ^{1}H nucleus. Spectra were recorded at 363 K using a 5 mm QNP probe. Polymer samples were examined as 5-15 % (w/v) solutions. A mixture of tetrachloroethylene (TCE) and deuterated benzene (C_6D_6) (2/1 v/v) was used as solvent. Chemical shift values are given in units of ppm, relative to an internal reference of tetramethylsilane. Abbreviations used in the description of the materials synthesis include singlet (s), doublet (d), triplet (t), quartet (q), quintet (quin), and multiplet (m).

6.2.3 High Resolution/Orbitrap Electrospray Ionization-Mass Spectrometry (ESI-MS)

Mass spectra were recorded on a Q Exactive (Orbitrap) mass spectrometer (Thermo Fischer Scientific, San Jose, CA, USA) equipped with a HESI II probe. The spectra were recorded in positive mode and the analyt was dissolved in a THF/MeOH (Chapter 4, 3:2, doped with 100 µmol sodium trifluoroacetate, c = 0.01 g mL^{-1}) or in a DCM/MeOH solution (Chapter 5, 3:1, doped with 100 µmol sodium trifluoroacetate, c = 0.01 g mL^{-1}). The instrument was calibrated in the m/z range 74 to 1822 using premixed calibration solutions (Thermo Scientific). The Fourier-Transform resolution was set to 140 000. A constant spray voltage of 3.6 kV and a dimensionless sheath gas of 5 were applied. The capillary temperature and the S-lens RF level were set to 320 °C and 68.0, respectively. The flow rate was set to 5 µL min^{-1}.

6.2.4 Dynamic Light Scattering (DLS)

The apparent hydrodynamic diameters (D_h) were determined at 5, 25 and 45 ° by means of a dynamic light scattering (DLS) analysis using a Zetasizer Nano ZS light scattering apparatus (Malvern Instruments, UK) equipped with He-Ne laser (at a wavelength of 633 nm, 4 mW). The Nano ZS instrument incorporates a non-invasive backscattering (NIBS) optic with a detection angle of 173 °. For micelles formation, µ**PMMA-PEG-PEG** was dispersed in water while for **PMMA-*b*-PEG-Dode**, the nanoprecipitation method with THF and water was employed. The prepared samples were stabilized in quartz cuvettes prior to DLS analysis at the chosen temperature. All values of the apparent hydrodynamic diameter for the mikto-arm polymers and micelles were averaged over triplicate measurements (11 runs/measurement), and were automatically provided by the instrument using a cumulative analysis in combination with the autocorrelation functions.

6.2.5 Ultraviolet/Visible (UV/Vis) Spectroscopy

The UV/Vis spectra were recorded on a Cary 100 UV/Visible Spectrophotometer (Agilent Technologies, USA) equipped with a tungsten halogen light source (190-900 nm, accuracy +/- 2 nm) and a R928 PMT detector. Spectra were recorded in DCM at 20 °C and collected between 200 and 800 nm. Samples were baseline corrected with respect to the pure solvent. The pyrene-functional block copolymers and mikto-arm star polymers in Chapter 3 were investigated employing a concentration of $7.22 \cdot 10^{-5}$ mmol mL^{-1}.

Furthermore, concentrations of $4.52 \cdot 10^{-5}$ mmol mL^{-1} for the chloro pyrene oxime and its cycloadducts and of $1.23 \cdot 10^{-5}$ mmol mL^{-1} for PyOHSty (all Chapter 5) were selected. The light-sensitive copolymer samples in Chapter 5 were recorded with a concentration of $6.25 \cdot 10^{-2}$ mg mL^{-1}.

6.2.6 Fluorescence Spectroscopy

Fluorescence spectra were measured on a Varian Cary Eclipse Fluorescence Spectrometer using quartz cuvettes loaded with 400 µL of samples. An excitation wavelength of 344 nm was used and the emission was recorded from 355 to 800 nm. All spectra were recorded in DCM at 20 °C (pyrene-functional block copolymers and mikto-arm star polymers in Chapter 3: c = $1.81 \cdot 10^{-5}$ mmol mL^{-1}, chloro pyrene oxime and its cycloadducts in Chapter 5: c = $1.13 \cdot 10^{-5}$ mmol mL^{-1}; PyOHSty in Chapter 5: c = $3.98 \cdot 10^{-7}$ mmol mL^{-1}, light-sensitive copolymer samples in Chapter 5: c = $1.04 \cdot 10^{-2}$ mg mL^{-1}).

6.2.7 Attenuated Total Reflectance-Infrared Spectroscopy (ATR-IR)

All IR measurements were performed on a Bruker Alpha ATR-IR Spectrometer with a range of 400 to 4000 cm^{-1} at ambient temperature.

6.2.8 Differential Scanning Calometry (DSC)

Differential scanning calorimetry studies were carried out with a Mettler-Toledo STAR system under nitrogen atmosphere using a sample mass of 5 mg. The glass transition temperature T_g is reported as the midpoint of the step change in the heat capacity and the melting point is reported as the minimum of the endothermic peak at a heating rate of 20 K min^{-1} starting from -75 °C up to a temperature of 250 °C of the second heating scan.

6.2.9 Time-of-Flight Secondary Ion Mass Spectrometry (ToF-SIMS)

Time-of-flight secondary ion mass spectrometry (ToF-SIMS) was conducted with a TOF.SIMS5 instrument (ION-TOF GmbH, Münster, Germany), equipped with a Bi cluster liquid metal primary ion source and a non-linear time-of-flight analyzer. The Bi source was operated in the bunched mode providing 0.7 ns Bi_3^+ ion pulses at 25 keV energy. Spectra were calibrated on the CH^-, CH_2^-, CH_3^-, or on the C^+, CH^+,

CH_2^+, and CH_3^+. Based on these datasets, the chemical assignments for characteristic fragments were determined.

6.2.10 Diffusion-Ordered Spectroscopy (DOSY NMR)

DOSY experiments based on ^{1}H NMR were performed in $CDCl_3$ (c = 8.9 mg mL^{-1}) at 298.00 K on a Bruker AM 400 spectrometer at an operating frequency of 400 MHz using a stimulated echo sequence incorporating bipolar gradient pulses and a longitudinal eddy current delay (BPP-LED) with the standard Bruker pulse program, ledbpgp2s. The gradient strength was linearly incremented in 96 steps from 5 % up to 95 % of the maximum gradient strength. Diffusion times and gradient pulse durations were optimized for each experiment in order to achieve a 95 % decrease in the signal intensities at the largest gradient amplitude. After Fourier transformation and phase correction, the diffusion dimension of the 2D DOSY spectra was processed by means of the Bruker Topspin software package (version 3.2), and analyzed with the Bruker Dynamic Center. Spectra for the pristine polymer and the corresponding single-chain nanoparticles were measured and mean values were taken from the experimentally determined diffusion coefficients of the characteristic NMR-peaks. The hydrodynamic diameter was obtained *via* the application of the Stokes-Einstein in **Equation 2.4** with η = 0.536 mPa s for chloroform, k_b = 1.38 $\times$ 10^{-23} m^2 kg s^{-2} K^{-1} and T = 298 K.

6.3 Synthetic Procedures of Chapter 3

6.3.1 Synthesis of the Small Molecules

Synthesis of Methyl 6-oxo-6-(pyren-1-yl)hexanoate

According to literature,[492], 2.43 g of pyrene (12.00 mmol, 1.2 eq.) and 1.56 mL of methyl adipoyl chloride (1.79 g, 10.00 mmol, 1.0 eq.) were dissolved in dry DCM (50 mL). At -10 °C, 1.60 g of $AlCl_3$ (12.00 mmol, 1.2 eq.) were added portion-wise over 20 minutes. Subsequently, the reaction mixture was allowed to reach ambient temperature and stirred overnight. Residual $AlCl_3$ was quenched by the addition of ice followed by saturation of the aqueous phase with NaCl. After addition of DCM (150 mL), the organic phase was separated, washed with brine and dried over $MgSO_4$. After removal of the solvent under

reduced pressure, the purification *via* column chromatography (silica gel, $CHCl_3$) yielded the product as yellow solid (2.22 g, 6.45 mmol, 65 %).

^{1}H NMR ($CDCl_3$, 600 MHz): δ / ppm = 8.90 (d, 1 H, H_{Py}), 8.33-7.99 (m, 8 H, H_{Py}), 3.69 (s, 3 H, CH_3), 3.27-3.23 (m, 2 H, COCH_2), 2.45-2.41 (m, 2 H, CH_2COCH$_3$), 1.95-1.90 (m, 2 H, COCH$_2$CH_2), 1.88-1.79 (m, 2 H, CH_2CH$_2$COCH$_3$). ^{13}C NMR ($CDCl_3$, 100 MHz): δ / ppm = 204.68 (s, 1 C), 174.05 (s, 1 C), 133.84 (s, 1 C), 132.68 (s, 1 C), 131.27 (s, 1 C), 130.69 (s, 1 C), 129.72 (s, 1 C), 129.62 (s, 1 C), 127.52 (s, 1 C), 127.23 (s, 1 C), 126.54 (s, 1 C), 126.38 (s, 1 C), 126.18 (s, 1 C), 125.99 (s, 1 C), 125.08 (s, 1 C), 124.90 (s, 1 C), 124.79 (s, 1 C), 124.17 (s, 1 C), 51.71 (s, 1 C), 42.24 (s, 1 C), 34.09 (s, 1 C), 24.80 (s, 1 C), 24.45 (s, 1 C).

For ^{1}H and ^{13}C NMR spectra, refer to **Figures B.1** and **B.2**.

Synthesis of Methyl 4-(3-(pyren-1-yl)-2*H*-azirin-2-yl)butanoate

The presented synthesis is a variation of reference [422]. 2.00 g of methyl 6-oxo-6-(pyren-1-yl)hexanoate (5.81 mmol, 1.0 eq.) were dissolved in toluene (15 mL) followed by the addition of 1.33 mL of *N,N*-dimethylhydrazine (1.05 g, 17.43 mmol, 3.0 eq.) and 10.00 µL of TFA (cat.). The reaction mixture was refluxed for 5 h. After reaching ambient temperature, the organic phase was washed with water (3 ×) and dried over $MgSO_4$. The crude product was obtained after removal of the solvent and employed for the following step without further purification.

The yellow oil from the first step was dissolved in iodomethane (20 mL). After stirring at 40 °C overnight, the precipitate was dissolved in DCM followed by precipitation in diethyl ether at ambient temperature. The product was collected by filtration and immediately utilized for the last step.

The iodo salt was dissolved in dry DMF (0.163 mmol mL^{-1}), and the reaction mixture was cooled down to 0 °C. Subsequently, 1.2 eq. of NaH were added in one portion followed by stirring at 0 °C for one hour. Diethyl ether (20 × the amount of DMF) was added, and the formed precipitate was removed *via* filtration. After removal of the solvent under reduced pressure, the crude product was purified *via* column chromatography (silica gel, $CHCl_3$) yielding the targeted compound as yellow solid (1.00 g, 2.93 mmol, 50 %).

^{1}H NMR ($CDCl_3$, 400 MHz): δ / ppm = 9.17 (d, 1 H, H_{Py}), 8.39-8.07 (m, 8 H, H_{Py}), 3.67 (s, 3 H, CH_3), 2.53-2.42 (m, 3 H, CH_2COCH$_3$, CNCH), 1.95-1.90 (m, 2 H, COCH$_2$CH_2), 2.03-1.87 (m, 3 H, CH_2CH$_2$COCH$_3$, CNCHCH_2), 1.73-1.66 (m, 1 H, CNCHCH_2). ^{13}C NMR ($CDCl_3$, 100 MHz): δ / ppm = 174.11 (s, 1 C), 170.76 (s, 1 C), 134.57 (s, 1 C), 131.24 (s, 1 C), 131.12 (s, 1 C), 130.81 (s, 1 C), 130.19 (s, 1 C), 130.17 (s, 1 C), 129.20 (s, 1 C), 127.30 (s, 1 C), 126.91 (s, 1 C), 126.83 (s, 1 C), 126.72 (s, 1 C), 124.85 (s, 1 C), 124.73 (s, 1 C), 124.23 (s, 1 C), 124.23 (s, 1 C), 123.79 (s, 1 C), 51.67 (s, 1 C), 33.94 (s, 1 C), 32.78 (s, 1 C), 29.86 (s, 1 C), 23.05 (s, 1 C).

For ^{1}H and ^{13}C NMR spectra, refer to **Figure 3.1**.

6.3.2 Synthesis of the Pristine Polymer Blocks

Synthesis of PMMA-alkyne

According to literature,[84] 111.5 mg of $CuBr_2$ (0.49 mmol, 0.5 eq.), 10.0 g of MMA (99.90 mmol, 100.0 eq.), 271.5 µL of HMTETA (230.0 mg, 0.999 mmol, 1.0 eq.), 204.8 mg of prop-2-ynyl 2-bromo-2-methylpropanoate (0.999 mmol, 1.0 eq.) and 10.68 mL of dry anisole were placed in a Schlenk flask and degassed *via* three freeze-pump-thaw cycles. After 25 min at 90 °C, the polymerization was stopped by opening the flask and exposing the catalyst to air. The copper catalyst was removed by filtration though neutral Al_2O_3. The final polymer was obtained as a white powder (2.8 g) after precipitation in water and drying under high vacuum.

Table 6.1. Summary of the characterization results for **PMMA-alkyne** listed in tabular form. A PMMA calibration was employed for the calculation of $M_{n,\,SEC(THF)}$. Refer to **Figure 3.3** for the SEC trace and the ^{1}H NMR spectrum.

Species	$M_{n,\,SEC(THF)}$ / g mol^{-1}	$Đ$
PMMA-alkyne	4000	1.1

Synthesis of PS-SH

0.5 g of DoPAT (1.4 mmol, 1.0 eq.), 8.5 mg of DMAP (69.3 µmol, 0.05 eq.) and 562 µL of dry MeOH (444.4 mg, 13.9 mmol, 10.0 eq.) were dissolved in dry THF (5 mL). At 0 °C, 328.1 mg of EDC·HCl (1.7 mmol, 1.2 eq.) were added, and the reaction mixture was left at ambient temperature overnight. After

removal of the solvent under reduced pressure, the residue was dissolved in ethyl acetate, washed with sat. $NaHCO_3$ solution, 1H HCl and brine. Drying over $MgSO_4$ and removal of the solvent under reduced pressure afforded DoPAT-OMe as orange oil (498 mg, 1.3 mmol, 97 %).

In a round-bottom flask, 15.2 mg of AIBN (92.6 µmol, 0.1 eq.) and 334.9 mg of DoPAT-OMe (0.9 mmol, 1.0 eq.) were dissolved in 9.6 g of styrene (9.2 mmol, 10.0 eq.). After purging the reaction mixture for 30 min with argon, the flask was placed in a preheated oil bath at 60 °C for 17 h. The polymerization was stopped *via* cooling with liquid nitrogen and opening the flask to air. After two-fold precipitation in ice-cold MeOH, 2.2 g of a slight yellow polymer were received.

Table 6.2. Summary of the characterization results for **PS-OMe** listed in tabular form. A PS calibration was employed for the calculation of $M_{n,\,SEC(THF)}$.

Species	$M_{n,\,SEC(THF)}$ / g mol^{-1}	$Đ$
PS-OMe	2700	1.1

For the aminolysis of the RAFT end group, 150.0 mg of PS-OMe were dissolved in dry DMF (1.5 mL), and 10.3 µL of hexylamine (7.9 mg, 78.3 µmol, 1.2 eq.) were added. To prevent the oxidation of thiols to disulfides, 5.0 mg of DTT were added to the reaction mixture. After stirring at ambient temperature overnight, the final polymer was received as white powder *via* precipitation in ice-cold MeOH.

Table 6.3. Summary of the characterization results for **PS-SH** listed in tabular form. A PS calibration was employed for the calculation of $M_{n,\,SEC(THF)}$. Refer to **Figures 3.4** and **3.5** for the ^{1}H NMR spectrum and the SEC trace, respectively.

Species	$M_{n,\,SEC(THF)}$ / g mol^{-1}	$Đ$
PS-SH	2600	1.1

Reduction to PEG-SH

To remove residual PEG-SS-PEG of the commercially available material, 0.4 g of PEG-SH were dissolved in dry DMF (2 mL). 92.6 mg of DTT (0.6 mmol, 3.0 eq.) for disulfide cleavage and 0.01 mL of triethylamine as catalyst were added. After stirring the reaction mixture at ambient temperature for three days, the polymer was obtained by two-fold precipitation in ice-cold diethyl ether.

Table 6.4. Summary of the characterization results for **PEG-SH** listed in tabular form. A PMMA calibration was employed for the calculation of $M_{n,\,SEC(THF)}$. Refer to **Figures 3.4** and **3.5** for the ^{1}H NMR spectrum and the SEC trace, respectively.

Species	$M_{n,\,SEC(THF)}$ / g mol^{-1}	$Đ$
PEG-SH	2600	1.1

6.3.3 Block Copolymer Formation *via* Interrupted CuAAC Ligation

The following procedure presents a variation of the process reported in reference [178]. Under argon atmosphere, 50 mg of PMMA-alkyne (1.1 eq.), 22.7 mg of PEG-N_3 (1.0 eq.), 4.0 mg of Az-Py (17.3 µmol, 1.2 eq.), 3.4 µL of DIPEA (2.6 mg, 19.8 µmol, 1.4 eq.) and 0.3 mg of CuI (1.6 µmol, 0.1 eq.) were dissolved in dry DCM (1 mL). After stirring at 0 °C for 1 h, the reaction mixture was left at ambient temperature overnight. After 24 h, 0.6 mg of resin-N_3 were added to the reaction mixture to remove the slight excess of PMMA-alkyne. Past further 24 h, the copper catalyst was removed *via* filtration through a column of neutral Al_2O_3. PMMA-*b*-PEG was obtained by precipitation in ice-cold hexane and drying.

Table 6.5. Summary of the characterization results for **PMMA-*b*-PEG** listed in tabular form. A PMMA calibration was employed for the calculation of $M_{n,\,SEC(THF)}$. Refer to **Figure 3.3** for the SEC trace and the ^{1}H NMR spectrum.

Species	$M_{n,\,SEC(THF)}$ / g mol^{-1}	$Đ$
PMMA-*b*-PEG	6500	1.1

6.3.4 Modification of the Block Copolymer *via* Radical Thiol-Ene Ligation

Under argon atmosphere, 20.0 mg of PMMA-*b*-PEG (1.0 eq.), 1.0 eq. of a thiol derivative (9.1 mg of PS-SH, 8.0 mg of PEG-SH or 0.8 mg of 1-dodecanethiol) and 1.0 mg of AIBN (6.0 µmol, 1.5 eq.) were dissolved in 1,4-dioxane (1 mL). Subsequently, the flask was placed in an oil bath at 60 °C for 29 h. The modified block copolymer species were received *via* precipitation in ice-cold hexane and drying under vacuum.

Table 6.6. Summary of the characterization results for **PMMA-*b*-PEG** modified with three different thiols listed in tabular form. A PMMA calibration was employed for the calculation of $M_{n,\,SEC(THF)}$. Refer to **Figures 3.4** and **3.5** for ^{1}H NMR spectra and SEC traces, respectively.

Species	$M_{n,\,SEC(THF)}$ / g mol^{-1}	$Đ$
μPMMA-PEG-PS	6600	1.2
μPMMA-PEG-PEG	6300	1.2
PMMA-*b*-PEG-Dode	7700	1.1

6.4 Synthetic Procedures of Chapter 4

6.4.1 Synthesis of the Small Molecules

Synthesis of prop-2-yn-1-yl 4-((2-formyl-3-methylphenoxy)methyl)benzoate (Ph-alkyne)

The synthesis consists of five steps from which step 1 to 4 were accomplished according to literature (step 1,[515] step 2,[337] step 3,[334] step 4[334]).

For the fifth step, 2.00 g of 4-((2-formyl-3-methylphenoxy)methyl)benzoic acid (7.40 mmol, 1.0 eq.), 4.28 mL of propargyl alcohol (4.15 g, 74.00 mmol, 10.0 eq., dried over sodium sulfate prior to reaction) and 45.2 mg of DMAP (0.37 mmol, 0.05 eq.) were dissolved in dry THF (30 mL). At 0 °C, 2.13 g of EDC·HCl (11.1 mmol, 1.5 eq.) were added, and the reaction mixture was stirred for three days at ambient temperature. After removal of the solvent under reduced pressure, the residue was dissolved in a mixture of DCM and water (1:1). The organic phase was washed with 1N HCl, sat. $NaHCO_3$ solution, water and brine, and dried over magnesium sulfate. Without further purification, the product was obtained as pale yellow powder after removal of the solvent under reduced pressure (2.21 g, 7.18 mmol, 97 %).

^{1}H NMR ($CDCl_3$, 400 MHz): δ / ppm = 10.76 (s, 1 H, CO*H*), 8.10 (d, 2 H, ^3J = 8.4 Hz, $H_{arom.}$), 7.52 (d, 2 H, ^3J = 8.6 Hz, $H_{arom.}$), 7.36 (t, 1 H, ^3J = 7.8 Hz, $H_{arom.}$), 6.85 (d, 2 H, ^3J = 8.4 Hz, $H_{arom.}$), 5.23 (s, 2 H, CH_2Ph), 4.94 (d, 2 H, ^4J = 2.5 Hz, CH_2CCH), 2.59 (s, 3 H, CH_3), 2.53 (d, 1 H, ^4J = 2.5 Hz, CH_2CC*H*). ^{13}C NMR ($CDCl_3$, 100 MHz): δ / ppm = 192.10 (s, 1 C), 165.54 (s, 1 C), 161.99 (s, 1 C), 142.48 (s, 1 C), 141.99 (s, 1 C), 134.54 (s, 1 C), 130.40 (s, 2 C), 129.36 (s, 1 C), 127.02 (s, 2 C), 124.88 (s, 1 C), 123.83 (s, 1 C), 110.43 (s, 1 C), 77.77 (s, 1 C), 75.23 (s, 1 C), 70.01 (s, 1 C), 52.69 (s, 1 C), 21.61 (s, 1 C).

ESI-MS: $[M+Na^+]^+/z_{exp.} = 331.0932$,
$[M+Na^+]^+/z_{theo.} = 331.0941$.

Refer to **Figures C.1** and **C.2** for the ^{1}H NMR and ^{13}C NMR spectrum of prop-2-yn-1-yl 4-((2-formyl-3-methylphenoxy)methyl)benzoate (Ph-alkyne), respectively.

6.4.2 Synthesis of the Parent Polymer Species

Synthesis of PE-N_3

PE-N_3 was obtained according to a previously described modification strategy.[125] 5 g of PE-I and 400 mg of NaN_3 were suspended in DMF (50 mL), and heated at 150 °C under argon atmosphere for two hours. After reaching ambient temperature, 10 mL of MeOH were added to precipitate the resulting functionalized PE derivative. The final polymer species, PE-N_3, was obtained after filtration and drying up to constant weight.

Table 6.7. Summary of the characterization results for **PE-N_3** listed in tabular form. A PE calibration was employed for the calculation of $M_{n,\,SEC(TCB)}$. The comparison of the magnetic resonance of the protons next to the azide group at 3.00 ppm and the backbone magnetic resonances between 1.55 and 0.95 ppm delivers $M_{n,\,NMR}$. Refer to **Figure 4.1** for the SEC trace and the ^{1}H NMR spectrum.

Species	$M_{n,\,SEC(TCB)}$ / g mol^{-1}	$Đ$	$M_{n,\,SEC(THF)}$ / g mol^{-1}	$Đ$	$M_{n,\,NMR}$
PE-N_3	1100	1.28	-	-	1200

Synthesis of PE-Ph

In a pressure tube, 0.1 g of PE-N_3 (0.091 mmol, 1.00 eq.), 35.9 mg of Ph-alkyne (0.116 mmol, 1.29 eq.), 1.9 mg of $CuSO_4 \cdot 5H_2O$ (0.0076 mmol, 0.08 eq.) and 1.8 mg of sodium ascorbate (0.0091 mmol, 0.10 eq.) were suspended in a mixture of toluene and DMF (10 mL, toluene:DMF = 7:3). The suspension was deoxygenated *via* purging with argon for 10 min and subsequently heated to 100 °C for 3 days. After reaching ambient temperature, 10 mL of MeOH were added to precipitate the functionalized PE species. PE-Ph was obtained by filtration, washing with MeOH and drying.

Table 6.8. Summary of the characterization results for **PE-Ph** listed in tabular form. A PE calibration was employed for the calculation of $M_{n,\,SEC(TCB)}$. The comparison of the magnetic resonance of the benzylic methyl group of the *ortho*-methylbenzaldehyle at 2.50 ppm and the backbone magnetic resonances between 1.55 and 0.95 ppm delivers $M_{n,\,NMR}$. Refer to **Figure 4.1** for the SEC trace and the ^{1}H NMR spectrum.

Species	$M_{n,\,SEC(TCB)}$ / g mol^{-1}	$Đ$	$M_{n,\,SEC(THF)}$ / g mol^{-1}	$Đ$	$M_{n,\,NMR}$
PE-Ph	1200	1.25	-	-	1600

Synthesis of the furan-protected maleimide-terminated polymer blocks

The presented polymerization procedure was adapted from the literature.[556] In a Schlenk flask, a suspension of 88.0 mg of iron powder (1.570 mmol, 10.0 eq.), 35.0 mg of $CuBr_2$ (0.157 mmol, 1.0 eq.) and 451.0 µL of Me_6TREN (389.0 mg, 1.730 mmol, 11.0 eq.) in DMSO (1.6 mL) was degassed *via* purging with argon for 20 min. Subsequently, 40.3 mg of PG-Mal initiator (0.157 mmol, 1.0 eq.) dissolved in 3.1 mL of styrene (2.8 g, 27.0 mmol, 240.0 eq.) were added to the Schlenk flask, and the polymerization mixture was deoxygenated *via* three freeze-pump-thaw cycles. After stirring at 30 °C for 22 h, the polymerization was stopped by dilution with THF, and the copper catalyst was removed by filtration through neutral Al_2O_3. The protected maleimide terminated polystyrene block (PS-Mal (pro)) was obtained as white powder *via* two-fold precipitation in ice-cold methanol and subsequent drying (700 mg). For PS2-Mal (pro), the amount of the catalytic system (copper compound and ligand) and reducing agent was lowered by a factor of 10.

The presented polymerization procedure is adapted from the literature.[556] In a Schlenk flask, a suspension of 8.8 mg of iron powder (0.157 mmol, 1.0 eq.), 3.5 mg of $CuBr_2$ (0.0157 mmol, 0.1 eq.) and 45.1 µL of Me_6TREN (38.9 mg, 0.173 mmol, 1.1 eq.) in acetonitrile (1.8 mL) was degassed *via* purging with argon for 20 min. 40.3 mg of PG-Mal initiator (0.157 mmol, 1.0 eq.) dissolved in 3.6 mL of MMA (3.4 g, 27.0 mmol, 222.0 eq.) were added to the Schlenk flask, and the polymerization mixture was deoxygenated *via* three freeze-pump-thaw cycles. After stirring at 30 °C for 5 h, the polymerization was stopped by dilution with THF, and the copper catalyst was removed by filtration through neutral Al_2O_3. PMMA-Mal (pro) was obtained *via* two-fold precipitation in ice-cold water and drying (800 mg).

Table 6.9. Summary of the characterization results for **PS-Mal (pro)**, **PS2-Mal (pro)** and **PMMA-Mal (pro)** terminated with a furan-protected maleimide end group listed in tabular form. A PS and PMMA calibration were employed for the calculation of $M_{n,\,SEC(THF)}$ for **PS-Mal (pro)**, **PS2-Mal (pro)** and **PMMA-Mal (pro)**, respectively. The comparison of magnetic resonance d and e and the backbone magnetic resonances between 7.20 and 6.20 ppm delivers $M_{n,\,NMR}$ for **PS-Mal (pro)** and **PS2-Mal (pro)**, while magnetic resonance k at 6.25 ppm was compared to the backbone magnetic resonance e at 3.53 ppm for the calculation of $M_{n,\,NMR}$ for **PMMA-Mal (pro)**. Refer to **Figures C.5** and **C.8** for the SEC traces and to **Figures C.3**, **C.4** and **C.8** for the ^{1}H NMR spectra.

Species	$M_{n,\,SEC(TCB)}$ / g mol^{-1}	$Đ$	$M_{n,\,SEC(THF)}$ / g mol^{-1}	$Đ$	$M_{n,\,NMR}$
PS-Mal (pro)	-	-	5000	1.08	5100
PMMA-Mal (pro)	-	-	5500	1.23	3800
PS2-Mal (pro)	-	-	2200	1.08	2800

Removal of Furan as Protecting Group of the Maleimide-Terminated Polymer Species PS-Mal (pro), PS2-Mal (pro) and PMMA-Mal (pro)

The deprotection step was accomplished in bulk in a drying oven under vacuum using elevated temperatures. After 24 h at 110 °C, the ^{1}H NMR spectra in **Figures C.3** and **C.4** indicate complete removal of the furan moiety for PS-Mal (pro) and PMMA-Mal (pro) while the SEC traces in **Figure C.5** display successful retention of the narrow polymer distribution. In comparison, PS2-Mal (pro) was completely deprotected after 120 h at 100 °C (refer to **Figure C.8** for SEC trace and ^{1}H NMR spectra).

Table 6.10. Summary of the characterization results for **PS-Mal**, **PS2-Mal** and **PMMA-Mal** terminated with a free maleimide end group listed in tabular form. $M_{n,\,SEC(TCB)}$ is obtained by the utilization of a PE calibration. A PS and PMMA calibration were employed for the calculation of $M_{n,\,SEC(THF)}$ for **PS-Mal (pro)**, **PS2-Mal (pro)** and **PMMA-Mal (pro)**, respectively. The comparison of magnetic resonance d and e and the backbone magnetic resonances between 7.20 and 6.20 ppm delivers $M_{n,\,NMR}$ for **PS-Mal** and **PS2-Mal**, while the magnetic resonance l at 6.71 ppm was compared to the backbone magnetic resonance e at 3.53 ppm for the calculation of $M_{n,\,NMR}$ for **PMMA-Mal**. Refer to **Figures C.5**, **4.3** and **C.8** for the SEC traces and to **Figures C.3**, **C.4** and **C.8** for the ^{1}H NMR spectra.

Species	$M_{n,\,SEC(TCB)}$ / g mol^{-1}	$Đ$	$M_{n,\,SEC(THF)}$ / g mol^{-1}	$Đ$	$M_{n,\,NMR}$
PS-Mal	2300	1.10	5000	1.10	5000
PMMA-Mal	1500	1.38	5300	1.20	4000
PS2-Mal	1000	1.15	2300	1.15	2800

6.4.3 UV Light-Induced End Group Modification and Block Copolymer Formation

1.0 eq. of PE-Ph and 5.0 eq. of *N*-ethyl maleimide (or 1.0 eq. of a maleimide-terminal polymer (PS-Mal, PS2-Mal or PMMA-Mal)) were dissolved in a mixture of ACN and toluene (1:1, $4 \cdot 10^{-5}$ mol L^{-1}). The reaction mixture was heated to 100 °C, and subsequently placed in a custom-build photoreactor. The solution was irradiated for an hour while stirring. A compact lamp was employed as irradiation source (Philips PL-L cleo, for emission spectra refer to **Figure A.1**). In order to keep the reactants in solution, the reaction mixture was taken from the photoreactor and again heated to 100 °C. In total, the heating-irradiation cycle was repeated five times to ensure full conversion. After removal of close to 90 % of the solvent, MeOH was added in order to precipitate the modified polymer or the block copolymer. The final polymer species were directly analyzed after filtration and drying.

While, the NMR and SEC results of the light-induced end group modification of PE-Ph are depicted in **Figure 4.2**, the results for the block copolymer formation are visualized in **Figures 4.3** and **C.8**. A summary of the results for the light-induced modification of PE-Ph listed in tabular form is provided in **Table 4.1** in the Results and Discussion Section.

6.4.4 Surface Modification

Surface preparation

One side polished silicon (Si) wafers (CZ, orientation <100>, B-doped, resistivity 1-100 Ω cm) with approx. 1.5 nm natural oxide and approx. 250 nm (SHE-Europe Ltd., Scotland) thermal silicon dioxide (SiO_2) over-layer were cut into square pieces and thoroughly rinsed with water. Dry samples were exposed to air plasma for 15 min just before polymer deposition. The plasma-activated surfaces were functionalized with APTES according to a procedure reported in literature.[557]

4-maleimidobutyroyl chloride was synthesized and attached to the surfaces functionalized with APTES according to literature.[554, 557]

Synthesis of PE-Ph-I

In a pressure tube, 0.1 g of PE-N_3 (0.091 mmol, 1.00 eq.), 35.9 mg of Ph-alkyne (0.116 mmol, 1.29 eq.), 47.8 mg of dried $Cu(ClO_4)_2$ (0.182 mmol, 2.00 eq.), 60.4 mg of KI (0.364 mmol, 4.00 eq.), 12.6 µL of

NEt_3 (9.2 mg, 0.091 mmol, 1.0 eq.) and 4.8 mg of TBTA (0.0091 mmol, 0.10 eq.) were suspended in a mixture of toluene and DMF (10 mL, toluene:DMF = 7:3). The suspension was deoxygenated *via* purging with argon for 10 min, and subsequently heated to 100 °C for 3 days. After reaching ambient temperature, 10 mL of MeOH were added to precipitate the functionalized PE species. PE-Ph-I was obtained by filtration, washing with MeOH and drying. The ^{1}H NMR spectrum of PE-Ph-I in **Figure C.9** indicates that a mixture of iodo-functionalized and non-iodo-functionalized species was obtained.

6.5 Synthetic Procedures of Chapter 5

6.5.1 Synthesis of the Small Molecules

Synthesis of 1-Pyrenecarbaldehyde Oxime

Under inert atmosphere, 2.00 g of 1-pyrenecarboxaldehyde (8.69 mmol, 1.00 eq.) were dissolved in a mixture of dry DCM and MeOH (1:1, 300 mL). 1.81 g of hydroxylamine hydrochloride (26.06 mmol, 3.00 eq.) and 2.14 g of sodium acetate (26.06 mmol, 3.0 eq.) were subsequently added to the solution, and the resulting suspension was stirred for 24 h at ambient temperature. Thereupon, the solvent was removed under reduced pressure, and the crude product was dissolved in DCM and washed twice with 1N HCl. After drying over $MgSO_4$ and removal of the solvent under reduced pressure, the final product (2.05 g, mmol, 96 %) was isolated as a light yellow solid.

^{1}H NMR ($CDCl_3$, 400 MHz): δ / ppm = 9.15 (s, 1 H, CO*H*), 8.60 (d, 1 H, ^3J = 9.4 Hz, H_{Py}), 8.37 (d, 1 H, ^3J = 8.0 Hz, H_{Py}), 8.24-8.02 (m, 7 H, H_{Py}). ^{13}C NMR ($CDCl_3$, 100 MHz): δ / ppm = 149.67 (s, 1 C), 132.50 (s, 1 C), 131.31 (s, 1 C), 130.66 (s, 1 C), 129.10 (s, 1 C), 128.70 (s, 1 C), 128.45 (s, 1 C), 127.39 (s, 1 C), 126.26 (s, 1 C), 125.93 (s, 1 C), 125.68 (s, 1 C), 125.21 (s, 1 C), 125.01 (s, 1 C), 124.95 (s, 1 C), 124.92 (s, 1 C), 124.63 (s, 1 C), 122.80 (s, 1 C).

ESI-MS: $[M+H^+]^+/z_{exp.}$ = 246.0910,
$[M+H^+]^+/z_{theo.}$ = 246.0913,
$[M+Na^+]^+/z_{exp.}$ = 268.0728,
$[M+Na^+]^+/z_{theo.}$ = 268.0733.

Refer to **Figures D.1** and **D.2** for ^{1}H and ^{13}C NMR spectra, respectively.

Synthesis of *N*-hydroxypyrene-1-carbimidoyl chloride (chloro pyrene oxime, PyOCl)

Based on a literature procedure,[558] 1.00 g of 1-pyrenecarbaldehyde oxime (4.08 mmol, 1.00 eq.) and 0.544 g of *N*-chlorsuccinimide (4.08 mmol, 1.00 eq.) were dissolved in dry DMF (15 mL), and the reaction mixture was stirred at 60 °C for 4 h. After reaching ambient temperature, the crude product mixture was directly purified *via* column chromatography (silica gel, cyclohexane:dichloromethane = gradient from 3:1 to 1.5:1) yielding the product as a yellow solid (0.50 g, 1.79 mmol, 44 %).

^{1}H NMR ($CDCl_3$, 400 MHz): δ / ppm = 8.14-7.44 (m, 9 H, H_{Py}). ^{13}C NMR ($CDCl_3$, 100 MHz): δ / ppm = 132.69 (s, 1 C), 132.57 (s, 1 C), 130.81 (s, 1 C), 130.44 (s, 1 C), 129.75 (s, 1 C), 129.55 (s, 1 C), 129.43 (s, 1 C), 126.75 (s, 1 C), 126.73 (s, 1 C), 126.54 (s, 1 C), 126.50 (s, 1 C), 124.44 (s, 1 C), 123.95 (s, 1 C), 123.48 (s, 1 C), 123.40 (s, 1 C), 106.76 (s, 1 C).

ESI-MS: $[M+H^+]^+/z_{exp.}$ = 280.0517,
$[M+H^+]^+/z_{theo.}$ = 280.0524,
$[M+Na^+]^{1+}/z_{exp.}$ = 302.0338,
$[M+Na^+]^+/z_{theo.}$ = 302.0343.

Elemental analysis ($C_{17}H_{10}NOCl$): calculated: N 5.01; C 73.00; H 3.60,
found: N 4.69; C 73.96, H 3.79.

Refer to **Figures 5.1** and **5.2** for ^{1}H and ^{13}C NMR spectra, respectively.

Synthesis of pyrene-1-carbaldehyde O-(4-vinylbenzoyl) oxime (PyOHSty)

1.94 g of 1-pyrenecarbaldehyde oxime (7.92 mmol, 1.0 eq.), 1.29 g of 4-vinylbenzoic acid (8.71 mmol, 1.1 eq.) and 4.8 mg of DMAP (0.40 mmol, 0.05 eq.) were dissolved in a mixture of DCM and THF (1:1, 50 mL). After cooling down to 0 °C, 1.82 g of EDC·HCl (9.50 mmol, 1.2 eq.) were added, and the reaction mixture was stirred at ambient temperature overnight. After removal of the solvent under reduced pressure, the residue was dissolved in DCM. The organic phase was washed with sat. $NaHCO_3$, 1H HCl, water and brine. Drying over $MgSO_4$ and removal of the solvent delivered the crude product, which was purified *via* column chromatography (cyclohexane: DCM = 1:4). The targeted compound was received as pale yellow solid (2.82 g, 7.54 mmol, 95 %).

^{1}H NMR ($CDCl_3$, 400 MHz): δ / ppm = 9.55 (s, 1 H, CO*H*), 8.76 (d, 1 H, ^{3}J = 8.0 Hz, H_{Py}), 8.62 (d, 1 H, ^{3}J = 8.0 Hz, H_{Py}), 8.29-8.05 (m, 7 H, H_{Py}), 8.19 (d, 2 H, ^{3}J = 8.4 Hz, H_{Ph}), 7.56 (d, 2 H, ^{3}J = 8.2 Hz, H_{Ph}), 6.81 (dd, 1 H, ^{3}J = 17.8 Hz, ^{3}J = 11.2 Hz, C*H*CH_2), 5.93 (d, 1 H, ^{3}J = 17.6 Hz, CHCH_2), 5.45 (d, 1 H, ^{3}J = 10.8 Hz, CHCH_2). ^{13}C NMR ($CDCl_3$, 100 MHz): δ / ppm = 164.06 (s, 1 C), 155.99 (s, 1 C), 142.65 (s, 1 C), 136.13 (s, 1 C), 133.94 (s, 1 C), 131.34 (s, 1 C), 130.68 (s, 1 C), 130.30 (s, 2 C), 129.68 (s, 1 C), 129.47 (s, 1 C), 127.95 (s, 1 C), 127.53 (s, 1 C), 126.94 (s, 1 C), 126.58 (s, 2 C), 126.51 (s, 2 C), 126.28 (s, 1 C), 125.16 (s, 1 C), 125.03 (s, 1 C), 124.58 (s, 1 C), 122.88 (s, 2 C), 117.07 (s, 1 C).

ESI-MS: $[M+H^+]^+/z_{exp.}$ = 376.1325,
$[M+H^+]^+/z_{theo.}$ = 376.1332,
$[M+Na^+]^+/z_{exp.}$ = 398.1143,
$[M+Na^+]^+/z_{theo.}$ = 398.1151.

Refer to **Figures 5.8** and **5.9** for ^{1}H and ^{13}C NMR spectra, respectively.

6.5.2 Small Molecule Synthesis Induced *via* Visible Light Irradiation

In a round bottom flask, the respective dipolarophile (268.1 µmol, 5.0 eq.) and the chloro oxime derivative (15.0 mg, 53.6 µmol, 1.0 eq.) were dissolved in dry DCM (60 mL) and subsequently irradiated with an LED setup (410-420 nm, refer to **Figure A.2** for the emission spectrum) in a distance of 5 cm in a custom-built photoreactor for one hour. The solvent was removed under reduced pressure, and the cycloadducts were purified *via* column chromatography.

In order to elucidate the effectiveness of ambient laboratory light compared to the LED setup, the same stoichiometry of reactants was dissolved in DCM (similar concentrations). While one half of the solution was irradiated with the LED setup, the other half was left standing on a laboratory bench exposed to ambient light. After one hour, the solvent was removed and the crude mixture was immediately analyzed *via* NMR spectroscopy.

For the photoligation of biotin-mal, 1.0 eq. of PyOCl and 1.0 eq. of the dienophilic compound were dissolved in a mixture of DCM and DMSO (1:1). The reaction mixture was subsequently irradiated with the same LED setup for one hour. After removal of the solvent, residual chloro pyrene oxime was dissolved in DCM and separated from the insoluble product. The modified biotin species was analyzed *via* NMR spectroscopy.

For ^{13}C NMR spectroscopy experiments, 1.0 eq. of the chloro pyrene oxime was dissolved in 0.5 mL of $CDCl_3$ ($c = 9.64 \cdot 10^{-5}$ mol L^{-1}). Immediately after the addition of 0.9 eq. of *N*-ethyl maleimide in the absence of any light source, a ^{13}C NMR spectrum (256 scans) was recorded. Likewise - in another experiment - after irradiation of the reactants with the LED setup in a NMR tube, a further ^{13}C NMR spectrum was recorded.

Cycloadduct C1

^1H NMR ($CDCl_3$, 400 MHz): δ / ppm = 9.21 (d, ^3J = 9.2 Hz, 1 H, H_{Py}), 8.26-7.99 (m, 8 H, H_{Py}), 5.30 (dd, ^3J = 9.9 Hz, ^3J = 8.0 Hz, 1 H, C*H*), 4.01 (d, ^3J = 7.8 Hz, 1 H, CH_2), 4,01 (d, ^3J = 9,4 Hz, 1 H, CH_2), 3.89 (s, 3 H, OCH_3). ^{13}C NMR ($CDCl_3$, 100 MHz): δ / ppm = 171.04 (s, 1 C), 157.20 (s, 1 C), 132.80 (s, 1 C), 131.36 (s, 1 C), 130.84 (s, 1 C), 129.55 (s, 1 C), 129.39 (s, 1 C), 129.15 (s, 1 C), 127.25 (s, 1 C), 126.77 (s, 1 C), 126.54 (s, 1 C), 126.17 (s, 1 C), 126.06 (s, 1 C), 126.02 (s, 1 C), 125.26 (s, 1 C), 124.56 (s, 1 C), 124.45 (s, 1 C), 122.24 (s, 1 C), 77.34 (s, 1 C), 53.08 (s, 1 C), 42.37 (s, 1 C).

ESI-MS: $[M+H^+]^+/z_{exp.}$ = 330.1119,
$[M+H^+]^+/z_{theo.}$ = 330.1125,
$[M+Na^+]^+/z_{exp.}$ = 352.0939,
$[M+Na^{1+}]^+/z_{theo.}$ = 352.0944.

Cycloadduct C2

^1H NMR ($CDCl_3$, 400 MHz): δ / ppm = 9.05 (d, ^3J = 9.4 Hz, 1 H, H_{Py}), 8.36 (d, ^3J = 8.1 Hz, 1 H, H_{Py}), 8.23-8.00 (m, 7 H, H_{Py}), 5.57 (d, ^3J = 9.6 Hz, 1 H, C*H*), 5.15 (d, ^3J = 9.6 Hz, 1 H, C*H*), 3.65-3.51 (m, 2 H, CH_2), 1.16 (t, ^3J = 7.2 Hz, 3 H, CH_3). ^{13}C NMR ($CDCl_3$, 100 MHz): δ / ppm = 172.05 (s, 1 C), 170.78 (s, 1 C), 153.81 (s, 1 C), 133.19 (s, 1 C), 131.25 (s, 1 C), 130.64 (s, 1 C), 129.81 (s, 1 C), 129.69 (s, 1 C), 129.46 (s, 1 C), 128.08 (s, 1 C), 127.25 (s, 1 C), 126.56 (s, 1 C), 126.41 (s, 1 C), 126.18 (s, 1 C), 125.44 (s, 1 C), 125.18 (s, 1 C), 124.50 (s, 1 C), 124.30 (s, 1 C), 119.90 (s, 1 C), 79.46 (s, 1 C), 57.18 (s, 1 C), 34.85 (s, 1 C), 12.91 (s, 1 C).

ESI-MS: $[M+H^+]^+/z_{exp.}$ = 369.1228,
$[M+H^+]^+/z_{theo.}$ = 369.1234,
$[M+Na^+]^+/z_{exp.}$ = 391.1044,
$[M+Na^+]^+/z_{theo.}$ = 391.1053.

Cycloadduct C3

^{1}H NMR ($CDCl_3$, 400 MHz): δ / ppm = 9.30 (d, ^{3}J = 9.5 Hz, 1 H, H_{Py}), 8.26-7.99 (m, 8 H, H_{Py}), 7.56-7.34 (m, 5 H, H_{Ph}), 5.87 (dd, ^{3}J = 10.8 Hz, ^{3}J = 8.2 Hz, 1 H, C*H*), 4.14 (dd, ^{2}J = 16.6 Hz, ^{3}J = 11.0 Hz, 1 H, CH_2), 3.72 (dd, ^{2}J = 16.6 Hz, ^{3}J = 8.0 Hz, 1 H, CH_2). ^{13}C NMR ($CDCl_3$, 100 MHz): δ / ppm = 157.33 (s, 1 C), 141.15 (s, 1 C), 132.53 (s, 1 C), 131.42 (s, 1 C), 130.91 (s, 1 C), 129.47 (s, 1 C), 129.23 (s, 1 C), 129.00 (s, 2 C), 128.94 (s, 1 C), 128.43 (s, 1 C), 127.29 (s, 1 C), 126.69 (s, 1 C),126.49 (s, 1 C), 126.15 (s, 1 C), 126.13 (s, 2 C), 126.04 (s, 1 C), 125.93 (s, 1 C), 125.33 (s, 1 C), 124.59 (s, 1 C), 124.56 (s, 1 C), 123.35 (s, 1 C), 81.92 (s, 1 C), 46.70 (s, 1 C).

ESI-MS: $[M+H^+]^+/z_{exp.}$ = 348.1378,
$[M+H^+]^+/z_{theo.}$ = 348.1383,
$[M+Na^+]^+/z_{exp.}$ = 370.1196,
$[M+Na^+]^+/z_{theo.}$ = 370.1202.

Cycloadduct C4

^{1}H NMR ($CDCl_3$, 400 MHz): δ / ppm = 8.84 (d, ^{3}J = 9.4 Hz, 1 H, H_{Py}), 8.25-8.01 (m, 8 H, H_{Py}), 5.62 (d, ^{3}J = 5.8 Hz, 1 H, C*H*), 5.22 (d, ^{3}J = 5.6 Hz, 1 H, C*H*), 4.43-4.35 (m, 2 H, CH_2), 4.05-3.95 (m, 2H, CH_2), 1.41 (t, ^{3}J = 7.0 Hz, 3 H, CH_3), 0.87 (t, ^{3}J = 7.2 Hz, 3 H, CH_3). ^{13}C NMR ($CDCl_3$, 100 MHz): δ / ppm = 169.12 (s, 1 C), 167.80 (s, 1 C), 154.86 (s, 1 C), 132.75 (s, 1 C), 131.31 (s, 1 C), 130.84 (s, 1 C), 129.96 (s, 1 C), 129.26 (s, 1 C), 129.11 (s, 1 C), 127.26 (s, 1 C), 126.95 (s, 1 C), 126.53 (s, 1 C), 126.13 (s, 1 C), 126.01 (s, 1 C), 125.19 (s, 1 C), 125.12 (s, 1 C), 124.42 (s, 1 C), 124.41 (s, 1 C), 121.48 (s, 1 C), 81.68 (s, 1 C), 62.73 (s, 1 C), 62.44 (s, 1 C), 59.95 (s, 1 C), 14.30 (s, 1 C), 13.83 (s, 1 C).

ESI-MS: $[M+H^+]^{1+}/z_{exp.}$ = 416.1488,
$[M+H^+]^+/z_{theo.}$ = 416.1492,
$[M+Na^+]^+/z_{exp.}$ = 438.1307,
$[M+Na^+]^+/z_{theo.}$ = 438.1313.

Cycloadduct C5

^{1}H NMR ($CDCl_3$, 400 MHz): δ / ppm = 8.28-8.03 (m, 9 H, H_{Py}), 4.56 (q, ^{3}J = 7.0 Hz, 2 H, CH_2), 4.05 (q, ^{3}J = 7.0 Hz, 2 H, CH_2), 1.49 (t, ^{3}J = 7.0 Hz, 3 H, CH_3), 0.86 (t, ^{3}J = 7.0 Hz, 3 H, CH_3). ^{13}C NMR

($CDCl_3$, 100 MHz): δ / ppm = 162.18 (s, 1 C), 160.60 (s, 1 C), 160.43 (s, 1 C), 156.58 (s, 1 C), 132.82 (s, 1 C), 131.35 (s, 1 C), 130.85 (s, 1 C), 129.97 (s, 1 C), 128.96 (s, 1 C), 128.90 (s, 1 C), 127.60 (s, 1 C), 127.40 (s, 1 C), 126.53 (s, 1 C), 126.12 (s, 1 C), 125.97 (s, 1 C), 124.78 (s, 1 C), 124.56 (s, 1 C), 124.52 (s, 1 C), 124.21 (s, 1 C), 121.32 (s, 1 C), 117.69 (s, 1 C), 63.25 (s, 1 C), 62.06 (s, 1 C), 14.22 (s, 1 C), 13.64 (s, 1 C).

ESI-MS: $[M+H^+]^+/z_{exp.}$ = 414.1330,
$[M+H^+]^+/z_{theo.}$ = 414.1336,
$[M+Na^+]^+/z_{exp.}$ = 436.1151,
$[M+Na^+]^+/z_{theo.}$ = 436.1155.

The ^1H and ^{13}C NMR spectra of the cycloadducts are collected in **Figures D.5** to **D.14**.

6.5.3 Polymer End Group Transformation Induced *via* Visible Light Irradiation

The poly(ethylene glycol) methyl ether derivative equipped with a maleimide (P1) or pentene (P2) termini (4.80 µmol, 1.00 eq.) and chloro pyrene oxime (5.00 eq.) were dissolved in dry DCM (20 mL). The reaction mixtures were placed in the photoreactor and irradiated for 4 h while stirring (410-420 nm, refer to **Figure A.2** for the emission spectrum). For ESI-MS measurements, the crude reaction mixtures were directly analyzed without any additional purification steps. For ^1H NMR analysis, PC1 was precipitated in ice-cold Et_2O twice.

End group modified polymer species PC1

^1H NMR ($CDCl_3$, 400 MHz): δ / ppm = 9.11 (d, ^3J = 9.4 Hz, 1 H, H_{Py}), 8.33-8.03 (m, 8 H, H_{Py}), 5.63 (d, ^3J = 9.6 Hz, 1 H, C*H*), 5.26 (d, ^3J = 9.6 Hz, 1 H, C*H*), 4.14-4.10 (m, 2 H, CH_2OCO), 3.83-3.79 (m, 2 H, CH_2N), 3.64 (bs, PEG backbone), 3.37 (s, 3 H, OCH_3), 2.34-2.31 (m, 2 H, OCOCH_2), 1.95-1.88 (m, 2 H, $CH_2CH_2CH_2N$).

The ^1H NMR spectrum of **PC1** is displayed in **Figure D.16**. For ESI-MS analysis of the end group modification of the polymers, refer to **Figures 5.6** and **D.15** as well as **Table D.1**.

6.5.4 Copolymerization of PyOHSty

1.5 mg of AIBN ($9.13 \cdot 10^{-3}$ mmol, 1.0 eq.), 10.0 mg of CDB ($36.71 \cdot 10^{-3}$ mmol, 4.0 eq.), 3.0 g of styrene (28.80 mmol, 3154.4 eq.) and a variable amount of PyOHSty (1.33/0.80/0.27 mmol) were dissolved in *ortho*-chlorobenzene (2 mL), and subsequently degassed *via* purging with argon for 30 min. The polymerization was conducted at 60 °C for 26.5 h. Chain growth was stopped *via* cooling with liquid nitrogen and the final polymer was purified *via* three-fold precipitation in ice-cold methanol.

Table 5.1 summarizes the characterization results for the distinct polymer species. The ^{1}H NMR spectra of the polymer species are displayed in **Figures 5.11**, **D.17** and **D.18** while the SEC traces are presented in **Figure 5.12**.

6.5.5 LED Irradiation of CDB PS PyOHSty 1-3

8.0 mg of CDB PS PyOHSty 1-3 were dissolved in DCM (400 mL) and the solution was deoxygenated *via* purging with argon for 1 h. Subsequently, the polymer solutions were irradiated with an LED setup (430-435 nm, 3×3 W, refer to **Figure A.2** for the emission spectrum) for 2.5 h. Subsequently, the solvent was removed under reduced pressure, and the irradiated polymer species were purified *via* precipitation in ice-cold methanol.

Table 5.1 summarizes the characterization results for the distinct polymer species. The ^{1}H NMR spectra of the polymer species are displayed in **Figures 5.11** and **D.17** while the SEC traces are presented in **Figure 5.12**.

CHAPTER 7

CONCLUSION AND OUTLOOK

The benefit of spatiotemporal control as well as economic aspects allow light-induced ligation protocols to thrive in polymer chemistry. Without the employment of catalysts or additives and neglecting high energy activation for two photon processes, efficient and fast photo-induced ligation reactions have become a powerful tool for the construction of sophisticated macromolecular architectures in addition to smart matter in material science.

As a result, the current thesis both broadens the application of photochemically induced ligation reactions in order to expand present frontiers and establishes novel approaches for synthetic chemistry and macromolecular design. In detail, synthetic strategies affording 2*H*-azirines were explored targeting the successful preparation of a photoreactive pyrene-substituted 2*H*-azirine derivative with a carboxylic ester moiety. Furthermore, the photoactivation of the 2*H*-azirine species was demonstrated. Nevertheless, further functionalization steps based on conventional methods were not successful. Consequently, future experiments may include advanced protocols for the activation of the ester moiety without the destruction of the photoreactive unit. For example, selected enzymes are able to accelerate ester hydrolysis in a mild fashion. Moreover, a novel approach for the synthesis of mid-reactive block copolymers based on a CuAAC ligation interrupted by 2*H*-azirines was developed, which was further expanded for the efficient two-step synthesis of mikto-arm star polymers by utilizing subsequent radical thiol-ene ligation. The CuAAC reaction of a PMMA block with a terminal alkyne group and a PEG species capped with an azide functionality delivered a functional block copolymer species. It featured a readily accessible vinyl

functionality at its junction point adjacent to the pyrene unit as fluorescent chromophore. The midpoint-reactive block copolymer was further modified with a small molecule thiol and macromolecular thiols, hence yielding a modified block copolymer and mikto-arm star polymer species in a two-step procedure, respectively. Finally, due to their unique structural composition, the polymer species formed micelles in water showing a behavior similar to unimolecular micelles, as clearly evidenced by in-depth DLS studies. In addition to the efficient two-step synthesis of mikto-arm star polymers, the CuAAC reaction interrupted by 2*H*-azirines holds the potential for further application in macromolecular design. This multicomponent approach can be readily employed for the synthesis of a sequence-defined macromolecule *via* the repetition of interrupted CuAAC ligation followed by radical thiol-ene addition, *e.g.*, starting from a polymeric azide derivative, which facilitates the purification process. The interaction of the pyrene units along the macromolecular chain might lead to interesting molecular dynamics in solution. In addition, brush copolymers with two different polymeric arm types can be synthesized in a facile manner utilizing a simple polyalkyne. The CuAAC reaction interrupted by 2*H*-azirines could potentially facilitate the synthesis of complex macromolecular architectures in the future.

The subsequent part of the current thesis introduced a novel ligation method for polyethylene (PE) derivatives in the area of photochemistry. Herein, the synthesis route yielding a PE species equipped with a photoreactive moiety was described in detail. Most importantly, it was demonstrated that the light-induced Diels–Alder cycloaddition of *ortho*-methylbenzaldehyde as photoactive end group is orthogonal to elevated temperatures, which were required for the solubilization of the PE block. Thus, the photoligation of the photoreactive PE species resulted in a well-defined end group modified PE derivative as well as block copolymers, which are proven to be stable under the conditions employed for analysis. Indeed, these materials containing PE derivatives were obtained photochemically for the first time. Therefore, such photoreactive PE species might be applied in further areas related to photochemistry and polymer chemistry including direct laser writing. However, the grafting of the photoactive PE species onto APTES-functionalized silicon wafer failed due to the fact that the attached maleimide groups or the APTES coating were not stable under the reaction conditions. Thus, further surface substrates require to be tested under elevated temperatures (*e.g.*, polymeric films) in order to afford surfaces with high hydrophobicity arising from the grafted PE species.

Chapter 5 addressed the photochemistry of pyrene-substituted chloro oximes and oxime ester, which are similar in structure but different in reactivity. By equipping a chloro oxime species with pyrene as light-harvesting unit, nitrile oxides as reactive 1,3-dipoles were generated upon LED light or ambient laboratory light exposure. The precursor compound was highly sensitive towards light irradiation, and as a result, the subsequent 1,3-dipole cycloaddition was extraordinary fast and compatible with a vast range of dienophiles, while being orthogonal to distinct functional groups. Nevertheless, in-depth NMR analysis strongly suggested that the cycloaddition was substantially accelerated upon light irradiation. Therefore, the approach presented in this part of the current thesis included a facile incorporation of pyrene as a chromophore as well as the formation of synthetically valuable isoxazoline and isoxazoles in the mildest fashion. Consequently, the chloro pyrene oxime is an ideal candidate to label sensitive compounds including biologically relevant molecules with a fluorophore. In contrast, the pyrene-substituted oxime ester derivative cleaved *via* homolytic bond scission induced by visible light irradiation. A synthesis route towards a monomer carrying the corresponding light-sensitive group was established followed by RAFT-mediated copolymerization with styrene. Subsequently, the light-induced fragmentation process of the oxime ester along the polymer backbone was investigated by varying the content of the photoreactive moiety, and it suggested that intramolecular radical coupling induced chain compaction. As a result, the presented approach adds another method into the toolbox for the synthesis of SCNPs. Furthermore, the pyrene-substituted oxime ester moiety can be used as initiator and catalyst for visible light-induced polymerization processes and thiol-ene additions in future experiments, respectively.

In summary, the current thesis describes recent advances in the area of efficient conjugation protocols for the application in macromolecular design including the synthesis of novel photoreactive units and their analysis under considerably mild conditions.

Nevertheless, significant challenges are still in front of us regarding environmental protection supported by photochemistry. The employment of light with wavelengths between 400 and 450 nm to trigger chemical reactions presents a small step in the right direction. Photoreactive moieties have to be designed, which allow for the activation with higher wavelength values in order to use the full range of visible light. Concomitantly, for λ-orthogonal applications the absorption bands, whose excitation result in the formation of the reactive species, have to be clearly definable. Moreover, it is necessary to identify further photoreactive units, which can be triggered by sunlight instead of high energy irradiation sources. As a

result, continuous research in the interface of photochemistry and polymer science is a crucial condition for future applications in order to rely entirely on solar energy for chemical activation.

BIBLIOGRAPHY

[1] D. Schmaljohann, *Adv. Drug Delivery Rev.* **2006**, *58*, 1655–1670.

[2] K. Cho, X. Wang, S. Nie, Z. G. Chen, D. M. Shin, *Clin. Cancer Res.* **2008**, *14*, 1310–1316.

[3] A. Kumari, S. K. Yadav, S. C. Yadav, *Colloids Surf. B* **2010**, *75*, 1–18.

[4] K. S. Soppimath, T. M. Aminabhavi, A. R. Kulkarni, W. E. Rudzinski, *J. Control. Release* **2001**, *70*, 1 –20.

[5] I. Vroman, L. Tighzert, *Materials* **2009**, *2*, 307–344.

[6] R. A. Gross, B. Kalra, *Science* **2002**, *297*, 803–807.

[7] Y. Yang, M. W. Urban, *Chem. Soc. Rev.* **2013**, *42*, 7446–7467.

[8] S. H. Cho, S. R. White, P. V. Braun, *Adv. Mater.* **2009**, *21*, 645–649.

[9] R. S. Trask, H. R. Williams, I. P. Bond, *Bioinspir. Biomim.* **2007**, *2*, P1–P9.

[10] D. Paul, L. Robeson, *Polymer* **2008**, *49*, 3187–3204.

[11] J.-M. Lehn, *Chem. Soc. Rev.* **2007**, *36*, 151–160.

[12] T. F. A. de Greef, E. W. Meijer, *Nature* **2008**, *453*, 171–173.

[13] F. Croce, G. B. Appetecchi, L. Persi, B. Scrosati, *Nature* **1998**, *394*, 456–458.

[14] J. Song, Y. Wang, C. Wan, *J. Power Sources* **1999**, *77*, 183–197.

[15] S.-I. Na, S.-S. Kim, J. Jo, D.-Y. Kim, *Adv. Mater.* **2008**, *20*, 4061–4067.

[16] H. C. Kolb, M. G. Finn, K. B. Sharpless, *Angew. Chem. Int. Ed.* **2001**, *40*, 2004–2021.

[17] C. Barner-Kowollik, F. E. Du Prez, P. Espeel, C. J. Hawker, T. Junkers, H. Schlaad, W. Van Camp, *Angew. Chem. Int. Ed.* **2011**, *50*, 60–62.

[18] V. Balzani, A. Credi, M. Venturi, *ChemSusChem* **2008**, *1*, 26–58.

[19] G. Ciamician, *Science* **1912**, *36*, 385–394.

[20] M. F. Hohmann-Marriott, R. E. Blankenship, *Annu. Rev. Plant Biol.* **2011**, *62*, 515–548.

[21] G. Delaittre, A. S. Goldmann, J. O. Mueller, C. Barner-Kowollik, *Angew. Chem. Int. Ed.* **2015**, *54*, 11388–11403.

[22] M. Buback, *Macromol. Symp.* **2009**, *275-276*, 90–101.

[23] S. Chatani, C. J. Kloxin, C. N. Bowman, *Polym. Chem.* **2014**, *5*, 2187–2201.

[24] E. J. Park, G. T. Carroll, N. J. Turro, J. T. Koberstein, *Soft Matter* **2009**, *5*, 36–50.

[25] M. A. Tasdelen, G. Yilmaz, B. Iskin, Y. Yagci, *Macromolecules* **2012**, *45*, 56–61.

[26] S. Yamago, Y. Nakamura, *Polymer* **2013**, *54*, 981–994.

[27] M. Chen, M. Zhong, J. A. Johnson, *Chem. Rev.* **2016**, *116*, 10167–10211.

[28] T. F. Scott, A. D. Schneider, W. D. Cook, C. N. Bowman, *Science* **2005**, *308*, 1615–1617.

[29] J. Ryu, M. D'Amato, X. Cui, K. N. Long, H. Jerry Qi, M. L. Dunn, *Appl. Phys. Lett.* **2012**, *100*, 161908.

[30] A. Lendlein, H. Jiang, O. Jünger, R. Langer, *Nature* **2005**, *434*, 879–882.

[31] J. T. Offenloch, M. Gernhard, J. P. Blinco, H. Frisch, H. Mutlu, C. Barner-Kowollik, *Chem. Eur. J.* **2019**, *25*, 3700–3709.

[32] D. S. Tyson, F. Ilhan, M. A. B. Meador, D. D. Smith, D. A. Scheiman, M. A. Meador, *Macromolecules* **2005**, *38*, 3638–3646.

[33] S. Arumugam, S. V. Orski, J. Locklin, V. V. Popik, *J. Am. Chem. Soc.* **2012**, *134*, 179–182.

[34] K. Hiltebrandt, K. Elies, D. R. D'hooge, J. P. Blinco, C. Barner-Kowollik, *J. Am. Chem. Soc.* **2016**, *138*, 7048–7054.

[35] J. O. Mueller, N. K. Guimard, K. K. Oehlenschlaeger, F. G. Schmidt, C. Barner-Kowollik, *Polym. Chem.* **2014**, *5*, 1447–1456.

[36] C. Heiler, J. T. Offenloch, E. Blasco, C. Barner-Kowollik, *ACS Macro Lett.* **2017**, *6*, 56–61.

[37] M. Eing, B. Tuten, J. P. Blinco, C. Barner-Kowollik, *Chem. Eur. J.* **2018**, *24*, 12246–12249.

[38] H. Staudinger, *Ber. d. Deut. Chem. Ges.* **1920**, *53*, 1073–1085.

[39] H. Staudinger, J. Fritschi, *Helv. Chim. Acta* **1922**, *5*, 785–806.

[40] G. Odian, *Principles of Polymerization*, 4th ed., Wiley-Interscience, Hoboken, N.J, **2004**.

[41] B. Yamada, P. B. Zetterlund, *Handbook of Radical Polymerization*, *General Chemistry of Radical Polymerization*, (Eds.: K Matyjaszewski, T. P. Davis), John Wiley & Sons, Hoboken, New Jersey, **2002**, Chapter 3, pp. 117–186.

[42] A. Sarac, *Prog. Polym. Sci.* **1999**, *24*, 1149–1204.

[43] J. Franck, E. Rabinowitsch, *Trans. Faraday Soc.* **1934**, *30*, 120–130.

[44] E. T. Denisov, *Die Makromolekulare Chemie* **1984**, *8*, 63–78.

[45] T. Sato, S. Inui, H. Tanaka, T. Ota, M. Kamachi, K. Tanaka, *J. Polym. Sci. Part A: Polym. Chem.* **1987**, *25*, 637–652.

[46] G. Moad, E. Rizzardo, D. H. Solomon, S. R. Johns, R. I. Willing, *Makromol. Chem. Rapid Commun.* **1984**, *5*, 793–798.

[47] P. S. Engel, *Chem. Rev.* **1980**, *80*, 99–150.

[48] D. Liu, A. B. Padias, H. K. J. Hall, *Macromolecules* **1995**, *28*, 622–626.

[49] S. Masuda, K. Minagawa, M. Tsuda, M. Tanaka, *Eur. Polym. J.* **2001**, *37*, 705 –710.

[50] F. R. Mayo, *J. Am. Chem. Soc.* **1968**, *90*, 1289–1295.

[51] D. B. Priddy, *Adv. Polym. Sci.* **1994**, *111*, 67–114.

[52] J.-P. Fouassier, J. Lalevee, *Photoinitiators for Polymer Synthesis*, 1st ed., Wiley-VCH, Weinheim, **2012**, p. 75.

[53] Y. Yagci, A. Onen, W. Schnabel, *Macromolecules* **1991**, *24*, 4620–4623.

[54] E. D. Günersel, Y. Hepuzer, Y. Yagci, *Angew. Makromol. Chem.* **1999**, *264*, 88–91.

[55] W. A. Green, *Industrial Photoinitiators - A Technical Guide*, 1st ed., CRC Press, Boca Raton, **2010**, pp. 22–26.

[56] O. N. Tretinnikov, V. V. Pilipenko, L. K. Prikhodchenko, *Polymer Science Series B* **2012**, *54*, 427–433.

[57] X. Jiang, X. Luo, J. Yin, *J. Photochem. Photobiol. A* **2005**, *174*, 165 –170.

[58] K. J. Ivin, *J. Polym. Sci. Part A: Polym. Chem.* **1999**, *38*, 2137–2146.

[59] S. Beuermann, M. Buback, *Pulsed Laser Experiments Directed Toward the Detailed Study of Free-Radical Polymerizations*, (Ed.: K. Matyjaszewski), ACS Symposium Series, Washington, **1998**, Chapter 6, pp. 84–103.

[60] D. Britton, F. Heatley, P. A. Lovell, *Macromolecules* **1998**, *31*, 2828–2837.

[61] T. Sato, D. Ito, M. Kuki, H. Tanaka, T. Ota, *Macromolecules* **1991**, *24*, 2963–2967.

[62] M. D. Zammit, T. P. Davis, D. M. Haddleton, K. G. Suddaby, *Macromolecules* **1997**, *30*, 1915–1920.

[63] P. A.G. M. Scheren, G. T. Russell, D. F. Sangster, R. G. Gilbert, A. L. German, *Macromolecules* **1995**, *28*, 3637–3649.

[64] K. Matyjaszewski, T. P. Davis, *Handbook of Radical Polymerization*, *Fundamentals of Atom Transfer Radical Polymerization*, (Eds.: K. Matyjaszewski, T. P. Davis), John Wiley & Sons, Hoboken, NJ, USA, **2002**, Chapter 11, pp. 523–628.

[65] K. Matyjaszewski, *Handbook of Radical Polymerization*, *General Concepts and History of Living Radical Polymerization*, (Eds.: K. Matjyaszewski, T. P. Davis), John Wiley & Sons, Hoboken, New Jersey, **2002**, Chapter 8, pp. 361–406.

[66] M. Szwarc, *J. Polym. Sci. Part A: Polym. Chem.* **1998**, *36*, 9–15.

[67] M. Szwarc, M. Levy, R. Milkovich, *J. Am. Chem. Soc.* **1956**, *78*, 2656–2657.

[68] M. Szwarc, *Nature* **1956**, *178*, 1168–1169.

[69] O. W. Webster, *Science* **1991**, *251*, 887–893.

[70] A. D. Jenkins, P. Kratochvíl, R. F. T. Stepto, U. W. Suter, *Pure Appl. Chem.* **1996**, *68*, 2287–2311.

[71] J.-S. Wang, K. Matyjaszewski, *J. Am. Chem. Soc.* **1995**, *117*, 5614–5615.

[72] M. Kato, M. Kamigaito, M. Sawamoto, T. Higashimura, *Macromolecules* **1995**, *28*, 1721–1723.

[73] D. P. Curran, *Synthesis* **1988**, *6*, 489–513.

[74] T. Nishikawa, M. Kamigaito, M. Sawamoto, *Macromolecules* **1999**, *32*, 2204–2209.

[75] J. Qiu, S. G. Gaynor, K. Matyjaszewski, *Macromolecules* **1999**, *32*, 2872–2875.

[76] K. Min, K. Matyjaszewski, *Macromolecules* **2007**, *40*, 7217–7222.

[77] K. Matyjaszewski, T. E. Patten, J. Xia, *J. Am. Chem. Soc.* **1997**, *119*, 674–680.

[78] K. Matyjaszewski, S. Coca, S. G. Gaynor, M. Wei, B. E. Woodworth, *Macromolecules* **1998**, *31*, 5967–5969.

[79] J.-S. Wang, K. Matyjaszewski, *Macromolecules* **1995**, *28*, 7572–7573.

[80] J. Xia, K. Matyjaszewski, *Macromolecules* **1997**, *30*, 7692–7696.

[81] W. Jakubowski, K. Matyjaszewski, *Macromolecules* **2005**, *38*, 4139–4146.

[82] W. Jakubowski, K. Matyjaszewski, *Angew. Chem. Int. Ed.* **2006**, *45*, 4482–4486.

[83] K. Min, H. Gao, K. Matyjaszewski, *Macromolecules* **2007**, *40*, 1789–1791.

[84] Y. Kwak, K. Matyjaszewski, *Polym. Int.* **2009**, *58*, 242–247.

[85] P. Leclère, G. Moineau, M. Minet, P. Dubois, R. Jérôme, J. L. Brédas, R. Lazzaroni, *Langmuir* **1999**, *15*, 3915–3919.

[86] G. Moineau, M. Minet, P. Teyssié, R. Jérôme, *Macromol. Chem. Phys.* **2000**, *201*, 1108–1114.

[87] B. Zhao, W. J. Brittain, *Macromolecules* **2000**, *33*, 8813–8820.

[88] K. L. Beers, S. G. Gaynor, K. Matyjaszewski, S. S. Sheiko, M. Möller, *Macromolecules* **1998**, *31*, 9413–9415.

[89] A. M. Kasko, A. M. Heintz, C. Pugh, *Macromolecules* **1998**, *31*, 256–271.

[90] V. Coessens, K. Matyjaszewski, *Macromol. Rapid Commun.* **1999**, *20*, 66–70.

[91] K. Matyjaszewski, Y. Nakagawa, S. G. Gaynor, *Macromol. Rapid Commun.*, *18*, 1057–1066.

[92] V. Coessens, Y. Nakagawa, K. Matyjaszewski, *Polym. Bull.* **1998**, *40*, 135–142.

[93] E. G. Koulouri, J. K. Kallitsis, G. Hadziioannou, *Macromolecules* **1999**, *32*, 6242–6248.

[94] J. Chiefari, Y. K. B. Chong, F. Ercole, J. Krstina, J. Jeffery, T. P. T. Le, R. T. A. Mayadunne, G. F. Meijs, C. L. Moad, G. Moad, E. Rizzardo, S. H. Thang, *Macromolecules* **1998**, *31*, 5559–5562.

[95] E. Rizzardo, J. Chiefari, B. Y. Chong, F. Ercole, J. Krstina, J. Jeffery, T. P. Le, R. T. Mayadunne, G. F. Meijs, C. L. Moad, G. Moad, S. H. Thang, *Macromol. Symp.* **1999**, *143*, 291–307.

[96] G. Moad, J. Chiefari, Y. Chong, J. Krstina, R. T. Mayadunne, A. Postma, E. Rizzardo, S. H. Thang, *Polym. Int.* **2000**, *49*, 993–1001.

[97] J. Chiefari, E. Rizzardo, *Handbook of Radical Polymerization*, *Control of Free-Radical Polymerization by Chain Transfer Methods*, (Eds.: K. Matyjaszewski, T. P. Davis), John Wiley & Sons, Hoboken, New Jersey, **2002**, Chapter 12, pp. 629–690.

[98] *Handbook of RAFT Polymerization*, (Ed.: C. Barner-Kowollik), Wiley-VCH, Weinheim, **2008**.

[99] T. H. Epps, III, R. K. O'Reilly, *Chem. Sci.* **2016**, *7*, 1674–1689.

[100] M. Hillmyer, *Curr. Opin. Solid State Mater. Sci.* **1999**, *4*, 559–564.

[101] Y. K. Chong, T. P. T. Le, G. Moad, E. Rizzardo, S. H. Thang, *Macromolecules* **1999**, *32*, 2071–2074.

[102] K. Skrabania, A. Miasnikova, A. M. Bivigou-Koumba, D. Zehm, A. Laschewsky, *Polym. Chem.* **2011**, *2*, 2074–2083.

[103] H. Willcock, R. K. O'Reilly, *Polym. Chem.* **2010**, *1*, 149–157.

[104] R. T. A. Mayadunne, E. Rizzardo, J. Chiefari, J. Krstina, G. Moad, A. Postma, S. H. Thang, *Macromolecules* **2000**, *33*, 243–245.

[105] W. Shen, Q. Qiu, Y. Wang, M. Miao, B. Li, T. Zhang, A. Cao, Z. An, *Macromol. Rapid Commun.* **2010**, *31*, 1444–1448.

[106] Z. Wang, J. He, Y. Tao, L. Yang, H. Jiang, Y. Yang, *Macromolecules* **2003**, *36*, 7446–7452.

[107] A. Postma, T. P. Davis, G. Moad, M. S. O'Shea, *Macromolecules* **2005**, *38*, 5371–5374.

[108] S. Perrier, P. Takolpuckdee, C. A. Mars, *Macromolecules* **2005**, *38*, 2033–2036.

[109] A. J. Inglis, S. Sinnwell, T. P. Davis, C. Barner-Kowollik, M. H. Stenzel, *Macromolecules* **2008**, *41*, 4120–4126.

[110] A. S. Goldmann, T. Tischer, L. Barner, M. Bruns, C. Barner-Kowollik, *Biomacromolecules* **2011**, *12*, 1137–1145.

[111] K. K. Oehlenschlaeger, J. O. Mueller, J. Brandt, S. Hilf, A. Lederer, M. Wilhelm, R. Graf, M. L. Coote, F. G. Schmidt, C. Barner-Kowollik, *Adv. Mater.* **2014**, *26*, 3561–3566.

[112] K. K. Oehlenschlaeger, J. O. Mueller, N. B. Heine, M. Glassner, N. K. Guimard, G. Delaittre, F. G. Schmidt, C. Barner-Kowollik, *Angew. Chem. Int. Ed.* **2012**, *52*, 762–766.

[113] P. Vana, L. Albertin, L. Barner, T. P. Davis, C. Barner-Kowollik, *J. Polym. Sci. Part A: Polym. Chem.* **2002**, *40*, 4032–4037.

[114] H. De Brouwer, M. A. J. Schellekens, B. Klumperman, M. J. Monteiro, A. L. German, *J. Polym. Sci. Part A: Polym. Chem.* **2000**, *38*, 3596–3603.

[115] J. F. Quinn, L. Barner, C. Barner-Kowollik, E. Rizzardo, T. P. Davis, *Macromolecules* **2002**, *35*, 7620–7627.

[116] F. D'Agosto, C. Boisson, *Aust. J. Chem.* **2010**, *63*, 1155–1158.

[117] M. D. Lechner, K. Gehrke, E. H. Nordmeier, *Makromolekulare Chemie*, Birkhaeuser Verlag, Basel, **2010**.

[118] K. J. Ivin, J. J. Rooney, C. D. Stewart, M. L. H. Green, R. Mahtab, *J. Chem. Soc. Chem. Commun.* **1978**, 604–606.

[119] P. Cossee, *J. Catal.* **1964**, *3*, 80–88.

[120] R. Kempe, *Chem. Eur. J.* **2007**, *13*, 2764–2773.

[121] L. Sita, *Angew. Chem. Int. Ed.* **2009**, *48*, 2464–2472.

[122] G. J. P. Britovsek, S. A. Cohen, V. C. Gibson, M. van Meurs, *J. Am. Chem. Soc.* **2004**, *126*, 10701–10712.

[123] V. C. Gibson, *Science* **2006**, *312*, 703–704.

[124] G. J. Domski, J. M. Rose, G. W. Coates, A. D. Bolig, M. Brookhart, *Prog. Polym. Sci.* **2007**, *32*, 30–92.

[125] R. Briquel, J. Mazzolini, T. Le Bris, O. Boyron, F. Boisson, F. Delolme, F. D'Agosto, C. Boisson, R. Spitz, *Angew. Chem. Int. Ed.* **2008**, *47*, 9311–9313.

[126] J. Mazzolini, E. Espinosa, F. D'Agosto, C. Boisson, *Polym. Chem.* **2010**, *1*, 793–800.

[127] J. Mazzolini, I. Mokthari, R. Briquel, O. Boyron, F. Delolme, V. Monteil, D. Bertin, D. Gigmes, F. D'Agosto, C. Boisson, *Macromolecules* **2010**, *43*, 7495–7503.

[128] C. J. Han, M. S. Lee, D.-J. Byun, S. Y. Kim, *Macromolecules* **2002**, *35*, 8923–8925.

[129] S. Norsic, C. Thomas, F. D'Agosto, C. Boisson, *Angew. Chem. Int. Ed.* **2015**, *54*, 4631–4635.

[130] W. N. Ottou, S. Norsic, F. D'Agosto, C. Boisson, *Macromol. Rapid Commun.* **2018**, 1800154.

[131] Y. Zhao, L. Wang, A. Xiao, H. Yu, *Prog. Polym. Sci.* **2010**, *35*, 1195–1216.

[132] E. Espinosa, M. Glassner, C. Boisson, C. Barner-Kowollik, F. D'Agosto, *Macromol. Rapid Commun.* **2011**, *32*, 1447–1453.

[133] R. Godoy Lopez, C. Boisson, F. D'Agosto, R. Spitz, F. Boisson, D. Gigmes, D. Bertin, *J. Polym. Sci. Part A: Polym. Chem.* **2007**, *45*, 2705–2718.

[134] D. A. Shipp, J.-L. Wang, K. Matyjaszewski, *Macromolecules* **1998**, *31*, 8005–8008.

[135] K. A. Davis, K. Matyjaszewski, *Macromolecules* **2001**, *34*, 2101–2107.

[136] C. J. Hawker, V. V. Fokin, M. G. Finn, K. B. Sharpless, *Aust. J. Chem.* **2007**, *60*, 381–383.

[137] C. Barner-Kowollik, A. J. Inglis, *Macromol. Chem. Phys.* **2009**, *210*, 987–992.

[138] B. S. Sumerlin, A. P. Vogt, *Macromolecules* **2010**, *43*, 1–13.

[139] M. J. S. Dewar, S. Olivella, J. J. P. Stewart, *J. Am. Chem. Soc.* **1986**, *108*, 5771–5779.

[140] O. Diels, K. Alder, *Justus Liebigs Ann. Chem.* **1928**, *460*, 98–122.

[141] R. B. Woodward, R. Hoffmann, *Angew. Chem. Int. Ed.* **1969**, *8*, 781–853.

[142] K. N. Houk, *J. Am. Chem. Soc.* **1973**, *95*, 4092–4094.

[143] J. G. Martin, R. K. Hill, *Chem. Rev.* **1961**, *61*, 537–562.

[144] K. C. Nicolaou, S. A. Snyder, T. Montagnon, G. Vassilikogiannakis, *Angew. Chem. Int. Ed.* **2002**, *41*, 1668–1698.

[145] I. Fleming, *Molekülorbitale und Reaktionen organischer Verbindungen*, 1st ed., Wiley-VCH, Weinheim, **2012**, pp. 264–294.

[146] K. N. Houk, *Acc. Chem. Res.* **1975**, *8*, 361–369.

[147] K. N. Houk, R. J. Loncharich, J. F. Blake, W. L. Jorgensen, *J. Am. Chem. Soc.* **1989**, *111*, 9172–9176.

[148] A.-C. Knall, C. Slugovc, *Chem. Soc. Rev.* **2013**, *42*, 5131–5142.

[149] G. Delaittre, N. K. Guimard, C. Barner-Kowollik, *Acc. Chem. Res.* **2015**, *48*, 1296–1307.

[150] E. Blasco, M. B. Sims, A. S. Goldmann, B. S. Sumerlin, C. Barner-Kowollik, *Macromolecules* **2017**, *50*, 5215–5252.

[151] J. T. Offenloch, S. Norsic, H. Mutlu, M. Taam, O. Boyron, C. Boisson, F. D'Agosto, C. Barner-Kowollik, *Polym. Chem.* **2018**, *9*, 3633–3637.

[152] J. Willenbacher, K. N. R. Wuest, J. O. Mueller, M. Kaupp, H.-A. Wagenknecht, C. Barner-Kowollik, *ACS Macro Lett.* **2014**, *3*, 574–579.

[153] A. J. Inglis, T. Paulöhrl, C. Barner-Kowollik, *Macromolecules* **2010**, *43*, 33–36.

[154] M. Glassner, G. Delaittre, M. Kaupp, J. P. Blinco, C. Barner-Kowollik, *J. Am. Chem. Soc.* **2012**, *134*, 7274–7277.

[155] A. J. Inglis, L. Nebhani, O. Altintas, F. G. Schmidt, C. Barner-Kowollik, *Macromolecules* **2010**, *43*, 5515–5520.

[156] S. Billiet, K. De Bruycker, F. Driessen, H. Goossens, V. Van Speybroeck, J. M. Winne, F. E. Du Prez, *Nat. Chem.* **2014**, *6*, 815–821.

[157] S. Vandewalle, S. Billiet, F. Driessen, F. E. Du Prez, *ACS Macro Letters* **2016**, *5*, 766–771.

[158] L. Xiao, Y. Chen, K. Zhang, *Macromolecules* **2016**, *49*, 4452–4461.

[159] X. Chen, M. A. Dam, K. Ono, A. Mal, H. Shen, S. R. Nutt, K. Sheran, F. Wudl, *Science* **2002**, *295*, 1698–1702.

[160] K. Pahnke, J. Brandt, G. Gryn'ova, P. Lindner, R. Schweins, F. G. Schmidt, A. Lederer, M. L. Coote, C. Barner-Kowollik, *Chem. Sci.* **2015**, *6*, 1061–1074.

[161] K. Pahnke, J. Brandt, G. Gryn'ova, C. Y. Lin, O. Altintas, F. G. Schmidt, A. Lederer, M. L. Coote, C. Barner-Kowollik, *Angew. Chem. Int. Ed.* **2016**, *55*, 1514–1518.

[162] R. Huisgen, *Angew. Chem. Int. Ed.* **1963**, *2*, 633–645.

[163] R. Huisgen, *Angew. Chem. Int. Ed.* **1963**, *2*, 565–598.

[164] J. Mulzer, *Natural Product Synthesis via 1,3-Dipolar Cycloadditions*, Wiley-Blackwell, Hoboken, New Jersey, **2008**, Chapter 12, pp. 77–95.

[165] V. V. Rostovtsev, L. G. Green, V. V. Fokin, K. B. Sharpless, *Angew. Chem.* **2002**, *114*, 2708–2711.

[166] C. W. Tornøe, C. Christensen, M. Meldal, *J. Org. Chem.* **2002**, *67*, 3057–3064.

[167] F. Himo, T. Lovell, R. Hilgraf, V. V. Rostovtsev, L. Noodleman, K. B. Sharpless, V. V. Fokin, *J. Am. Chem. Soc.* **2005**, *127*, 210–216.

[168] L. Zhang, X. Chen, P. Xue, H. H. Y. Sun, I. D. Williams, K. B. Sharpless, V. V. Fokin, G. Jia, *J. Am. Chem. Soc.* **2005**, *127*, 15998–15999.

[169] S. Ding, G. Jia, J. Sun, *Angew. Chem. Int. Ed.* **2014**, *53*, 1877–1880.

[170] L. K. Rasmussen, B. C. Boren, V. V. Fokin, *Org. Lett.* **2007**, *9*, 5337–5339.

[171] F. Wei, W. Wang, Y. Ma, C.-H. Tung, Z. Xu, *Chem. Commun.* **2016**, *52*, 14188–14199.

[172] Y.-M. Wu, J. Deng, Y. Li, Q.-Y. Chen, *Synthesis* **2005**, *8*, 1314–1318.

[173] X. Zhang, R. P. Hsung, H. Li, *Chem. Commun.* **2007**, 2420–2422.

[174] W. Wang, F. Wei, Y. Ma, C.-H. Tung, Z. Xu, *Org. Lett.* **2016**, *18*, 4158–4161.

[175] Z. Zhang, Q. Zhou, F. Ye, Y. Xia, G. Wu, M. L. Hossain, Y. Zhang, J. Wang, *Adv. Syn. Catal.* **2015**, *357*, 2277–2286.

[176] Y. Xing, G. Sheng, J. Wang, P. Lu, Y. Wang, *Org. Lett.* **2014**, *16*, 1244–1247.

[177] W. Wang, X. Peng, F. Wei, C.-H. Tung, Z. Xu, *Angew. Chem. Int. Ed.* **2016**, *55*, 649–653.

[178] W. Zhou, M. Zhang, H. Li, W. Chen, *Org. Lett.* **2017**, *19*, 10–13.

[179] V. D. Bock, H. Hiemstra, J. H. van Maarseveen, *Eur. J. Org. Chem.* **2005**, *2006*, 51–68.

[180] L. Liang, D. Astruc, *Coord. Chem. Rev.* **2011**, *255*, 2933 –2945.

[181] L. Li, Z. Zhang, *Molecules* **2016**, *21*, 1393–1414.

[182] M. Meldal, C. W. Tornøe, *Chem. Rev.* **2008**, *108*, 2952–3015.

[183] D. D. Díaz, S. Punna, P. Holzer, A. K. McPherson, K. B. Sharpless, V. V. Fokin, M. G. Finn, *J. Polym. Sci. Part A: Polym. Chem.* **2004**, *42*, 4392–4403.

[184] C. Li, M. G. Finn, *J. Polym. Sci. Part A: Polym. Chem.* **2006**, *44*, 5513–5518.

[185] M. Meldal, *Macromol. Rapid Commun.* **2008**, *29*, 1016–1051.

[186] D. Fournier, R. Hoogenboom, U. S. Schubert, *Chem. Soc. Rev.* **2007**, *36*, 1369–1380.

[187] K. Kempe, A. Krieg, C. R. Becer, U. S. Schubert, *Chem. Soc. Rev.* **2012**, *41*, 176–191.

[188] Y. Shi, X. Cao, H. Gao, *Nanoscale* **2016**, *8*, 4864–4881.

[189] B. S. Sumerlin, N. V. Tsarevsky, G. Louche, R. Y. Lee, K. Matyjaszewski, *Macromolecules* **2005**, *38*, 7540–7545.

[190] W. H. Binder, C. Kluger, *Macromolecules* **2004**, *37*, 9321–9330.

[191] D. Quemener, T. P. Davis, C. Barner-Kowollik, M. H. Stenzel, *Chem. Commun.* **2006**, 5051–5053.

[192] G. Mantovani, V. Ladmiral, L. Tao, D. M. Haddleton, *Chem. Commun.* **2005**, 2089–2091.

[193] J. A. Opsteen, J. C. M. van Hest, *Chem. Commun.* **2005**, 57–59.

[194] V. Ladmiral, G. Mantovani, G. J. Clarkson, S. Cauet, J. L. Irwin, D. M. Haddleton, *J. Am. Chem. Soc.* **2006**, *128*, 4823–4830.

[195] P. Wu, A. K. Feldman, A. K. Nugent, C. J. Hawker, A. Scheel, B. Voit, J. Pyun, J. M. J. Fréchet, K. B. Sharpless, V. V. Fokin, *Angew. Chem. Int. Ed.* **2004**, *43*, 3928–3932.

[196] O Altintas, M. Josse, T. Abbasi, J. De Winter, V. Trouillet, P. Gerbaux, M. Wilhelm, C. Barner-Kowollik, *Polym. Chem.* **2015**, *6*, 2854–2868.

[197] *Thiol-X Chemistries in Polymer and Materials Science*, (Eds.: A. Lowe, C. Bowman), The Royal Society of Chemistry, Cambridge, **2013**, pp. 1–317.

[198] C. Hoyle, C. Bowman, *Angew. Chem. Int. Ed.* **2010**, *49*, 1540–1573.

[199] C. E. Hoyle, T. Y. Lee, T. Roper, *J. Polym. Sci. Part A: Polym. Chem.* **2004**, *42*, 5301–5338.

[200] C. E. Hoyle, A. B. Lowe, C. N. Bowman, *Chem. Soc. Rev.* **2010**, *39*, 1355–1387.

[201] M. S. Kharash, J. Read, F. R. Mayo, *Chem. Ind.* **1938**, *57*, 752–754.

[202] L. M. Campos, K. L. Killops, R. Sakai, J. M. J. Paulusse, D. Damiron, E. Drockenmuller, B. W. Messmore, C. J. Hawker, *Macromolecules* **2008**, *41*, 7063–7070.

[203] G. Chen, S. Amajjahe, M. H. Stenzel, *Chem. Commun.* **2009**, 1198–1200.

[204] J. T. Offenloch, H. Mutlu, C. Barner-Kowollik, *Macromolecules* **2018**, *51*, 2682–2689.

[205] E. Ceausescu, S. Bittman, V. Fieroiu, E. G. Badea, E. Gruber, A. Ciupitoiu, V. Apostol, *J. Macromol. Sci. Chem.* **1985**, *22*, 525–539.

[206] F. Schapman, J. Couvercelle, C. Bunel, *Polymer* **1998**, *39*, 4955–4962.

[207] A. B. Lowe, *Polymer* **2014**, *55*, 5517–5549.

[208] J. W. Chan, H. Zhou, C. E. Hoyle, A. B. Lowe, *Chem. Mater.* **2009**, *21*, 1579–1585.

[209] T. Pauloehrl, G. Delaittre, M. Bastmeyer, C. Barner-Kowollik, *Polym. Chem.* **2012**, *3*, 1740–1749.

[210] Z. P. Tolstyka, J. T. Kopping, H. D. Maynard, *Macromolecules* **2008**, *41*, 599–606.

[211] V. Lima, X. Jiang, J. Brokken-Zijp, P. J. Schoenmakers, B. Klumperman, R. Van Der Linde, *J. Polym. Sci. Part A: Polym. Chem.* **2005**, *43*, 959–973.

[212] J. M. Spruell, B. A. Levy, A. Sutherland, W. R. Dichtel, J. Y. Cheng, J. F. Stoddart, A. Nelson, *J. Polym. Sci. Part A: Polym. Chem.* **2009**, *47*, 346–356.

[213] P. P. Kalelkar, G. R. Alas, D. M. Collard, *Macromolecules* **2016**, *49*, 2609–2617.

[214] H. Feng, X Lu, W. Wang, N.-G. Kang, J. W. Mays, *Polymers* **2017**, *9*, 494–524.

[215] N. Hadjichristidis, M. Pitsikalis, H. Iatrou, *Synthesis of Block Copolymers*, (Ed.: V. Abetz), Springer, Berlin Heidelberg, **2005**, pp. 1–124.

[216] Y. Kwak, Renaud Nicolaß, K. Matyjaszewski, *Macromolecules* **2008**, *41*, 4585–4596.

[217] N. V. Tsarevsky, B. S. Sumerlin, K. Matyjaszewski, *Macromolecules* **2005**, *38*, 3558–3561.

[218] Z. Zarafshani, Ö. Akdemir, J.-F. Lutz, *Macromol. Rapid Commun.* **2008**, *29*, 1161–1166.

[219] C. Boyer, A. Granville, T. P. Davis, V. Bulmus, *J. Polym. Sci. Part A: Polym. Chem.* **2009**, *47*, 3773–3794.

[220] F. S. Bates, M. F. Schulz, A. K. Khandpur, S. Förster, J. H. Rosedale, K. Almdal, K. Mortensen, *Faraday Discuss.* **1994**, *98*, 7–18.

[221] M. W. Matsen, F. S. Bates, *Macromolecules* **1996**, *29*, 7641–7644.

[222] M. W. Matsen, *Macromolecules* **2012**, *45*, 2161–2165.

[223] J. E. Poelma, K. Ono, D. Miyajima, T. Aida, K. Satoh, C. J. Hawker, *ACS Nano* **2012**, *6*, 10845–10854.

[224] F. S. Bates, *Science* **1991**, *251*, 898–905.

[225] J. K. Kim, S. Y. Yang, Y. Lee, Y. Kim, *Prog. Polym. Sci.* **2010**, *35*, 1325–1349.

[226] S. Park, D. H. Lee, J. Xu, B. Kim, S. W. Hong, U. Jeong, T. Xu, T. P. Russell, *Science* **2009**, *323*, 1030–1033.

[227] C. M. Bates, M. J. Maher, D. W. Janes, C. J. Ellison, C. G. Willson, *Macromolecules* **2014**, *47*, 2–12.

[228] A. Rösler, G. W. Vandermeulen, H.-A. Klok, *Adv. Drug Delivery Rev.* **2012**, *64*, 270–279.

[229] R. K. O'Reilly, C. J. Hawker, K. L. Wooley, *Chem. Soc. Rev.* **2006**, *35*, 1068–1083.

[230] H. Wei, S.-X. Cheng, X.-Z. Zhang, R.-X. Zhuo, *Prog. Polym. Sci.* **2009**, *34*, 893–910.

[231] T. Kamegawa, Y. Ishiguro, H. Seto, H. Yamashita, *J. Mater. Chem. A* **2015**, *3*, 2323–2330.

[232] Y. Zou, X. Zhou, Y. Zhu, X. Cheng, D. Zhao, Y. Deng, *Acc. Chem. Res.* **2019**, *52*, 714–725.

[233] J. R Schaefgen, P. J. Flory, *J. Am. Chem. Soc.* **1948**, *70*, 2709–2718.

[234] M. Morton, T. E. Helminiak, S. D. Gadkary, F. Bueche, *J. Polym. Sci.* **1962**, *57*, 471–482.

[235] N. Hadjichristidis, M. Pitsikalis, H. Iatrou, P. Driva, G. Sakellariou, M. Chatzichristidi in *Polymer Science: A Comprehensive Reference*, (Eds.: K. Matyjaszewski, M. Möller), Elsevier, Amsterdam, **2012**, pp. 29 –111.

[236] *Miktoarm Star Polymers, From Basics of Branched Architecture to Synthesis, Self-assembly and Applications*, (Ed.: A. Kakkar), The Royal Society of Chemistry, Cambridge, **2017**, pp. 1–227.

[237] N. Hadjichristidis, *J. Polym. Sci. Part A: Polym. Chem.* **2000**, *37*, 857–871.

[238] K. Khanna, S. Varshney, A. Kakkar, *Polym. Chem.* **2010**, *1*, 1171–1185.

[239] V. Pitto, B. I. Voit, T. J. A. Loontjens, R. A.T. M. van Benthem, *Macromol. Chem. Phys.* **2004**, *205*, 2346–2355.

[240] R. T. A. Mayadunne, J. Jeffery, G. Moad, E. Rizzardo, *Macromolecules* **2003**, *36*, 1505–1513.

[241] K. Matyjaszewski, P. J. Miller, J. Pyun, G. Kickelbick, S. Diamanti, *Macromolecules* **1999**, *32*, 6526–6535.

[242] S. Abraham, C.-S. Ha, I. Kim, *J. Polym. Sci. Part A: Polym. Chem.* **2005**, *43*, 6367–6378.

[243] T. Erdogan, Z. Ozyurek, G. Hizal, U. Tunca, *J. Polym. Sci. Part A: Polym. Chem.* **2004**, *42*, 2313–2320.

[244] U. Tunca, Z. Ozyurek, T. Erdogan, G. Hizal, *J. Polym. Sci. Part A: Polym. Chem.* **2004**, *42*, 4228–4236.

[245] C. Gordin, C. Delaite, H. Medlej, D. Josien-Lefebvre, K. Hariri, M. Rusu, *Polym. Bull.* **2009**, *63*, 789–801.

[246] H. Gao, K. Matyjaszewski, *J. Am. Chem. Soc.* **2007**, *129*, 11828–11834.

[247] H. Gao, N. V. Tsarevsky, K. Matyjaszewski, *Macromolecules* **2005**, *38*, 5995–6004.

[248] A. Vora, K. Singh, D. C. Webster, *Polymer* **2009**, *50*, 2768–2774.

[249] O. Altintas, G. Hizal, U. Tunca, *J. Polym. Sci. Part A: Polym. Chem.* **2006**, *44*, 5699–5707.

[250] Y. Zhang, C. Li, S. Liu, *J. Polym. Sci. Part A: Polym. Chem.* **2009**, *47*, 3066–3077.

[251] H. Durmaz, F. Karatas, U. Tunca, G. Hizal, *J. Polym. Sci. Part A: Polym. Chem.* **2006**, *44*, 499–509.

[252] T. P. Lodge, A. Rasdal, Z. Li, M. A. Hillmyer, *J. Am. Chem. Soc.* **2005**, *127*, 17608–17609.

[253] F. Nederberg, E. Appel, J. P. K. Tan, S. H. Kim, K. Fukushima, J. Sly, R. D. Miller, R. M. Waymouth, Y. Y. Yang, J. L. Hedrick, *Biomacromolecules* **2009**, *10*, 1460–1468.

[254] H. Yin, S.-W. Kang, Y. H. Bae, *Macromolecules* **2009**, *42*, 7456–7464.

[255] V. W. Kuhn, H. Majer, *Die Makromolekulare Chemie* **1956**, *18*, 239–253.

[256] D. Mecerreyes, V. Lee, C. J. Hawker, J. L. Hedrick, A. Wursch, W. Volksen, T. Magbitang, E. Huang, R. D. Miller, *Adv. Mater.* **2001**, *13*, 204–208.

[257] O. Altintas, C. Barner-Kowollik, *Macromol. Rapid Commun.* **2016**, *37*, 29–46.

[258] J. P. Cole, A. M. Hanlon, K. J. Rodriguez, E. B. Berda, *J. Polym. Sci. Part A: Polym. Chem.* **2016**, *55*, 191–206.

[259] J. Willenbacher, B. V.K. J. Schmidt, D. Schulze-Suenninghausen, O. Altintas, B. Luy, G. Delaittre, C. Barner-Kowollik, *Chem. Commun.* **2014**, *50*, 7056–7059.

[260] O. Shishkan, M. Zamfir, M. A. Gauthier, H. G. Börner, J.-F. Lutz, *Chem. Commun.* **2014**, *50*, 1570–1572.

[261] S. C. Solleder, R. V. Schneider, K. S. Wetzel, A. C. Boukis, M. A. R. Meier, *Macromol. Rapid Commun.* **2017**, *38*, 1600711.

[262] T. Chidanguro, D. R. Blank, A. Garrett, C. M. Reese, J. M. Schekman, X. Yu, D. L. Patton, N. Ayres, Y. C. Simon, *Dalton Trans.* **2018**, *47*, 8663–8669.

[263] E. B. Berda, E. J. Foster, E. W. Meijer, *Macromolecules* **2010**, *43*, 1430–1437.

[264] E. Harth, B. V. Horn, V. Y. Lee, D. S. Germack, C. P. Gonzales, R. D. Miller, C. J. Hawker, *J. Am. Chem. Soc.* **2002**, *124*, 8653–8660.

[265] O. Altintas, J. Willenbacher, K. N. R. Wuest, K. K. Oehlenschlaeger, P. Krolla-Sidenstein, H. Gliemann, C. Barner-Kowollik, *Macromolecules* **2013**, *46*, 8092–8101.

[266] J. T. Offenloch, J. Willenbacher, P. Tzvetkova, C. Heiler, H. Mutlu, C. Barner-Kowollik, *Chem. Commun.* **2017**, *53*, 775–778.

[267] C. Heiler, S. Bastian, P. Lederhose, J. P. Blinco, E. Blasco, C. Barner-Kowollik, *Chem. Commun.* **2018**, *54*, 3476–3479.

[268] J. Willenbacher, O. Altintas, V. Trouillet, N. Knofel, M. J. Monteiro, P. W. Roesky, C. Barner-Kowollik, *Polym. Chem.* **2015**, *6*, 4358–4365.

[269] N. D. Knöfel, H. Rothfuss, J. Willenbacher, C. Barner-Kowollik, P. W. Roesky, *Angew. Chem. Int. Ed.* **2017**, *56*, 5131–5131.

[270] C. K. Lyon, A. Prasher, A. M. Hanlon, B. T. Tuten, C. A. Tooley, P. G. Frank, E. B. Berda, *Polym. Chem.* **2015**, *6*, 181–197.

[271] O. Altintas, C. Barner-Kowollik, *Macromol. Rapid Commun.* **2012**, *33*, 958–971.

[272] A. Sanchez-Sanchez, I. Asenjo-Sanz, L. Buruaga, J. A. Pomposo, *Macromol. Rapid Commun.* **2012**, *33*, 1262–1267.

[273] B. T. Tuten, D. Chao, C. K. Lyon, E. B. Berda, *Polym. Chem.* **2012**, *3*, 3068–3071.

[274] D. E. Whitaker, C. S. Mahon, D. A. Fulton, *Angew. Chem. Int. Ed.* **2012**, *52*, 956–959.

[275] O. Altintas, E. Lejeune, P. Gerstel, C. Barner-Kowollik, *Polym. Chem.* **2012**, *3*, 640–651.

[276] S. Mavila, C. E. Diesendruck, S. Linde, L. Amir, R. Shikler, N. G. Lemcoff, *Angew. Chem. Int. Ed.* **2013**, *52*, 5767–5770.

[277] A. P. P. Kröger, R. J. Boonen, J. M. Paulusse, *Polymer* **2017**, *120*, 119–128.

[278] A. M. Hanlon, C. K. Lyon, E. B. Berda, *Macromolecules* **2016**, *49*, 2–14.

[279] E. Blasco, B. T. Tuten, H. Frisch, A. Lederer, C. Barner-Kowollik, *Polym. Chem.* **2017**, *8*, 5845–5851.

[280] J. Steinkoenig, H. Rothfuss, A. Lauer, B. T. Tuten, C. Barner-Kowollik, *J. Am. Chem. Soc.* **2017**, *139*, 51–54.

[281] G. Li, F. Tao, L. Wang, Y. Li, R. Bai, *Polymer* **2014**, *55*, 3696–3702.

[282] Z. Grubisic, P. Rempp, H. Benoit, *J. Polym. Sci. Pol. Lett.* **1967**, *5*, 753–759.

[283] K. F. Morris, C. S. Johnson, *J. Am. Chem. Soc.* **1992**, *114*, 3139–3141.

[284] P. Groves, *Polym. Chem.* **2017**, *8*, 6700–6708.

[285] A. Sanchez-Sanchez, S. Akbari, A. Etxeberria, A. Arbe, U. Gasser, A. J. Moreno, J. Colmenero, J. A. Pomposo, *ACS Macro Lett.* **2013**, *2*, 491–495.

[286] A. J. Moreno, F. Lo Verso, A. Sanchez-Sanchez, A. Arbe, J. Colmenero, J. A. Pomposo, *Macromolecules* **2013**, *46*, 9748–9759.

[287] A. E. Cherian, F. C. Sun, S. S. Sheiko, G. W. Coates, *J. Am. Chem. Soc.* **2007**, *129*, 11350–11351.

[288] H. Rothfuss, N. D. Knöfel, P. W. Roesky, C. Barner-Kowollik, *J. Am. Chem. Soc.* **2018**, *140*, 5875–5881.

[289] S. Mavila, I. Rozenberg, N. G. Lemcoff, *Chem. Sci.* **2014**, *5*, 4196–4203.

[290] M. A. J. Gillissen, I. K. Voets, E. W. Meijer, A. R. A. Palmans, *Polym. Chem.* **2012**, *3*, 3166–3174.

[291] X. Fan, Z. Li, X. J. Loh, *Polym. Chem.* **2016**, *7*, 5898–5919.

[292] K. Landfester, *Angew. Chem. Int. Ed.* **2009**, *48*, 4488–4507.

[293] J. F.G. A. Jansen, E. M. M. de Brabander-van den Berg, E. W. Meijer, *Science* **1994**, *266*, 1226–1229.

[294] J. F.G. A. Jansen, E. W. Meijer, E. M. M. de Brabander-van den Berg, *J. Am. Chem. Soc.* **1995**, *117*, 4417–4418.

[295] C. Porsch, Y. Zhang, M. I. Montañez, J.-M. Malho, M. A. Kostiainen, A. M. Nyström, E. Malmström, *Biomacromolecules* **2015**, *16*, 2872–2883.

[296] Y. H. Kim, O. W. Webster, *J. Am. Chem. Soc.* **1990**, *112*, 4592–4593.

[297] J. Guo, H. Hong, G. Chen, S. Shi, T. R. Nayak, C. P. Theuer, T. E. Barnhart, W. Cai, S. Gong, *ACS Appl. Mater. Inter.* **2014**, *6*, 21769–21779.

[298] Z. Jia, Q. Fu, J. Huang, *Macromolecules* **2006**, *39*, 5190–5193.

[299] X. Pang, L. Zhao, M. Akinc, J. K. Kim, Z. Lin, *Macromolecules* **2011**, *44*, 3746–3752.

[300] Q. Guo, C. Liu, T. Tang, J. Huang, X. Zhang, G. Wang, *J. Polym. Sci. Part A: Polym. Chem.* **2013**, *51*, 4572–4583.

[301] R. Savic, T. Azzam, A. Eisenberg, D. Maysinger, *Langmuir* **2006**, *22*, 3570–3578.

[302] Y. Wang, L. Li, J. Li, B. Yang, C. Wang, W. Fang, F. Ji, Y. Wen, F. Yao, *RSC Adv.* **2016**, *6*, 17728–17739.

[303] L. Qiu, Q. Liu, C.-Y. Hong, C.-Y. Pan, *J. Mater. Chem. B* **2016**, *4*, 141–151.

[304] B. Helms, J. M. Fréchet, *Adv. Syn. Catal.* **2006**, *348*, 1125–1148.

[305] C. N. Moorefield, G. R. Newkome, *C. R. Chim.* **2003**, *6*, 715–724.

[306] C. Deraedt, N. Pinaud, D. Astruc, *J. Am. Chem. Soc.* **2014**, *136*, 12092–12098.

[307] M. Filali, M. A. R. Meier, U. S. Schubert, J.-F. Gohy, *Langmuir* **2005**, *21*, 7995–8000.

[308] G. Ciamician, P. Silber, *Ber. Dtsch. Chem. Ges.* **1886**, *19*, 2899–2900.

[309] G. Ciamician, P. Silber, *Ber. Dtsch. Chem. Ges.* **1901**, *34*, 1530–1543.

[310] G. Ciamician, P. Silber, *Ber. Dtsch. Chem. Ges.* **1901**, *34*, 2040–2046.

[311] M. Buback, R. G. Gilbert, R. A. Hutchinson, B. Klumperman, F. Kuchta, B. G. Manders, K. F. O'Driscoll, G. T. Russell, J. Schweer, *Macromol. Chem. Phys.* **1995**, *196*, 3267–3280.

[312] J. H. Lambert, *Photometria, sive de mensura et gradibus luminis, colorum et umbrae*, Sumptibus Vidae Eberhardi Klett, Augsburg, **1760**.

[313] Beer, *Ann. Phys.* **1852**, *162*, 78–88.

[314] P. W. Atkins, J. de Paula, *Physikalische Chemie*, 4th ed., Wiley-VCH, Weinheim, **2006**, pp. 281–573.

[315] P. W. Atkins, J. de Paula, *Physikalische Chemie*, 4th ed., Wiley-VCH, Weinheim, **2006**, pp. 485–486.

[316] J. Franck, E. G. Dymond, *Trans. Faraday Soc.* **1926**, *21*, 536–542.

[317] E. Condon, *Phys. Rev.* **1926**, *28*, 1182–1201.

[318] A. Jablonski, *Nature* **1933**, *133*, 839–840.

[319] D. Woehrle, M. W. Tausch, W.-D. Stohrer, *"Die konzeptionellen und theoretischen Grundlagen der Photochemie" in Photochemie: Konzepte, Methoden, Experimente.* Wiley-VCH Verlag GmbH & Co. KGaA, Weinheim, **1998**, pp. 62–68.

[320] V. Balzani, P. Ceroni, A. Juris, *Photochemistry and photophysics: Concepts, research, applications*, 1st ed., Wiley-VCH, Weinheim, **2014**, pp. 55–81.

[321] H. G. O. Becker, *Einfuerung in die Photochemie*, 3rd ed., Wiley-VCH, Weinheim, **1991**, pp. 48–94.

[322] M. Persico, G. Granucci in *Photochemistry: A Modern Theoretical Perspective*, Springer International Publishing, Cham, **2018**, pp. 25–78.

[323] J. L. Segura, N. Martín, *Chem. Rev.* **1999**, *99*, 3199–3246.

[324] T. Kametani, M. Tsubuki, Y. Shiratori, Y. Kato, H. Nemoto, M. Ihara, K. Fukumoto, F. Satoh, H. Inoue, *J. Org. Chem.* **1977**, *42*, 2672–2676.

[325] J. J. McCullough, *Acc. Chem. Res.* **1980**, *13*, 270–276.

[326] P. G. Sammes, *Tetrahedron* **1976**, *32*, 405–422.

[327] G. Porter, M. F. Tchir, *J. Chem. Soc. A* **1971**, 3772–3777.

[328] E. F. Zwicker, L. I. Grossweiner, N. C. Yang, *J. Am. Chem. Soc.* **1963**, *85*, 2671–2672.

[329] B. J. Arnold, S. M. Mellows, P. G. Sammes, T. W. Wallace, *J. Chem. Soc. Perkin Trans. 1* **1974**, 401–409.

[330] K. R. Huffman, M. Loy, E. F. Ullman, *J. Am. Chem. Soc.* **1965**, *87*, 5417–5423.

[331] J. L. Charlton, M. Alauddin, *Tetrahedron* **1987**, *43*, 2873–2889.

[332] W. C. Agosta, R. A. Caldwell, J. Jay, L. J. Johnston, B. R. Venepalli, J. C. Scaiano, M. Singh, S. Wolff, *J. Am. Chem. Soc.* **1987**, *109*, 3050–3057.

[333] T. Krappitz, F. Feist, I. Lamparth, N. Moszner, H. John, J. P. Blinco, T. R. Dargaville, C. Barner-Kowollik, *Mater. Horiz.* **2019**, *6*, 81–89.

[334] T. Pauloehrl, G. Delaittre, V. Winkler, A. Welle, M. Bruns, H. G. Börner, A. M. Greiner, M. Bastmeyer, C. Barner-Kowollik, *Angew. Chem. Int. Ed.* **2012**, *51*, 1071–1074.

[335] M. Winkler, J. O. Mueller, K. K. Oehlenschlaeger, L. Montero de Espinosa, M. A. R. Meier, C. Barner-Kowollik, *Macromolecules* **2012**, *45*, 5012–5019.

[336] B. Grosch, C. N. Orlebar, E. Herdtweck, W. Massa, T. Bach, *Angew. Chem. Int. Ed.* **2003**, *42*, 3693–3696.

[337] K. K. Oehlenschlaeger, J. O. Mueller, N. B. Heine, M. Glassner, N. K. Guimard, G. Delaittre, F. G. Schmidt, C. Barner-Kowollik, *Angew. Chem. Int. Ed.* **2013**, *52*, 762–766.

[338] M. A. Tasdelen, Y. Yagci, *Angew. Chem. Int. Ed.* **2013**, *52*, 5930–5938.

[339] T. Gruendling, K. K. Oehlenschlaeger, E. Frick, M. Glassner, C. Schmid, C. Barner-Kowollik, *Macromol. Rapid Commun.* **2011**, *32*, 807–812.

[340] K. Hiltebrandt, M. Kaupp, E. Molle, J. P. Menzel, J. P. Blinco, C. Barner-Kowollik, *Chem. Commun.* **2016**, *52*, 9426–9429.

[341] S. Arumugam, V. V. Popik, *J. Am. Chem. Soc.* **2011**, *133*, 15730–15736.

[342] C. M. Preuss, T. Tischer, C. Rodriguez-Emmenegger, M. M. Zieger, M. Bruns, A. S. Goldmann, C. Barner-Kowollik, *J. Mater. Chem. B* **2014**, *2*, 36–40.

[343] L. Stolzer, A. S. Quick, D. Abt, A. Welle, D. Naumenko, M. Lazzarino, M. Wegener, C. Barner-Kowollik, L. Fruk, *Chem. Commun.* **2015**, *51*, 3363–3366.

[344] K. N. R. Wuest, V. Trouillet, A. S. Goldmann, M. H. Stenzel, C. Barner-Kowollik, *Macromolecules* **2016**, *49*, 1712–1721.

[345] M. Kaupp, T. Tischer, A. F. Hirschbiel, A. P. Vogt, U. Geckle, V. Trouillet, T. Hofe, M. H. Stenzel, C. Barner-Kowollik, *Macromolecules* **2013**, *46*, 6858–6872.

[346] J. S. Clovis, A. Eckell, R. Huisgen, R. Sustmann, G. Wallbillich, V. Weberndörfer, *Chem. Ber.* **1967**, *100*, 1593–1601.

[347] J. S. Clovis, A. Eckell, R. Huisgen, R. Sustmann, *Chem. Ber.* **1967**, *100*, 60–70.

[348] Y. Wang, C. I. Rivera Vera, Q. Lin, *Org. Lett.* **2007**, *9*, 4155–4158.

[349] V. Lohse, P. Leihkauf, C. Csongar, G. Tomaschewski, *J. Prak. Chem.* **1988**, *330*, 406–414.

[350] A. Padwa, S. Nahm, E. Sato, *J. Org. Chem.* **1978**, *43*, 1664–1671.

[351] M. Dietrich, G. Delaittre, J. P. Blinco, A. J. Inglis, M. Bruns, C. Barner-Kowollik, *Adv. Funct. Mater.* **2012**, *22*, 304–312.

[352] Y. R. Prasad, A. L. Rao, L. Prasoona, K. Murali, P. R. Kumar, *Bioorg. Med. Chem. Lett.* **2005**, *15*, 5030–5034.

[353] W. Song, Y. Wang, J. Qu, Q. Lin, *J. Am. Chem. Soc.* **2008**, *130*, 9654–9655.

[354] Y. Wang, W. J. Hu, W. Song, R. K. V. Lim, Q. Lin, *Org. Lett.* **2008**, *10*, 3725–3728.

[355] Z. Li, L. Qian, L. Li, J. C. Bernhammer, V. Huynh, Han, J. Lee, S. Q. Yao, *Angew. Chem. Int. Ed.* **2015**, *55*, 2002–2006.

[356] W. Feng, L. Li, C. Yang, A. Welle, O. Trapp, P. A. Levkin, *Angew. Chem. Int. Ed.* **2015**, *54*, 8732–8735.

[357] P. Lederhose, K. N. R. Wust, C. Barner-Kowollik, J. P. Blinco, *Chem. Commun.* **2016**, *52*, 5928–5931.

[358] P. An, Z. Yu, Q. Lin, *Chem. Commun.* **2013**, *49*, 9920–9922.

[359] Y. Wang, W. Song, W. Hu, Q. Lin, *Angew. Chem. Int. Ed.* **2009**, *48*, 5330–5333.

[360] D. Estupiñán, C. Barner-Kowollik, L. Barner, *Angew. Chem. Int. Ed.* **2018**, *57*, 5925–5929.

[361] C. Rodriguez-Emmenegger, C. M. Preuss, B. Yameen, O. Pop-Georgievski, M. Bachmann, J. O. Mueller, M. Bruns, A. S. Goldmann, M. Bastmeyer, C. Barner-Kowollik, *Adv. Mater.* **2013**, *25*, 6123–6127.

[362] D. Abt, B. V.K. J. Schmidt, O. Pop-Georgievski, A. S. Quick, D. Danilov, N. Y. Kostina, M. Bruns, W. Wenzel, M. Wegener, C. Rodriguez-Emmenegger, C. Barner-Kowollik, *Chem. Eur. J.* **2015**, *21*, 13186–13190.

[363] K. Hiltebrandt, T. Pauloehrl, J. P. Blinco, K. Linkert, H. G. Boerner, C. Barner-Kowollik, *Angew. Chem. Int. Ed.* **2015**, *54*, 2838–2843.

[364] A. Padwa, *Acc. Chem. Res.* **1976**, *9*, 371–378.

[365] A. Padwa, M. Dharan, J. Smolanoff, I. Wetmore S., *Pure Appl. Chem.* **1973**, *33*, 269–284.

[366] A. Padwa, J. Smolanoff, *J. Am. Chem. Soc.* **1971**, *93*, 548–550.

[367] A. Padwa, M. Dharan, J. Smolanoff, S. I. Wetmore, *J. Am. Chem. Soc.* **1973**, *95*, 1945–1954.

[368] H. Heimgartner, *Angew. Chem. Int. Ed.* **1991**, *30*, 238–264.

[369] E. Albrecht, J. Averdung, E. W. Bischof, A. Heidbreder, T. Kirschberg, F. Müller, J. Mattay, *J. Photochem. Photobiol. A* **1994**, *82*, 219–232.

[370] A. Padwa, M. Dharan, J. Smolanoff, S. I. Wetmore, *J. Am. Chem. Soc.* **1973**, *95*, 1954–1961.

[371] A. Padwa, J. Smolanoff, S. I. Wetmore, *J. Org. Chem.* **1973**, *38*, 1333–1340.

[372] F. W. Fowler in, (Eds.: A. Katritzky, A. Boulton), Advances in Heterocyclic Chemistry, Academic Press, Cambridge, **1971**, pp. 45–76.

[373] D. J. Anderson, A. Hassner, *J. Org. Chem.* **1973**, *38*, 2565–2566.

[374] V. Nair, *J. Org. Chem.* **1972**, *37*, 802–804.

[375] V. Nair, *J. Org. Chem.* **1968**, *33*, 2121–2123.

[376] R. K. V. Lim, Q. Lin, *Chem. Commun.* **2010**, *46*, 7993–7995.

[377] E. Vedejs, T. H. Eberlein, D. L. Varie, *J. Am. Chem. Soc.* **1982**, *104*, 1445–1447.

[378] E. Vedejs, T. H. Eberlein, D. J. Mazur, C. K. McClure, D. A. Perry, R. Ruggeri, E. Schwartz, J. S. Stults, D. L. a. Varie, *J. Org. Chem.* **1986**, *51*, 1556–1562.

[379] H. G. Giles, R. A. Marty, P. D. Mayo, *Can. J. Chem.* **1976**, *54*, 537–542.

[380] J. E. Baldwin, R. C. G. Lopez, *J. Chem. Soc. Chem. Commun.* **1982**, 1029–1030.

[381] G. Hofstra, J. Kamphuis, H. Bos, *Tetrahedron Lett.* **1984**, *25*, 873–876.

[382] T. Pauloehrl, A. Welle, K. K. Oehlenschlaeger, C. Barner-Kowollik, *Chem. Sci.* **2013**, *4*, 3503–3507.

[383] M. Glassner, K. K. Oehlenschlaeger, A. Welle, M. Bruns, C. Barner-Kowollik, *Chem. Commun.* **2013**, *49*, 633–635.

[384] C. Lang, S. Bestgen, A. Welle, R. Müller, P. W. Roesky, C. Barner-Kowollik, *Chem. Eur. J.* **2015**, *21*, 14728–14731.

[385] H. Wagenknecht, *ChemPhysChem* **2013**, *14*, 3197–3198.

[386] A. Lauer, D. E. Fast, J. Steinkoenig, A.-M. Kelterer, G. Gescheidt, C. Barner-Kowollik, *ACS Macro Lett.* **2017**, *6*, 952–958.

[387] J. P. Menzel, B. B. Noble, A. Lauer, M. L. Coote, J. P. Blinco, C. Barner-Kowollik, *J. Am. Chem. Soc.* **2017**, *139*, 15812–15820.

[388] D. E. Fast, A. Lauer, J. P. Menzel, A.-M. Kelterer, G. Gescheidt, C. Barner-Kowollik, *Macromolecules* **2017**, *50*, 1815–1823.

[389] F. Bures, *RSC Adv.* **2014**, *4*, 58826–58851.

[390] Y. Wang, W. J. Hu, W. Song, R. K. V. Lim, Q. Lin, *Org. Lett.* **2008**, *10*, 3725–3728.

[391] P. An, Z. Yu, Q. Lin, *Chem. Commun.* **2013**, *49*, 9920–9922.

[392] P. An, Z. Yu, Q. Lin, *Org. Lett.* **2013**, *15*, 5496–5499.

[393] Z. Yu, L. Y. Ho, Z. Wang, Q. Lin, *Bioorg. Med. Chem. Lett.* **2011**, *21*, 5033–5036.

[394] E. Blasco, Y. Sugawara, P. Lederhose, J. P. Blinco, A.-M. Kelterer, C. Barner-Kowollik, *ChemPhotoChem* **2017**, *1*, 159–163.

[395] T. M. Figueira-Duarte, K. Müllen, *Chem. Rev.* **2011**, *111*, 7260–7314.

[396] X. Feng, J.-Y. Hu, C. Redshaw, T. Yamato, *Chem. Eur. J.* **2016**, *22*, 11898–11916.

[397] J. M. Casas-Solvas, J. D. Howgego, A. P. Davis, *Org. Biomol. Chem.* **2014**, *12*, 212–232.

[398] R. Meyer, *Ber. Dtsch. Chem. Ges.* **1912**, *45*, 1609–1633.

[399] H. Toiserkani, G. Yilmaz, Y. Yagci, L. Torun, *Macromol. Chem. Phys.* **2010**, *211*, 2389–2395.

[400] F. M. Winnik, *Chem. Rev.* **1993**, *93*, 587–614.

[401] M. Ciftci, M. U. Kahveci, Y. Yagci, X. Allonas, C. Ley, H. Tar, *Chem. Commun.* **2012**, *48*, 10252–10254.

[402] C. Zhao, D. Wu, X. Lian, Y. Zhang, X. Song, H. Zhao, *J. Phys. Chem. B* **2010**, *114*, 6300–6308.

[403] F. M. Winnik, *Macromolecules* **1990**, *23*, 233–242.

[404] K. Kalyanasundaram, J. K. Thomas, *J. Am. Chem. Soc.* **1977**, *99*, 2039–2044.

[405] F. M. Winnik, S. T. Regismond, *Colloids Surf. A* **1996**, *118*, 1–39.

[406] C. L. Zhao, M. A. Winnik, G. Riess, M. D. Croucher, *Langmuir* **1990**, *6*, 514–516.

[407] G. Kwon, M. Naito, M. Yokoyama, T. Okano, Y. Sakurai, K. Kataoka, *Langmuir* **1993**, *9*, 945–949.

[408] M. A. Winnik, F. M. Winnik, *Fluorescence Studies of Polymer Association in Water*, American Chemical Society, Washington, **1993**, Chapter 18, pp. 485–505.

[409] K. S. Arora, N. J. Turro, *J. Polym. Sci. Part B: Polym. Phys.* **1987**, *25*, 243–262.

[410] J. Seixas de Melo, T. Costa, M. d. G. Miguel, B. Lindman, K. Schillén, *J. Phys. Chem. B* **2003**, *107*, 12605–12621.

[411] C. Pietsch, R. Hoogenboom, U. S. Schubert, *Polym. Chem.* **2010**, *1*, 1005–1008.

[412] S. Farhangi, J. Duhamel, *Macromolecules* **2016**, *49*, 353–361.

[413] J. P. Blinco, K. E. Fairfull-Smith, B. J. Morrow, S. E. Bottle, *Aust. J. Chem.* **2011**, *64*, 373–389.

[414] H. Mutlu, C. W. Schmitt, N. Wedler-Jasinski, H. Woehlk, K. E. Fairfull-Smith, J. P. Blinco, C. Barner-Kowollik, *Polym. Chem.* **2017**, *8*, 6199–6203.

[415] M.-C. Li, R.-M. Ho, Y.-D. Lee, *J. Mater. Chem.* **2011**, *21*, 2451–2454.

[416] M.-C. Li, R.-M. Ho, Y.-D. Lee, *J. Mater. Chem. C* **2013**, *1*, 1601–1606.

[417] J. You, E. Kim, *J. Nanosci. Nanotechno.* **2016**, *16*, 10927–10934.

[418] M.-H. Chi, C.-H. Su, M.-H. Cheng, P.-Y. Chung, C.-H. Peng, J.-T. Chen, *Macromol. Rapid Commun.* **2016**, *37*, 2037–2044.

[419] Y. Chen, G. Ji, S. Guo, B. Yu, Y. Zhao, Y. Wu, H. Zhang, Z. Liu, B. Han, Z. Liu, *Green Chem.* **2017**, *19*, 5777–5781.

[420] Y. Xu, N. Mao, C. Zhang, X. Wang, J. Zeng, Y. Chen, F. Wang, J.-X. Jiang, *Appl. Catal. B* **2018**, *228*, 1–9.

[421] K. Venkataraman, V. N. Iyer, *The Chemistry of Synthetic Dyes*, *Vol. V*, (Ed.: K. Venkataraman), Academic Press, New York, **1971**, p. 200.

[422] J. O. Mueller, F. G. Schmidt, J. P. Blinco, C. Barner-Kowollik, *Angew. Chem. Int. Ed.* **2015**, *54*, 10284–10288.

[423] P. Lederhose, Z. Chen, R. Müller, J. P. Blinco, S. Wu, C. Barner-Kowollik, *Angew. Chem. Int. Ed.* **2016**, *55*, 12195–12199.

[424] P. Lederhose, D. Abt, A. Welle, R. Müller, C. Barner-Kowollik, J. P. Blinco, *Chem. Eur. J.* **2017**, *24*, 576–580.

[425] L. Delafresnaye, N. Zaquen, R. P. Kuchel, J. P. Blinco, P. B. Zetterlund, C. Barner-Kowollik, *Adv. Funct. Mater.* **2018**, 1800342.

[426] B. T. Tuten, J. P. Menzel, K. Pahnke, J. P. Blinco, C. Barner-Kowollik, *Chem. Commun.* **2017**, *53*, 4501–4504.

[427] D. E. Marschner, H. Frisch, J. T. Offenloch, B. T. Tuten, C. R. Becer, A. Walther, A. S. Goldmann, P. Tzvetkova, C. Barner-Kowollik, *Macromolecules* **2018**, *51*, 3802–3807.

[428] V. X. Truong, F. Li, F. Ercole, J. S. Forsythe, *ACS Macro Lett.* **2018**, *7*, 464–469.

[429] J. A. Pincock, *Acc. Chem. Res.* **1997**, *30*, 43–49.

[430] J. Jiang, X. Tong, Y. Zhao, *J. Am. Chem. Soc.* **2005**, *127*, 8290–8291.

[431] F. Feist, J. P. Menzel, T. Weil, J. P. Blinco, C. Barner-Kowollik, *J. Am. Chem. Soc.* **2018**, *140*, 11848–11854.

[432] C. K. Prier, D. A. Rankic, D. W. C. MacMillan, *Chem. Rev.* **2013**, *113*, 5322–5363.

[433] M. H. Shaw, J. Twilton, D. W. C. MacMillan, *J. Org. Chem.* **2016**, *81*, 6898–6926.

[434] Y.-Q. Zou, J.-R. Chen, X.-P. Liu, L.-Q. Lu, R. L. Davis, K. A. Jørgensen, W.-J. Xiao, *Angew. Chem. Int. Ed.* **2011**, *51*, 784–788.

[435] C. Pac, M. Ihama, M. Yasuda, Y. Miyauchi, H. Sakurai, *J. Am. Chem. Soc.* **1981**, *103*, 6495–6497.

[436] M. A. Ischay, M. E. Anzovino, J. Du, T. P. Yoon, *J. Am. Chem. Soc.* **2008**, *130*, 12886–12887.

[437] A. E. Hurtley, M. A. Cismesia, M. A. Ischay, T. P. Yoon, *Tetrahedron* **2011**, *67*, 4442–4448.

[438] N. A. Romero, D. A. Nicewicz, *Chem. Rev.* **2016**, *116*, 10075–10166.

[439] M. Göppert-Mayer, *Ann. Phys.* **1931**, *401*, 273–294.

[440] W. Kaiser, C. G. B. Garrett, *Phys. Rev. Lett.* **1961**, *7*, 229–231.

[441] I. D. Abella, *Phys. Rev. Lett.* **1962**, *9*, 453–455.

[442] R. R. Birge, B. M. Pierce, *Int. J. Quantum Chem.* **1986**, *29*, 639–656.

[443] G. S. He, L.-S. Tan, Q. Zheng, P. N. Prasad, *Chem. Rev.* **2008**, *108*, 1245–1330.

[444] M. Pawlicki, H. A. Collins, R. G. Denning, H. L. Anderson, *Angew. Chem. Int. Ed.* **2009**, *48*, 3244–3266.

[445] F. Helmchen, W. Denk, *Nat. Methods* **2005**, *2*, 932–940.

[446] D. J. Birch, *Spectrochim. Acta Part A* **2001**, *57*, 2313–2336.

[447] S. Sumalekshmy, M. M. Henary, N. Siegel, P. V. Lawson, Wu, K. Schmidt, J.-L. Brédas, J. W. Perry, C. J. Fahrni, *J. Am. Chem. Soc.* **2007**, *129*, 11888–11889.

[448] H. Kim, M. Seo, M. An, J. Hong, S. Tian Yu, J. Choi, O. Kwon, K. Lee, B. Cho, *Angew. Chem. Int. Ed.* **2008**, *47*, 5167–5170.

[449] Z.-Q. Liu, M. Shi, F.-Y. Li, Q. Fang, Z.-H. Chen, T. Yi, C.-H. Huang, *Org. Lett.* **2005**, *7*, 5481–5484.

[450] S. Charier, O. Ruel, J. Baudin, D. Alcor, J. Allemand, A. Meglio, L. Jullien, *Angew. Chem. Int. Ed.* **2004**, *43*, 4785–4788.

[451] C. D. Harvey, K. Svoboda, *Nature* **2007**, *450*, 1195–1200.

[452] S. Wecksler, A. Mikhailovsky, P. C. Ford, *J. Am. Chem. Soc.* **2004**, *126*, 13566–13567.

[453] A. P. Goodwin, J. L. Mynar, Y. Ma, G. R. Fleming, J. M. J. Fréchet, *J. Am. Chem. Soc.* **2005**, *127*, 9952–9953.

[454] M. Khurana, H. A. Collins, A. Karotki, H. L. Anderson, D. T. Cramb, B. C. Wilson, *Photochem. Photobiol.* **2007**, *83*, 1441–1448.

[455] C. LaFratta, J. Fourkas, T. Baldacchini, R. Farrer, *Angew. Chem. Int. Ed.* **2007**, *46*, 6238–6258.

[456] S. H. Wong, M. Thiel, P. Brodersen, D. Fenske, G. A. Ozin, M. Wegener, G. von Freymann, *Chem. Mater.* **2007**, *19*, 4213–4221.

[457] S. M. Kuebler, K. L. Braun, W. Zhou, J. Cammack, T. Yu, C. K. Ober, S. R. Marder, J. W. Perry, *J. Photochem. Photobiol. A* **2003**, *158*, 163–170.

[458] E. Walker, P. M. Rentzepis, *Nat. Photonics* **2008**, *2*, 406–408.

[459] S. Kawata, Y. Kawata, *Chem. Rev.* **2000**, *100*, 1777–1788.

[460] Z. Yu, T. Y. Ohulchanskyy, P. An, P. N. Prasad, Q. Lin, *J. Am. Chem. Soc.* **2013**, *135*, 16766–16769.

[461] A. S. Quick, H. Rothfuss, A. Welle, B. Richter, J. Fischer, M. Wegener, C. Barner-Kowollik, *Adv. Funct. Mater.* **2014**, *24*, 3571–3580.

[462] D. A. Parthenopoulos, P. M. Rentzepis, *Science* **1989**, *245*, 843–845.

[463] K. D. Belfield, Y. Liu, R. A. Negres, M. Fan, G. Pan, D. J. Hagan, F. E. Hernandez, *Chem. Mater.* **2002**, *14*, 3663–3667.

[464] Z. Sekkat, H. Ishitobi, S. Kawata, *Opt. Commun.* **2003**, *222*, 269–276.

[465] N. K. Urdabayev, A. Poloukhtine, V. V. Popik, *Chem. Commun.* **2006**, 454–456.

[466] B. H. Cumpston, S. P. Ananthavel, S. Barlow, D. L. Dyer, J. E. Ehrlich, L. L. Erskine, A. A. Heikal, S. M. Kuebler, I.-Y. S. Lee, D. McCord-Maughon, J. Qin, H. Röckel, M. Rumi, X.-L. Wu, S. R. Marder, J. W. Perry, *Nature* **1999**, *398*, 51–54.

[467] P. Mueller, M. M. Zieger, B. Richter, A. S. Quick, J. Fischer, J. B. Mueller, L. Zhou, G. U. Nienhaus, M. Bastmeyer, C. Barner-Kowollik, M. Wegener, *ACS Nano* **2017**, *11*, 6396–6403.

[468] C.-J. Carling, J.-C. Boyer, N. R. Branda, *J. Am. Chem. Soc.* **2009**, *131*, 10838–10839.

[469] M. Haase, H. Schäfer, *Angew. Chem. Int. Ed.* **2011**, *50*, 5808–5829.

[470] F. Wang, X. Liu, *Chem. Soc. Rev.* **2009**, *38*, 976–989.

[471] S. Wu, J. P. Blinco, C. Barner-Kowollik, *Chem. Eur. J.* **2017**, *23*, 8325–8332.

[472] F. Auzel, *Chem. Rev.* **2004**, *104*, 139–174.

[473] W. Wu, L. Yao, T. Yang, R. Yin, F. Li, Y. Yu, *J. Am. Chem. Soc.* **2011**, *133*, 15810–15813.

[474] J. Lai, Y. Zhang, N. Pasquale, K. Lee, *Angew. Chem. Int. Ed.* **2014**, *53*, 14419–14423.

[475] B. Yan, J.-C. Boyer, N. R. Branda, Y. Zhao, *J. Am. Chem. Soc.* **2011**, *133*, 19714–19717.

[476] Y. Yang, Q. Shao, R. Deng, C. Wang, X. Teng, K. Cheng, Z. Cheng, L. Huang, Z. Liu, X. Liu, B. Xing, *Angew. Chem. Int. Ed.* **2012**, *51*, 3125–3129.

[477] Z. Chen, W. Sun, H.-J. Butt, S. Wu, *Chem. Eur. J.* **2015**, *21*, 9165–9170.

[478] L. Zhao, J. Peng, Q. Huang, C. Li, M. Chen, Y. Sun, Q. Lin, L. Zhu, F. Li, *Adv. Funct. Mater.* **2013**, *24*, 363–371.

[479] C.-J. Carling, F. Nourmohammadian, J. Boyer, N. Branda, *Angew. Chem. Int. Ed.* **2010**, *49*, 3782–3785.

[480] Z. Chen, Y. Xiong, R. Etchenique, S. Wu, *Chem. Commun.* **2016**, *52*, 13959–13962.

[481] E. Ruggiero, A. Habtemariam, L. Yate, J. C. Mareque-Rivas, L. Salassa, *Chem. Commun.* **2014**, *50*, 1715–1718.

[482] A. Stepuk, D. Mohn, R. N. Grass, M. Zehnder, K. W. Krämer, F. Pellé, A. Ferrier, W. J. Stark, *Dent. Mater.* **2012**, *28*, 304–311.

[483] Q. Xiao, Y. Ji, Z. Xiao, Y. Zhang, H. Lin, Q. Wang, *Chem. Commun.* **2013**, *49*, 1527–1529.

[484] P. W. Neber, A. V. Friedolsheim, *Justus Liebigs Ann. Chem.* **1926**, *449*, 109–134.

[485] C. O'Brien, *Chem. Rev.* **1964**, *64*, 81–89.

[486] J. J. Li, *Name Reactions - A collection of Detailed Reaction Mechanisms*, 3rd, Springer, Berlin, **2003**.

[487] K. L. Stevens, D. K. Jung, M. J. Alberti, J. G. Badiang, G. E. Peckham, J. M. Veal, M. Cheung, P. A. Harris, S. D. Chamberlain, M. R. Peel, *Org. Lett.* **2005**, *7*, 4753–4756.

[488] G. A. Grasa, T. J. Colacot, *Org. Lett.* **2007**, *9*, 5489–5492.

[489] C. Ruecker, *Chem. Rev.* **1995**, *95*, 1009–1064.

[490] K. Okamoto, T. Shimbayashi, M. Yoshida, A. Nanya, K. Ohe, *Angew. Chem. Int. Ed.* **2016**, *55*, 7199–7202.

[491] L. Crombie, R. C. F. Jones, C. J. Palmer, *J. Chem. Soc., Perkin Trans. 1* **1987**, 317–331.

[492] C. Danieli, A. Cornia, C. Cecchelli, R. Sessoli, A.-L. Barra, G. Ponterini, B. Zanfrognini, *Polyhedron* **2009**, *28*, 2029–2035.

[493] C. J. Dürr, P. Lederhose, L. Hlalele, D. Abt, A. Kaiser, S. Brandau, C. Barner-Kowollik, *Macromolecules* **2013**, *46*, 5915–5923.

[494] P. Theato, *Multi-Component and Sequential Reactions in Polymer Synthesis*, Springer Nature, Basel, **2015**.

[495] O. Kreye, T. Tóth, M. A. R. Meier, *J. Am. Chem. Soc.* **2011**, *133*, 1790–1792.

[496] S. Cui, X. Pan, H. Gebru, X. Wang, J. Liu, J. Liu, Z. Li, K. Guo, *J. Mater. Chem. B* **2017**, *5*, 679–690.

[497] F. Bahadori, A. Dag, H. Durmaz, N. Cakir, H. Onyuksel, U. Tunca, G. Topcu, G. Hizal, *Polymers* **2014**, *6*, 214–242.

[498] L. Hong, J. He, Y. Chen, T. Kakuchi, *Polym. Chem.* **2016**, *7*, 3599–3607.

[499] B. Iskin, G. Yilmaz, Y. Yagci, *Polym. Chem.* **2011**, *2*, 2865–2871.

[500] S. S. Yanari, F. A. Bovey, R. Lumry, *Nature* **1963**, *200*, 242–244.

[501] M. T. Vala, J. Haebig, S. A. Rice, *J. Chem. Phys.* **1965**, *43*, 886–897.

[502] N. Nishiyama, *Nat. Nanotechnol.* **2007**, *2*, 203–204.

[503] W. Kloepffer, *Ann. N.Y. Acad. Sci.* **1981**, *366*, 373–386.

[504] F. Hirayama, *J. Chem. Phys.* **1965**, *42*, 3163–3171.

[505] S. Cui, X. Pan, H. Gebru, X. Wang, J. Liu, J. Liu, Z. Li, K. Guo, *J. Mater. Chem. B* **2017**, *5*, 679–690.

[506] F. Wang, T. K. Bronich, A. V. Kabanov, R. D. Rauh, J. Roovers, *Bioconjugate Chem.* **2005**, *16*, 397–405.

[507] S. Ozlem, B. Iskin, G. Yilmaz, M. Kukut, J. Hacaloglu, Y. Yagci, *Eur. Polym. J.* **2012**, *48*, 1755–1767.

[508] L. Hong, J. He, Y. Chen, T. Kakuchi, *Polym. Chem.* **2016**, *7*, 3599–3607.

[509] H. Gao, K. Matyjaszewski, *Prog. Polym. Sci.* **2009**, *34*, 317–350.

[510] N. Chen, L.-T. Yan, X.-M. Xie, *Macromolecules* **2013**, *46*, 3544–3553.

[511] Y. K. Choi, Y. H. Bae, S. W. Kim, *Macromolecules* **1998**, *31*, 8766–8774.

[512] C. Barner-Kowollik, M. Bastmeyer, E. Blasco, G. Delaittre, P. Müller, B. Richter, M. Wegener, *Angew. Chem. Int. Ed.* **2017**, *56*, 15828–15845.

[513] A. Padwa in, (Ed.: A. R. Katritzky), Advances in Heterocyclic Chemistry, Academic Press, Cambridge, **2010**, pp. 1–31.

[514] C. E. Mortimer, U. Mueller, *Chemie - Das Basiswissen der Chemie*, 10th ed., Thieme, Stuttgart, **2010**, p. 692.

[515] F. M. Hauser, S. R. Ellenberger, *Synthesis* **1987**, *8*, 723–724.

[516] In *CRC Handbook of Chemistry and Physics*, (Ed.: W. M. Haynes), **2010**.

[517] A. Theisen, C. Johann, M. P. Deacon, S. E. Harding, *Refractive Increment Data-Book for Polymer and Biomolecular Scientists*, 1st ed., Nottingham University Press, Nottingham, **2000**.

[518] D. N. Barsoum, N. Okashah, X. Zhang, L. Zhu, *J. Org. Chem.* **2015**, *80*, 9542–9551.

[519] C.-W. Wu, L. R. Yarbrough, F. Y. H. Wu, *Biochemistry* **1976**, *15*, 2863–2868.

[520] R. H. Wollenberg, J. E. Goldstein, *Synthesis* **1980**, *9*, 757–758.

[521] A. Saha, A. Bhattacharjya, *Chem. Commun.* **1997**, 495–496.

[522] G. D. Vilela, R. R. da Rosa, P. H. Schneider, I. H. Bechtold, J. Eccher, A. A. Merlo, *Tetrahedron Lett.* **2011**, *52*, 6569–6572.

[523] A. P. Kozikowski, *Acc. Chem. Res.* **1984**, *17*, 410–416.

[524] Y.-S. Lee, B. H. Kim, *Bioorg. Med. Chem. Lett.* **2002**, *12*, 1395–1397.

[525] S. Dadiboyena, A. Nefzi, *Eur. J. Med. Chem.* **2010**, *45*, 4697–4707.

[526] I. Singh, Z. Zarafshani, J.-F. Lutz, F. Heaney, *Macromolecules* **2009**, *42*, 5411–5413.

[527] K. Gutsmiedl, C. T. Wirges, V. Ehmke, T. Carell, *Org. Lett.* **2009**, *11*, 2405–2408.

[528] T. D. Svejstrup, W. Zawodny, J. J. Douglas, D. Bidgeli, N. S. Sheikh, D. Leonori, *Chem. Commun.* **2016**, *52*, 12302–12305.

[529] S. Grecian, V. Fokin, *Angew. Chem.* **2008**, *120*, 8409–8411.

[530] T. V. Hansen, P. Wu, V. V. Fokin, *J. Org. Chem.* **2005**, *70*, 7761–7764.

[531] A. Hassner, K. M. Lokanatha Rai, *Synthesis* **1989**, *1*, 57–59.

[532] J. T. Offenloch, S. Bastian, H. Mutlu, C. Barner-Kowollik, *ChemPhotoChem* **2019**, *3*, 66–70.

[533] Y. Koyama, Y.-G. Lee, S. Kuroki, T. Takata, *Tetrahedron Lett.* **2015**, *56*, 7038–7042.

[534] J. N. Kim, E. K. Ryu, *Heterocycles* **1990**, *31*, 1693–1697.

[535] C. Grundmann, *Synthesis* **1970**, *7*, 344–359.

[536] T. Pauloehrl, G. Delaittre, M. Bruns, M. Meißler, H. G. Boerner, M. Bastmeyer, C. Barner-Kowollik, *Angew. Chem. Int. Ed.* **2012**, *51*, 9181–9184.

[537] Y. Miyake, H. Takahashi, N. Akai, K. Shibuya, A. Kawai, *Chem. Lett.* **2014**, *43*, 1275–1277.

[538] J. Lalevée, X. Allonas, J. P. Fouassier, H. Tachi, A. Izumitani, M. Shirai, M. Tsunooka, *J. Photochem. Photobiol. A* **2002**, *151*, 27–37.

[539] G. Delzenne, U. Laridon, H. Peeters, *Eur. Polym. J.* **1970**, *6*, 933–943.

[540] J. Xu, G. Ma, K. Wang, J. Gu, S. Jiang, J. Nie, *J. Appl. Polym. Sci.* **2012**, *123*, 725–731.

[541] C. Dworak, R. Liska, *J. Polym. Sci. Part A: Polym. Chem.* **2010**, *48*, 5865–5871.

[542] E. Reichmanis, C. W. Wilkins, E. A. Chandross, *J. Electrochem. Soc.* **1980**, *127*, 2514–2517.

[543] P. Xiao, J. Zhang, F. Dumur, M. A. Tehfe, F. Morlet-Savary, B. Graff, D. Gigmes, J. P. Fouassier, J. Lalevée, *Prog. Polym. Sci.* **2015**, *41*, 32–66.

[544] S. Telitel, F. Dumur, D. Gigmes, B. Graff, J. Fouassier, J. Lalevée, *Polymer* **2013**, *54*, 2857–2864.

[545] M.-A. Tehfe, F. Dumur, B. Graff, F. Morlet-Savary, D. Gigmes, J.-P. Fouassier, J. Lalevée, *Polym. Chem.* **2013**, *4*, 2313–2324.

[546] J. Cheng, L. Chun, J. Bo, Q.-j. Yin, *e-Polymers* **2012**, *12*, 1–10.

[547] M. Tsunooka, S. Imono, K. Nakayama, H. Kuwabara, M. Tanaka, *J. Polym. Sci. A Polym. Chem.* **1986**, *24*, 317–330.

[548] G. Smets, *Polym. J.* **1985**, *17*, 153–165.

[549] K. Suyama, M. Tsunooka, *Polym. Degrad. Stab.* **1994**, *45*, 409–413.

[550] K.-H. Song, M. Tsunooka, M. Tanaka, *Makromol. Chem. Rapid Commun.* **1988**, *9*, 519–524.

[551] K.-H. Song, A. Urano, M. Tsunooka, M. Tanaka, *J. Polym. Sci. Part C: Polym. Lett.* **1987**, *25*, 417–421.

[552] K.-H. Song, M. Tsunooka, M. Tanaka, *Polym. Degrad. Stab.* **1989**, *26*, 255–267.

[553] E. Murtezi, Y. Yagci, *Macromol. Rapid Commun.* **2014**, *35*, 1782–1787.

[554] G. Mantovani, F. Lecolley, L. Tao, D. M. Haddleton, J. Clerx, J. J.L. M. Cornelissen, K. Velonia, *J. Am. Chem. Soc.* **2005**, *127*, 2966–2973.

[555] J. Brandrup, E. H. Immergut, E. A. Grulke, *Polymer Handbook*, 4th ed., John Wiley Sons, New York, **2003**.

[556] P. V. Mendonça, A. C. Serra, J. F. Coelho, A. V. Popov, T. Guliashvili, *Eur. Polym. J.* **2011**, *47*, 1460–1466.

[557] B. Yameen, C. Rodriguez-Emmenegger, C. M. Preuss, O. Pop-Georgievski, E. Verveniotis, V. Trouillet, B. Rezek, C. Barner-Kowollik, *Chem. Commun.* **2013**, *49*, 8623–8625.

[558] Y.-G. Lee, Y. Koyama, M. Yonekawa, T. Takata, *Macromolecules* **2009**, *42*, 7709–7717.

CHAPTER 8

APPENDIX

A Emission Spectra

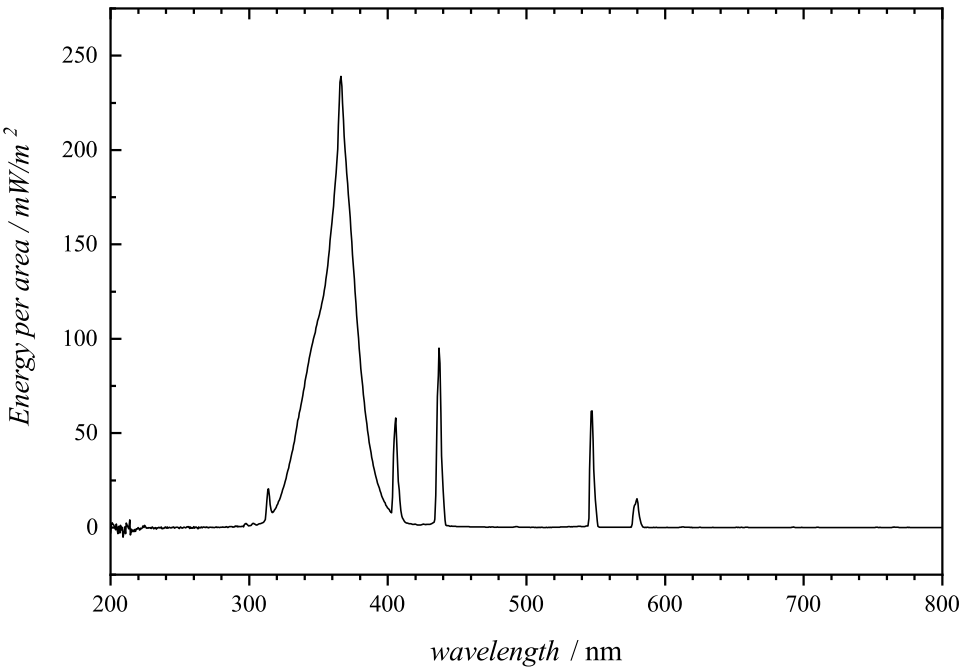

Figure A.1. Emission spectrum of the compact lamp Philips PL-L cleo ($\lambda_{max.}$ = 365 nm). The presented lamp was employed to trigger the cycloaddition between **PE-Ph** and various maleimide species. Adapted with permission from reference [151]. Copyright (2018) Royal Society of Chemistry.

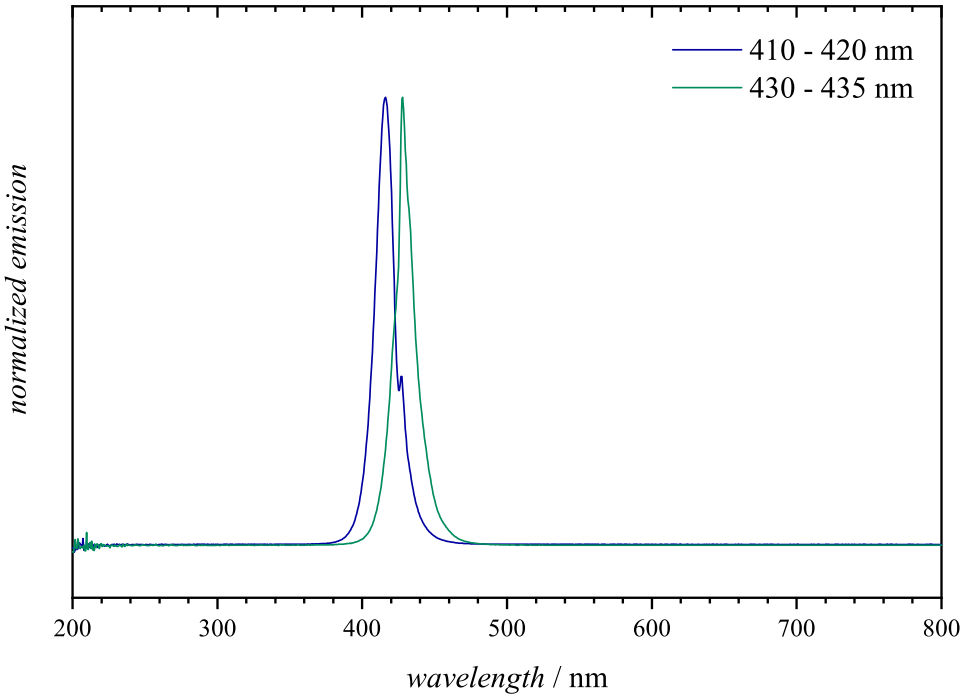

Figure A.2. Emission spectra of the LED setups employed in the current thesis. Adapted with permission from [532]. Copyright (2018) Wiley-VCH.

B Additional Figures of Chapter 3

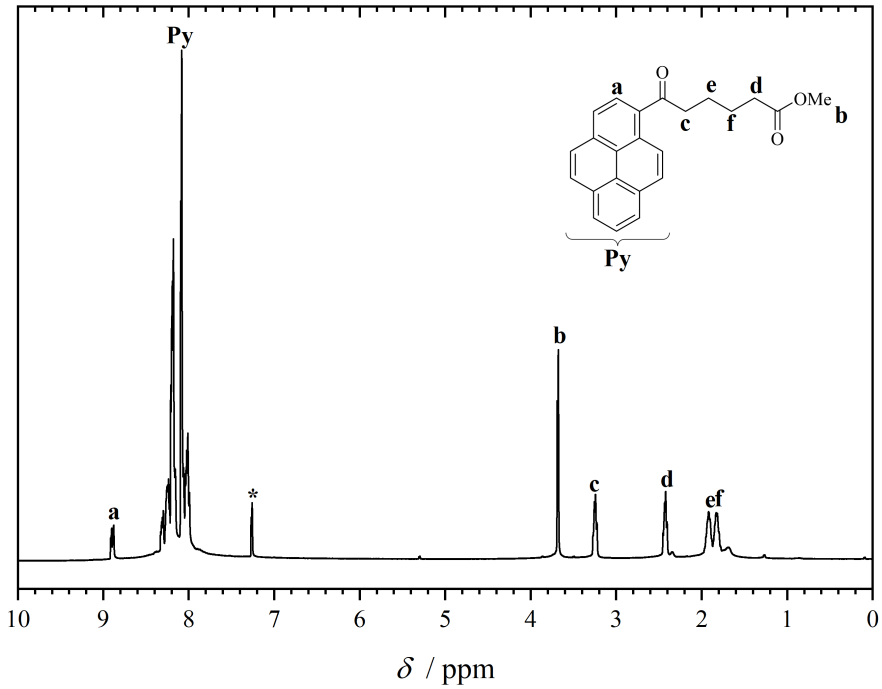

Figure B.1. ^{1}H NMR spectrum (400 MHz, $CDCl_3$, 298 K) of methyl 4-(3-(pyren-1-yl)-2*H*-azirin-2-yl)butanoate. The magnetic resonance marked with an asterisk is assigned to $CHCl_3$.

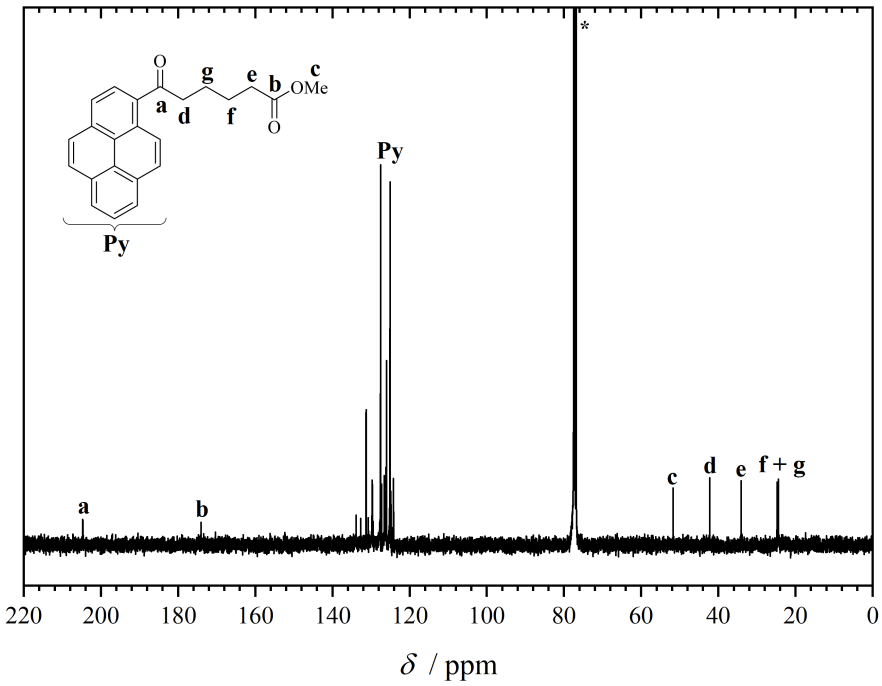

Figure B.2. ^{13}C NMR spectrum (100 MHz, $CDCl_3$, 298 K) of methyl 4-(3-(pyren-1-yl)-2*H*-azirin-2-yl)butanoate. The magnetic resonance marked with an asterisk is assigned to $CHCl_3$.

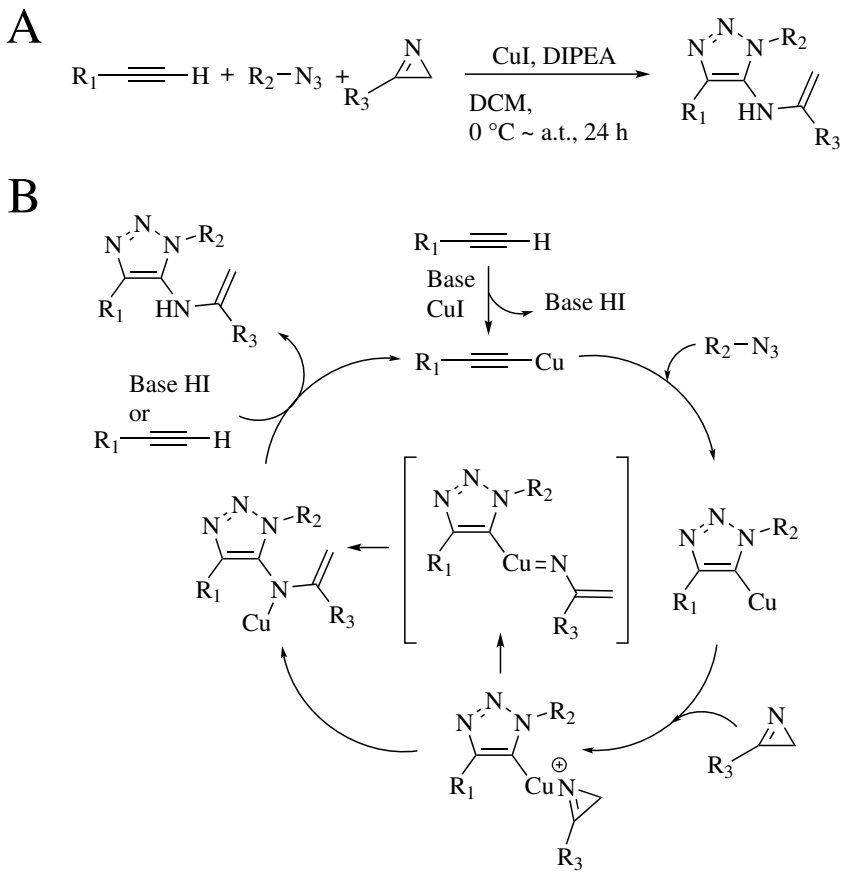

Figure B.3. Proposed mechanism of the CuAAC interrupted by 2*H*-azirines. Adapted with permission from [178]. Copyright (2017) American Chemical Society.

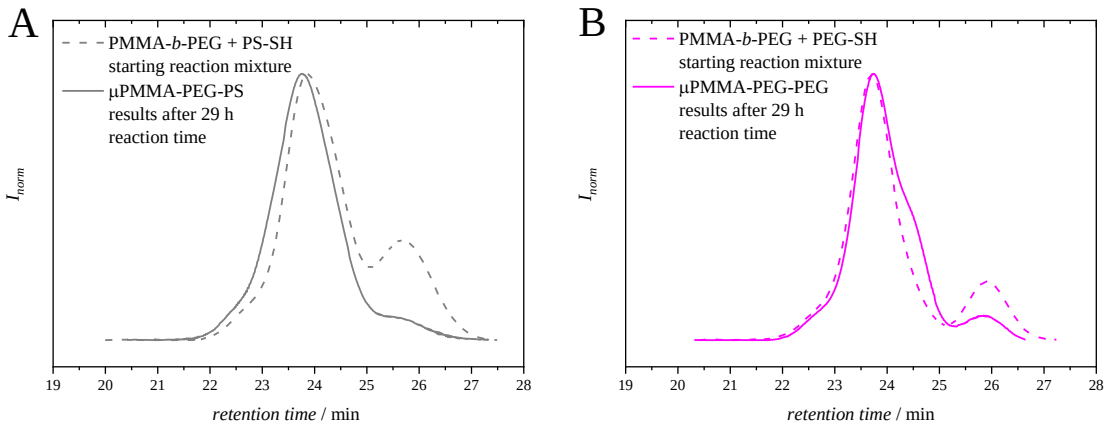

Figure B.4. SEC (THF, 35 °C, RI) traces of the polymer mixtures consisting of the block copolymer species and a thiol-terminated polymer (**A: PS-SH**) and (**B: PEG-SH**) before and after modification *via* radical thiol-ene addition. Adapted with permission from reference [204]. Copyright (2018) American Chemical Society.

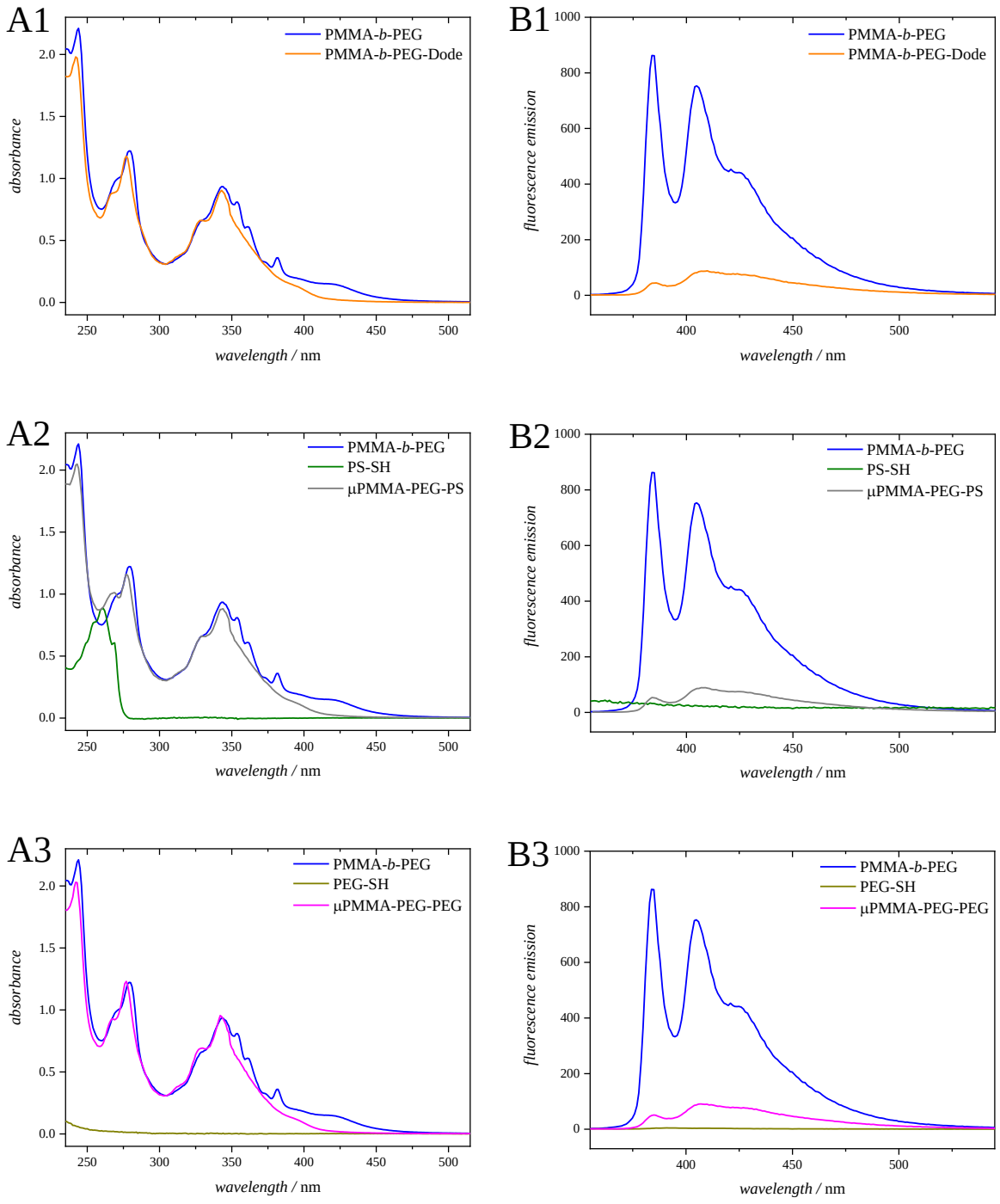

Figure B.5. UV/Vis (**A1** to **A3**) and fluorescence (**B1** to **B3**, $\lambda_{exc.}$ = 344 nm) spectra of **PMMA-*b*-PEG**, **PMMA-*b*-PEG-Dode** and the mikto-arm star polymers in DCM at ambient temperature. A concentration of $1.81 \cdot 10^{-5}$ mmol mL^{-1} and of $7.22 \cdot 10^{-5}$ mmol mL^{-1} was employed for UV/Vis and fluorescence measurements, respectively. Adapted with permission from reference [204]. Copyright (2018) American Chemical Society.

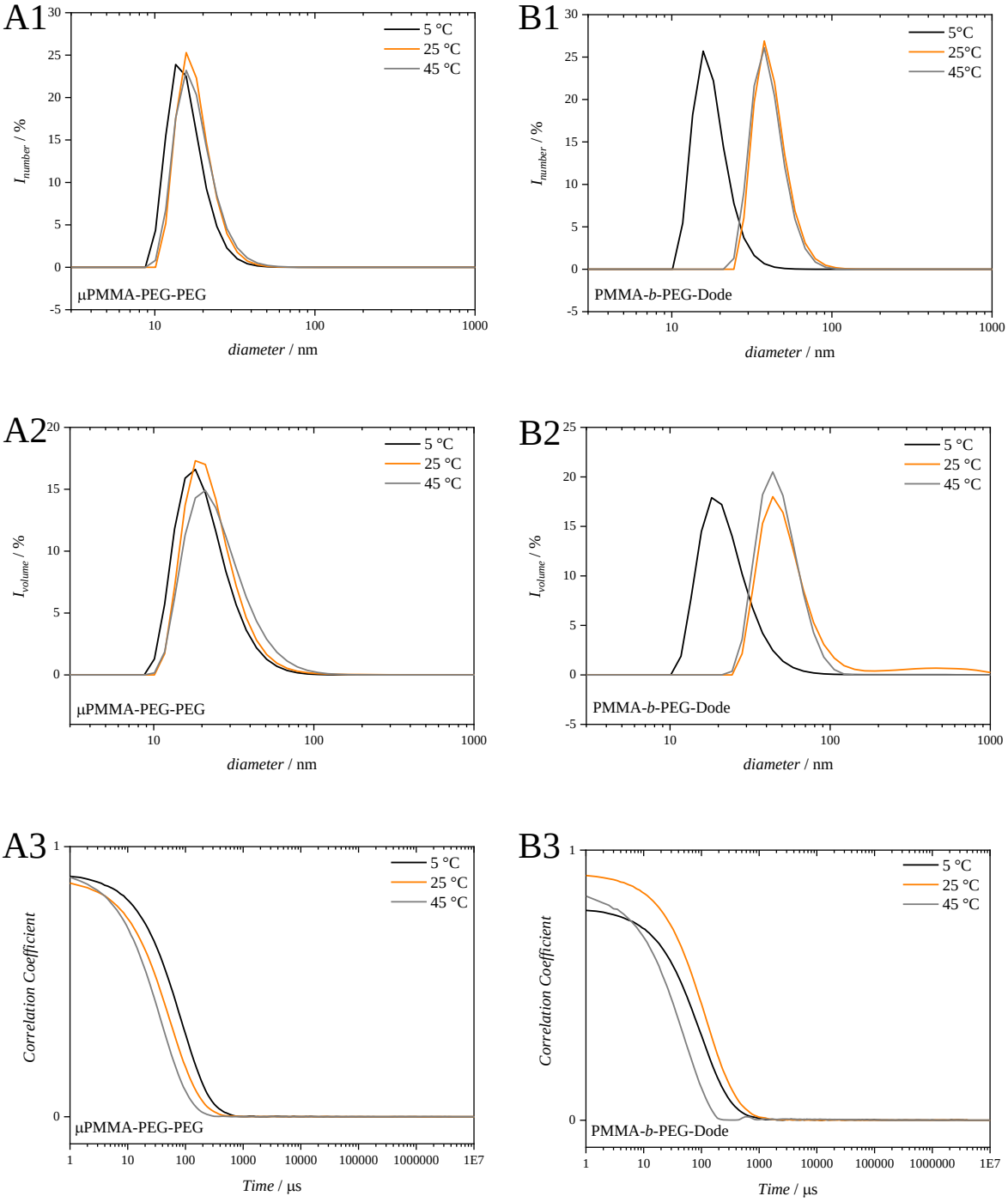

Figure B.6. Temperature-dependent DLS studies of μ-**PMMA-PEG-PEG** (**A1** to **A3**) and **PMMA-*b*-PEG-Dode** (**B1** to **B3**) in water. The measurements were conducted with a concentration of 1 mg mL^{-1}. Adapted with permission from reference [204]. Copyright (2018) American Chemical Society.

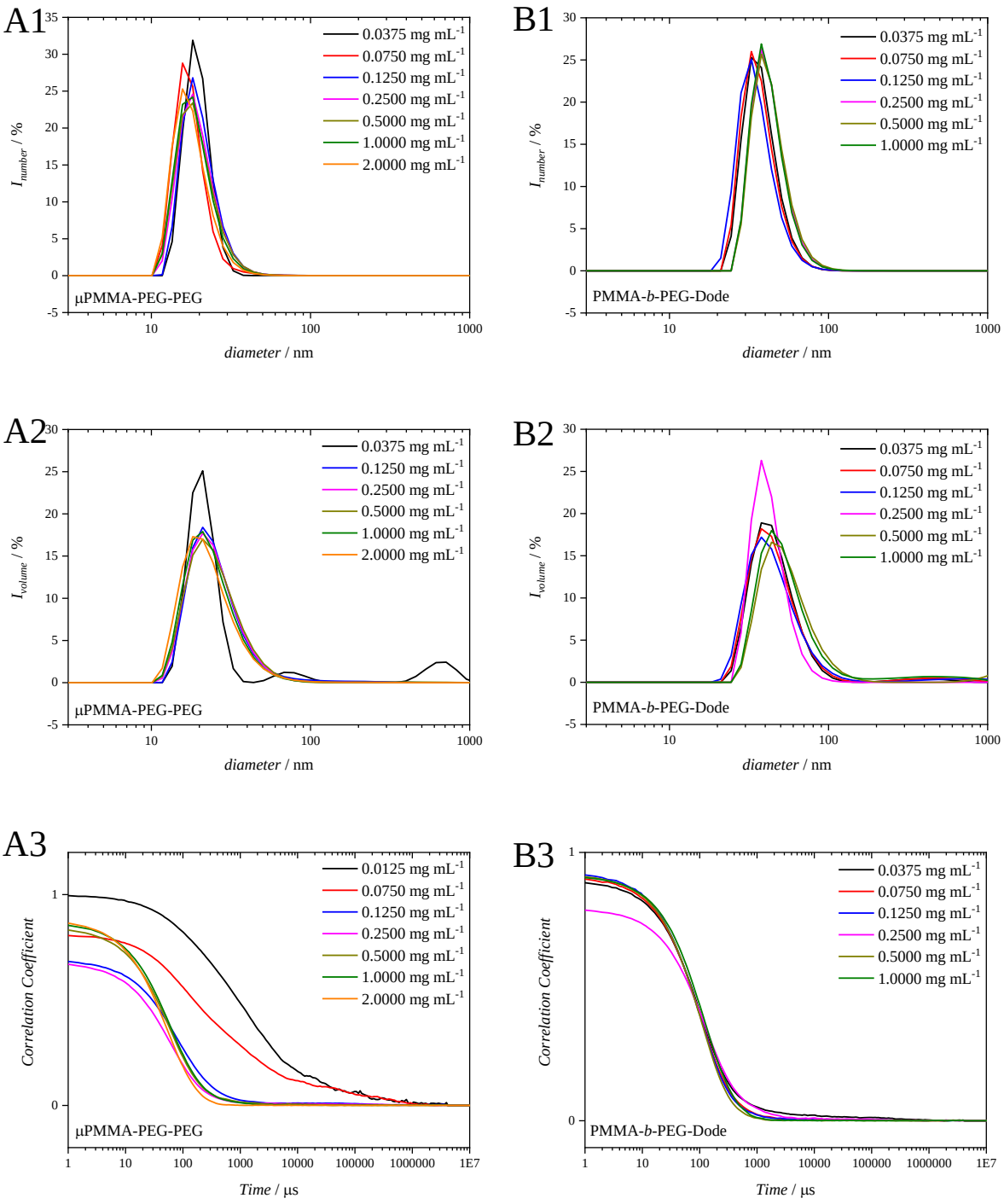

Figure B.7. Concentration-dependent DLS studies of μ-**PMMA-PEG-PEG** (**A1** to **A3**) and **PMMA-*b*-PEG-Dode** (**B1** to **B3**) in water. The measurements were conducted at 25 °C. Adapted with permission from reference [204]. Copyright (2018) American Chemical Society.

C Additional Figures of Chapter 4

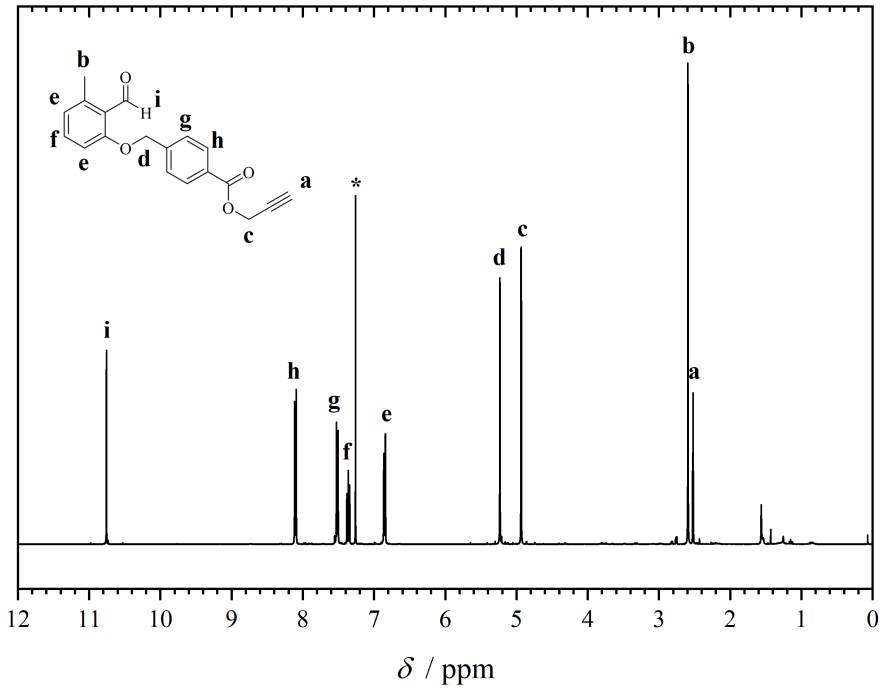

Figure C.1. ^{1}H NMR spectrum (400 MHz, $CDCl_3$, 298 K) of prop-2-yn-1-yl 4-((2-formyl-3-methylphenoxy)-methyl)benzoate (**Ph-alkyne**). The magnetic resonance marked with an asterisk is assigned to $CHCl_3$. Adapted with permission from reference [151]. Copyright (2018) Royal Society of Chemistry.

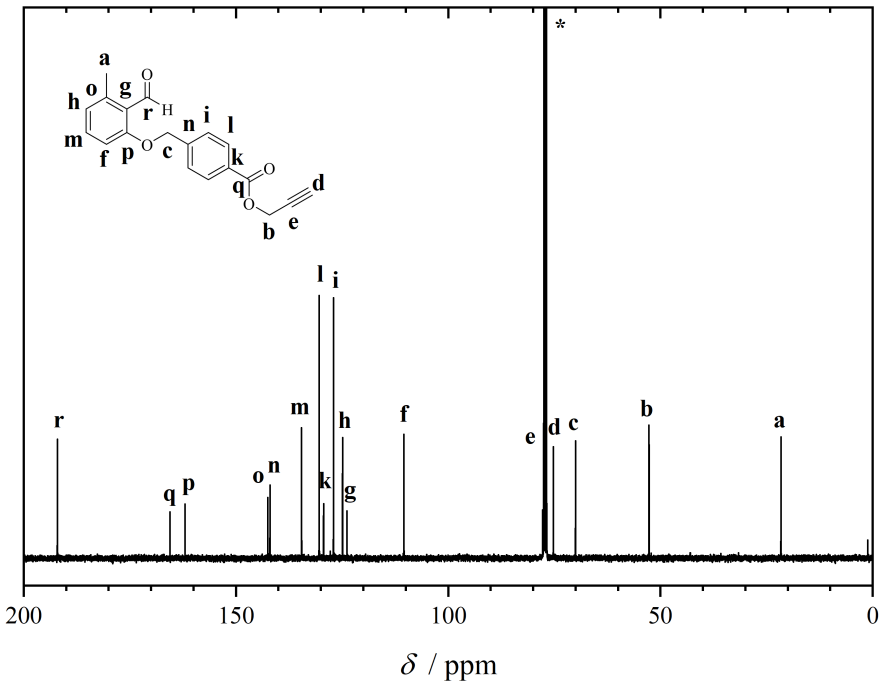

Figure C.2. ^{13}C NMR spectrum (100 MHz, $CDCl_3$, 298 K) of prop-2-yn-1-yl 4-((2-formyl-3-methylphenoxy)-methyl)benzoate (**Ph-alkyne**). The magnetic resonance marked with an asterisk is assigned to $CHCl_3$. Adapted with permission from reference [151]. Copyright (2018) Royal Society of Chemistry.

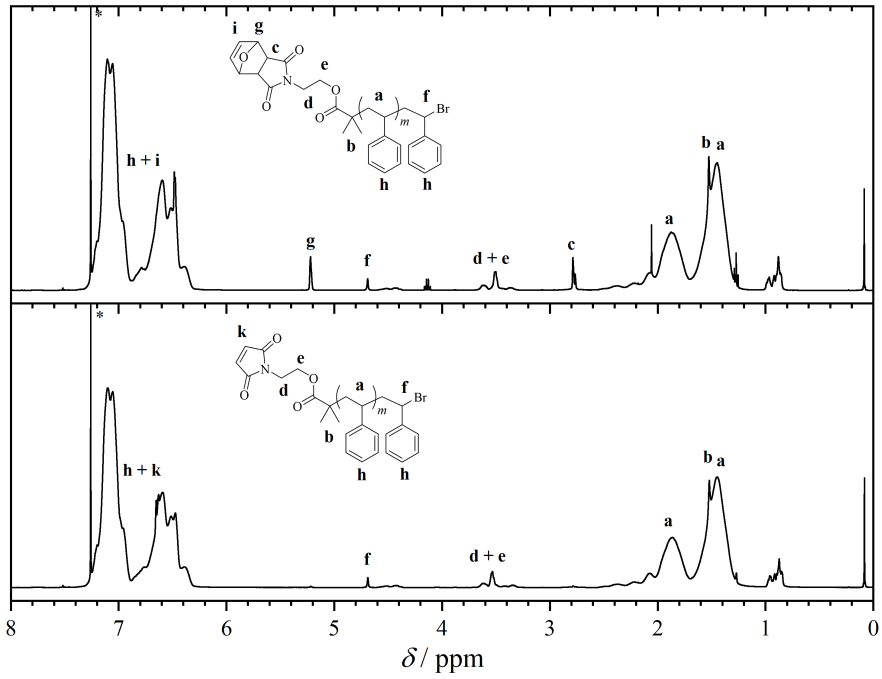

Figure C.3. ^{1}H NMR spectrum (400 MHz, $CDCl_3$, 298 K) of **PS-Mal** before (top) and after removal of the furan group (bottom). The magnetic resonance marked with an asterisk is assigned to $CHCl_3$. Adapted with permission from reference [151]. Copyright (2018) Royal Society of Chemistry.

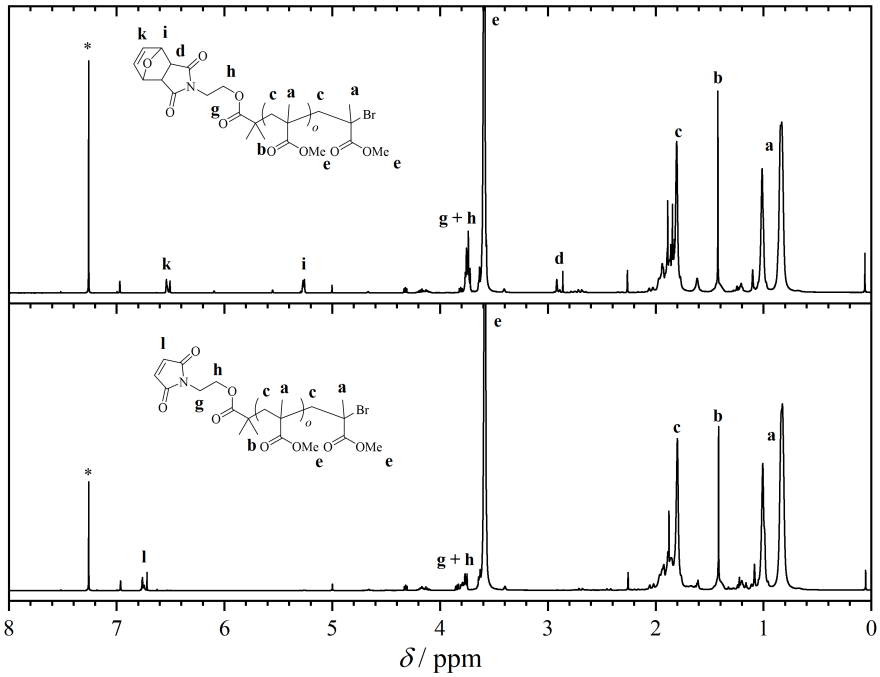

Figure C.4. ^{1}H NMR spectrum (400 MHz, $CDCl_3$, 298 K) of **PMMA-Mal** before (top) and after removal of the furan group (bottom). The magnetic resonance marked with an asterisk is assigned to $CHCl_3$. Adapted with permission from reference [151]. Copyright (2018) Royal Society of Chemistry.

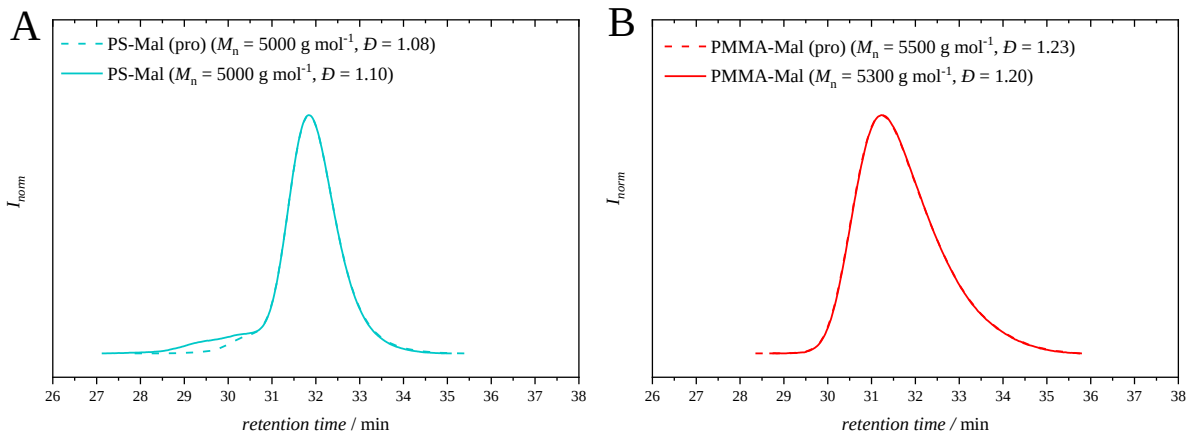

Figure C.5. SEC (THF, 35 °C, RI) traces of **PS-Mal** (**A**) and **PMMA-Mal** (**B**) before and after removal of the furan group. Adapted with permission from reference [151]. Copyright (2018) Royal Society of Chemistry.

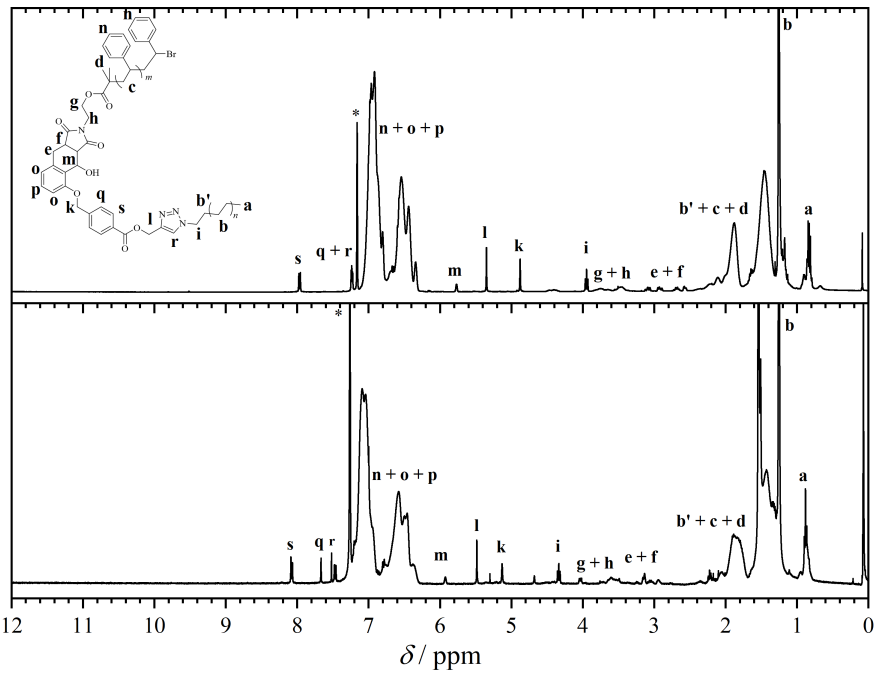

Figure C.6. ^{1}H NMR spectrum (400 MHz) of **PE-*b*-PS** in C_6D_6/TCE at 90 °C (top spectrum) and in $CDCl_3$ at ambient temperature (bottom spectrum). The magnetic resonances marked with an asterisk is assigned to C_6H_6 and $CHCl_3$.

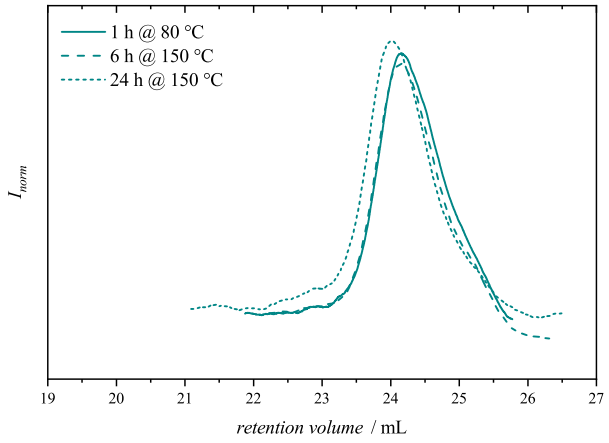

Figure C.7. Preparation-dependent HT SEC (TCB, 150 °C, RI) results of **PE-*b*-PS** indicate that no degradation of the block copolymer occurs while dissolving it at elevated temperature in TCB. Adapted with permission from reference [151]. Copyright (2018) Royal Society of Chemistry.

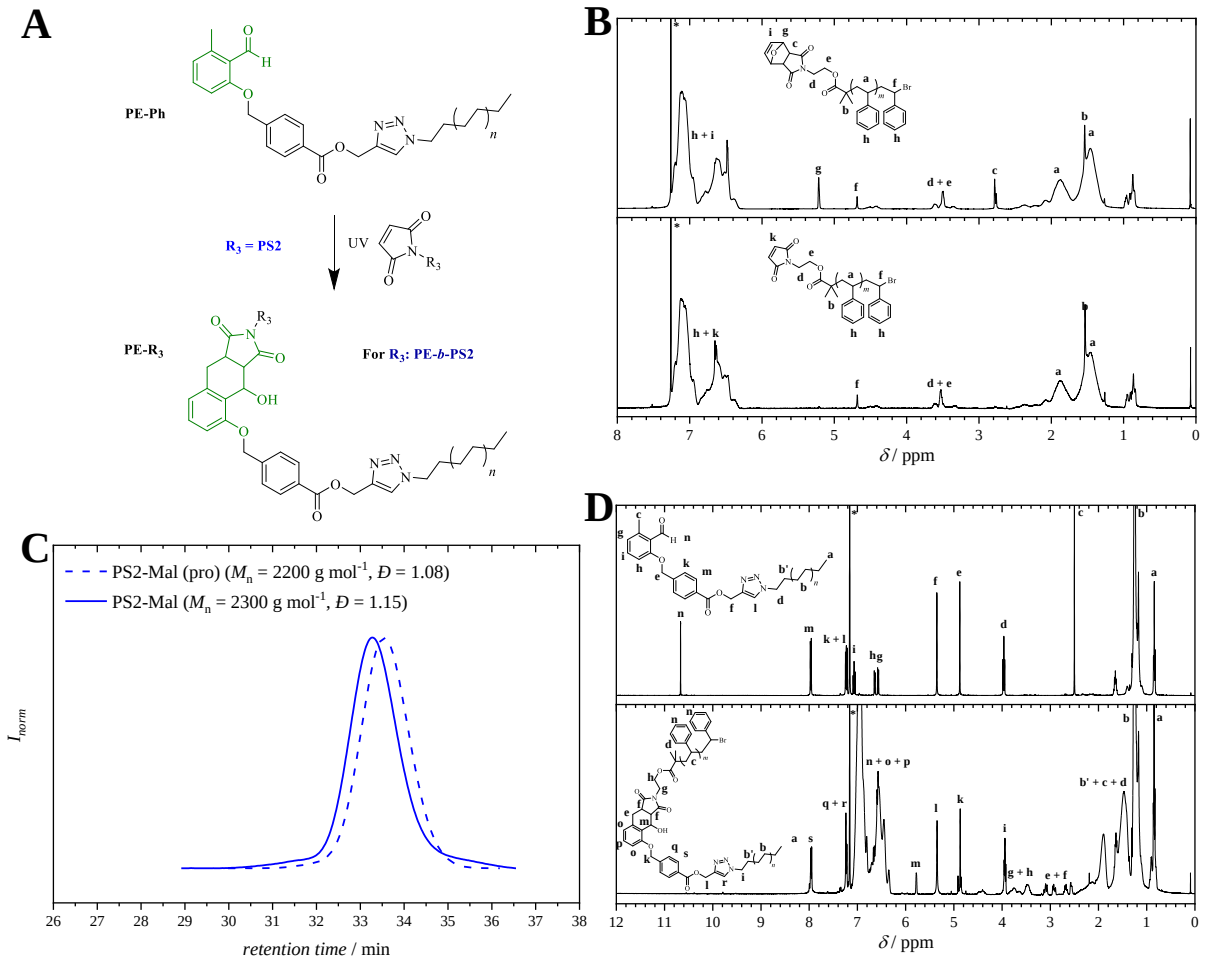

Figure C.8. **A**: Reaction scheme of the light-induced block copolymer formation of **PE-Ph** and maleimide-terminated **PS2**. **B**: ^{1}H NMR spectra (400 MHz, $CDCl_3$, 298 K) of **PS2-Mal** before (top spectrum) and after deprotection (bottom spectrum) under vacuum at elevated temperatures. The magnetic resonance marked with an asterisk is assigned to $CHCl_3$. **C**: SEC (THF, 35 °C, RI) traces of the same polymer species. **D**: HT ^{1}H NMR spectra (400 MHz, C_6D_6/TCE, 90 °C) of **PE-Ph** as parent polymer (top spectrum) and of the block copolymer **PE-*b*-PS2** (bottom spectrum) indicating the successful synthesis of the block copolymer. However, due to a refractive index with a value of approximately 0 for the block polymer species, no HT SEC trace in TCB can be recorded. The magnetic resonances marked with an asterisk are assigned to C_6H_6.

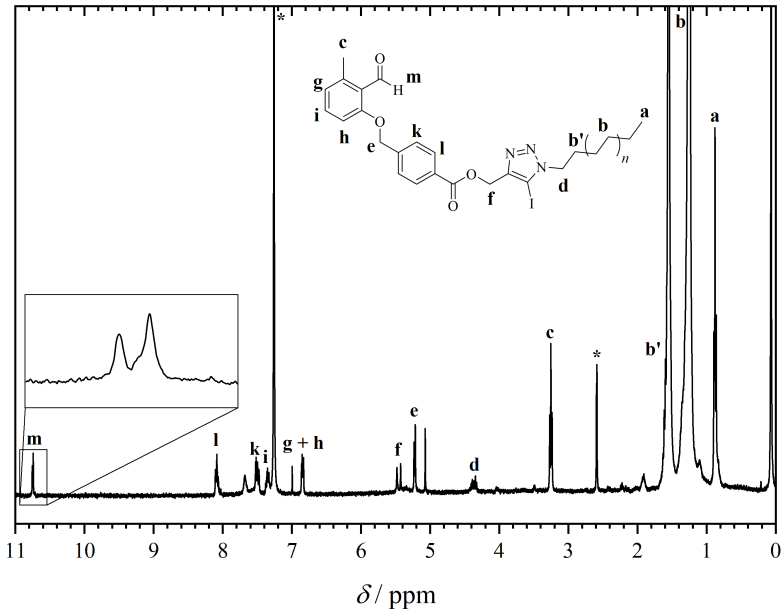

Figure C.9. ^{1}H NMR spectrum (400 MHz, $CDCl_3$, 298 K) of **PE-Ph-I**. The magnetic resonance marked with an asterisk is assigned to $CHCl_3$. The enlargement of the magnetic resonance associated with the aldehyde proton reveals that the iodo-triazole formation reaction results in the formation of two polymer species.

D Additional Figures of Chapter 5

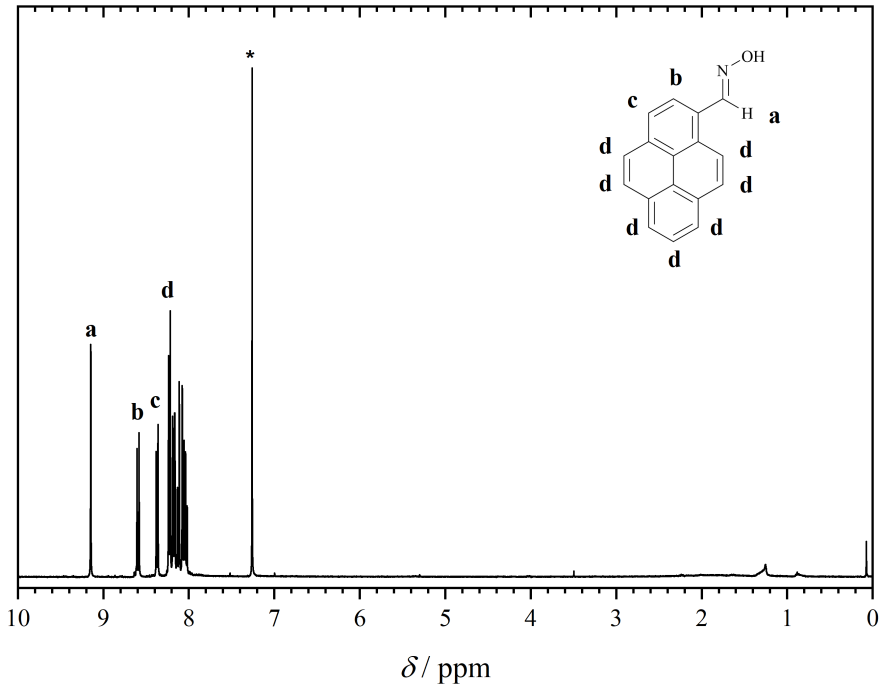

Figure D.1. ^{1}H NMR spectrum (400 MHz, $CDCl_3$, 298 K) of 1-pyrenecarbaldehyde oxime. The magnetic resonance marked with an asterisk is assigned to $CHCl_3$. Adapted with permission from reference [532]. Copyright (2019) Wiley-VCH Verlag GmbH & Co. KGaA, Weinheim.

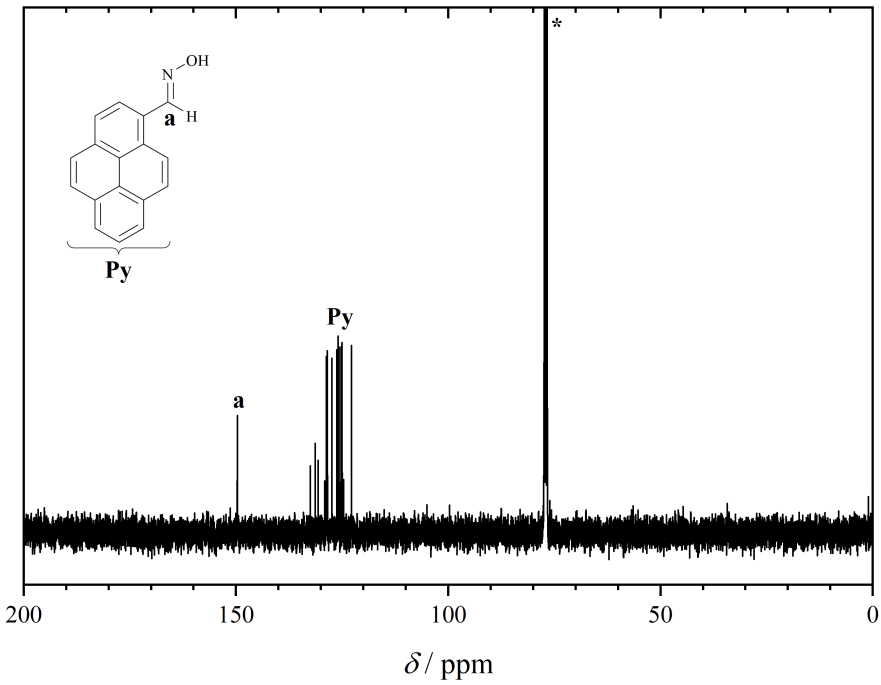

Figure D.2. ^{13}C NMR spectrum (100 MHz, $CDCl_3$, 298 K) of 1-pyrenecarbaldehyde oxime. The magnetic resonance marked with an asterisk is assigned to $CHCl_3$. Adapted with permission from reference [532]. Copyright (2019) Wiley-VCH Verlag GmbH & Co. KGaA, Weinheim.

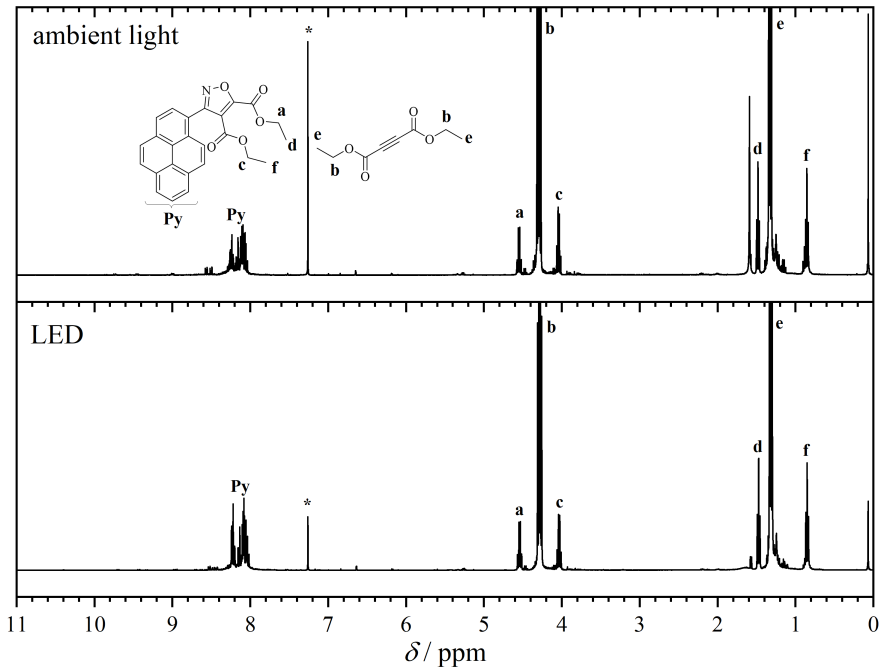

Figure D.3. Comparison of the ^1H NMR spectra (400 MHz, $CDCl_3$, 298 K) of the crude reaction mixtures of chloro pyrene oxime and diethyl acetylenedicarboxylate after exposure to ambient light (top spectrum) or LED irradiation (bottom spectrum). The magnetic resonance marked with an asterisk is assigned to $CHCl_3$. Adapted with permission from reference [532]. Copyright (2019) Wiley-VCH Verlag GmbH & Co. KGaA, Weinheim.

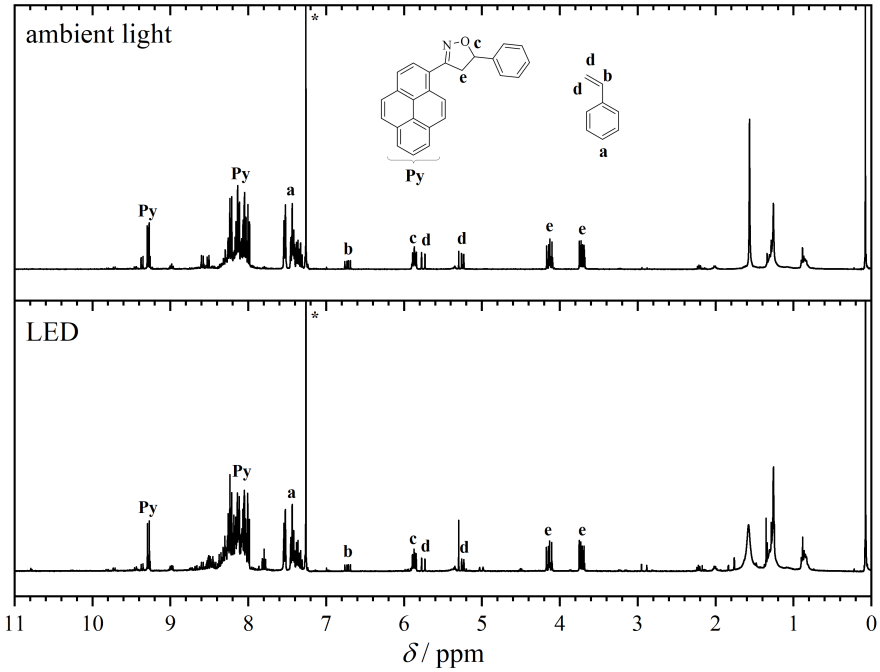

Figure D.4. Comparison of the ^{1}H NMR spectra (400 MHz, $CDCl_3$, 298 K) of the crude reaction mixtures of chloro pyrene oxime and styrene after exposure to ambient light (top spectrum) or LED irradiation (bottom spectrum). The magnetic resonance marked with an asterisk is assigned to $CHCl_3$. Adapted with permission from reference [532]. Copyright (2019) Wiley-VCH Verlag GmbH & Co. KGaA, Weinheim.

Table D.1. Comparison of the assigned signals of the high resolution ESI-MS results for the light-induced end group modification of **P1** and **P2** listed in tabular form (for ESI-MS spectra, refer to **Figures 5.6** and **D.15**). Adapted with permission from reference [532]. Copyright (2019) Wiley-VCH Verlag GmbH & Co. KGaA, Weinheim.

Polymer Species	**Sum formula**	**m/z$_{exp.}$**	**m/z$_{theo.}$**	**Δm/z**
P1	$[OMe\text{-}P(EG)_{45}Mal + 3\ Na^+]^{3+}$	749.0718	749.0718	0.0000
PC1	$[OMe\text{-}P(EG)_{39}Mal\text{-}Py + 3\ Na^+]^{3+}$	742.0422	742.0422	0.0000
P2	$[OMe\text{-}P(EG)_{46}Pentene + 3\ Na^+]^{3+}$	736.0812	736.0803	0.0009
PC2	$[OMe\text{-}P(EG)_{41}Pentene\text{-}Py + 3\ Na^+]^{3+}$	743.7261	743.7261	0.0000

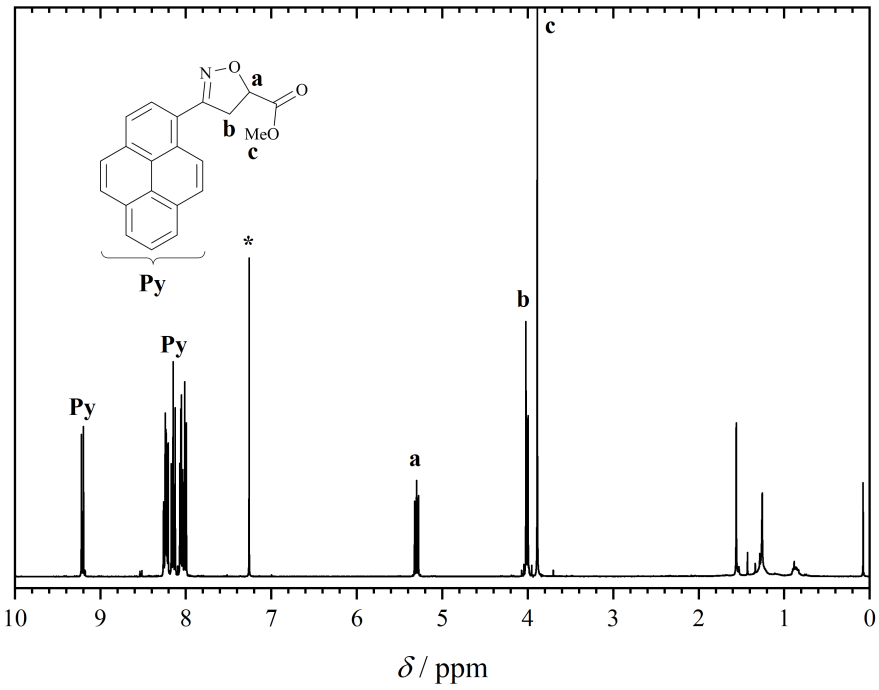

Figure D.5. ^{1}H NMR spectrum (400 MHz, $CDCl_3$, 298 K) of **C1**. The magnetic resonance marked with an asterisk is assigned to $CHCl_3$. Adapted with permission from reference [532]. Copyright (2019) Wiley-VCH Verlag GmbH & Co. KGaA, Weinheim.

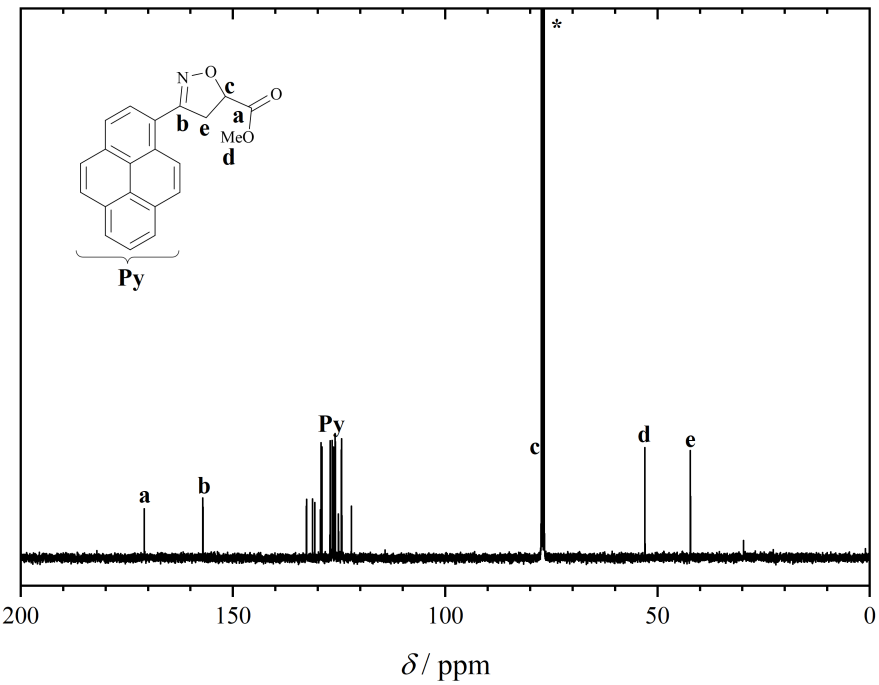

Figure D.6. ^{13}C NMR spectrum (100 MHz, $CDCl_3$, 298 K) of **C1**. The magnetic resonance marked with an asterisk is assigned to $CHCl_3$. Adapted with permission from reference [532]. Copyright (2019) Wiley-VCH Verlag GmbH & Co. KGaA, Weinheim.

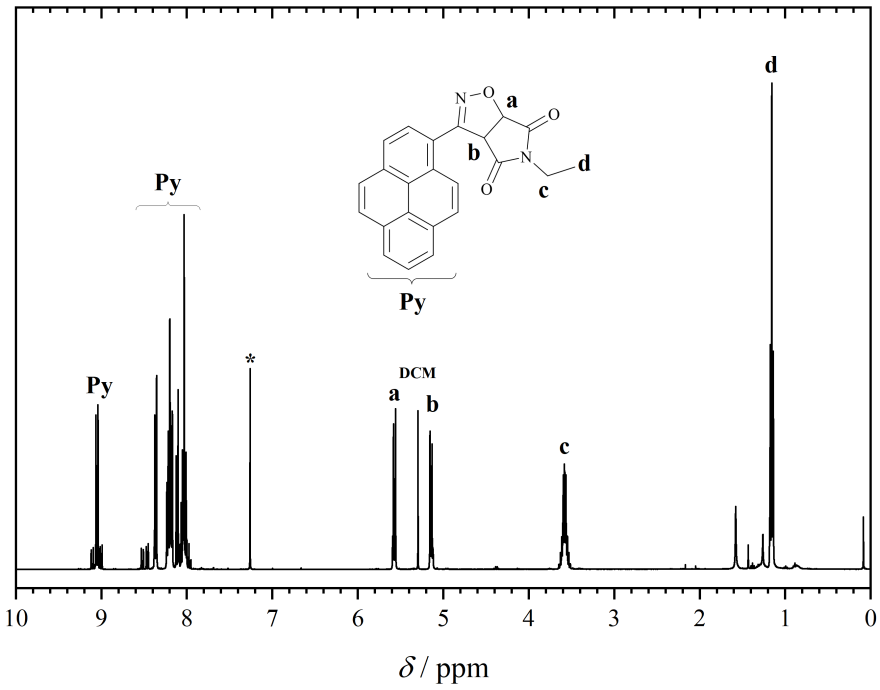

Figure D.7. ^{1}H NMR spectrum (400 MHz, $CDCl_3$, 298 K) of **C2**. The magnetic resonance marked with an asterisk is assigned to $CHCl_3$. Adapted with permission from reference [532]. Copyright (2019) Wiley-VCH Verlag GmbH & Co. KGaA, Weinheim.

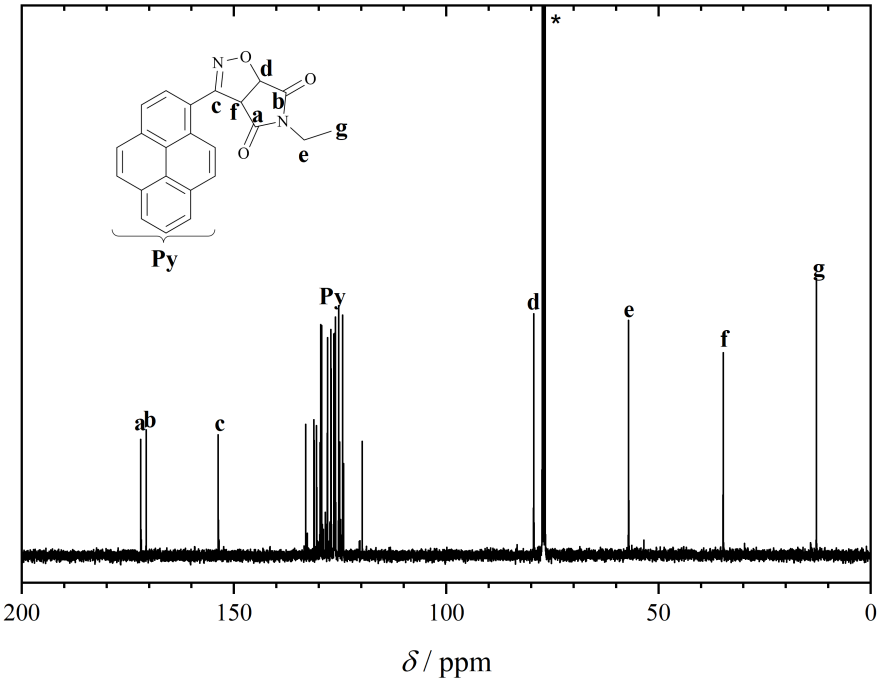

Figure D.8. ^{13}C NMR spectrum (100 MHz, $CDCl_3$, 298 K) of **C2**. The magnetic resonance marked with an asterisk is assigned to $CHCl_3$. Adapted with permission from reference [532]. Copyright (2019) Wiley-VCH Verlag GmbH & Co. KGaA, Weinheim.

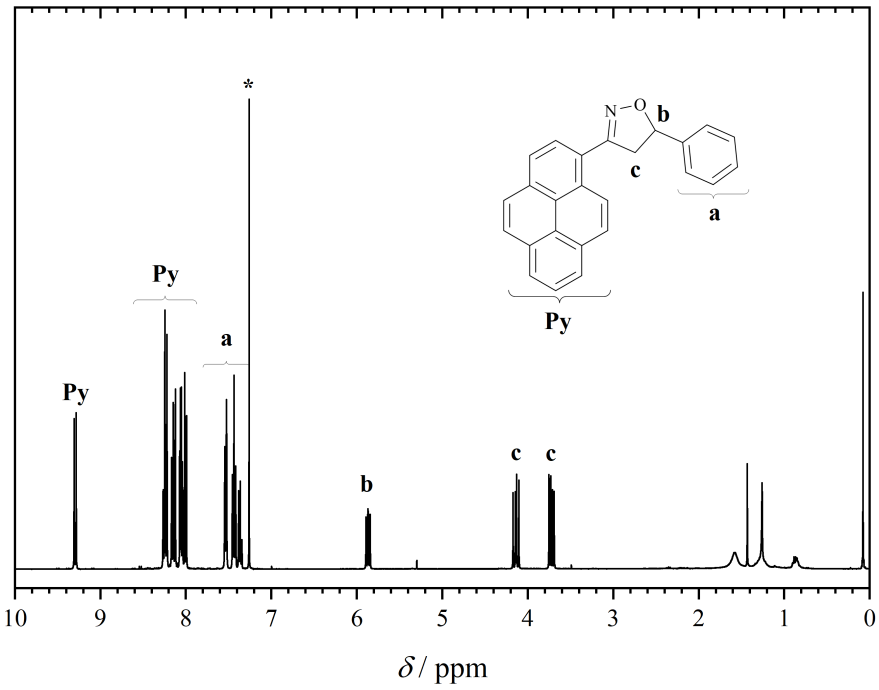

Figure D.9. ^{1}H NMR spectrum (400 MHz, $CDCl_3$, 298 K) of **C3**. The magnetic resonance marked with an asterisk is assigned to $CHCl_3$. Adapted with permission from reference [532]. Copyright (2019) Wiley-VCH Verlag GmbH & Co. KGaA, Weinheim.

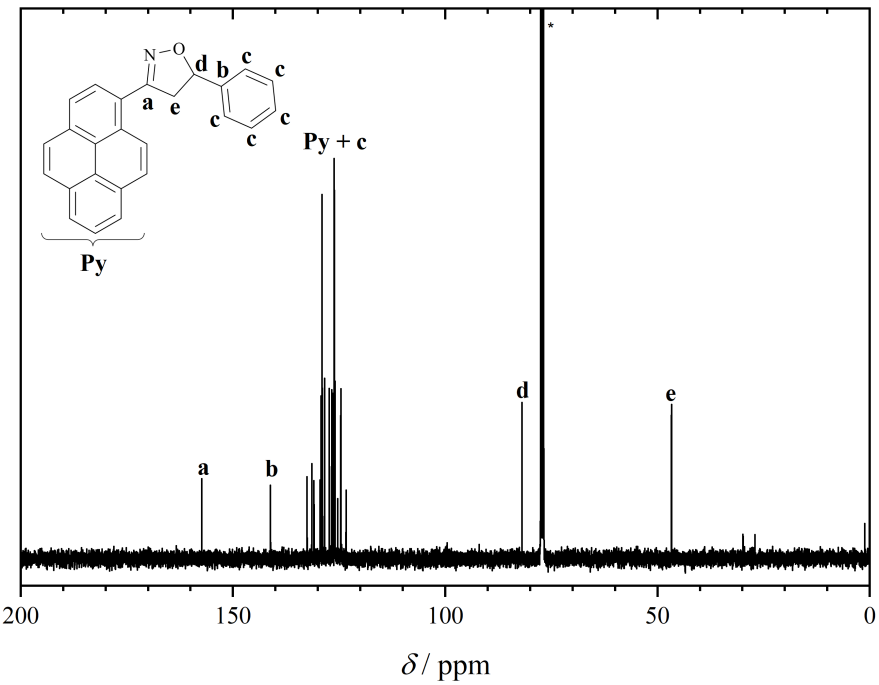

Figure D.10. ^{13}C NMR spectrum (100 MHz, $CDCl_3$, 298 K) of **C3**. The magnetic resonance marked with an asterisk is assigned to $CHCl_3$. Adapted with permission from reference [532]. Copyright (2019) Wiley-VCH Verlag GmbH & Co. KGaA, Weinheim.

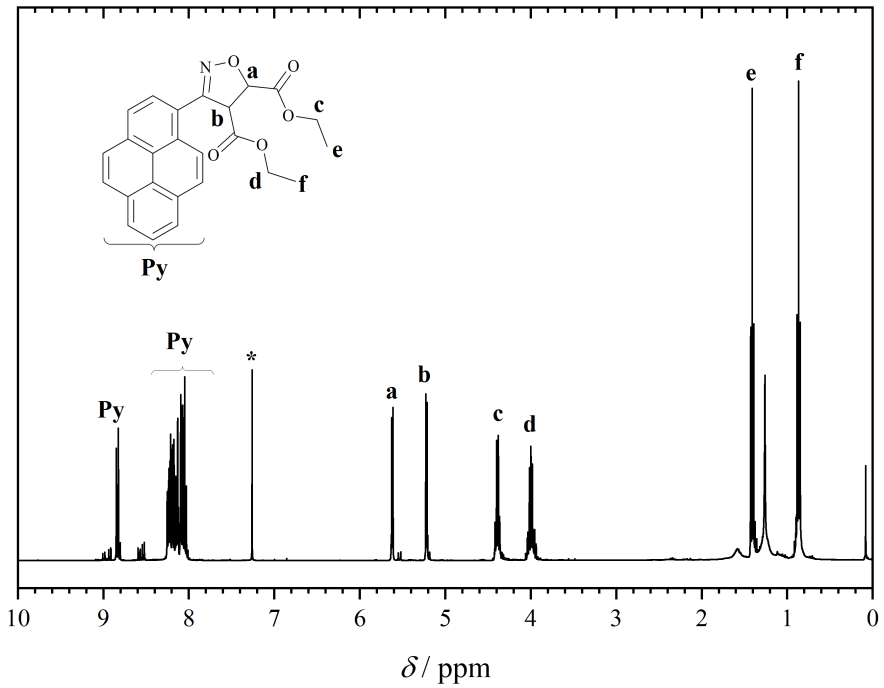

Figure D.11. ^{1}H NMR spectrum (400 MHz, $CDCl_3$, 298 K) of **C4**. The magnetic resonance marked with an asterisk is assigned to $CHCl_3$. Adapted with permission from reference [532]. Copyright (2019) Wiley-VCH Verlag GmbH & Co. KGaA, Weinheim.

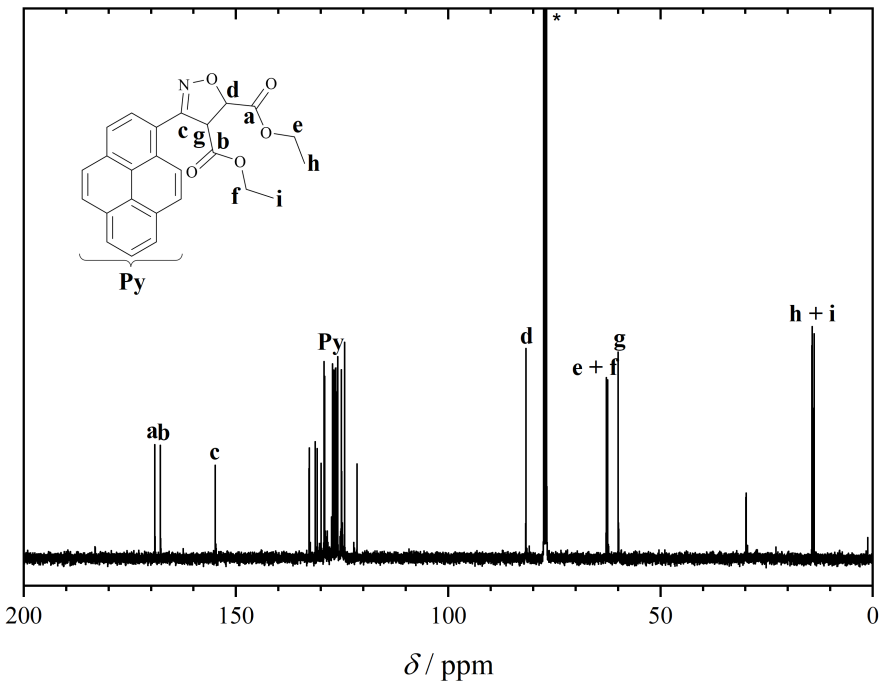

Figure D.12. ^{13}C NMR spectrum (100 MHz, $CDCl_3$, 298 K) of **C4**. The magnetic resonance marked with an asterisk is assigned to $CHCl_3$. Adapted with permission from reference [532]. Copyright (2019) Wiley-VCH Verlag GmbH & Co. KGaA, Weinheim.

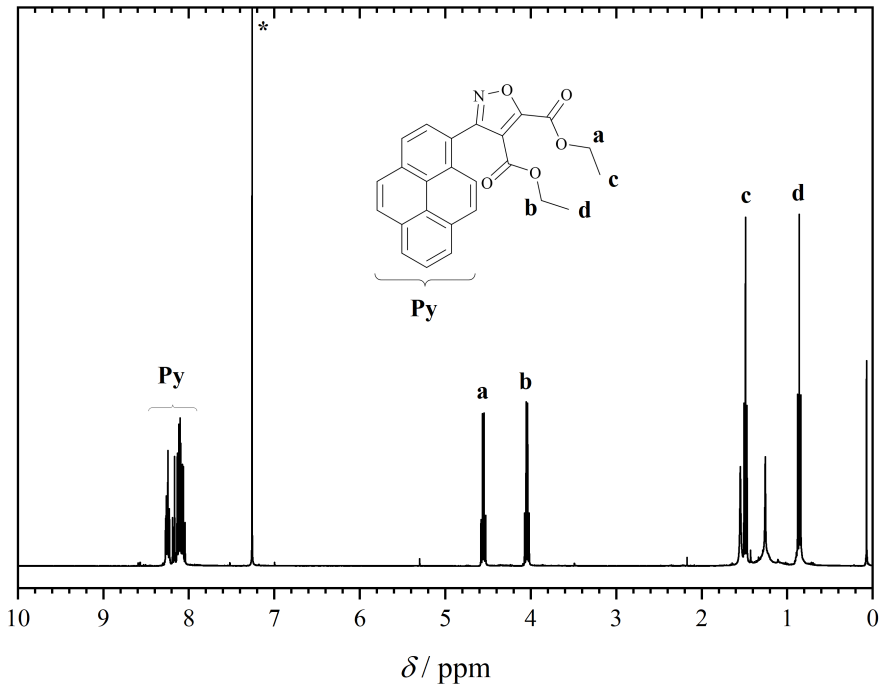

Figure D.13. ^{1}H NMR spectrum (400 MHz, $CDCl_3$, 298 K) of **C5**. The magnetic resonance marked with an asterisk is assigned to $CHCl_3$. Adapted with permission from reference [532]. Copyright (2019) Wiley-VCH Verlag GmbH & Co. KGaA, Weinheim.

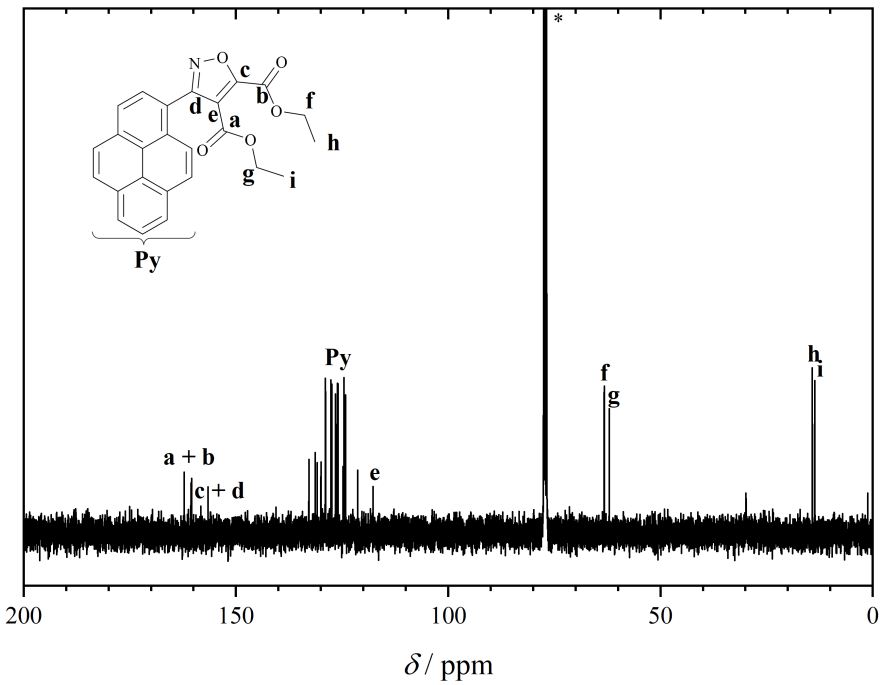

Figure D.14. ^{13}C NMR spectrum (100 MHz, $CDCl_3$, 298 K) of **C5**. The magnetic resonance marked with an asterisk is assigned to $CHCl_3$. Adapted with permission from reference [532]. Copyright (2019) Wiley-VCH Verlag GmbH & Co. KGaA, Weinheim.

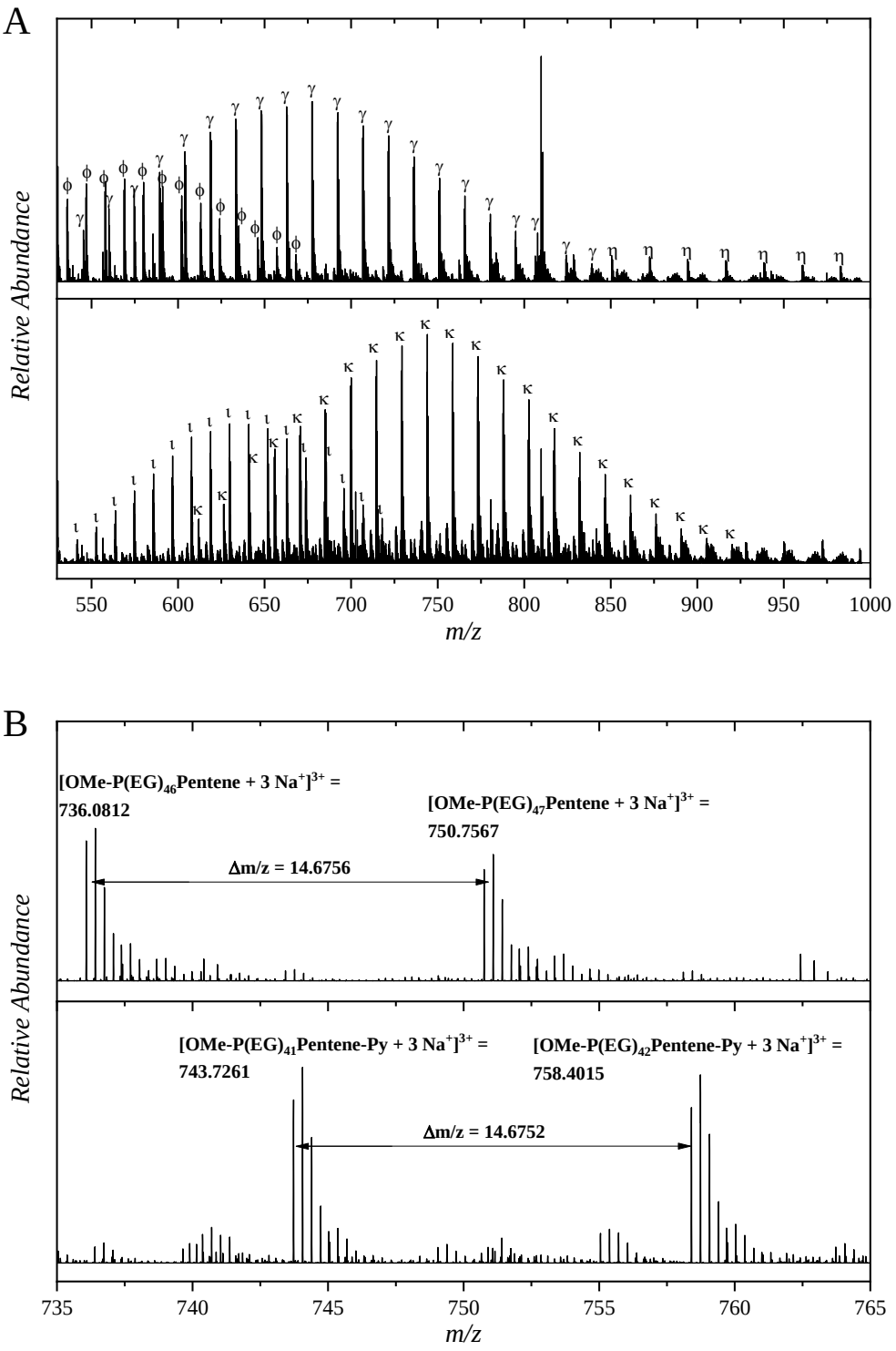

Figure D.15. **A**: Full ESI-MS spectrum of **P2** and **PC2**. Double-, tripel- and four-times-charged species are identified for **P2** (ϕ: double-charged, γ: triple-charged, η: four-times-charged), whereas double- and tripel-charged polymer distributions are visible for **PC2** (ι: double-charged, κ: triple-charged). **B**: Zoom-in into the tripel-charged species of the ESI-MS spectra of **P2** and **PC2**. Adapted with permission from reference [532]. Copyright (2019) Wiley-VCH Verlag GmbH & Co. KGaA, Weinheim.

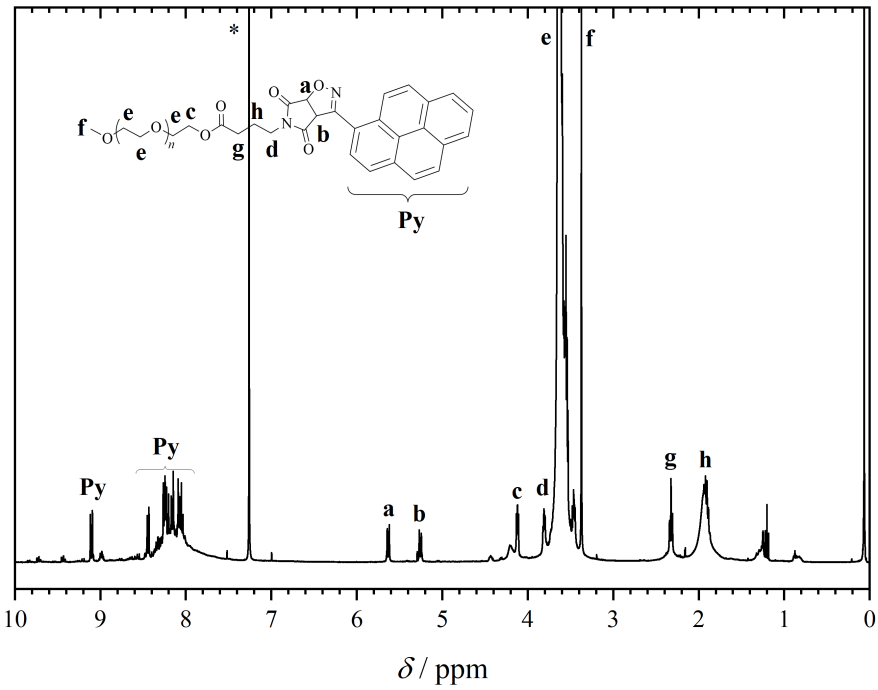

Figure D.16. ^{1}H NMR spectrum (400 MHz, $CDCl_3$, 298 K) of **PC1**. The magnetic resonance marked with an asterisk is assigned to $CHCl_3$. Adapted with permission from reference [532]. Copyright (2019) Wiley-VCH Verlag GmbH & Co. KGaA, Weinheim.

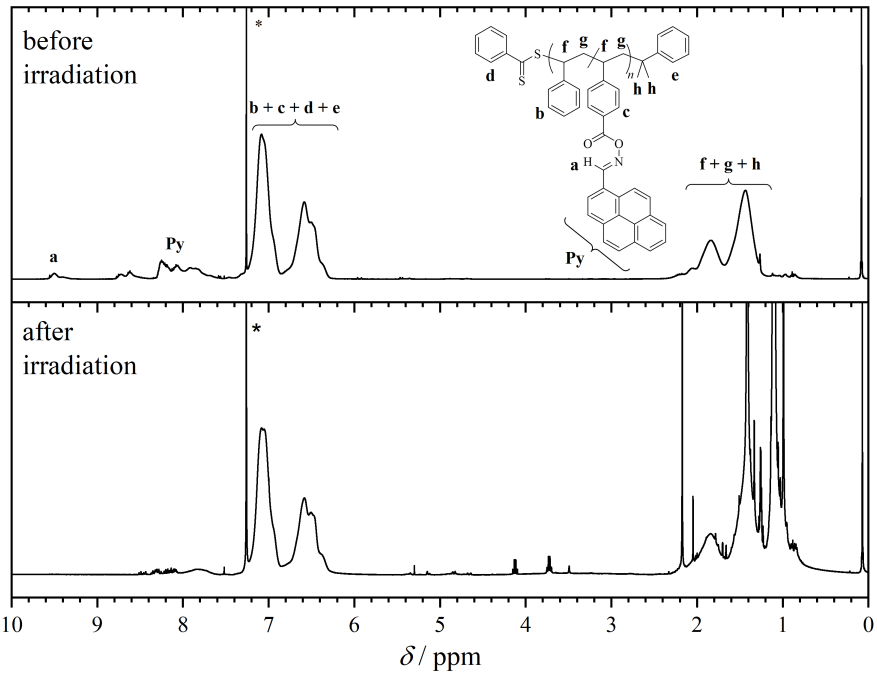

Figure D.17. ^{1}H NMR spectra (400 MHz, $CDCl_3$, 298 K) of **CDB PS PyOHSty 2** before (top spectrum) and after exposure to LED light (430-435 nm, bottom spectrum). The magnetic resonance marked with an asterisk is assigned to $CHCl_3$.

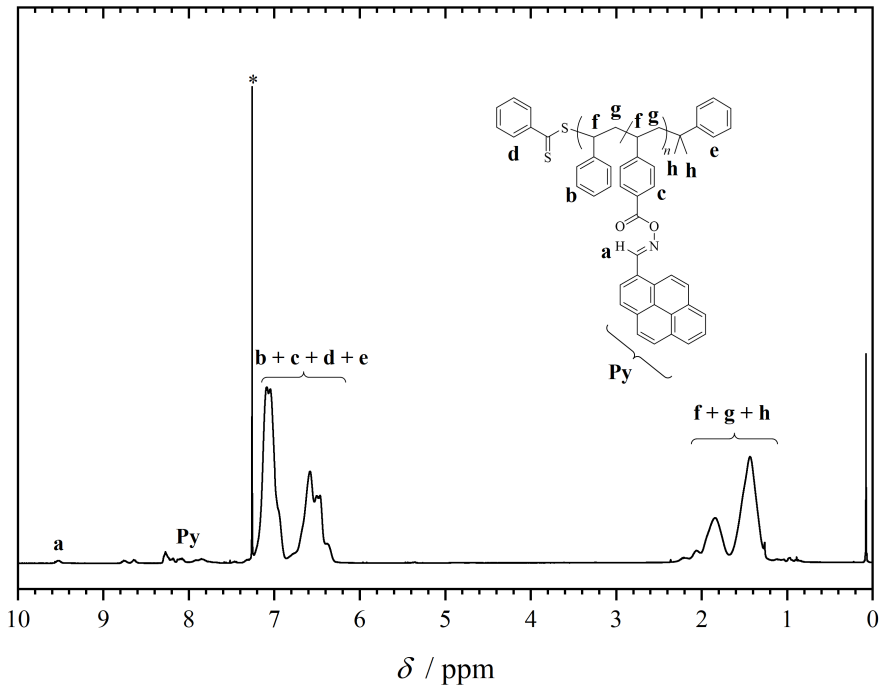

Figure D.18. ^{1}H NMR spectrum (400 MHz, $CDCl_3$, 298 K) of **CDB PS PyOHSty 3**. The magnetic resonance marked with an asterisk is assigned to $CHCl_3$.

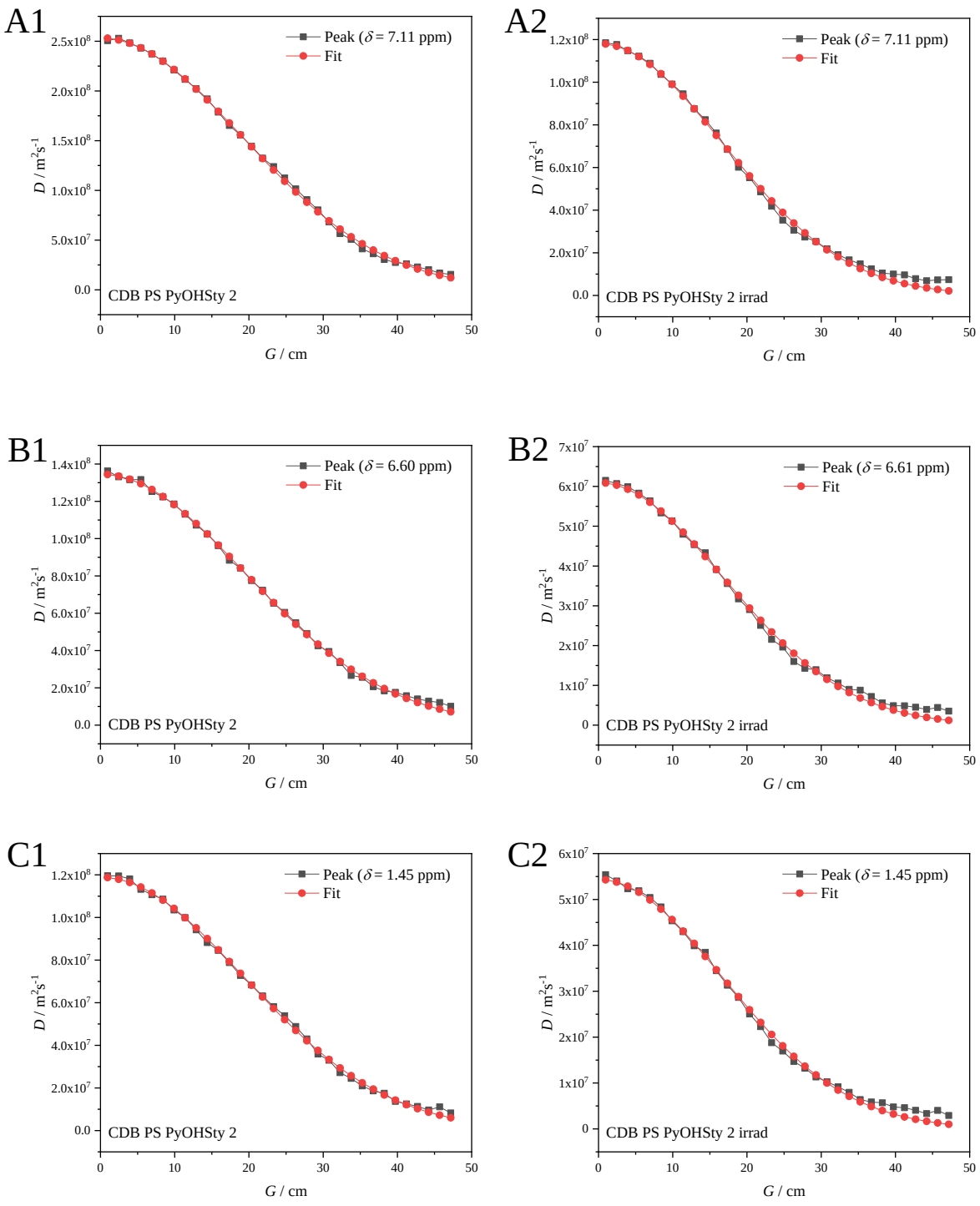

Figure D.19. DOSY NMR data fit of the polymeric species **CDB PS PyOHSty 2** before (**A1** to **C1**) and after LED irradiation (**A2** to **C2**).

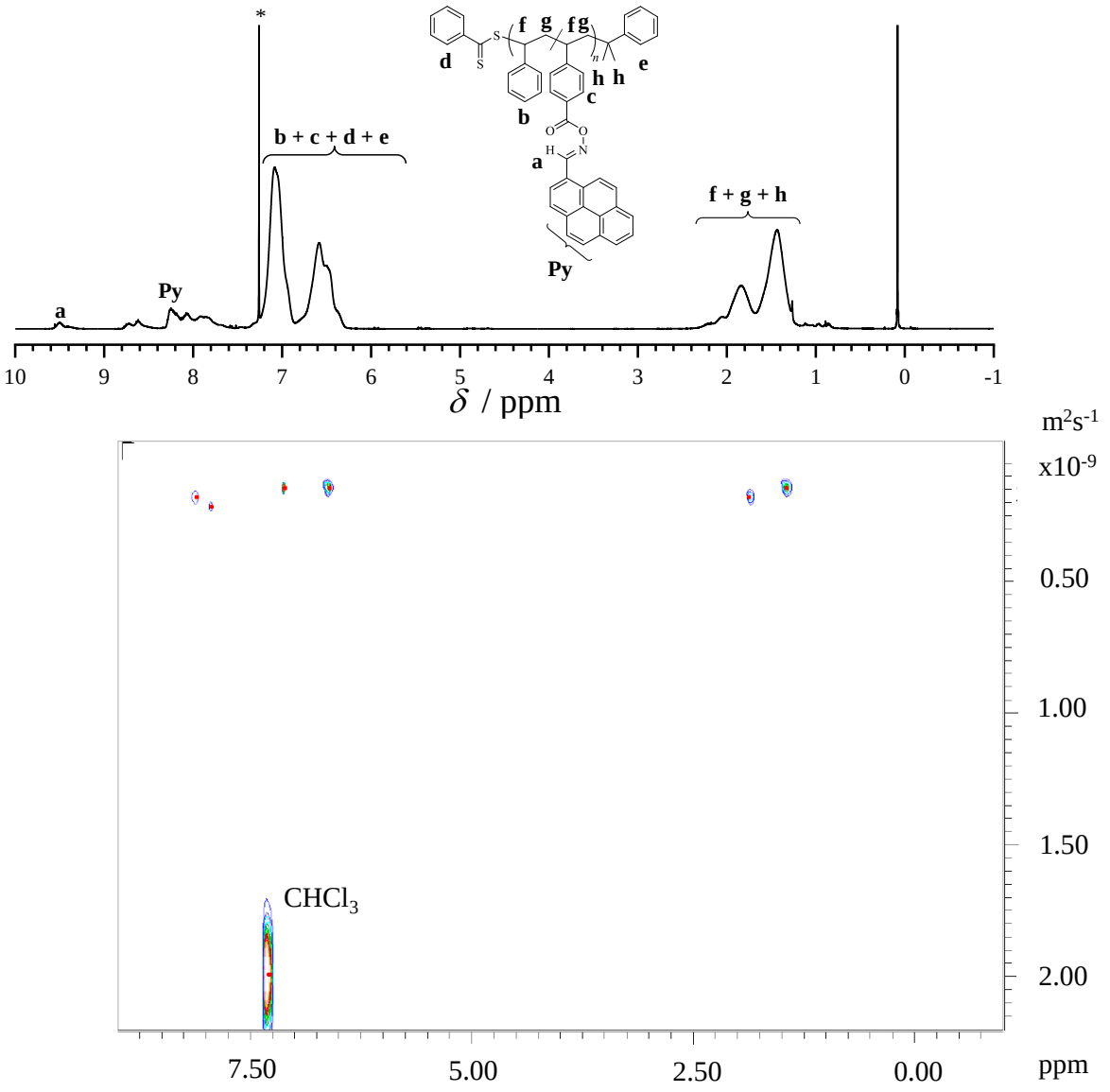

Figure D.20. DOSY NMR spectrum (400 MHz, $CDCl_3$, 298 K) of **CDB PS PyOHSty 2**. The magnetic resonance marked with an asterisk is assigned to $CHCl_3$.

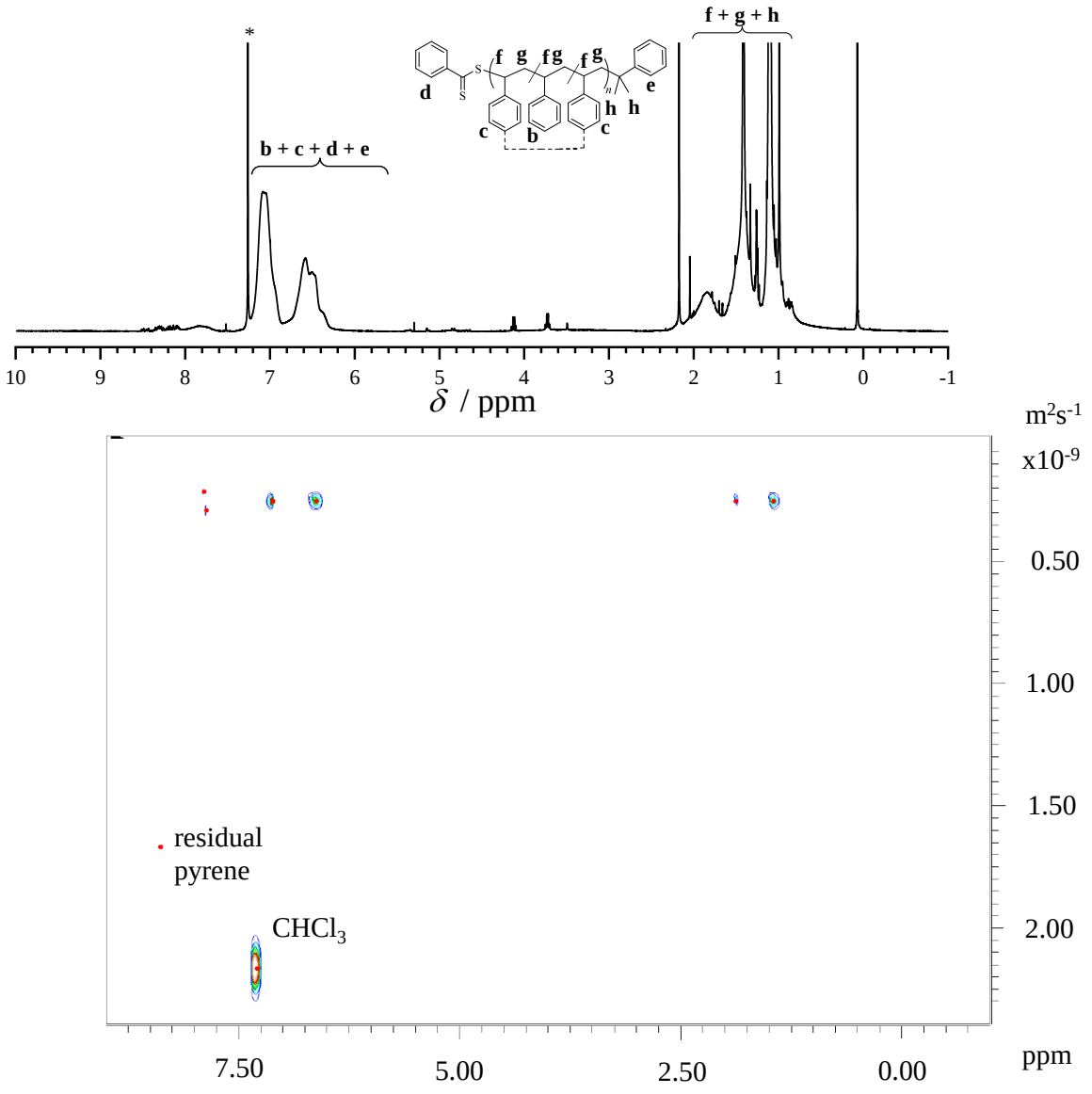

Figure D.21. DOSY NMR spectrum (400 MHz, $CDCl_3$, 298 K) of **CDB PS PyOHSty 2** after exposure to LED light (430-435 nm). The magnetic resonance marked with an asterisk is assigned to $CHCl_3$.

LIST OF PUBLICATIONS AND CONFERENCE DISTRIBUTIONS

Peer Reviewed Publications

8 *Contemporary Photoligation Chemistry - The Visible Light Challenge*
Offenloch, J. T.*; Gernhardt, M.*; Blinco, J. P.; Frisch, H.; Mutlu, H.; Barner-Kowollik, C. *Chem. Eur. J.*, **2019**, *25*, 3700-3709.

7 *Pyrene Tagged Chloro Oximes as Ambient Light Accelerated Ligation Agents*
Offenloch, J. T.; Bastian, S.; Mutlu, H.; Barner-Kowollik, C. *ChemPhotoChem* **2019**, *3*, 66-70.

6 *Light Induced Polyethylene Ligation*
Offenloch, J. T.; Norsic, S.; Mutlu, H.; Taam, M.; Boyron, O.; Boisson, C.; D'Agosto, F.; Barner-Kowollik, C. *Polym. Chem.* **2018**, *9*, 3633-3637.

5 *Visible Light [2+2] Cycloadditions for Reversible Polymer Ligation*
Marschner, D.; Frisch, H.; Offenloch, J. T.; Tuten, B. T.; Becer, R.; Walther, A.; Goldmann, A. S.; Tzvetkova, P.; Barner-Kowollik, C. *Macromolecules* **2018**, *51*, 3802-3807.

*Both authors contributed equally.

4 *Interrupted CuAAC Ligation: An Efficient Approach to Fluorescence Labeled Three-Armed Mikto Star Polymers*

Offenloch, J. T.; Mutlu, H.; Barner-Kowollik, C. *Macromolecules* **2018**, *51*, 2682-2689.

3 *Degradable Fluorescent Single-Chain Nanoparticles Based on Metathesis Polymers*

Offenloch, J. T.; Willenbacher, J.; Tzvetkova, P.; Heiler, C.; Mutlu, H.; Barner-Kowollik, C. *Chem. Commun.* **2017**, *53*, 775-778.

2 *Photochemically Induced Folding of Single Chain Polymer Nanoparticles in Water*

Heiler, C.; Offenloch, J. T.; Blasco, E.; Barner-Kowollik, C. *ACS Macro Lett.* **2017**, *6*, 56-61.

1 *Polybutadiene Functionalization via an Efficient Avenue*

Geiselhart, C. M.; Offenloch, J. T.; Mutlu, H.; Barner-Kowollik, C. *ACS Macro Lett.* **2016**, *5*, 1146-1151.

Conference Contributions

1 *Light Induced Polyethylene Ligation* (Poster Presentation)

Offenloch, J. T.; Norsic, S.; Mutlu, H.; Taam, M.; Boyron, O.; Boisson, C.; D'Agosto, F.; Barner-Kowollik, C., **Makro 2018**, September 24-27, **2018**, Karlsruhe, **Germany**.

2 *Interrupted CuAAC Ligation: An Efficient Approach to Fluorescence Labeled Three-Armed Mikto Star Polymers* (Poster Presentation)

Offenloch, J. T.; Mutlu, H.; Barner-Kowollik, C., **Bordeaux Polymer Conference (BPC)**, May 28-31, **2018**, Bordeaux, **France**.

3 *Photochemical Access to Self-Immolative Fluorescent Single-Chain Nanoparticles Based on Metathesis Polymers* (Poster Presentation)

Offenloch, J. T.; Willenbacher, J.; Tzvetkova, P.; Heiler, C.; Mutlu, H.; Barner-Kowollik, C., **European Symposium of Photopolymer Science (ESPS)**, September 12-14, **2016**, Leipzig, **Germany**.

ACKNOWLEDGEMENTS

An erster Stelle möchte ich mich bei Prof. Dr. Christopher Barner-Kowollik für die Möglichkeit meine Promotion in der macroarc Gruppe machen zu dürfen bedanken. Darüber hinaus bin ich dankbar für das spannende Thema, die nie endende Motivation und den Enthusiasmus, deine Unterstützung und die Freiheit, meine Forschung in viele erfolgsversprechende Richtungen lenken zu können. Und vielen Dank dafür, dass ich meine Forschungsergebnisse auf zahlreichen Konferenzen vorstellen durfte.

Ein nicht minder kleinerer Dank richte ich an Dr. Hatice Mutlu. Die Ausarbeitung von Projekten auf Basis von außergewöhnlichen Ideen sowie deine allzeit vorhandene Hilfe haben nicht nur einen besonderen Teil zu dieser Arbeit beigetragen, sondern du hast mich auch darüber hinaus geprägt. Dein niemals endendes Engagement und Optimismus waren ein wesentlicher Treibstoff während meiner Promotion. Ich wünsche dir, du gehst deinen Weg wo immer er dich auch führen wird.

Darüber hinaus, danke ich dem Fonds der Chemischen Industrie (FCI) und der Landesgraduiertenförderung für die finanzielle Unterstützung sowie Franck D'Agosto und Sébastien Norsic für die Zusammenarbeit im Polyethylen Projekt.

Hatice Mutlu, Rihannon Batchelor, Charlotte Petit, Carolin Heiler, Andrea Lauer und Markus Zieger danke ich für das Durchlesen und die Korrektur dieser Arbeit.

Fast vier Jahre lang waren wir zusammen in einem Labor und deswegen möchte ich Hannah Rothfuß für die unkomplizierte, problemlose und immer unterhaltsame Laborarbeit danken. Auch Chemie macht zu zweit mehr Spaß. ("Und nein, bitte kein Licht; die Jalousie bleibt unten...")

Einen super großen Dank möchte ich an meine Azubis Katharina Maier und Simon Bastian richten. Ihr wart eine großartige Unterstützung im Labor. Ich hoffe, ich konnte euch auch einiges zurückgeben. Des Weiteren danke ich Birgit Huber für die Hilfe bei der Synthese der Pyren-Verbindungen und Dr. Alexander Welle für die ToF-SIMS Messungen.

Ich danke auch den folgenden (ehemaligen) Kollegen für die Unterstützung bei der Betreuung des Massenspektrometers: Diego Estupignan, Kai Hiltebrandt, Astrid Hirschbiel, Michael Kaupp, Waldemar Konrad, Andrea Lauer, Edgar Molle und Charlotte Petit.

Dr. Maria Schneider-Baumann und Katharina Elies danke ich für die tadellose Wartung der SEC Systeme (auch am Massenspektrometer) sowie für die Tatsache, dass wir immer alles hatten, was wir brauchten und falls nicht, so wurde alles super fix erledigt. Evelyn Stühring danke ich für das Erledigen von allen administrativen Angelegenheiten.

Natürlich möchte ich auch der ganzen macroarc Gruppe danken, sei es für die sehr gute Arbeitsatmosphäre, Unterstützung oder auch für die schönen Zeiten obwohl sich wirklich viel verändert hat.

Ein Dank möchte ich auch an das Sportinstitut vom KIT richten: Die Kurse waren ein wichtiger Bestandteil meiner Promotion. Besonders hervorzuheben ist hierbei der TôsôX Kurs.

Und zu guter Letzt: Vielen Dank Jonas, dass du immer für mich da bist!

DECLARATION

Hiermit erkläre ich, Janin Tanja Offenloch, dass ich die vorliegende Dissertation selbstständig im Rahmen der Betreuung durch Prof. Dr. Christopher Barner-Kowollik verfasst habe und keine anderen als die von mir angegebenen Quellen und Hilfsmittel benutzt habe, die wörtlich oder inhaltlich übernommenen Stellen als solche kenntlich gemacht und die Regeln zur Sicherung guter wissenschaftlicher Praxis des KIT in der jeweils gültigen Fassung beachtet wurden. Darüber hinaus stimmt die elektronische Version der Arbeit mit der schriftlichen überein, und die Abgabe und die Archivierung der Primärdaten sind gemäß Abs. A (6) der Regeln zur Sicherung guter wissenschaftlicher Praxis des KIT beim Institut gesichert.

Des Weiteren erkläre ich, dass ich mich derzeit in keinem laufenden Promotionsverfahren befinde und auch keine vorausgegangenen Promotionsversuche unternommen habe.

Ort, Datum

Unterschrift